Bioinspired Electrocatalytic Hydrogen Production: Synthetic and Biological Approaches

by

Joseph A. Laureanti

A Dissertation Presented in Partial Fulfillment
of the Requirements for the Degree
Doctor of Philosophy

Approved February 2017 by the
Graduate Supervisory Committee:

Anne Katherine Jones, Chair
Thomas Moore
Kevin Redding

ARIZONA STATE UNIVERSITY

May 2017

ABSTRACT

Development of efficient and renewable electrocatalytic systems is foundational to creation of effective means to produce solar fuels. Many redox enzymes are functional electrocatalysts when immobilized on an electrode, but long-term stability of isolated proteins limits use in applications. Thus there is interest in developing bio-inspired functional catalysts or electrocatalytic systems based on living organisms. This dissertation describes efforts to create both synthetic and biological electrochemical systems for electrocatalytic hydrogen production.

The first part of this dissertation describes the preparation of three different types of proton reduction catalysts. First, four bioinspired diiron complexes of the form (μ-SRS)Fe(CO)$_3$[Fe(CO)(N-N)] for SRS = 1,2-benzenedithiolate (bdt) and 1,3-propanedithiolate (pdt) and N-N = 2,2'-bipyridine (bpy) and 2,2'-bypyrimidine (bpym), are described. Electrocatatlytic experiments show that although the byprimidinal complexes are not catalysts, the bipyridyl complexes produce hydrogen from acetic acid under reducing conditions. Second, three new mononuclear Fe^{II} carbonyl complexes of the form [Fe(CO)(bdt)(PPh_2)$_2$] in which P_2 = bis-phosphine: 4,5-Bis(diphenylphosphino)-9,9-dimethylxanthene (Xantphos), 1,2-Bis(diphenylphosphino)benzene (dppb), or cis-1,2-Bis(diphenylphosphino)ethylene (dppv) are described. All are functional bio-inspired models of the distal Fe site of [FeFe]-hydrogenases. Of these, the Xanthphos complex is the most stable to redox reactions and active as an electrocatalyst. Third, a molybdenum catalyst based on the redox non-innocent PDI ligand framework is also shown to produce hydrogen in the presence of acid.

The second part of this dissertation describes creating functional interfaces between chemical and biological models at electrode surfaces to create electroactive systems. First, covalent tethering of the redox probe ferrocene to thiol-functionalized reduced graphene oxide is demonstrated. I demonstrate that this attachment is via the thiol functional groups. Second, I demonstrate the ability to use electricity in combination with light to drive production of hydrogen by the anaerobic, phototrophic microorganism *Heliobacterium modesticaldum*.

DEDICATION

To my wife, for not leaving me after being so poor for so long. I love you! I would most definitely not be where I am today without you by my side.

To my daughters: Tinley and Stella for making everyday awesome and forcing me to take myself a little less serious everyday. You two are capable of anything!

To my grandparents, Nana and Tata & Grams and Gramps, who never gave up on me and never stopped encouraging me.

To my mom for always being there for me.

ACKNOWLEDGMENTS

Graduate school would not have been possible without an incredible amount of help from Professor Ana Moore, who allowed me to work in her lab as a clumsy undergraduate student and guided me through my transition into graduate school. I would also like to acknowledge Professor Tom Moore and Kevin Redding for allowing me to work on projects under your guidance my first year and for continuing to put up with me over the years.

I would like to thank all of my fellow IGERT students who have been there, sometimes more-or-less, week in and week out throughout our graduate school experience. I would also like to thank the National Science Foundation for the very generous financial support during the fellowship and the opportunities that resulted as a direct consequence of participating in the IGERT-SUN program. I also need to thank LightWorks for funding the work with *Heliobacterium modesticaldum.*

I would also like to thank my lab members, most notably for tolerating me, and for always being there to chat about anything serious or completely random. I'm not sure how you all managed to deal with me, I know it always wasn't easy, but I am very glad to have had the opportunity to share the lab and learn from everyone.

Lastly, and most importantly, I need to thank my advisor Anne K. Jones. I have learned more from you in the past four years than I have from anyone in my entire life. Not only are you an amazing scientist, you are also a very positive role model for me. I had no idea how I was supposed to be an effective father and finish graduate school. You never pressured me to put work ahead of family, and you have no idea how much that means to me and my family! Thank you!

TABLE OF CONTENTS

CHAPTER Page

APPENDIX Page

LIST OF TABLES

LIST OF FIGURES

Figure Page

Figure Page

LIST OF SCHEMES

LIST OF ABBREVIATIONS

AcOH	Acetic Acid
adt	Azadithiolate (SCH_2NHCH_2S)
adt^{Bn}	$(SCH_2)_2NBn$
bdt	1,2-Benzenedithiolate
BES	Bio-Electrochemical System
BPV	Bio-Photovoltaic Cell
bpy	2,2'-bipyridine
bpym	2,2'-bipyrimidine
Cb_{562}	Cytochrome b_{562} (*E. coli*)
CCCP	Carbonyl Cyanide *m*-chlorophenyl hydrazone
DBMIB	2,5-Dibromo-3-methyl-6-isopropylbenzoquinone
DCM	Methylene Chloride
DCMU	3-(3,4-Dichlorophenyl)-1,1-dimethylurea
DFT	Density Functional Theory
dppb	1,2-Bis(diphenylphosphino)-benzene
dppf	1,1'-Bis(diphenylphosphino)ferrocene
dppv	1,2-Bis(diphenylphosphino)ethylene
EET	Extracellular Electron Transfer
EEU	Extracellular Electron Uptake
EPPG	Edge-Plane Pyrolytic Graphite
Fc	Ferrocene

FcCA	Ferrocene Carboxylic Acid
Fd	Ferrodoxin
FdI	Ferredoxin I (*Spirulina platensis*)
Fe_D	Distal Iron
Fe_P	Proximal Iron
FTIR	Fourier Transform Infrared Spectroscopy
GC	Gas Chromatograph
GO	Graphene Oxide
HbRC	Heliobacterial Reaction Center
HER	Hydrogen Evolution Reaction
HOMO	Highest Occupied Molecular Orbital
ITO	Indium Tin Oxide
KCN	Potassium Ferricyanide
LB	Langmuir-Blodgett
LED	Light Emitting Diode
LUMO	Lowest Unoccupied Molecular Orbital
Me_3NO	Trimethylamine N-oxide
MES	2-[N'-Morpholino]ethane-sulfonic acid
MET	Microbial Electrochemical Technologies
Methylene-H_4MPT	Methenyltetrahydromethanopterin
MFC	Microbial Fuel Cell
MOPS	3-(N-Morpholino)propanesulfonic acid

mRGO	Mercaptan-rich Reduced Graphene Oxide
OCP	Open Circuit Potential
p-TsOH	*p*-Toluenesulfonic Acid
PCP	Pentachlorophenol
pdt	1,3-Propanedithiolate
$PFc^{*Et}{}_2$	$Et_2PCH_2C_5Me_4FeCp^*$
PMA	Phenyl Mercuric Acetate
PMFC	Photosynthetic Microbial Fuel Cell
PSI	Photosystem I
PSII	Photosystem II
RC	Reaction Center
RGO	Reduced Graphene Oxide
RPM	Revolutions Per Minute
SHE	Standard Hydrogen Electrode
SP	Square Pyramidal
TAPS	N'-Tris[hydroxymethyl]methyl-3-amino-propane-sulfonic acid
TBAPF6	Tetrabutylammonium Hexafluorophosphate
TBP	Trigonal Bipyramidal
TCD	Thermal Conductivity Detector
THF	Tetrahydrofuran
TOF	Turn Over Frequency
tRGO	Thermally Reduced Graphene Oxide

Xantphos	4,5-Bis(diphenylphosphino)-9,9-dimethylxanthene
XPS	X-ray Photoelectron Spectroscopy

Chapter 1

Introduction: An overview of biomimetic active site analogues of the [FeFe]-hydrogenase active site, extracellular electron transfer, and the summary and scope of this dissertation

Joseph A. Laureanti

School of Molecular Sciences
Arizona State University, Tempe, AZ 85287

Overview of Hydrogenases

Biologically, chemical reactions are catalyzed by enzymes, protein catalysts, evolved throughout millions of years of selective pressure.[1-3] Enzymes may employ a variety of chemical structures in the active site: amino acids[1-4], nucleic acids[5], or even metallocofactors.[6]

Hydrogenases are redox active metalloenzymes, also known as oxidoreductases, that are essential to energy conservation and regulation in diverse microbial systems.[7] There are three types of hydrogenases which are distinguished by active site composition: [Fe], [FeFe], and [NiFe].[8,9] The [FeFe] and [NiFe]-hydrogenases evolved independently but are functionally related, Figure 1-1. Unlike [Fe] hydrogenases, [FeFe] and [NiFe]-hydrogenases each contain [FeS] clusters that shuttle electrons to and from the protein surface to the buried active site where catalysis occurs.[8] [Fe]-hydrogenases are referred to as H_2-forming methenyltetrahydromethanopterin (methylene-H_4MPT) dehydrogenase because they employ H_2 as a hydride donor to catalyze the reversible reduction of methylene-H_4MPT$^+$, producing methylene-H_4MPT and a free proton.[8] [Fe]-hydrogenases exist only in methanogenic archaea and are not capable of reducing exogenous substrates. The [Fe]-hydrogenase active site contains a five-coordinate low-spin Fe^{II} with the first coordination sphere completed by two carbonyls, water, a cysteine ligand, and a pyridine cofactor.[10-12] In contrast to [FeFe] and [NiFe]-hydrogenases, [Fe]-hydrogenases are severely inhibited by the presence of isocyanide ligands.[13]

[NiFe]-hydrogenases are generally found in strict anaerobes and facultative anaerobes and have been discovered in archaea, eubacteria, cyanobacteria, and some eukarya.[14-18] [NiFe]-hydrogenases generally consist of multiple subunits with one subunit

housing the active site, which in the resting state, Ni-SI_a, consists of Fe^{II} and Ni^{II} centers bridged by cysteinyl thiolate ligands.[15] The rest of the first coordination spheres are completed by two cyano and one carbonyl ligand for the low-spin Fe^{II} species and two cysteinyl thiolate ligands for Ni^{II}.[19,20] Evidence suggests that throughout the catalytic cycle the Fe ion does not change oxidation state (i.e. maintains as Fe^{II}), and all electron transfer occurs at the nickel, which cycles between Ni^{II} and Ni^{III}.[7] [NiFe]-hydrogenase are characterized by four general groups: 1) Uptake hydrogenases, 2) Cyanobacterial uptake hydrogenases and H_2 sensors, 3) Bidirectional heteromultimeric cytoplasmic hydrogenases, and 4) H_2-evolving, energy-conserving, membrane-associated hydrogenases.[15]

While [NiFe]-hydrogenase are generally thought of as H_2-uptake hydrogenase, the [FeFe]-hydrogenase are generally considered H_2-producing hydrogenase. However, recent observations are challenging this paradigm by providing examples of [FeFe]-hydrogenase that are biased towards H_2 uptake rather than H_2 production. The H-cluster of [FeFe]-hydrogenase contains an azadithiolate (S-H_2C-NH-CH_2-S) chain bridging the two iron ions. The proximal iron shares a cysteinyl thiolate with a standard [4Fe-4S] cluster.[21] Unseen in nature outside of hydrogenases is the presence of carbonyl and cyano ligands. Proximal and distal iron ions share a bridging carbonyl with each also ligated to an additional carbonyl and a cyano ligand. The well known complex [(μ-pdt)-$Fe_2(CO)_6$] (pdt = 1,3-propanedithiol) is the simplest structural and functional model of the H-cluster, but it shows relatively poor catalytic activity.[22] Many structural and functional mimics have been developed since the structural elucidation by X-ray diffraction of the structure of [FeFe]-hydrogenases.[21,23]

Microbial Extracellular Electron Transfer

The earliest experiments interfacing microorganisms with electrodes employed two photosynthetic organisms that were shown to produce current upon illumination.[24] Although these experiments incorporated the use of both live microorganisms and electrodes, the reactions taking place at the electrodes did not directly involve interactions with the microorganisms. Instead, photosynthetically produced oxygen or hydrogen served as the reactive species at the electrode surface. After these pioneering experiments, it has now been shown that organisms across various genera can both directly and indirectly associate with exogenous metal oxides and use them as either terminal electron acceptors or as primary electron donors to metabolism.[25,26] Three mechanisms for extracellular electron transfer and uptake have been proposed: 1) direct association of the outer membrane with the inorganic substrate, 2) the use of pili or nanowires to connect the bacterium with the electrode surface, and 3) electron transfer via exogenous redox active molecules that can shuttle electrons between the organism and the inorganic substrate, **Figure 1-2**.[27] Lovley and co-workers suggest that the interaction of *Geobacter* sp. with inorganic substrates is completed *via* pili and or c-type cytochromes, but the data supporting these findings are incomplete, inconclusive and often contradictory.[28-30] In general, outer-membrane *c*-type cytochromes have proven a common theme in organisms known for extracellular electron transfer. El-Naggar and co-workers have shown that *Shewanella* sp. produce appendages, that do not resemble pili, that contain both lipid and protein.[31] These results strongly suggest that *Shewanella* sp. encapsulates c-type cytochromes in extensions of the periplasm towards the inorganic substrate.[31] Finally, it has been shown that *Shewanella* sp., as well as some gram-positive

bacteria, are capable of synthesizing flavins for excretion to the surrounding environment.[32-34] Flavins have also been shown to interact with specific outer-membrane *c*-type cytochromes and to increase the current produced in a microbial fuel cell.[35]

Summary and Scope of this Dissertation

I have two foci for this dissertation: descriptions of new coordination complexes capable of proton reduction to hydrogen and interfacing of microorganisms and electrodes to produce functional systems. I start by describing the structures and catalytic properties of a collection of three new diiron structural and functional mimics of the [FeFe]-hydrogenase active site designed to probe the effects of N,N'-heterocyclic ligands on the metallo-center (Chapter 2). Then, electrocatalytic hydrogen production by three new biomimetic pentacoordinate mononuclear Fe^{II} carbonyls containing 1,2-benzenedithiol is described (Chapter 3). In Chapter 4, I describe electrocatalysis by a molybdenum-oxo species. Chapter 5 describes covalent immobilization of ferrocene carboxylic acid at mercaptan rich reduced graphene oxide sheets deposited on a gold surface. In chapter 6 I present a brief review of extracellular electron transfer pertaining to photosynthetic microoganisms. In Chapter 7, I investigate the properties of extracellular electron uptake by the thermophilic anaerobe *H. modesticaldum* at a carbon cloth biocathode.

Figures

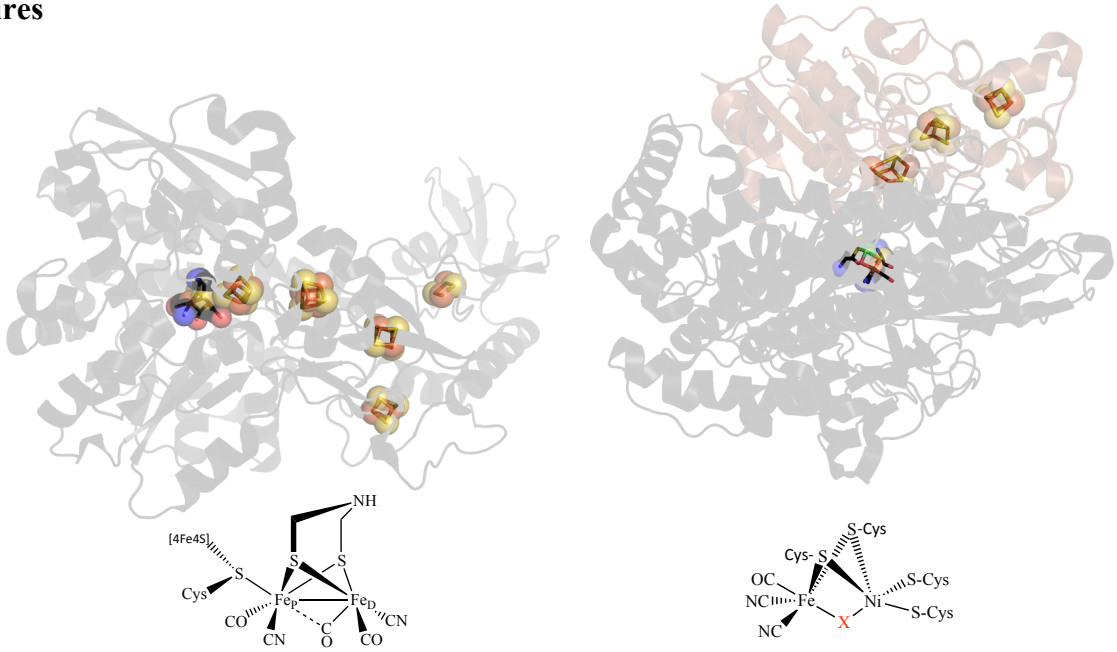

Figure 1-1. Tertiary structure and close up of active site of (A) [FeFe]-hydrogenase from *Clostridium pastuerinum* (PDB ID = 4xdc) and (B) quaternary structure [NiFe]-hydrogenase from *Ralstonia eutropha* (PDB ID = 4ttt). Metallocenters are shown in space filling representation. Atoms are represented by the following colors: yellow, orange, black, blue, red, for sulphur, iron, carbon, nitrogen, and oxygen, respectively.

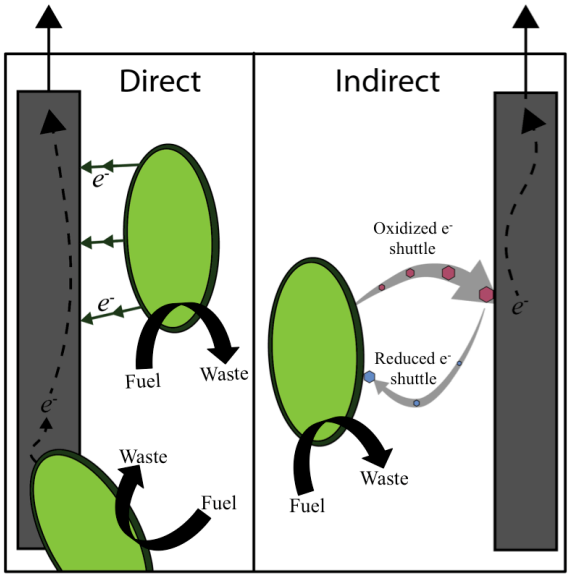

Figure 1-2. Direct microbial EET vs mediated microbial EET. Schematic for direct electron transfer (left) includes two models: EET facilitated by "nanowires" (top), and EET facilitated by direct association of the outer membrane of a microorganism with the electrode surface (bottom). Schematic for mediated electron transfer (right) in which a microorganism utilizes diffusion of a soluble redox mediator to facilitate EET. In each case, the microorganisms catabolize a fuel (for example, industrial waste) and extracted electrons are transferred to the electrode surface.

References

1. Dewar, M. J., & Storch, D. M. (1985). Alternative view of enzyme reactions. *P. Natl. Acad. Sci. USA*. ***82***(8), 2225–2229.

2. Warshel, A., Sharma, P. K., Kato, M., Xiang, Y., Liu, H., & Olsson, M. H. M. (2006). Electrostatic basis for enzyme catalysis. *Chem. Rev. 106*(8), 3210–3235. http://doi.org/10.1021/cr0503106.

3. Albery, W. J. & Knowles, J. R. (1976) Free-energy profile of the reaction catalyzed by triosephosphate isomerase. *Biochemistry.* **15,** 5627–5631.

4. Kedishvili, N. Y. *et al.* Expression and kinetic characterization of recombinant human stomach alcohol dehydrogenase. Active-site amino acid sequence explains substrate specificity compared with liver isozymes. *J. Biol. Chem.* **270,** 3625–3630 (1995).

5. Chambon, P. (1975). Eukaryotic nuclear RNA polymerases. *Annu. Rev. Biochem.* ***44***, 613–638. http://doi.org/10.1146/annurev.bi.44.070175.003145.

6. Waldron, K. J., Rutherford, J. C., Ford, D. & Robinson, N. J. Metalloproteins and metal sensing. *Nature.* **460,** 823–830 (2009).

7. Shafaat, H. S., Rüdiger, O., Ogata, H. & Lubitz, W. *BBA - Bioenergetics.* **1827,** 986–1002 (2013).

8. Lubitz, W.; Ogata, H.; Rüdiger, O.; Reijerse, E. Hydrogenases. *Chem. Rev*. **114,** 4081–4148 (2014).

9. Frey, M. Hydrogenases: hydrogen-activating enzymes. (2002) *Chem. Eur. J. of Chem. Bio.* **3,** 153–160

10. Wang, X. *et al.* The iron centre of the cluster-free hydrogenase (Hmd): low-spin Fe(ii) or low-spin Fe(0)? *Chem Commun.* **3555** (2008). doi:10.1039/b805262j

11. Salomone-Stagni, M. *et al.* The iron-site structure of [Fe]-hydrogenase and model systems: an X-ray absorption near edge spectroscopy study. *Dalton T.* **39,** 3057 (2010).

12. Guo, Y. *et al.* Characterization of the Fe Site in Iron−Sulfur Cluster-Free Hydrogenase (Hmd) and of a Model Compound via Nuclear Resonance Vibrational Spectroscopy (NRVS). *Inorg. Chem.* **47,** 3969–3977 (2008).

13. Shima, S. & Ataka, K. Isocyanides inhibit [Fe]-hydrogenase with very high affinity. *FEBS Lett.* **585,** 353–356 (2010).

14. Vignais, P. M., Billoud, B., & Meyer, J. (2001). Classification and phylogeny of hydrogenases. *FEMS Microbiol. Rev.* ***25***(4), 455–501.

15. Vignais, P. M. & Billoud, B. Occurrence, Classification, and Biological Function of Hydrogenases: An Overview. *Chem. Rev.* **107,** 4206–4272 (2007).

16. Tamagnini, P. *et al.* Hydrogenases and Hydrogen Metabolism of Cyanobacteria. *Microbiol. Mol. Biol. R.* **66,** 1–20 (2002).

17. Tamagnini, P. *et al.* Cyanobacterial hydrogenases: diversity, regulation and applications. *FEMS Microbiol. Rev.* **31,** 692–720 (2007).

18. Thauer, R. K. *et al.* Hydrogenases from Methanogenic Archaea, Nickel, a Novel Cofactor, and H_2 Storage. *Annu. Rev. Biochem.* **79,** 507–536 (2010).

19. Goris, T. *et al.* A unique iron-sulfur cluster is crucial for oxygen tolerance of a [NiFe]-hydrogenase. *Nat. Chem. Biol.* **7,** 310–318 (2011).

20. Abou Hamdan, A. *et al.* O_2-independent formation of the inactive states of NiFe hydrogenase. *Nat. Chem. Biol.* **9,** 15–17 (2012).

21. Nicolet, Y., Piras, C., Legrand, P., Hatchikian, C. E. & Fontecilla-Camps, J. C. *Desulfovibrio desulfuricans* iron hydrogenase: the structure shows unusual coordination to an active site Fe binuclear center. *Structure* **7,** 13–23 (1999).

22. Tard, C. & Pickett, C. J. Structural and Functional Analogues of the Active Sites of the [Fe]-, [NiFe]-, and [FeFe]-Hydrogenases. *Chem. Rev.* **109,** 2245–2274 (2009).

23. Peters, J. W., Lanzilotta, W. N., Lemon, B. J. & Seefeldt, L. C. (1998) X-ray crystal structure of the Fe-only hydrogenase (CpI) from *Clostridium pasteurianum* to 1.8 angstrom resolution. *Science.* **282,** 1853–1858

24. Berk, R. S. & Canfield, J. H. Bioelectrochemical energy conversion. *Appl. Microbiol.* (1964).

25. Hernandez, M. E. & Newman, D. K. Extracellular electron transfer. *Cell. Mol. Life Sci.* (2001).

26. Lovley, D. R. *et al. Geobacter metallireducens* gen. nov. sp. nov., a microorganism capable of coupling the complete oxidation of organic compounds to the reduction of iron and other metals. *Arch. Microbiol*. **159,** 336–344 (1993).

27. Torres, C. I. *et al.* A kinetic perspective on extracellular electron transfer by anode-respiring bacteria. *FEMS Microbiol. Rev.* **34,** 3–17 (2010).

28. Smith, J. A. *et al.* Going Wireless: Fe(III) Oxide Reduction without Pili by *Geobacter sulfurreducens* Strain JS-1. *Appl. Environ. Microb.* **80,** 4331–4340 (2014).

29. Lovley, D. R. Bug juice: harvesting electricity with microorganisms. *Nat. Rev. Micro.* **4,** 497–508 (2006).

30. Yates, M. D. *et al.* Measuring conductivity of living *Geobacter sulfurreducens* biofilms. *Nat. Nanotechnol.* **11,** 910–913 (2016).

31. Pirbadian, S. *et al. Shewanella oneidensis* MR-1 nanowires are outer membrane and periplasmic extensions of the extracellular electron transport components. *P. Natl. Acad. Sci. USA*. **111,** 12883–12888 (2014).

32. Yang, Y. *et al.* Enhancing Bidirectional Electron Transfer of *Shewanella oneidensis* by a Synthetic Flavin Pathway. *ACS Synth. Biol.* **4,** 815–823 (2015).

33. Marsili, E. *et al. Shewanella* secretes flavins that mediate extracellular electron transfer. *P. Natl. Acad. Sci. USA*. **105,** 3968–3973 (2008).

34. Canstein, von, H., Ogawa, J., Shimizu, S. & Lloyd, J. R. Secretion of Flavins by *Shewanella* Species and Their Role in Extracellular Electron Transfer. *Appl. Environ. Microb.* **74,** 615–623 (2008).

35. Xu, S., Jangir, Y. & El-Naggar, M. Y. Disentangling the roles of free and cytochrome-bound flavins in extracellular electron transport from *Shewanella oneidensis* MR-1. *Electrochim. Acta.* **198,** 49–55 (2016).

Chapter 2

Synthesis and electrocatalytic activity of [FeFe]-H_2ase model complexes with non-innocent chelating nitrogen-donor ligands

Souvik Roy,[a,b][‡] Joseph A. Laureanti,[a][‡] Thomas L. Groy,[a] and Anne K. Jones*[a]

[a]School of Molecular Sciences, Arizona State University

Tempe, Arizona, 85287, USA

[b]Present address: Department of Chemistry – Ångström Laboratory, Uppsala University

Lägerhyddsvägen 1, 75120 Uppsala, Sweden

[‡]These authors contributed equally to this work

Reproduced with permission from:

Roy, S., Laureanti, J. A., Groy, T. L. and Jones, A. K. (2017), Synthesis and Electrocatalytic Activity of [FeFe]-Hydrogenase Model Complexes with Non-Innocent Chelating Nitrogen-Donor Ligands. Eur. J. Inorg. Chem.. doi:10.1002/ejic.201700123

Abstract

To probe the influence of redox non-innocent ligands on a well-known class of [FeFe]-hydrogenase models, three new asymmetrically disubstituted diiron complexes of the general formula (μ-SRS)[Fe(CO)$_3$][Fe(CO)(N–N)] {SRS = propane-1,3-dithiolate (pdt) or benzene-1,2-dithiolate (bdt), and N–N = 2,2'-bipyridine (bipy) or 2,2'-bipyrimidine (bpym)} have been synthesized from their parent hexacarbonyls and characterized. The new complexes (μ-pdt)Fe$_2$(CO)$_4$(κ^2-bpym) (**2**), (μ-bdt)Fe$_2$(CO)$_4$(κ^2-bipy) (**3**), and (μ-bdt)Fe$_2$(CO)$_4$(κ^2-bpym) (**4**) were fully characterized by spectroscopic and electrochemical techniques, and the results are compared to those of a related complex (μ-pdt)Fe$_2$(CO)$_4$(κ^2-bipy) (**1**). The crystal structures of **2**–**4** show that in each complex, the two iron units are in an eclipsed orientation, and the N–N ligand lies in the basal plane. IR spectra and electrochemical analyses indicate that electron density at the iron centers decreases in the order **1**>**2**>**3**>**4**. Furthermore, **2** undergoes a ligand-centered reduction at the same potential that the hexacarbonyl precursor undergoes its first reduction. However, unlike the 2,2'-bipy derivatives **1** and **3**, the 2,2'-bpym complexes **2** and **4** are not effective catalysts for electrochemical proton reduction from acetic acid.

Introduction

Electrochemical reduction of protons to produce hydrogen (H_2) as a fuel is an appealing approach for storing transient electrical energy produced by renewable energy sources.[1,2] Although platinum-group metals efficiently catalyze the hydrogen evolution reaction (HER), there is consensus that catalysts based on earth-abundant elements are necessary for large-scale production of H_2 because of the high cost and limited supply of noble metals. In this regard, hydrogenases serve as inspiration for the design of

inexpensive and efficient catalysts since these enzymes employ only nickel and iron at the active site.[3,4] [FeFe]-hydrogenases are exceptionally efficient. They can catalyze proton reduction with high turnover frequencies (TOF), 6000-9000 s^{-1}, under ambient conditions.[5-8] The X-ray crystal structure of [FeFe]-hydrogenase shows that its active site, commonly referred to as the H-cluster, is a unique six-iron cluster comprised of two subunits: a redox-active [4Fe4S] cubane that serves as a conduit for shuttling electrons, and a binuclear iron subsite [Fe_2S_2] at which the catalytic reaction takes place (**Scheme 2-1**).[9,10] The two iron centers in the [Fe_2S_2] unit are linked by a bridging dithiolate featuring a bridgehead amine (-SCH_2NHCH_2S-),[11,12] and are ligated to the diatomic ligands carbon monoxide (CO) and cyanide (CN^-) that are otherwise biologically uncommon. One of the iron atoms of the [Fe_2S_2] cluster, defined as the proximal iron (Fe_p), is connected to the cuboidal [4Fe4S] cluster *via* a cysteinyl thiolate, and the other iron center (distal iron, Fe_d) contains an open coordination site for substrate binding.

The [Fe_2S_2] subcluster of the H-cluster bears remarkable resemblance to a well-known organometallic compound (μ-$S_2C_3H_6$)$Fe_2(CO)_6$ that has been exploited by synthetic chemists to build a multitude of biomimetic diiron complexes that have provided a better understanding of the structure-function relationship of the enzyme.[13-18] While the hexacarbonyl complexes are poor electrocatalysts for proton reduction, replacing CO ligands with donor ligands leads to more efficient structural and functional models. However, in contrast to the natural system that utilizes the $Fe^{II}Fe^{I}$ oxidation state for reductive catalysis, most diiron model complexes rely on the $Fe^{I}Fe^{0}$ state, requiring high overpotentials for electrocatalysis.[19] Furthermore, theoretical studies have indicated

that electron density is delocalized throughout all six irons of the H-cluster,[20] but there are relatively few examples of diiron models with redox-active cofactors or ligands.[21-29]

Non-innocent ligands have attracted considerable interest because a change in the oxidation state of the ligand can modulate the electronic properties of the metal thereby facilitating redox catalysis.[30] In synthetic diiron models of hydrogenase, redox active ligands can serve as a proxy for the [4Fe4S] cluster. In particular, when a reducible organic ligand is appended to the diiron unit, reduction of the complex can occur either on the ligand or the Fe center, or the electron(s) can be delocalized over the entire metal-ligand framework. Such interaction between metal and a ligand may lower the large overpotential required for proton reduction. Recently, many diiron-dithiolato carbonyl complexes have been developed incorporating non-innocent ligands in the primary coordination sphere.[31] Chelating, nitrogen-based ligands, including 2,2'-bipyridine (bipy) and 2,2'-bipyrimidine (bpym), have found extensive application in inorganic and organometallic chemistry owing to their chelating ability, π-accepting character, and redox-activity.[32-35] Both ligands can be readily reduced by two one-electron processes producing first the radical anion and then the dianion.[36] Since replacement of CH by N lowers the energy of the molecular orbitals of the ligands, bpym is easier to reduce than bipy. Furthermore, bpym is also a better π-acceptor, stabilizing reduced metal center(s) by delocalizing the extra electron density into the lower-lying, empty π* orbitals. Theoretical studies also suggest that the asymmetric distribution of the electron density at the diiron center caused by chelating ligands favors proton reduction catalysis.[37]

Here, we report synthesis and characterization of three new diiron complexes each with a non-innocent nitrogen-ligand: (μ-pdt)$Fe_2(CO)_4(\kappa^2$-bpym) (**2**), (μ-bdt)$Fe_2(CO)_4(\kappa^2$-

bipy) (**3**), and (μ-bdt)$Fe_2(CO)_4(\kappa^2$-bpym) (**4**) (pdt = propane-1,3-dithiolate, bdt = benzene-1,2-dithiolate). The effect of the nitrogen ligands and bridging dithiolates on the electronic and catalytic properties of the complexes is evaluated spectroscopically and electrochemically, and the results are compared to the related diiron analogue (μ-pdt)$Fe_2(CO)_4(\kappa^2$-bipy) (**1**).[24] It has been postulated that conjugated aromatic-dithiolates yield more stable reduced diiron species than their aliphatic counterparts because of greater ligand-metal mixing of frontier orbitals.[38-42] However, there are few previous reports of asymmetrically di-substituted aromatic-dithiolate bridged diiron models, and **3** and **4** are the first examples with chelating nitrogen-ligands.[27,43,44]

Results and Discussion

Synthesis and Crystal Structures. Complexes **2**–**4** were synthesized from corresponding diiron-hexacarbonyl-dithiolate complexes (**Scheme 2-2**). The synthesis of **3** is similar to that already reported for **1**.[24] Refluxing the hexacarbonyl precursor, (μ-bdt)$Fe_2(CO)_6$, with 2,2'-bipyridine in toluene results in the formation of **3**, which can be isolated in moderate yield (38%). However, this synthetic route does not produce the 2,2'-bipyrimidine substituted derivatives. Instead, the 2,2'-bipyrimidine analogs, **2** and **4**, were prepared via reaction between the diiron hexacarbonyl precursor, (μ-pdt)$Fe_2(CO)_6$ or (μ-bdt)$Fe_2(CO)_6$, and 2,2'-bipyrimidine in acetonitrile in the presence of two equivalents of trimethylamine-*N*-oxide (Me_3NO). Although (μ-bdt)$Fe_2(CO)_6$ has been reported to undergo reactions with strong donor ligands to produce mononuclear Fe^{II} complexes of the form (bdt)Fe(CO)(L-L) or (bdt)$Fe(CO)_2L_2$ (L-L = chelating ligand, L = monodentate ligand), monometallic complexes were not isolated in the reactions with 2,2'-bipy and 2,2'-bpym.[45-47]

Solid state molecular structures of **2**, **3**, and **4** were determined by X-ray diffraction analysis of single crystals obtained from hexane/dichloromethane mixtures. The crystal structures of **2**, **3**, and **4** are shown in **Figure 2-1**, and selected bond lengths and bond angles are listed in **Table 2-1**. The nitrogen ligands (2,2'-bipy and 2,2'-bpym) coordinate a single iron in a basal-basal mode, consistent with their small bite angles (N-Fe-N = 80-81°, **Table 2-1**). The bond angles indicate that in all the complexes, the irons are in a distorted square pyramidal geometry, and the two iron units, $Fe(CO)_3$ and Fe(CO)(N-N), are eclipsed relative to one another. The Fe-Fe bond lengths in **2**, **3**, and **4** are 2.5520, 2.5052, and 2.5218 Å, respectively, noticeably longer than in the hexacarbonyl precursors.[48,49] In these complexes, the inter-ring C-C bond distances in the nitrogen-ligands (2,2'-bipy and 2,2'-bpym) are particularly significant as they reflect the extent of metal-to-ligand charge transfer. The LUMOs of 2,2'-bipy and 2,2'-bpym are π* orbitals with in-phase overlap between the *p*-orbitals of the two carbon atoms linking the rings.[50] Back-donation from the metal to the ligand shortens the C-C bond by increasing the electron density in the LUMO. The inter-pyridine C-C bonds in **1** and **3** (1.461 and 1.463 Å respectively), and inter-pyrimidine C-C bonds in **2** and **4** (1.462 and 1.467 Å, respectively) are shorter than that in the respective free ligands (1.490 and 1.511Å in 2,2'-bipy and 2,2'-bpym respectively) (**Table 2-1**).[51,52] This indicates metal-to-ligand backbonding in all four compounds.

Spectroscopic Characterization. Complexes **1**–**4** were characterized spectroscopically by FTIR, UV-vis and NMR, and the results are summarized in **Tables 2-2** and **2-3**. As shown in **Figure 2-2A**, IR spectra of all of the complexes in dichloromethane consist of three characteristic bands in the C-O stretching region, similar

to related diiron complexes with chelating donor ligands.[44,53,54] The average IR stretching frequency of the CO ligands is often used as a rough quantitative indicator of the electron densities about the metal centers since shifts of the C-O bands upon ligand substitution are correlated to the σ-donating and π-accepting abilities of the ligands. A shift in the average of the C-O stretching bands by 7-8 cm^{-1} towards higher energy for complexes **2** and **4** indicates that replacing 2,2'-bipy with 2,2'-bpym leads to strengthening of the C-O bonds. One explanation is that the stronger π-accepting 2,2'-bpym withdraws more electron density from the iron core at the expense of backbonding into carbonyls. In essence, back-bonding into 2,2'-bpym substitutes for back-bonding into the CO ligands. The average value of the CO bands for **2** is similar to that of the bis-phosphine analogue, $(\mu\text{-pdt})Fe_2(CO)_4(\kappa^2\text{-dppe})$ (dppe = $Ph_2PCH_2CH_2PPh_2$),[55] indicating that electron density on the diiron center of the 2,2'-bpym complex is similar to that of the dppe analogue. Changing the bridging ligand from pdt to bdt shifts the C-O stretching bands to higher energy by an average of 13 cm^{-1}. This is likely to be a result of the lower electron densities on the Fe centers in **3** and **4** caused by electron delocalization over the aromatic bdt ring. The IR spectra of the complexes indicate that the electron density of the diiron core decreases in the order **1** >**2** > **3** > **4**.

Three types of electronic transitions are present in the UV-vis spectra of low-spin iron complexes containing α-diimine ligands: ligand centered π–π* bands in the high energy UV region, metal-to-ligand charge transfer (MLCT) bands, and weak metal-centered d-d transitions.[36,56] As shown in **Figure 2-2B**, the ligand centered π–π* band appears at *ca.* 295 nm for the 2,2'-bipy complexes (**1** and **3**). For the 2,2'-bpym analogs **2** and **4**, this ligand-centered transition requires higher energy and consequently the

maximum is too short wavelength to observe (< 250 nm). Spectra from all four complexes feature an intense band in the region 335–350 nm ($\varepsilon > 10^3$ $M^{-1}cm^{-1}$) that is likely associated with the Fe-S core (Table 2). The weaker, lower energy bands likely arise from d-d transitions and Fe(dπ)–bipy(π*) charge transfers.

The ^{1}H NMR spectra of **1** and **2** show the expected signals for the propane-1,3-dithiolate bridge in the region 1.2–2.2 ppm, shifted slightly upfield compared to the parent hexacarbonyl complex. The signals for the aromatic protons of benzene-1,2-dithiolate in complexes **3** and **4** appear at 7.08-7.09 and 6.59 ppm, chemical shifts nearly identical to the corresponding hexacarbonyl starting material.[57] Interestingly, the chemical shifts of the resonances of the nitrogen ligands (2,2'-bipy and 2,2'-bpym) in **1**–**4** relative to the non-coordinated free ligand provide a qualitative description of the nature of the bonding between the Fe and the ligand. As listed in **Table 2-3**, the NMR spectra of the 2,2'-bipy derivatives, **1** and **3**, consist of four resonances in the aromatic region, consistent with symmetrical coordination of 2,2'-bipy. Notably, the resonances attributable to the protons at positions **3**, **4** and **5** of the 2,2'-bipy ligand, shift upfield in **1** and **3** relative to the free ligand. However, the resonance of the proton on the carbon adjacent to the coordinated nitrogen, H(6), is shifted downfield for **1** and upfield for **3**. Similarly, while upfield shifts are observed for the resonances of H(4) and H(5) of the 2,2'-bpym ligand in **2** and **4**, the resonance of the proton next to the coordinated nitrogen, H(6), undergoes a small downfield shift in **2** and upfield shift in **4**. Overall, the NMR data suggest that π-back donation from the iron center to the empty π* (LUMO) of the nitrogen-ligand increases the electron density over the ligand. However, the reason behind the different shifts observed for H(6) in pdt- and bdt-analogs is unclear.

Electrochemistry

Redox properties of complexes **1**–**4** were probed by cyclic voltammetry. Voltammograms are shown in **Figure 2-3**, and the reduction potentials are listed in **Table 2-4**. We have previously reported that **1** undergoes a two-electron reduction at -2.06 V with one metal-centered reduction and the other likely a ligand-centered reduction.[24] As shown in **Figure 2-3**, cyclic voltammograms of **2** show two irreversible reductive waves at E_p = –1.76 and –2.25 V, and a small oxidative wave at E_p = –1.55 V during the return scan. Interestingly, when the reductive scan is stopped prior to the second reduction, the first reductive event (E_p = –1.76 V) becomes reversible with $E_{1/2}$ = –1.72 V (i_p^c/i_p^a = 1.1), and the oxidative wave at –1.55 V disappears. Assuming the first reduction is a one-electron process, comparison of the reductive peak currents suggests that the second reduction involves two electrons (i_p^{red1} = 27 μA and i_p^{red2} = 54 μA; $i_p^{red2}/\ i_p^{red1}$ = 2). Typically, replacing two CO ligands from the hexacarbonyl complex (μ-pdt)$Fe_2(CO)_6$ with better donor ligands and/or weaker π-accepting ligands results in increased electron density on the Fe centers and renders the complex more difficult to reduce. However, this does not hold for **2** which is reduced at a potential almost identical to that of the all-CO parent compound (**Table 2-4**). This is all the more surprising in light of the observation that the lower energy of the C-O stretching bands in FTIR spectra from **2** suggests increased electron density in the diiron core. According to previous studies, the 2,2'-bipyrimidine ligand undergoes a reversible one-electron reduction (bpym/$bpym^{1-}$) at –2.12 V and a second, irreversible one-electron reduction ($bpym^{1-}$/$bpym^{2-}$) at –2.83 V.[36] Assuming that the diiron center withdraws electron density from the ligand rendering its reduction more facile, it is tempting to

assign the first reduction of **2** to the 2,2'-bpym unit. The second reduction at -2.24 V, a two-electron process, then likely corresponds to a metal-centered reduction forming a $Fe^{I}Fe^{0}$ species together with a ligand-centered reduction corresponding to the $bpym^{1-}/bpym^{2-}$ couple. According to this assignment, relative to the hexacarbonyl analogue, the metal-based reduction is 500 mV more negative for **2**, the largest shift among all of the diiron complexes discussed here. The small oxidation wave at –1.55 V on the return scan suggests an EC process in which the three electron reduced species, $Fe^{0}Fe^{I}(bpym^{2-})$, undergoes a fast chemical reaction forming a new species which can be reoxidized only at more positive potentials.

Complex **3** is reduced at a much less negative potential (E_p = -1.71 V) than **1** (E_p = −2.06 V), consistent with the electron withdrawing nature of bdt. Relative to the parent hexacarbonyl complex, (μ-bdt)$Fe_2(CO)_6$, the reduction potential of **3** is cathodically shifted by 440 mV. This shift is much higher than the 320 mV cathodic shift observed for the pdt complex, **1**. On the other hand, substitution of (μ-bdt)$Fe_2(CO)_6$ with 2,2'-bpym results in only 310 mV shift of the first reduction as observed for complex **4**. This is consistent both with the better π-accepting ability of the 2,2'-bpym ligand relative to 2,2'-bipy and with the FTIR results. Previous electrochemical investigations have shown that (μ-bdt)$Fe_2(CO)_6$ is reduced to a dianion in a reversible, two-electron process, and its phosphine derivatives undergo partially-reversible one-electron reductions.[27,47,58] To estimate the number of electrons transferred during the reduction of **3** and **4**, we compared the reductive peak currents to the oxidative peak currents corresponding to the oxidation of the complexes from $Fe^{I}Fe^{I}$ to $Fe^{II}Fe^{I}$ (*vide infra*). The ratio of the peak

currents for the two processes suggests that **3** and **4** likely undergo two-electron reduction (**Table 2-4**).

Complexes **1**–**4** all undergo irreversible oxidation in the range -0.14 to –0.27 V. Based on previous electrochemical studies of similar diiron complexes, this oxidation can be assigned to the $Fe^{II}Fe^{I}/Fe^{I}Fe^{I}$ couple.[19] The complexes with the 2,2'-bpym ligand, **2** and **4**, are more difficult to oxidize by 70–100 mV than the corresponding 2,2'-bipy complexes, **1** and **3**. This is consistent with the relative donating abilities of the ligands.

Electrocatalytic Proton Reduction

Electrocatalytic evolution of hydrogen from acetic acid by complexes **1**–**4** (0-40 mM) in acetonitrile was investigated by cyclic voltammetry. Although IR and NMR experiments show that none of the complexes react with acetic acid at low acid concentrations (0–10 mM) in the resting redox state, comparison to related complexes suggest that reduction should make them sufficiently basic to bind protons and catalyze hydrogen production. Furthermore, since the reduction potential for each complex is more negative than the standard reduction potential of acetic acid in acetonitrile (-1.36 V), such electrocatalysis is thermodynamically possible.[59] We reported previously that **1** homogeneously electrocatalyzes proton reduction from acetic acid with considerably less overpotential than related diiron analogues.[24] However, sequential addition of acetic acid (from 5 mM to 20 mM) to a solution of **2** did not increase the current of the reductive waves at –1.72 and –2.24 V (**Figure 2-4**). The first reduction peak, at –1.72 without acid, shifts 90 mV to more positive potential without significant change in the peak current. The reduction also becomes completely irreversible even when the scan was stopped prior to the second reduction. These results hint at a proton

coupled electron transfer process (CE or EC) in the presence of acid. For an EC process, a ligand-centered reduction produces $\mathbf{2}^{-}$; then, protonation of the 2,2'-bpym ligand of $\mathbf{2}^{-}$ yields **2H** which requires more negative potential to undergo further reduction and protonation. Thus, no catalysis is observed at this potential. Alternatively, for a CE process, the protonation occurs before reduction. The **2H** intermediate is reduced at more negative potentials (beyond -2.2 V), and the peak current increases slightly at higher acid concentration. However, this reduced and protonated intermediate appears to be unstable at higher acid concentrations (>15 mM) as indicated by a disappearance of the reduction peak at -1.71 V under these conditions (**Figure 2-7**). IR spectra of **2** recorded in the presence of acid (AcOH and *p*-TsOH) also show degradation of the complex (**Figure 2-8** and **2-9**).

The bdt-bridged analogues, **3** and **4**, are reduced at milder potentials than the analogous pdt complexes. However, addition of acetic acid to **3** does not lead to current enhancement at the primary reductive wave at −1.71 V (**Figure 2-10**). Instead, as shown in **Figure 2-5**, a new catalytic wave appears at $E_p = -2.05$ V, the potential of which becomes more negative with increasing acid. Such catalytic voltammograms are commonly observed for reduction of a weak acid by a less electron rich diiron complex.[58,60-62] The data suggests that catalytic reduction of protons from acetic acid ($pK_a^{MeCN} = 22.3$) by **3** proceeds via an E(ECEC) mechanism in which the doubly reduced species ($\mathbf{3}^{2-}$) undergoes protonation to form $\mathbf{3H}^{-}$.[58,62,63] Acetic acid is too weak to protonate $\mathbf{3H}^{-}$. Therefore, the latter is further reduced to $\mathbf{3H}^{2-}$ before the second protonation step, and $\mathbf{3}^{-}$ is regenerated after the release of H_2. The potential onset of

catalytic peak current for **3** is only slightly more positive than that of **1** although the primary reduction of **3** occurs at considerably more positive potential (350 mV).

The kinetics of the catalysis was also probed by cyclic voltammetry. As shown in **Figure 2-6A**, the catalytic peak current (i_{cat}) increases linearly with catalyst concentration indicating that the reaction is first order with respect to the concentration of the catalyst at fixed acid concentrations. **Figure 2-6B** shows that the ratio of the catalytic current to the reductive peak current in the absence of acid ($i_{\mathrm{cat}}/i_{\mathrm{p}}$) depends linearly on the square root of the acid concentration. This demonstrates first order dependence of the reaction on the acid concentration. A bimolecular catalytic rate constant (k) of 2.9 x 10^4 $M^{-1}s^{-1}$ can be estimated from the slope of this linear plot at a scan rate of 0.2 V s^{-1}. At the highest acid concentration studied (0.04 M), this corresponds to a TOF of 1170 s^{-1}. The catalytic rate was determined using equation 1, in which n is the number of electrons involved in the catalytic reaction, k is the rate constant, and v is the scan rate.[64]

$$\left(\frac{i_{\mathrm{cat}}}{i_{\mathrm{p}}}\right) = \left(\frac{n}{0.4463}\right)\sqrt{\frac{RTk[\mathrm{acid}]^x}{Fv}} \qquad (1)$$

The overpotential for the process, which is defined as the difference between the standard reduction potential of the acid and the half-wave potential for the catalytic wave, is *ca*. 620 mV for **3**, similar to that observed for **1** (680 mV).[59] Importantly, direct reduction of acetic acid on the glassy carbon electrode is negligible in the potential range −1.9 to −2.2 V (**Figure 2-11**). On the other hand, as shown in **Figure 2-4**, the electrochemical response of **4** towards acetic acid is similar to that of **2**. Addition of acetic acid does not affect the primary reduction wave of **4** at −1.58 V; instead a new

reductive wave appears at −2 V which grows only slightly with increasing acid concentration. In fact, a plateau in catalytic current is reached at the relatively low acid concentration of 4 mM. Although the complexes with the 2,2'-bpym ligand have more positive reduction potentials than the 2,2'-bipy analogues and might be expected to be more potent catalysts, they exhibit essentially no electrocatalytic activity towards proton reduction from acetic acid.

Conclusions

In summary, we have synthesized four [(μ-SRS){$Fe(CO)_3$}{Fe(CO)(N–N)}] complexes using two dithiolate-bridges and two chelating N-donor ligands (N–N). Complexes **3** and **4** are the first reported examples of benzene-1,2-dithiolate bridged asymmetric diiron complexes with chelating nitrogen-ligands. Unexpectedly, swapping 2,2'-bipy with 2,2'-bpym has a pronounced effect on both the electrochemical and catalytic properties of the diiron analogs. Since 2,2'-bpym has lower energy empty π* orbitals than 2,2'-bipy, it is easier to reduce, and it is a better π-acceptor ligand. This distinction in electronic properties of the two ligands leads to higher ν(CO) stretching frequencies and more positive reduction potentials for the complexes formed by replacing 2,2'-bipy with 2,2'-bpym. Notably, **2** undergoes a one-electron, ligand-centered reduction at the same potential as the hexacarbonyl precursor. However, this ligand-centered reduction does not mediate proton reduction catalysis at the diiron-site. Similarly, **4** is also inactive towards electrocatalytic proton reduction using a weak acid. This suggests that although 2,2'-bpym increases the electron density on the diiron center to the same extent as bis-phosphine ligands, the electronic properties of 2,2'-bpym are unsuitable for catalysis.

The second goal of this study was to investigate the impact of replacement of the aliphatic pdt ligand with benzene-1,2-dithiolate on diiron model complexes with chelating donor ligands. Since bdt is a significantly weaker donor than alkyl dithiolates, it might be expected to compensate for the negative shift of reduction potential caused by strong donor ligands on the iron center while maintaining the basicity of the diiron core. Although the bdt-bridged complex, **3**, is reduced at more positive potentials than the pdt complex, the potential of proton reduction catalysis and the rate of catalysis are similar for the two complexes. In short, the electronic properties of the diiron models can be tuned by different dithiolate-bridges and α-diimine ligands, but the impact of those variations on improving catalytic activity of the complexes is minimal.

Experimental Section

Reactions were performed under an inert atmosphere (nitrogen or argon) using a double manifold Schlenk vacuum line. The complexes (μ-pdt)$Fe_2(CO)_6$[65], (μ-bdt)$Fe_2(CO)_6$[23], and (μ-pdt)$Fe_2(CO)_4(\kappa^2$-bipy) were prepared according to literature methods. Anhydrous solvents and chemicals were of the highest available grades from Aldrich and were used as received. NMR spectra were recorded at room temperature on a Varian Liquid-State NMR spectrometer (400 or 500 MHz for ^{1}H). NMR chemical shifts are quoted in ppm; spectra are referenced to tetramethylsilane. FTIR spectra were recorded on a Bruker Vertex 70 spectrophotometer using a stainless steel sealed liquid spectrophotometer cell with CaF_2 windows. UV-vis measurements were performed on a Hewlett-Packard 8453 spectrophotometer using quartz cuvettes with a 1 cm path length.

*(μ-pdt)$Fe_2(CO)_4(\kappa^2$-bpym), (**2**).* (μ-pdt)$Fe_2(CO)_6$ (451 mg, 1.16 mmol) and trimethylamine-*N*-oxide (260 mg, 2.34 mmol) were dissolved in acetonitrile (10 mL) and stirred in the dark at room temperature for 15 min. Then the solution was anaerobically transferred to a suspension of 2,2'-bipyrimidine (370 mg, 2.33 mmol) in acetonitrile (5 mL) and heated to reflux in the dark for two hours. The reaction mixture was concentrated under reduced pressure, and the dark residue was purified *via* silica gel chromatography using 1:1 hexane/ethyl acetate with 1% triethylamine as eluent to give the desired product as a dark green solid. Yield: 230 mg, 41%. ^{1}H NMR (400 MHz, $CDCl_3$): δ = 9.04 (dd, 2H), 8.89 (dd, 2H), 7.30 (t, 2H), 2.20–2.17 (dt, 2H), 2.08 (m, 1H), 1.65 (td, 2H), 1.27 (m, 1H). IR (CH_2Cl_2, cm^{-1}): 2012, 1943, 1907. R_f = 0.3 (1:4 hexane/ethyl acetate, 1% NEt_3). m/z (ESI+)= 487.900 (calcd. 487.899)

*(μ-bdt)$Fe_2(CO)_4(\kappa^2$-bipy), (**3**).* A solution of (μ-bdt)$Fe_2(CO)_6$ (174 mg, 0.41 mmol) and 2,2'-bipyridine (130 mg, 0.83 mmol) in toluene (12 mL) was refluxed under argon until evolution of carbon monoxide ceased (2 h). The reaction mixture was concentrated under reduced pressure, and the dark residue was purified by column chromatography on silica gel. A dark bluish green solution eluted with 1:1 hexane/dichloromethane. Removal of the solvent yielded the product as a dark reddish brown solid. Yield: 80 mg, 38%. ^{1}H NMR (400 MHz, CD_2Cl_2): δ = 8.36 (s, 2H), 8.08 (s, 2H), 7.79 (s, 2H), 7.22 (s, 2H), 7.09 (s, 2H), 6.59 (s, 2H). IR (CH_2Cl_2, cm^{-1}): 2016, 1949, 1916. R_f = 0.5 (1:1 hexane/CH_2Cl_2). m/z (ESI+) = 519.893 (calc. 519.894)

Alternative synthetic procedure: A solution of (μ-bdt)$Fe_2(CO)_6$ (201 mg, 0.48 mmol) and trimethylamine-*N*-oxide (117 mg, 1.05 mmol) in acetonitrile (10 mL)

was stirred in the dark for 15 min. To this solution, 2,2'-bipyridine (112 mg, 0.72 mmol) in dichloromethane (3 mL) was introduced dropwise and anaerobically, and the mixture was stirred for one hour. The resulting solution was worked up as described above.

*(μ-bdt)$Fe_2(CO)_4(\kappa^2$-bpym), (**4**).* A solution of (μ-bdt)$Fe_2(CO)_6$ (160 mg, 0.38 mmol) and trimethylamine-*N*-oxide (85 mg, 0.76 mmol) in acetonitrile (10 mL) was stirred in the dark under nitrogen for 15 min. Then 2,2'-bipyrimidine (90 mg, 0.57 mmol) was added anaerobically, and the dark green reaction mixture was stirred for 2 h. The solvent was removed under reduced pressure, and the residue was thoroughly washed with hexane until the washings were colorless. The residue was re-dissolved in dichloromethane (25 mL) and filtered through celite and silica. Finally, upon evaporation of the solvent, the desired complex was obtained as a green powder. Yield: 90 mg, 45%. ^{1}H NMR (400 MHz, CD_2Cl_2): δ = 8.89 (br, 2H), 8.62 (s, 2H), 7.29 (br, 2H), 7.08 (s, 2H), 6.59 (s, 2H). IR (CH_2Cl_2, cm^{-1}): 2022, 1958–1927 (broad). m/z (ESI+) = 521.884 (calcd. 521.884). R_f not determined.

X-ray crystallography. Cell parameter measurements and single-crystal diffraction data collection were performed at low temperature (123 K) with a Bruker Smart APEX diffractometer. Graphite monochromated Mo Kα radiation (λ = 0.71073 Å) in the ω–φ scanning mode was used for the measurements. The structure was solved by direct methods and refined by fullmatrix least-squares on F^2. The following is the list of the programs used: data collection, Bruker Instrument Service v2010.9.0.0; cell refinement and data reduction, SAINT V7.68A; structure solution and refinement,

SHELXS-97; molecular graphics, XShell v6.3.1; preparation of material for publication, Bruker APEX2 v2010.9-1.30.

CCDC 1495905 (**2**), 1495907 (**3**), and 1495906 (**4**) contains the supplementary crystallographic data for this paper. These data can be obtained free of charge from The Cambridge Crystallographic Data Centre.

Electrochemistry. Electrochemical experiments were performed using either a CHI 1200A or a PG-STAT 128N Autolab electrochemical analyzer. A conventional three-electrode cell was used for recording cyclic voltammograms. The working electrode was a 3 mm diameter glassy carbon disk polished with 1 μm and 0.3 μm deagglomerated alpha alumina, successively, and sonicated for 15 min in ultrapure water prior to use. The supporting electrolyte was $[NBu_4][PF_6]$ (0.1 M in acetonitrile). A non-aqueous Ag/AgCl (CH_3CN) electrode was used as the reference electrode and a platinum wire was used as the counter electrode. Cyclic voltammograms were recorded either inside an inert glovebox or on the benchtop under an argon atmosphere. Potentials are reported relative to the ferrocene couple ($Fc^{+/0}$) measured as an internal standard after the final experiment. Concentrations of the complexes were determined spectrophotometrically based on the following extinction coefficients: ε(603 nm) = 3500 M^{-1} cm^{-1} (**1**), ε(634 nm) = 1950 M^{-1} cm^{-1} (**2**), ε(520 nm) = 2400 M^{-1} cm^{-1} (**3**), and ε(636 nm) = 1950 M^{-1} cm^{-1} (**4**).

Acknowledgements

This research was supported through the Center for Bio-Inspired Solar Fuel Production, an Energy Frontier Research Center funded by the U.S. Department of

Energy, Office of Sciences, Office of Basic Energy Sciences under Award Number DE-SC0001016. JAL acknowledges the NSF IGERT-SUN program for a graduate fellowship.

Figures

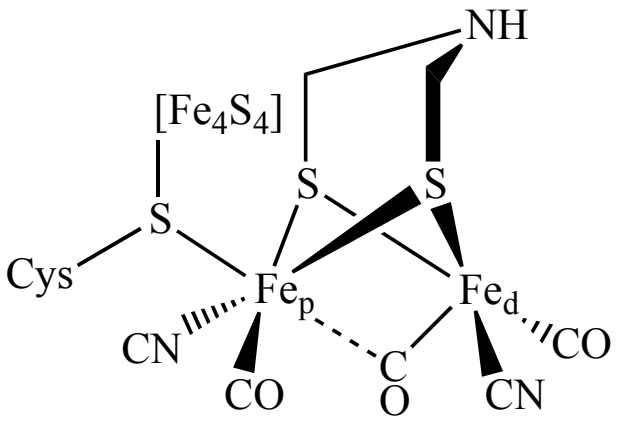

Scheme 2-1. Active site of [FeFe]-hydrogenase (H-cluster).

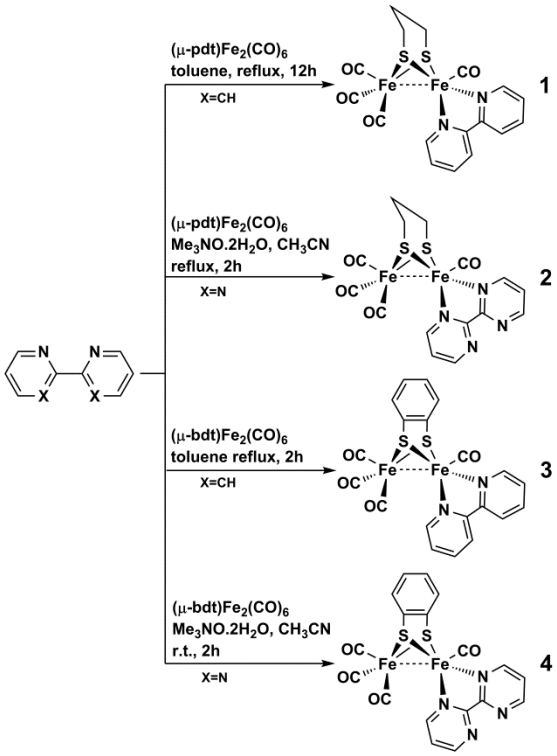

Scheme 2-2. Synthetic routes to complexes 1–4 from hexacarbonyl precursors and bidentate nitrogen-ligands.

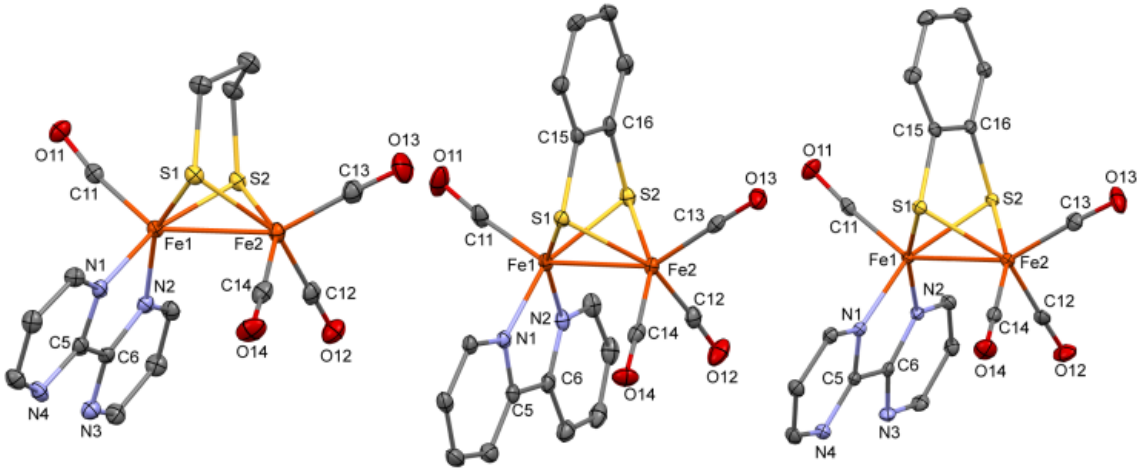

Figure 2-1. Hydrogen atoms have been omitted for clarity.

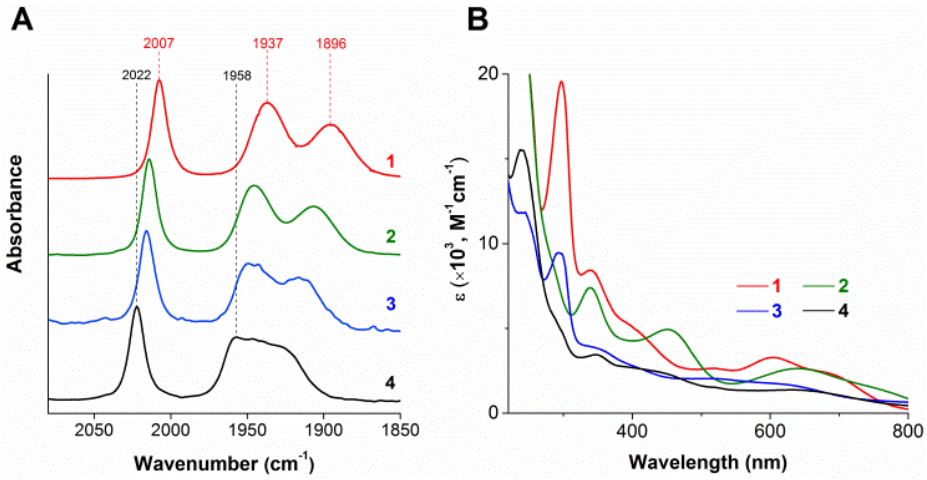

Figure 2-2. (A) IR and (B) UV-vis spectra of **1** (red trace), **2** (green trace), **3** (blue trace), and **4** (black trace) collected in dichloromethane and acetonitrile, respectively. UV-vis spectra were collected from solutions of approximately 0.1 mM complex.

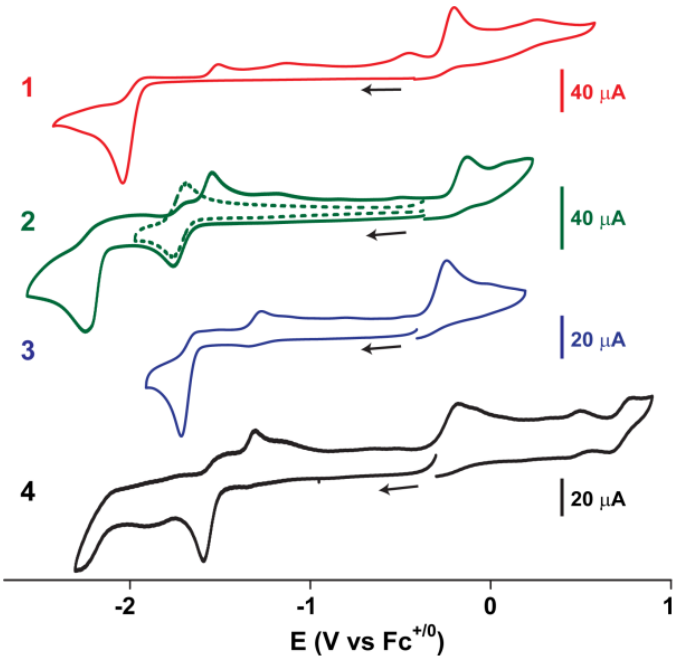

Figure 2-3. Cyclic voltammograms of **1** (1.2 mM), **2** (1.3 mM), **3** (0.88 mM), and **4** (1.6 mM) measured in 0.1 M $[NBu_4][PF_6]$/acetonitrile at a potential scan rate of 0.2 V s^{-1}. Arrows indicate the starting potential and scan direction. The dotted trace shows cyclic voltammogram of **2** when the scan direction was reversed at −1.97 V.

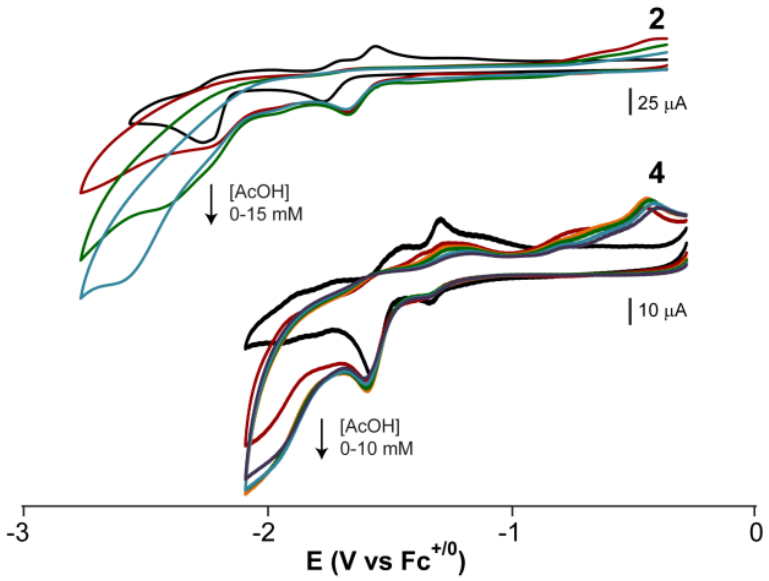

Figure 2-4. Cyclic voltammograms of **2** (1.3 mM) and **4** (1.6 mM) with various concentrations of acetic acid. Acid concentrations used: 0, 5, 10, 15 mM (complex **2**); 0, 2, 4, 6, 8, 10 mM (complex **4**). Black traces show the voltammograms in the absence of acid. Other experimental conditions are as described in **Figure 2-3**.

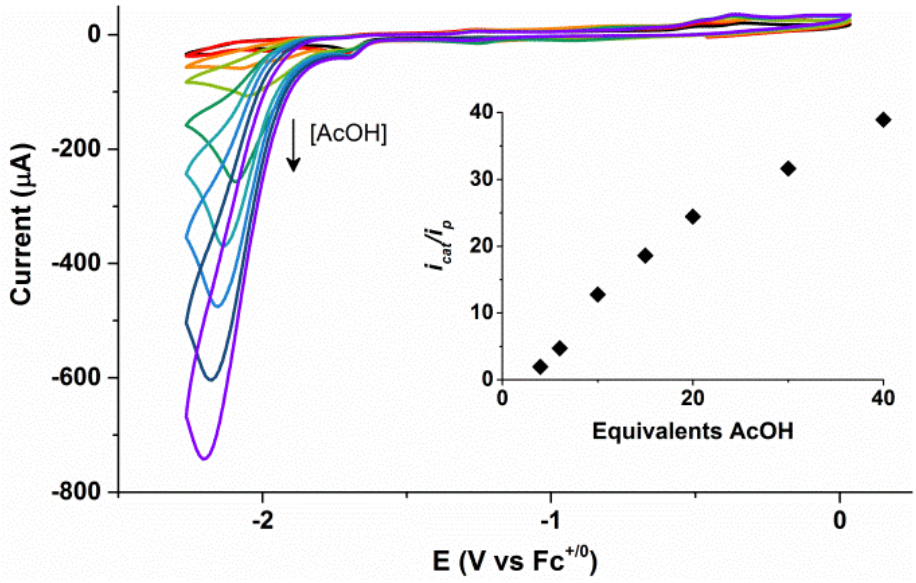

Figure 2-5. Cyclic voltammograms of **3** (1 mM) with various concentrations of acetic acid (0, 2, 4, 6, 10, 15, 20, 30, and 40 mM). Inset: The ratio $\boldsymbol{i_{cat}/i_p}$ as a function of the equivalents of acetic acid. Other experimental conditions are as described in **Figure 2-3**.

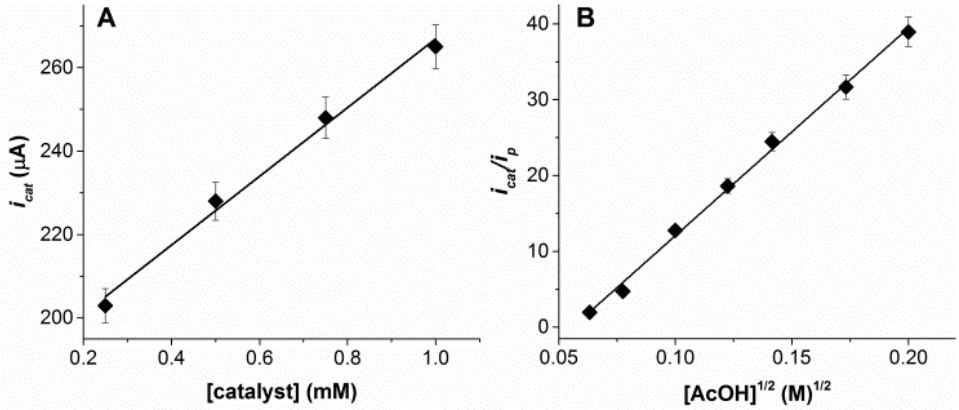

Figure 2-6. (A) Dependence of catalytic current ($\boldsymbol{i_{cat}}$) on the concentration of **3** in the presence of 10 mM acetic acid, and (B) $\boldsymbol{i_{cat}/i_p}$ as a function of $[AcOH]^{1/2}$ for **3** ($k = 2.9\times10^4$ M^{-1} s^{-1}; derived from the catalytic voltammograms shown in **Figure 2-5**). Lines are the best-linear fit to the data ($R^2 = 0.9924$ (A) and 0.9968 (B)).

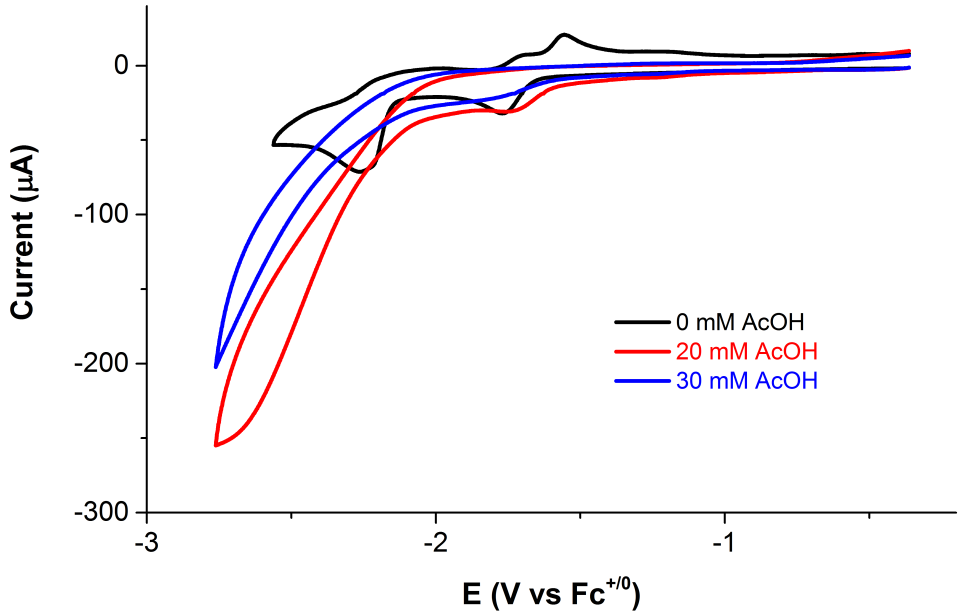

Figure 2-7. Cyclic voltammograms of **2** (1.3 mM) in the presence of a large excess of acetic acid. Lower current at higher concentration of acid suggests decomposition of the complex. Conditions: 0.1 M $[NBu_4][PF_6]$/ acetonitrile; potential scan rate 0.2 V s^{-1}; glassy carbon working electrode.

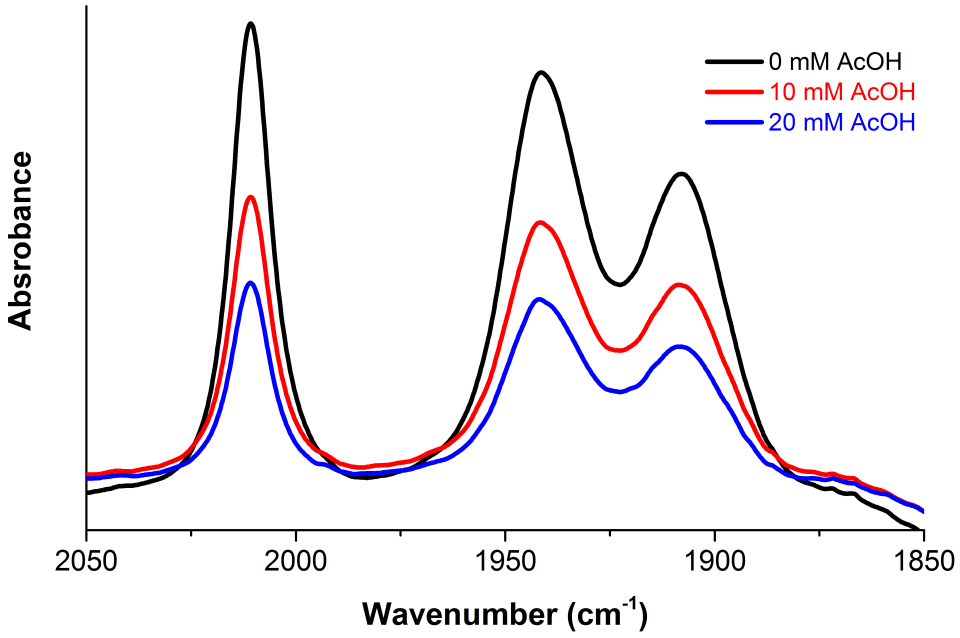

Figure 2-8. IR spectra of **2** in dicholoromethane in the presence of different amounts of acetic acid. The spectra were recorded within 5 min of an addition of acid to a ~1 mM solution of **2** in CH_2Cl_2. From the absorbance of the 2012 cm^{-1} stretching band, we can estimate that ~58% of complex degraded in the presence of 20 mM acetic acid.

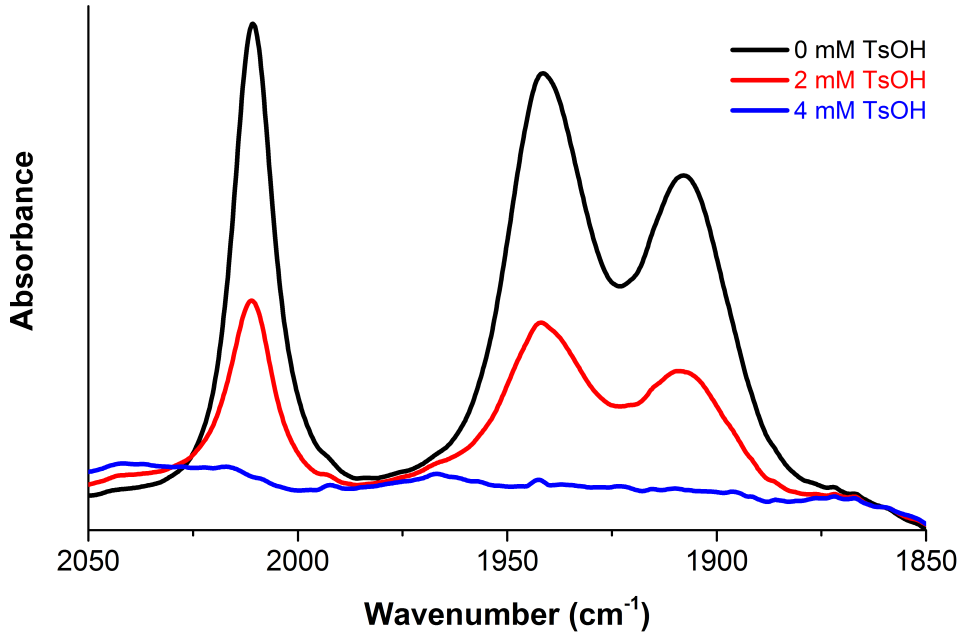

Figure 2-9. IR spectra of **2** (1 mM, CH_2Cl_2) in the presence of different amount of *p*-TsOH. In the presence of 4 mM acid, the complex decomposed completely within minutes.

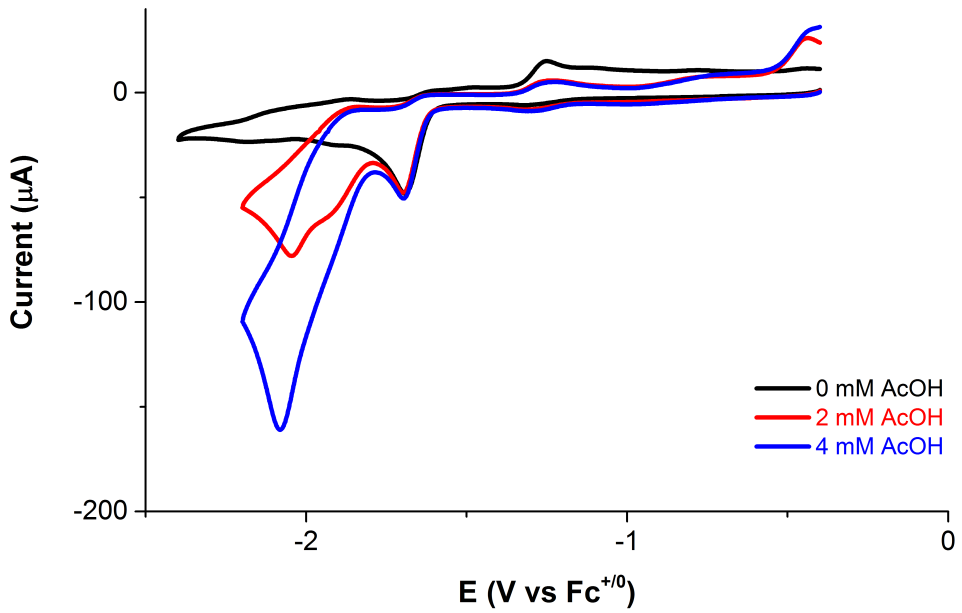

Figure 2-10. Cyclic voltammograms of **3** (0.88 mM) at low acid concentrations show that the catalytic wave develops at ~ −2.1 V. Conditions: supporting electrolyte 0.1 M $[NBu_4][PF_6]$/ acetonitrile; potential scan rate 0.2 V s^{-1}; glassy carbon working electrode.

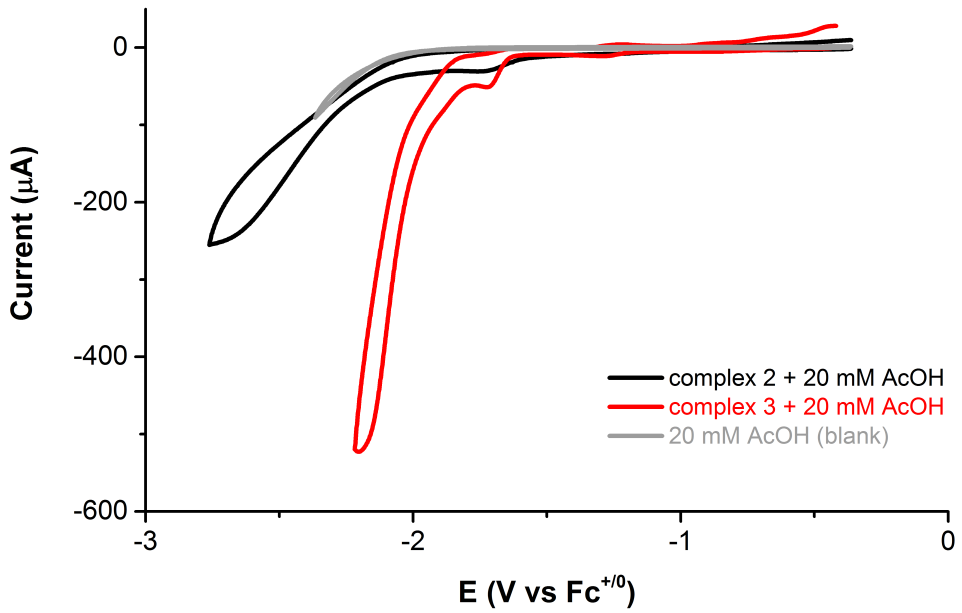

Figure 2-11. Cyclic voltammogram of 20 mM acetic acid without any catalyst (grey trace), and in the presence **2** (1.3 mM, black trace) and **3** (0.88 mM, red trace). Comparison of the red trace to the black trace demonstrates the poor catalytic activity of **2**. Conditions: supporting electrolyte 0.1 M $[NBu_4][PF_6]$/ acetonitrile; potential scan rate 0.2 V s^{-1}; glassy carbon working electrode.

Table 2- 1. Selected bond lengths (Å) and bond angles (°) for **2**, **3**, and **4**

Bond lengths	**2**	**3**	**4**	**Bond angles**	**2**	**3**	**4**
$Fe_{N-N} - Fe_{(CO)_3}$	2.5520	2.5052	2.5218	$S1 - Fe_{(CO)_3} - S2$	83.35	79.41	79.87
$Fe_{N-N} - CO^{ax}$	1.749	1.763	1.769	$S1 - Fe_{N-N} - S2$	85.99	81.27	81.31
$Fe_{(CO)_3} - CO^{ax}$	1.789	1.814	1.803	$CO^{ba} - Fe_{(CO)_3} - CO^{ba}$	92.8	89.6	93.2
$Fe_{N-N} - N1$	1.974	1.959	1.965	$N1 - Fe_{N-N} - N2$	80.57	81.36	81.25
$Fe_{N-N} - N2$	1.987	1.970	1.959	$Fe_{N-N} - Fe_{(CO)_3} - CO^{ax}$	151.3	148.8	151.12
$C5 - C6$	1.462	1.463	1.467	$Fe_{(CO)_3} - Fe_{N-N} - CO^{ax}$	141.59	148.4	143.33

Table 2-2. CO vibrational stretching frequencies and UV-vis absorptions for complexes **1**–**4** and analogous diiron complexes

Complex	**ν(CO), cm^{-1}**	**Average ν(CO), cm^{-1}**	**λ, nm (ε, M^{-1}cm^{-1})**
(μ-pdt)$Fe_2(CO)_6$	2072, 2033, 1993	2032	325, 452 (shoulder)
(μ-bdt)$Fe_2(CO)_6$[66]	2080, 2044, 2004	2043	-
1[24]	2007, 1937, 1896	1947	298, 342, 391 (5200), 519 (2700), 603 (3500), 685 (2500)
2	2012, 1943, 1907	1954	339 (5500), 449 (3700), 634 (1950)
3	2016, 1949, 1916	1960	292, 350 (2800), 390, 520 (2400), 625 (br, 1900)
4	2022, 1958–1927 (broad)	1968	347 (4100), 429 (3100), 636 (1950)
(μ-pdt)$Fe_2(CO)_4$(dppe)[55]	2019, 1949, 1904	1957	-
(μ-pdt)$Fe_2(CO)_4(I_{Me}$-CH_2-$I_{Me})$[67]	1996, 1920, 1872	1929	-

Table 2-3. ^{1}H NMR chemical shifts of 2,2'-bipyridine (bipy) and 2,2'-bipyrimidine (bpym)

Ring-position	**2,2'-bipy**	**1**	**3**	**2,2'-bpym**	**2**	**4**
C-3	8.43	8.03	8.08	–	–	–
C-4	7.82	7.74	7.79	8.98	8.89	8.62
C-5	7.31	7.23	7.22	7.43	7.30	7.29
C-6	8.65	8.73	8.36	8.98	9.04	8.89

Table 2-4. Electrochemical data for the ligands, diiron hexacarbonyl precursors, and complexes **1**–**4** in acetonitrile

Compound	**E_{ox}, V[a]**	**E_{red}, V[a]**	**(i_p^{red}/i_p^{ox})[b]**	**Note**
2,2'-bipy	-	-2.63 (r), -3.13 (i)	NA[c]	Ref.[66,67]
2,2'-bpym	-	-2.12 (r), -2.83 (i)	NA[c]	Ref.[36]
(μ-pdt)$Fe_2(CO)_6$	+0.74 (i)	-1.74 (r), -2.35 (i)	ND[d]	Ref.[68]
(μ-bdt)$Fe_2(CO)_6$	-	-1.27 (r)	NA[d]	Ref.[40]
1	-0.21(i)	-2.06 (i)	2.1	Ref.[24]
2	-0.14 (i)	-1.72 (r), -2.24 (i)	1.0, 2.1	This work
3	-0.27 (i)	-1.71 (i)	1.8	This work
4	-0.17 (i), 0.73 (p)	-1.58 (i)	1.9	This work

References

1. Gray, H. B. Powering the planet with solar fuel. *Nat. Chem.* **1,** 7–7 (2009).

2. Thapper, A. *et al.* Artificial Photosynthesis for Solar Fuels – an Evolving Research Field within AMPEA, a Joint Programme of the European Energy Research Alliance. *Green.* **3,** 43–57 (2013).

3. Fontecilla-Camps, J. C., Volbeda, A., Cavazza, C. & Nicolet, Y. Structure/function relationships of [NiFe]- and [FeFe]-hydrogenases. *Chem. Rev.* **107,** 4273–4303 (2007).

4. Lubitz, W., Ogata, H., Rüdiger, O. & Reijerse, E. Hydrogenases. *Chem. Rev.* **114,** 4081–4148 (2014).

5. Happe, R. P., Roseboom, W., Pierik, A. J., Albracht, S. P. J. & Bagley, K. A. Biological activition of hydrogen. *Nature.* **385,** 126–126 (1997).

6. Cammack, R., Frey, M. & Robson, R. *Hydrogen as a Fuel: Learning from Nature*. (Talor & Francis, 2001).

7. Frey, M. Hydrogenases: Hydrogen-activating enzymes. *Chem. Eur. J. of Chem. Bio.* **3,** 153–160 (2002).

8. Evans, D. J. & Pickett, C. J. Chemistry and the hydrogenases. *Chem. Soc. Rev.* **32,** 268–275 (2003).

9. Peters, J. W., Lanzilotta, W. N., Lemon, B. J. & Seefeldt, L. C. X-ray crystal structure of the Fe-only hydrogenase (CpI) from *Clostridium pasteurianum* to 1.8 angstrom resolution. *Science.* **282,** 1853–1858

10. Nicolet, Y., Piras, C., Legrand, P., Hatchikian, C. E. & Fontecilla-Camps, J. C. *Desulfovibrio desulfuricans* iron hydrogenase: the structure shows unusual coordination to an active site Fe binuclear center. *Structure.* **7,** 13–23 (1999).

11. Berggren, G. *et al.* Biomimetic assembly and activation of [FeFe]-hydrogenases. *Nature.* **499,** 66–69 (2013).

12. Adamska-Venkatesh, A. *et al.* Artificially maturated [FeFe] hydrogenase from *Chlamydomonas reinhardtii*: a HYSCORE and ENDOR study of a non-natural H-cluster. *Phys. Chem. Chem. Phys.* **17,** 5421–5430 (2015).

13. Gloaguen, F. & Rauchfuss, T. B. Small molecule mimics of hydrogenases: hydrides and redox. *Chem. Soc. Rev.* **38,** 100–108 (2009).

14. Heinekey, D. M. Hydrogenase enzymes: Recent structural studies and active site

models. *J. Organomet. Chem.* **694,** 2671–2680 (2009).

15. Tard, C. & Pickett, C. J. Structural and Functional Analogues of the Active Sites of the [Fe]-, [NiFe]-, and [FeFe]-Hydrogenases. *Chem. Rev.* **109,** 2245–2274 (2009).

16. Simmons, T. R., Berggren, G., Bacchi, M., Fontecave, M. & Artero, V. Mimicking Hydrogenases: From Biomimetics to Artificial Enzymes. *Coordin. Chem. Rev.* **270–271,** 127–150 (2014).

17. Rauchfuss, T. B. Diiron Azadithiolates as Models for the [FeFe]-Hydrogenase Active Site and Paradigm for the Role of the Second Coordination Sphere. *Acc. Chem. Res.* **48,** 2107–2116 (2015).

18. Gan, L., Jennings, D., Laureanti, J. & Jones, A. K. in *Top. Organometal. Chem.* **59,** 233–272. Springer International Publishing, 2015.

19. Felton, G. A. N. *et al.* Review of electrochemical studies of complexes containing the Fe2S2 core characteristic of [FeFe]-hydrogenases including catalysis by these complexes of the reduction of acids to form dihydrogen. *J.Organomet. Chem.* **694,** 2681–2699 (2009).

20. Schwab, D. E. *et al.* On the electronic structure of the hydrogenase H-cluster. *Chem. Commun.* 3696–3698 (2006). doi:10.1039/b604994j

21. Tard, C. *et al.* Synthesis of the H-cluster framework of iron-only hydrogenase. *Nature.* **433,** 610–613 (2005).

22. Si, Y. *et al.* Non-innocent bma ligand in a dissymetrically disubstituted diiron dithiolate related to the active site of the [FeFe] hydrogenases. *J. Inorg. Biochem.* **104,** 1038–1042 (2010).

23. Camara, J. M. & Rauchfuss, T. B. Combining acid-base, redox and substrate binding functionalities to give a complete model for the [FeFe]-hydrogenase. *Nat. Chem.* **4,** 26–30 (2012).

24. Roy, S., Groy, T. L. & Jones, A. K. Biomimetic model for [FeFe]-hydrogenase: asymmetrically disubstituted diiron complex with a redox-active 2,2'-bipyridyl ligand. *Dalton T.* **42,** 3843–3853 (2013).

25. Lansing, J. C., Camara, J. M., Gray, D. E. & Rauchfuss, T. B. Hydrogen Production Catalyzed by Bidirectional, Biomimetic Models of the [FeFe]-Hydrogenase Active Site. *Organometallics.* **33,** 5897–5906 (2014).

26. Roy, S. *et al.* Catalytic Hydrogen Evolution by Fe(II) Carbonyls Featuring a

Dithiolate and a Chelating Phosphine. *Inorg. Chem.* **53,** 8919–8929 (2014).

27. Karnahl, M. *et al.* Mixed-valence [FeIFeII] hydrogenase active site model complexes stabilized by a bidentate carborane bis-phosphine ligand. *Dalton T.* **41,** 12468–12477 (2012).

28. Ghosh, S. *et al.* Hydrogenase biomimetics: $Fe_2(CO)_4$(dppf)(μ-pdt) (dppf = 1,1'-bis(diphenylphosphino)ferrocene) both a proton-reduction and hydrogen oxidation catalyst. *Chem. Commun.* **50,** 945–947 (2014).

29. Hsieh, C.-H. *et al.* Redox active iron nitrosyl units in proton reduction electrocatalysis. *Nat. Commun.* **5,** (2014).

30. Allgeier, A. M. & Mirkin, C. A. Ligand design for electrochemically controlling stoichiometric and catalytic reactivity of transition metals. *Angew. Chem. Int. Ed.* **37,** 894–908 (1998).

31. Liu, Y.-C., Yen, T.-H., Chu, K.-T. & Chiang, M.-H. Utilization of Non-Innocent Redox Ligands in [FeFe] Hydrogenase Modeling for Hydrogen Production. *Comment. Inorg. Chem.* **36,** 141–181 (2016).

32. Balzani, V., Juris, A., Venturi, M., Campagna, S. & Serroni, S. Luminescent and Redox-Active Polynuclear Transition Metal Complexes. *Chem. Rev.* **96,** 759–834 (1996).

33. Kaes, C., Katz, A. & Hosseini, M. W. Bipyridine: The Most Widely Used Ligand. A Review of Molecules Comprising at Least Two 2,2'-Bipyridine Units. *Chem. Rev.* **100,** 3553–3590 (2000).

34. Armentano, D. *et al.* 2,2'-Bipyrimidine- and 2,3-bis(2-pyridyl)pyrazine-containing manganese(ii) compounds: structural and magnetic properties. *Dalton T.* 4626–4634 (2003). doi:10.1039/b311007a

35. Concepcion, J. J. *et al.* Making Oxygen with Ruthenium Complexes. *Acc. Chem. Res.* **42,** 1954–1965 (2009).

36. Ernst, S. & Kaim, W. Coordination characteristics of four isomeric .alpha.-diimine ligands. .pi. Molecular orbital perturbation calculations for the bidiazines and their correlation with the properties of group 6 metal carbonyl complexes. *J. Am. Chem. Soc.* **108,** 3578–3586 (1986).

37. Tye, J. W., Darensbourg, M. Y. & Hall, M. B. De novo design of synthetic di-iron(I) complexes as structural models of the reduced form of iron-iron hydrogenase. *Inorg. Chem.* **45,** 1552–1559 (2006).

38. Eisenberg, R. & Gray, H. B. Noninnocence in Metal Complexes: A Dithiolene Dawn. *Inorg. Chem.* **50,** 9741–9751 (2011).

39. Capon, J.-F., Gloaguen, F., Schollhammer, P. & Talarmin, J. Electrochemical proton reduction by thiolate-bridged hexacarbonyldiiron clusters. *J. Electroanal. Chem.* **566,** 241–247 (2004).

40. Capon, J.-F., Gloaguen, F., Schollhammer, P. & Talarmin, J. Activation of proton by the two-electron reduction of a di-iron organometallic complex. *J. Electroanal. Chem.* **595,** 47–52 (2006).

41. Schwartz, L. *et al.* Influence of an electron-deficient bridging o-carborane on the electronic properties of an [FeFe] hydrogenase active site model. *Dalton T.* 2379–2381 (2008). doi:10.1039/B802908N

42. Schwartz, L., Singh, P. S., Eriksson, L., Lomoth, R. & Ott, S. Tuning the electronic properties of Fe_2(μ-arenedithiolate)$(CO)_6$−n(PMe_3)n (n=0, 2) complexes related to the [Fe–Fe]-hydrogenase active site. *C.R. Chim.* **11,** 875–889 (2008).

43. Ezzaher, S., Gogoll, A., Bruhn, C. & Ott, S. Directing protonation in [FeFe] hydrogenase active site models by modifications in their second coordination sphere. *Chem. Commun.* **46,** 5775–5777 (2010).

44. Ezzaher, S. *et al.* Diiron chelate complexes relevant to the active site of the iron-only hydrogenase. *C.R. Chim.* **11,** 906–914 (2008).

45. Kaur-Ghumaan, S., Schwartz, L., Lomoth, R., Stein, M. & Ott, S. Catalytic Hydrogen Evolution from Mononuclear Iron(II) Carbonyl Complexes as Minimal Functional Models of the [FeFe] Hydrogenase Active Site. *Angew. Chem. Int. Ed. Engl.* **49,** 8033–8036 (2010).

46. Beyler, M. *et al.* Pentacoordinate iron complexes as functional models of the distal iron in [FeFe] hydrogenases. *Chem. Commun.* **47,** 11662 (2011).

47. Gao, S. *et al.* Di/mono-nuclear iron(i)/(ii) complexes as functional models for the 2Fe2S subunit and distal Fe moiety of the active site of [FeFe] hydrogenases: protonations, molecular structures and electrochemical properties. *Dalton T.* **41,** 12064–12074 (2012).

48. Cabeza, J. A., Martínez-García, M. A., Riera, V., Ardura, D. & García-Granda, S. Binuclear Iron(I), Ruthenium(I), and Osmium(I) Hexacarbonyl Complexes Containing a Bridging Benzene-1,2-dithiolate Ligand. Synthesis, X-ray Structures, Protonation Reactions, and EHMO Calculations. *Organometallics* **17,** 1471–1477 (1998).

49. Lyon, E. J., Georgakaki, I. P., Reibenspies, J. H. & Darensbourg, M. Y. Carbon Monoxide and Cyanide Ligands in a Classical Organometallic Complex Model for Fe-Only Hydrogenase. *Angew. Chem. Int. Ed. Engl.* **38,** 3178–3180

50. Irwin, M. *et al.* Experimental and Computational Study of the Structural and Electronic Properties of Fe-II(2,2 '-bipyridine)(mes)(2) and [Fe-II(2,2'-bipyridine)(mes)(2)](-), a Complex Containing a 2,2'-Bipyridyl Radical Anion. *Inorg. Chem.* **49,** 6160–6171 (2010).

51. Fernholt, L., Rømming, C. & Samdal, S. On the Structure of 2,2'-Bipyrimidine. Gas and Solid Phase Structure and Barrier to Internal Rotation. *Acta Chem. Scand. A.* **35A,** 707–715 (1981).

52. Gore-Randall, E., Irwin, M., Denning, M. S. & Goicoechea, J. M. Synthesis and Characterization of Alkali-Metal Salts of 2,2′- and 2,4′-Bipyridyl Radicals and Dianions. *Inorg. Chem.* **48,** 8304–8316 (2009).

53. Justice, A. K. *et al.* Chelate control of diiron(I) dithiolates relevant to the [Fe-Fe]-hydrogenase active site. *Inorg. Chem.* **46,** 1655–1664 (2007).

54. Orain, P.-Y. *et al.* Use of 1,10-phenanthroline in diiron dithiolate derivatives related to the [Fe-Fe] hydrogenase active site. *Dalton T.* 3754–3756 (2007). doi:10.1039/b709287c

55. Ezzaher, S. *et al.* Evidence for the formation of terminal hydrides by protonation of an asymmetric iron hydrogenase active site mimic. *Inorg. Chem.* **46,** 3426–3428 (2007).

56. Palmer, R. A. & Piper, T. S. 2,2‘-Bipyridine complexes. I. Polarized crystal spectra of tris(2,2’-bipyridine)copper(II), -nickel(II), -cobalt(II), -iron(II), and -ruthenium(II). *Inorg. Chem.* **5,** 864–& (1966).

57. Zhao, J., Wei, Z., Zeng, X. & Liu, X. Three diiron complexes bearing an aromatic ring as mimics of the diiron subunit of [FeFe]-hydrogenase: synthesis, electron transfer and coupled chemical reactions. *Dalton T.* **41,** 11125–11133 (2012).

58. Felton, G. A. N. *et al.* Hydrogen Generation from Weak Acids: Electrochemical and Computational Studies of a Diiron Hydrogenase Mimic. *J. Am. Chem. Soc.* **129,** 12521–12530 (2007).

59. Fourmond, V., Jacques, P.-A., Fontecave, M. & Artero, V. H_2 Evolution and Molecular Electrocatalysts: Determination of Overpotentials and Effect of Homoconjugation. *Inorg. Chem.* **49,** 10338–10347 (2010).

60. Capon, J.-F. *et al.* Electrochemical and theoretical investigations of the reduction

of $[Fe_2(CO)_5L\{\mu\text{-}SCH_2XCH_2S\}]$ complexes related to [FeFe] hydrogenase. *New J. Chem.* **31,** 2052–2064 (2007).

61. Roy, S., Nguyen, T.-A. D., Gan, L. & Jones, A. K. Biomimetic peptide-based models of [FeFe]-hydrogenases: utilization of phosphine-containing peptides. *Dalton T.* **44,** 14865–14876 (2015).

62. Gloaguen, F. Electrochemistry of Simple Organometallic Models of Iron–Iron Hydrogenases in Organic Solvent and Water. *Inorg. Chem.* **55,** 390–398 (2016).

63. Donovan, E. S., McCormick, J. J., Nichol, G. S. & Felton, G. A. N. Cyclic Voltammetric Studies of Chlorine-Substituted Diiron Benzenedithiolato Hexacarbonyl Electrocatalysts Inspired by the [FeFe]-Hydrogenase Active Site. *Organometallics.* **31,** 8067–8070 (2012).

64. Saveant, J.-M. Molecular Catalysis of Electrochemical Reactions. Mechanistic Aspects. *Chem. Rev.* **108,** 2348–2378 (2008).

65. Lyon, E. J., Georgakaki, I. P., Reibenspies, J. H. & Darensbourg, M. Y. Carbon monoxide and cyanide ligands in a classical organometallic complex model for Fe-only hydrogenase. *Angew. Chem. Int. Ed.* **38,** 3178–3180 (1999).

66. Zhao, J., Wei, Z., Zeng, X. & Liu, X. Three diiron complexes bearing an aromatic ring as mimics of the diiron subunit of [FeFe]-hydrogenase: synthesis, electron transfer and coupled chemical reactions. *Dalton T.* **41,** 11125 (2012).

67. Morvan, D. *et al.* N-heterocyclic carbene ligands in nonsymmetric diiron models of hydrogenase active sites. *Organometallics.* **26,** 2042–2052 (2007).

68. Tokel-Takvoryan, N. E., Hemingway, R. E. & Bard, A. J. Electrogenerated chemiluminescence. XIII. Electrochemical and electrogenerated chemiluminescence studies of ruthenium chelates. *J. Am. Chem. Soc.* **95,** 6582–6589 (1973).

69. Ohsawa, Y., Hanck, K. W. & DeArmond, M. K. A systematic electrochemical and spectroscopic study of mixed-ligand ruthenium(II) 2,2'-bipyridine complexes $[Ru(bpy)_3\text{-}nLn]^{2+}$ (n=0,1,2 and 3). *J. Electroanal. Chem. Inter. Electrochem.* **175,** 229–240 (1984).

70. Chong, D. *et al.* Electrocatalysis of hydrogen production by active site analogues of the iron hydrogenase enzyme: structure/function relationships. *Dalton T.* 4158–4163 (2003). doi:10.1039/B304283A

Chapter 3

Hydrogen Evolution by Three Mono-Fe Carbonyls with Chelating Bis-Phosphines and 1,2-Benzenedithiol as Functional [FeFe]-Hydrogenase Mimics

Joseph A. Laureanti,[a] Abhishek Debnath,[a] Shobeir K. S. Mazinani,[a] Thomas L. Groy,[a] Vladimiro Mujica,[a] Anne K. Jones*[a,]

[a]School of Molecular Sciences, Arizona State University
Tempe, AZ 85287

Abstract

Three pentacoordinate mononuclear iron carbonyls of the form (bdt)Fe(CO)P_2 [bdt = 1,2-benzenedithiol; P_2 = 4,5-Bis(diphenylphosphino)-9,9-dimethylxanthene (**1**), 1,2-Bis(diphenylphosphino)benzene (**2**), and cis-1,2-Bis(diphenylphosphino)ethylene (**3**)] are reported as functional models for the distal iron (Fe_d) of the H-cluster of [FeFe]-hydrogenases. X-ray crystal structures of the complexes show that although all are distorted trigonal bipyramidal complexes, there are significant structural differences. The CO ligand of **1** is in the apical plane, but **2** and **3** feature the CO in the equatorial plane. All three complexes are capable of binding external CO. Each complex is capable of electrocatalytic proton reduction from acetic acid with modest turnover frequencies (s^{-1}) and overpotentials (V): 45 and 0.32, 10 and 0.38, and 35 s^{-1} and 0.36 V, for **1**, **2**, and **3**, respectively.

Introduction

Production of solar fuels like hydrogen using renewable, fast and efficient catalysts is a growing research area. Hydrogenases are the biological catalysts that reduce protons to hydrogen at bimetallic active sites, [FeFe] and [NiFe], and can be thought of as organometallic catalysts containing the first row transition metals coordinated by thiolate ligands as well as the biologically unusual, π-accepting, CO and CN^- ligands.[1,2]

In [FeFe]-hydrogenases, although the active site known as the H-cluster includes two metals, a single, pentacoordinate Fe in a pseudo-square pyramidal geometry is the site of catalysis. For this reason, several groups have tried to produce catalytically functional mono-iron models of [FeFe]-hydrogenases. Liaw and co-workers produced the 16-electron Fe(II) species, $[Fe(CO)_2(CN)(S,NH\text{-}C_6H_4)]^-$.[3] However, the complex is not

stable as a monomer. Instead it readily reacts to form hexacoordinated complexes or dimers, and electrocatalysis has not been demonstrated. Sellman and co-workers employed 1,2-benzenedithiolate (bdt) to construct $[Fe(bdt)(PMe_3)_2(CO)_2]$ and noted that it has a tendency to lose CO, decomposing to a 16-electron complex.[4] Rachfuss and co-workers used that result as inspiration to create an H-cluster spectroscopic model: $(Et_4N)_2[Fe(bdt)(CN)_2(CO)]$.[5] Recently, two groups, Ott and co-workers as well as Roy and co-workers reported coordinatively unsaturated iron complexes coordinated by a carbonyl, a bdt and a chelating bis-phosphine can electrocatalytically reduce protons.[6-9]

Herein we describe the preparation and electrocatalytic properties of three penta-coordinate mono-iron(II) carbonyls completed by a P_2S_2 coordination environment . All three new complexes include sulfurs from 1,2-benzenedithiolate (bdt), a redox-active ligand in which electron density on the sulfur donors can be delocalized into the aromatic ring.[10] Three bis-phosphines with distinct bite angles are employed to systematically tune the properties of the complexes: 4,5-Bis(diphenylphosphino)-9,9-dimethylxanthene (Xantphos), 1,2-Bis(diphenylphosphino)benzene (dppb) and cis-1,2-Bis(diphenylphosphino)ethylene (dppv). Comparisons to catalysts already described in the literature are made.

Results

Synthesis and spectroscopic characterization. As shown in **Scheme 3-1**, three pentacoordinate monoiron(II)- carbonyl complexes, each containing a chelating bis-phosphine and a 1,2-benzenedithiol (bdt) ligand, were synthesized using anhydrous $FeCl_2$ as starting material: (κ^2-Xantphos)Fe(CO)(κ^2-bdt) **1**, (κ^2-dppb)Fe(CO)(κ^2-bdt) **2**, and (κ^2-dppv)Fe(CO)(κ^2-bdt) **3**, where Xantphos is 4,5-Bis(diphenylphosphino)-9,9-

dimethylxanthene, dppb is 1,2-Bis(diphenylphosphino)benzene and dppv is cis-1,2-Bis(diphenylphosphino)ethylene. The bdt ligand was chosen for the combination of its redox activity and strong π–donor propensity. The ligands Xantphos, dppb, and dppv were chosen because the variations in the bridge yield diverse electronic properties.[11,12] All three complexes were synthesized by introduction of the appropriate bis-phosphine in methylene chloride (**1**) or tetrahydrofuran (**2** and **3**) to an anhydrous methanolic solution of ferrous chloride. Then CO was sparged through the solution followed by addition of bdt in the presence of an appropriate base (triethylamine or MeO^-Na^+). Two of the complexes, **2** and **3** (circa 50% isolated yield), are diamagnetic and **1** is paramagnetic (40% yield). A single resonance is observed by ^{31}P NMR for **2** (84.67 ppm) and **3** (93.02 ppm) (**Figure 3-12)** whereas two peaks are observed for **1** at 55.93 and 48.65 ppm (**Figure 3-13**). By comparison, three groups, Eady, Orthaber, and Roy and co-workers prepared [Fe(bdt)(CO)($(C_6H_5)_2PN(CH_2(p\text{-}C_6H_4F))P(C_6H_5)_2$], [Fe(bdt)(CO)($P_2^{cyclo-hexyl}N_2^{phenyl}$)], and [Fe(bdt)(CO)(1,1'-diphenylphosphinoferrocene)] **4**, respectively.[8,9,13] All are diamagnetic pentacoordinated Fe^{II} carbonyls with distorted trigonal bipyrimidal geometry and display ^{31}P NMR chemical shifts at 111.5, 78.2, and 66.32 ppm, respectively. These values correlate well with the observed ^{31}P NMR chemical shifts found for **2** and **3**, which are also diamagnetic, while this directly contrasts the upfield chemical shift found for **1**, a paramagnetic complex.

The U-vis and IR spectra of compounds **1-3** are very similar to what might be predicted based on previous studies of related Fe-S complexes. The UV-vis spectra of all

three complexes include intense transitions in the ultraviolet region, 250-300 nm, indicative of π- π* transitions of the aromatic rings, but the optical absorbance maxima are quite different. As shown in **Figure 3-1**, in tetrahydrofuran (THF), **1** is a deep rose-purple, with absorbances at 411 ($\varepsilon = 2760\ M^{-1}\ cm^{-1}$), 496 ($\varepsilon = 7045\ M^{-1}\ cm^{-1}$), and 680 nm ($\varepsilon = 1935\ M^{-1}\ cm^{-1}$). By comparison, **2** is dark purple, with absorbances at 434 ($\varepsilon = 9812\ M^{-1}\ cm^{-1}$) and 572 nm ($\varepsilon = 7967\ M^{-1}\ cm^{-1}$). Complex **3** is dark green in THF with absorption maxima at 442 ($\varepsilon = 5762\ M^{-1}\ cm^{-1}$), 572 ($\varepsilon = 2794\ M^{-1}\ cm^{-1}$), and 663 nm ($\varepsilon = 1665\ M^{-1}\ cm^{-1}$). The transition at 663 nm overlaps the lower energy side of the 572 nm peak. Tentatively, these bands are all assigned to Fe-S charge transfer bands from the central Fe to the sulfur residues of the bdt ligand. Infrared spectra of compounds **1-3** in methylene chloride (DCM) consist of a single, broad peak in the CO-stretching region at 1925, 1919 and 1935 cm^{-1}, respectively (**Figure 3-2** grey traces). Although at 1919 cm^{-1} the energy of the transition for **2** is very similar to those of **4** and [Fe(bdt)(CO)(methyl-2-{bis-(diphenylphosphinomethyl)amino}acetate)] **5**, the ν_{CO} stretching frequencies of **1** and **3** are shifted to noticeably higher energy, 1925 and 1935 cm^{-1}, respectively. This suggests that the electron density localized about the Fe atom is decreasing in the order **2**>**1**>**3**.

Crystal structures. **Figure 3-3** shows structures for **1-3** determined by single-crystal X-ray diffraction. Selected bond lengths and bond angles are given in **Tables 3-1** and **3-2**. Additional crystallographic information is available in **Table 3-4**. All three complexes feature distorted trigonal bypyrimidal coordination geometry (TBP) around the iron, but the arrangement of ligands in axial and equatorial positions differs for the various complexes. For **2** and **3**, the CO ligand is in an equitorial position while the bdt

and dppb/dppv ligands are trans to one another occupying both axial and equitorial positions. On the other hand, the CO of **1** is in an axial position with a bdt thiolate trans in the other axial position. That means both phosphorous donors of the Xantphos ligand occupy equatorial positions. The very large bite angle of the Xantphos ligand in **1** (101.19°) is remarkably close to that of another, related monoiron compound previously reported, **4** (101.18°), and the large bite angle and the resulting unusual geometry it imposes may explain the reversiblity of electrochemical transitions of **1** (vide infra, **Figure 3-4**).[9]

The geometries of complexes **1-3** were further characterized by Adison's τ value, defined as $\tau = \frac{(\beta-\alpha)}{60}$ in which the variables β and α are defined as the angle between the two axial ligands and the larger of the basal angles, respectively.[14] For a pentacoordinate complex, τ is a measure of the degree of distortion from ideal square pyramidal (τ = 0) or ideal trigonal bipyramidal (τ = 1). For **1**, τ is 0.733 (based on β(C7-Fe1-S2) = 173.60° and α(P1-Fe1-S1) = 129.60°); for **2** τ is 0.932 (based on β(S1-Fe1-P2) = 160.01° and α(C7-Fe1-S2) = 104.08°); for **3** τ is 0.824 (based on β(S1-Fe1-P2) = 173.79° and α(C7-Fe1-S2) = 124.44°). The suggests that the distortion from ideal TBP increases from complex **2**<**3**<**1** paralleling the increase in the phosphine bite angle.

Reactivity towards CO. We showed in previous work that the comparable pentacoordinate complexes **4** and **5**, bind CO at the open coordination site.[9] **Figure 3-2** shows that complexes **1-3** can also coordinate CO at the vacant site, producing a hexavalent di-carbonyl species. Formation of the adduct can be observed via appearance of two new peaks in the Fourier transform infrared spectroscopy (FTIR) spectrum. Additionally, after binding CO, the ^{31}P NMR peaks from each of these complexes shifts

and splits (**Figure 3-12**). However, even after exposure to excess CO, the spectroscopic features of the pentaacordinate complexes are present in both FTIR and NMR spectra. This suggests that binding of CO is not quantitative. Reversibility of CO binding was demonstrated by sparging N_2 through a CO-saturated solution to regenerate the spectroscopic features of the pentacoordinate complex.

Electrochemistry and catalysis. Redox reactions of the three Fe^{II} complexes were probed by cyclic voltammetry. As shown in **Figure 3-4**, cyclic voltammograms of **1** show two reversible reductions at $E_{1/2}$ = -0.07 V (i_p^a/i_p^c= 1.15, ΔE_p = 0.12 V) and $E_{1/2}$ = -1.70 V (i_p^a/i_p^c = 1.02, ΔE_p = 0.12 V), and a reversible oxidation at $E_{1/2}$ = +0.42 V (i_p^a/i_p^c = 0.82, ΔE_p = 0.11 V) vs $Fc^{+/0}$ (Fc = ferrocene). The reduction at -0.06 V is assigned to the bdt ligand because of similarity to a reversible wave (+74 mV vs Fc^+/Fc) ascribed to a bdt ligand in a Au complex.[10,15] The oxidation at +0.45 V is thought to correspond to oxidation of the Fe^{II} to Fe^{III}. The reductive event at -1.65 V likely corresponds to the $Fe^{II/I}$ transition and generates the species responsible for proton reduction in the presence of acetic acid (vide infra, **Figure 3-5**). Cyclic voltammetry of **2** shows one reversible reduction at $E_{1/2}$ = -1.81 V (i_p^a/i_p^c= 0.99, ΔE_p = 0.14 V) and two irreversible processes centered at +0.31 and -0.38 V. Similarly, cyclic voltammograms from **3** include one reversible reduction at $E_{1/2}$ = -1.76 V (i_p^a/i_p^c = 0.93, ΔE_p = 0.11 V), one irreverisible oxidation centered at +0.26 V, and two irreversible reductions centered at -0.32 and -0.20 V. Although the oxidation of the Fe of **1** is reversible, that is not the case for **2** and **3.** It is likely that the large bite angle of Xantphos plays a role in stabilizing the oxidized Fe^{III} product.

Electrocatalytic proton reduction by **1-3** was explored using acetic acid ($pK_{a(THF)}$ = 24.42) as proton source.[16] As shown in **Figure 3-5**, sequential addition of acetic acid from 0.05 M to 5.0 M for **1** and 0.05 to 1.0 M for **2** and **3**, induces an irreversible reductive feature at the potential of the $Fe^{II/I}$ couple, the current of which increases with increasing acid concentration.This is characteristic of electrocatalytic proton reduction. In this potential range, direct proton reduction at the glassy carbon electrode is negligible (**Figure 3-7**). Gas chromatography was used to verify that hydrogen is produced during electrocatalysis and to determine the Faradaic efficiency: 99%, 94% and 92% for complexes **1-3**, respectively. The overpotential, potential beyond the equilibrium conditions that is required to initiate electrocatalysis, was determined using the method of Artero and co-workers as 0.32-1.0 V, 0.38-0.47 V, and 0.36-0.49 V, for complexes **1**, **2**, and **3**, respectively, **Table 3-3**.[17]

Equation 1 describes the relationship between the observed rate constant and the peak catalytic current, i_{cat}, in which n is the number of electrons in the reaction (2), F is faradays constant, A is the area of the electrode, D is the diffusion coefficient, k is the rate constant, and x is the order of the reaction with respect to acid. **Figure 3-8** shows that the catalytic peak current,

$$i_{cat} = nFA[cat]\sqrt{D(k[acid]^x)} \qquad \text{Eq 1}$$

$$\frac{i_{cat}}{i_p} = \left(\frac{n}{0.4463}\right)\sqrt{\frac{RT(k[acid]^x)}{Fv}} \qquad \text{Eq 2}$$

$$\frac{i_{cat}}{i_p} = \left(\frac{n}{0.4463}\right)\sqrt{\frac{RTk}{Fv}} \qquad \text{Eq 3}$$

i_{cat} depends linearly on catalyst concentration for complexes **1-3**. This demonstrates a first-order dependence of i_{cat} on the [catalyst] in the reaction at fixed concentrations of

acid. Similarly, showing a second order dependence on the concentration of acid in the experiment, the ratio of catalytic peak current (i_{cat}), to reductive peak current (i_p) in the absence of a proton source, $\left(\frac{i_{cat}}{i_p}\right)$, is linear with respect to [acetic acid] for catalyst concentrations in the range of 0.4 – 2.8 M for **1**, 0.1 – 0.5 M for **2**, and 0.2 – 0.8 M for **3**, **Figure 3-9**.[18] **Equation 2** displays the relationship between the rate constant and the observed value of $\left(\frac{i_{cat}}{i_p}\right)$, where ν is the scan rate (0.2 V s^{-1}). The maximum value observed for $\left(\frac{i_{cat}}{i_p}\right)$, in the linear region, is 10.5, 3.6, and 8.6 obtained for **1** (2.2 mM), **2** (0.82 mM), and **3** (1.1 mM), respectively. At high acid concentrations relative to the concentration of catalyst present in the experiment, the observed catalytic current becomes independent of the quantity of acid added to the solution. **Figure 3-10** shows an average of the values obtained for $\left(\frac{i_{cat}}{i_p}\right)$ vs. [AcOH] for complexes **1-3**. The turnover frequencies (TOF), calculated using **Equation 3**, are 45, 10, and 35 s^{-1}, for compounds **1-3**, respectively.[11]

Computational details: To complement the experimental results, the electronic structures of **1-3** were determined using DFT calculations. Comparisons of the frontier orbitals of **1-3** reveal three striking differences between **1** and the other two complexes (**Figure 3-6**). First, **2** and **3** have HOMOs that are delocalized over the Fe and the bdt ligand via iron *d* orbitals and sulfur *p* orbitals and π interactions with adjacent carbon atoms. In contrast, the HOMO of **1** is localized largely on the Fe and S atoms. Second, complexes **2-5**, show minimal bonding interactions between the phospohorus atoms and the iron whereas **1** shows electron density delocalized between the iron and the two

phosphorus atoms. This bonding interaction extends to the oxygen atom of the Xantphos bridge as well as the four phosphorus-carbon bonds at each phenyl ring. Third, the HOMO of **1** features greater electron density on the equatorial sulfur than the axial sulfur. On the other hand, the HOMO of **2** features relatively symmetric coordination to the two sulfur atoms. Conversely, the HOMO of **3** shows uneven electron density at the sulfurs and a concomittant shift to asymmetric electron density found at the bdt ligand. Previous DFT calculations showed that the majority of the orbital density for the LUMOs of **4** and **5**, is localized on the Fe *d* orbitals with minor density on the the sulfur and phosphorus. The LUMOs of **1-3** suggest a similar picture. The shapes of these LUMOs are important to understanding the reactivity of these complexes. In short, reduction of these **1-3** results in an accumulation of charge at the metal center, yielding a highly basic iron site. Furthermore, the significant iron component of the LUMOs is consistent with the abilities of these complexes to reversibly bind CO.

Conclusion

In summary, the rate of catalysis by **1-3** is in the range 10 – 45 s^{-1}, which is an order of magnitude greater than the related catalysts prepared by Eady and co-workers.[13] It is interesting to note that the value of $\left(\frac{i_{cat}}{i_p}\right)$ plateaus around [AcOH] = 1.0 M for complexes **2** and **3**, while for **1** a plateau of $\left(\frac{i_{cat}}{i_p}\right)$ is not observed until [AcOH] > 3.0 M, a result that may be due to stabilization of the Fe center by the large bite angle of the Xantphos ligand. Additionally, the degree of distortion from ideal geometry correlates with the increasing phosphine bite angle **2**<**3**<**1**. Complex **1**, the most distorted, has slightly better catalytic properties, i.e. higher turnover frequency at the lowest

electrochemical overpotential, than the other two complexes, and more reversible non-catalytic electrochemistry. This may be related to the strained geometry of **1** that prevents effective delocalization of electron density in the HOMO into the bdt ligand, a feature not yet observed for other 16-electron, pentacoordinate Fe^{II} species.

Although some pentacoordinate iron complexes like **5**, [Fe(bdt)(CO)$\left(P_2^{Phenyl}N_2^{Phenyl}\right)$], and [Fe(bdt)(CO)$((C_6H_5)_2PN(CH_2(p\text{-}C_6H_4F))P(C_6H_5)_2]$ have square pyramidal geometry, each of the new complexes reported here adopts a trigonal bipyramidal geometry.[8,9,13] The impact of geometry on the rate of catalysis for complexes **1**-**3** agrees well with two complexes synthesized by Roy and co-workers who used 1,1'-diphenylphosphinoferrocene (dppf, **4**), and (methyl-2-{bis-(diphenylphosphinomethyl)amino}acetate)] (NP_2, **5**), as the bis-phosphine ligand.[9] As with each complex in this study, **4** adopted a distorted trigonal bipyrimidal conformation and showed proton reduction rates that are comparable to complexes **1**-**3**. However, **5** adopts a distorted square pyramidal geometry and the rate of electrocatalytic proton reduction by **5** is an order of magnitude graeater than those of **1**-**4**. We have shown that the large bite angle of the bis-phosphine ligand, Xantphos, leads to stabilization of the iron atom during oxidation and reduction reactions and that the Xantphos ligand unanticipatedly allows electron delocalization to be spread about the iron and the Xantphos ligand.

Methods

General. All chemicals purchased were of the highest purity available and were used without further purification unless otherwise noted. Tetrahydrofuran was dried over sodium/benzophenone under a nitrogen atmosphere. Methanol was dried over iodine and

magnesium strips under a nitrogen atmosphere. All reactions were carried out under a dry nitrogen atmosphere using standard Schlenk and vacuum-line techniques unless otherwise noted. Anhydrous methanol and methylene chloride were purchased from Sigma-Aldrich, and deuterated solvents were purchased from Cambridge Isotope Laboratories. ^{1}H, ^{13}C, and ^{31}P NMR spectra were recorded at room temperature on a Varian Liquid-State NMR spectrometer. FTIR spectra were recorded on a Bruker VERTEX 70 spectrophotometer with an MCT detector using a stainless steel sealed liquid spectrophotometer cell with CaF_2 windows or by spotting a sample directly onto a CaF_2 window. UV-vis measurements were performed on a Hewlett-Packard 8453 spectrophotometer using quartz cuvettes with a 1 cm pathlength. Gas chromatography (GC) was completed on an SRI model 310 gas chromatograph equipped with a thermal conductivity detector (TCD), a 6' molecular sieve 13X packed column with Ar as the carrier gas. The gas chromatograph was calibrated using the peak area resulting from injections of known volumes of 1% H_2 in 99% N_2.

Fe(CO)(bdt)(Xantphos), ***1****.* To an anaerobic solution of anhydrous ferric chloride (85 mg, 0.63 mmol) in anhydrous methanol (5 mL), 4,5-Bis(diphenylphosphino)-9,9-dimethylxanthene (400 mg, 0.69 mmol) in 10 mL of methylene chloride (DCM) was added dropwise, resulting in a pale yellow solution. The solution was sparged with carbon monoxide (CO) for 15 min producing a dark, straw-colored solution. After 30 min of mixing, 1,2-benzenedithiol (80.0 μL, 0.69 mmol) and sodium (30.5 mg, 1.33 mmol) in 4 mL of methanol was added dropwise forming a deep rose solution that was allowed to stir for 1 hr. A dark reddish/purple solid was generated by removing solvent under reduced pressure. The desired compound was purified over silica using 3:2 ethyl

acetate:methylene chloride as eluent followed by crystallization using slow diffusion of methanol into a saturated solution of DCM at 0 °C. Yield: 150 mg (40%). $^{31}P\{^{1}H\}$ NMR (161.8 MHz, CD_2Cl_2): δ=55.93, 48.65. IR (CH_2Cl_2, cm^{-1}): *ν*(CO) 1925. UV-Vis (THF): λ_{max} (nm): 411 (2760 M^{-1} cm^{-1}), 496 (7045 M^{-1} cm^{-1}), 680 (1935 M^{-1} cm^{-1}). ESI mass spectrum (positive mode): *m/z* = $[(M - CO)^+]$ expected 774.1032 found 774.1023, $[(M - CO + H)^+]$ expected 775.1111, found 775.1131. Elemental Analysis calculated for $C_{46}H_{36}$ + CH_4 (for one methanol): C, 67.61 H, 4.84. Found: C, 67.82 H, 4.53.

Fe(CO)(bdt)(dppb), ***2****.* To an anaerobic solution of anhydrous ferric chloride (90 mg, 0.71 mmol) in anhydrous methanol (5 mL), 1,2-Bis(diphenylphosphino)-benzene (317 mg, 0.71 mmol) in 10 mL of tetrahydrofuran (THF) was added dropwise, resulting in a grey solution. The solution was sparged with CO for 15 min producing a dark brown solution. After mixing 30 min, a solution of 1,2-benzenedithiol (81.45 µL, 0.71 mmol) and triethylamine (197 µL, 1.4 mmol) in 2 mL of THF was added dropwise to form a dark purple solution and allowed to mix for 1 hr. Solvent was removed under reduced pressure yielding a dark purple solid. The desired product was purified over silica using 3:2 DCM:hexanes as eluent followed by crystallization using slow diffusion of isopropanol into a saturated solution of DCM at 0 °C. Yield: 159.4 mg (51%). ^{1}H NMR (CD_2Cl_2): δ=8.11 (q, 2H), 7.72 (m, 6H), 7.59 (m, 8H), 7.14 (q, 2H), 7.09 (t, 2H), 7.01 (t, 4H), 6.91 (t, 4H). $^{13}C\{^{1}H\}$ NMR (100 MHz, CD_2Cl_2): δ=144.97, 133.9, 133.2, 131.9, 130.9, 130.8, 129.8, 129.2, 128.7, 127.8, 121.3. $^{31}P\{^{1}H\}$ NMR (161.8 MHz, CD_2Cl_2): δ=84.67. IR (CH_2Cl_2 cm^{-1}): *ν*(CO) 1919. UV-Vis (THF): λ_{max} (nm): 434 (9812 M^{-1} cm^{-1}), 572 (7967 M^{-1} cm^{-1}). APCI mass spectrum (positive mode): *m/z* = $[(M + H)^+]$ expected 671.099, found 671.0467, $[(M - CO + H)^+]$ expected 643.100, found 643.0506.

Fe(CO)(bdt)(dppv), ***3***. To an anaerobic solution of anhydrous ferric chloride (80 mg, 0.631 mmol) in anhydrous methanol (4 mL), 1,2-Bis(diphenylphosphino)ethylene (275 mg, 0.631 mmol) in THF was added dropwise forming a dark green solution. The atmosphere was exchanged for CO producing a dark red solution that was stirred for 1 hr. 1,2-benzenedithiol (80.0 µl, 0.631 mmol) and sodium (32.0 mg, 1.39 mmol) in 4 mL of methanol was added dropwise forming a deep rose solution and was allowed to stir for 90 min. The solvent was removed under reduced pressure to obtain a dark greenish grey solid. The product was isolated as a dark green solid via purification over silica using toluene as eluent followed by a second silica column developed with 3:2 ethyl acetate:DCM. Crystallization was completed using slow diffusion of methanol into a saturated solution of DCM at 0 °C. Yield: 195 mg (50%). ^{1}H NMR (CD_2Cl_2): δ=8.02 (q, 2H), 7.78 (m, 5H), 7.49 (m, 6H), 7.25 (t, 2H), 7.09 (m, 7H), 6.96 (t, 4H). $^{13}C\{^{1}H\}$ NMR (100 MHz, CD_2Cl_2): δ=150.2, 133.2, 132.3, 130.8, 130.8, 129.2, 128.7, 128.2, 121.4. $^{31}P\{^{1}H\}$ NMR (161.8 MHz, CD_2Cl_2): δ=93.02. IR (CH_2Cl_2 cm^{-1}): *ν*(CO) 1930. UV-vis (THF): λ_{max} (nm): 442 (5762 M^{-1} cm^{-1}), 572 (2794 M^{-1} cm^{-1}), 663 (1665 M^{-1} cm^{-1}). APCI mass spectrum (positive mode): *m/z* = $[(M + H)^{+}]$ expected 621.079, found 621.0350, $[(M – CO + H)^{+}]$ expected 593.080, found 592.8994.

Reversible Binding of CO to complexes ***1-3***. A saturated solution of DCM containing1.5 – 2.0 mg of the desired catalyst was sparged with CO for 15 min. Formation of the CO adduct was monitored spectroscopically by FTIR and ^{31}P NMR. Removal of CO was accomplished by sparging the CO saturated solution with N_2 for 15-60 min and was confirmed by FTIR and ^{31}P NMR.

X-ray crystallography. A representative crystal of each compound was individually mounted on the end of a thin glass fiber using Apiezon type N grease and optically centered. Cell parameter measurements and single-crystal diffraction data collection were performed at low temperature (123 K) with a Bruker Smart APEX diffractometer. Graphite monochromated Mo Kα radiation (λ = 0.71073 Å) in the ω–φ scanning mode was used for the measurements. Each structure was solved by direct methods and refined by full-matrix least-squares on F^2. The following is the list of the programs used: data collection, Bruker Instrument Service v2010.9.0.0; cell refinement and data reduction, SAINT V8.32B; structure solution and refinement, SHELXL-2013; molecular graphics, XShell v6.3.1; preparation of material for publication, Bruker APEX2 v2013.6-2. Details of crystal data and parameters for data collection and refinement are listed in **Table 3-4**.

Electrochemistry. Electrochemical experiments were carried out using a PG-STAT 128N Autolab electrochemical analyzer controlled with GPES software. A conventional three electrode cell was employed for recording cyclic voltammograms. Glassy carbon working electrodes (BASi, West Lafayette, IN. 3.0 mm diameter) were prepared by sucessive polishing with 1.0 and 0.3 μm aqueous alumina slurries with 10 min sonication in ultrapure water following each polishing step. The supporting electrolyte was $TBAPF_6$ (0.1 M in THF). The Ag/Ag^+ psuedoreference electrode was prepared by immersing a silver wire anodized with AgCl into a glass chamber, equipped with a VyCor frit (BASi, West Lafayette, IN) and a septum and filling with 0.1 M $TBAPF_6$ in THF. A platinum wire was used as the counter electrode. Oxygen was removed from the electrochemical cell by sparging the solution for 15 min followed by

maintaining a constant stream of argon in the headspace during electrochemical experiments. All potentials are reported relative to the ferrocene/ferrocenium couple ($Fc^{+/0}$) measured as an internal reference and added after the final experiment. Catalyst concentrations were determined spectrophotometrically using the following extinction coefficients: ε(496 nm) = 7045 M^{-1} cm^{-1}, ε(434 nm) = 9812 M^{-1} cm^{-1}, and ε(442 nm) = 5762 M^{-1} cm^{-1} for **1**-**3**, respectively.

To determine Faradaic efficiency, controlled potential coulometry was completed in a 0.1 M $TBAPF_6$ solution in THF loaded in a custom electrochemical cell equiped with a gas-tight sampling port (**Figure 3-13**). The electrochemical cell was assembled in an anaerobic glovebox under a nitrogen atmosphere. The quantity of H_2 produced was determined via GC-TCD analysis of the headspace gases.

Overpotential calculations were completed using the half-wave potentials, determined as the potential corresponding to the maximum value of $\left(\frac{\mathrm{di}}{\mathrm{dE}}\right)$, that is, the first derivative of the current data from the cyclic voltammograms.

Computational Details. – The ORCA quantum chemistry package was used to perform *ab initio* calculations at DFT level.[19] The BP86[20,21] functional was used concurrently with the scalar relativistic zeroth order regular approximation (ZORA[22]) and relativistic def2-SVP basis set and the corresponding def2-SVP/J auxiliary basis set. For iron, def2-TZVPP, for phosphorous and sulfur def2-TZVP basis sets have been used throughout this work.[23] Also Van der Waals interactions were accounted for using the method of Grimme and coworkers.[24,25] Tables for geometrical parameters and Löwdin charge decomposition are shown in **Table 3-5**.

Figures

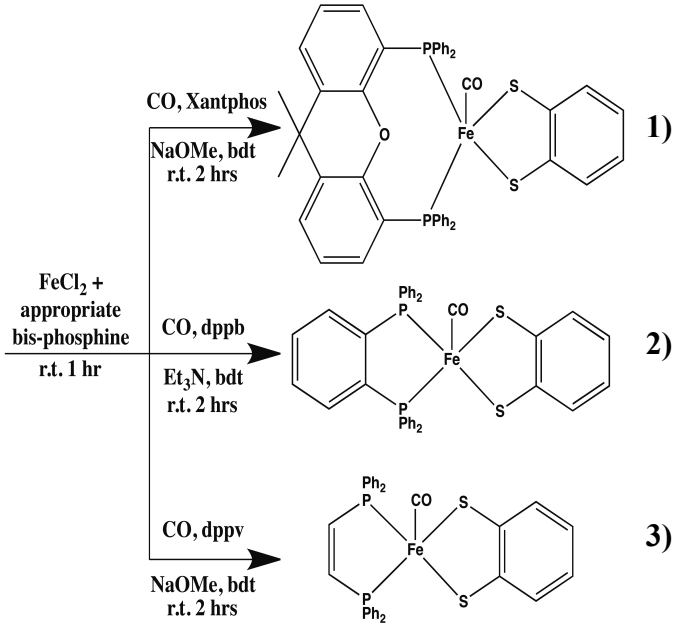

Scheme 3-1. Synthetic routes to complexes **1-3** from $FeCl_2$, 1,2-benzenedithiol, CO, and the appropriate bis-phosphine ligand.

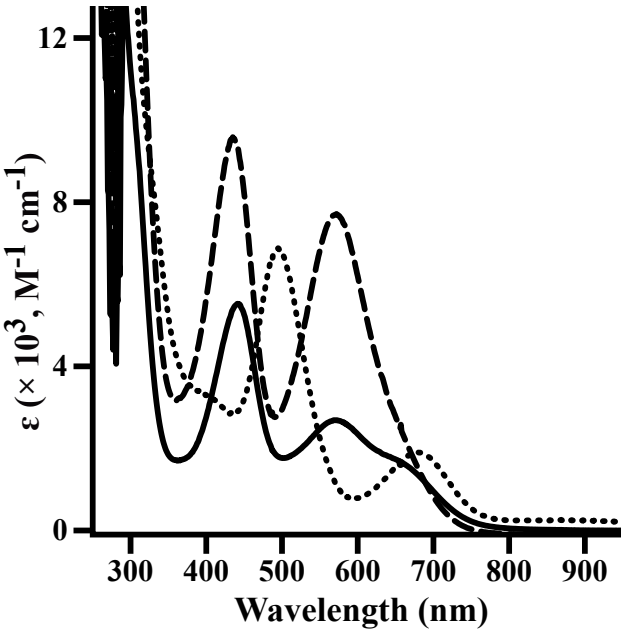

Figure 3-1. UV-vis spectra of compounds **1-3** in tetrahydrofuran (THF). **1** (Dotted trace), **2** (Dashed trace), and **3** (Solid trace). Spectra were recorded from solutions of approximately 0.1 mM of each complex in THF at room temperature.

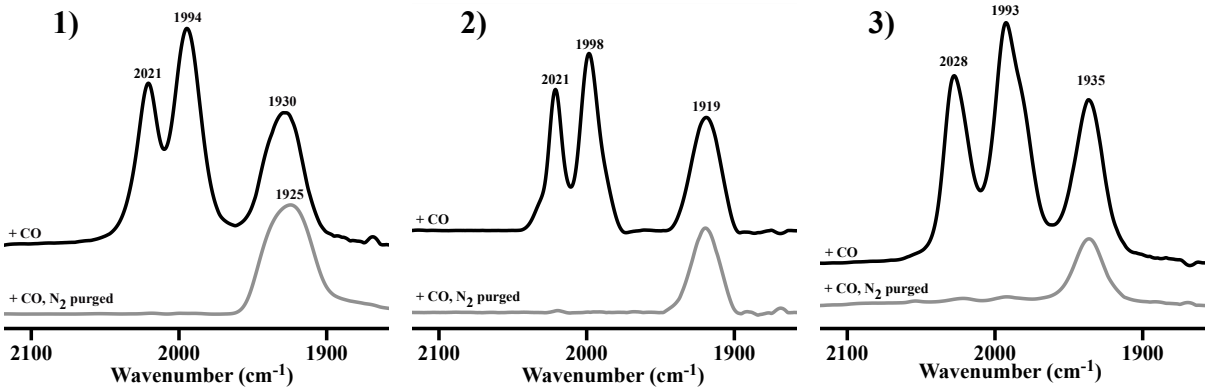

Figure 3-2. FTIR spectra in the presence and absence of CO for **1**, **2**, and **3**. Black traces show IR spectra after sparging CO through the solution. Gray traces show the IR spectra (**1**-**3**) after removal of CO via saturation with nitrogen.

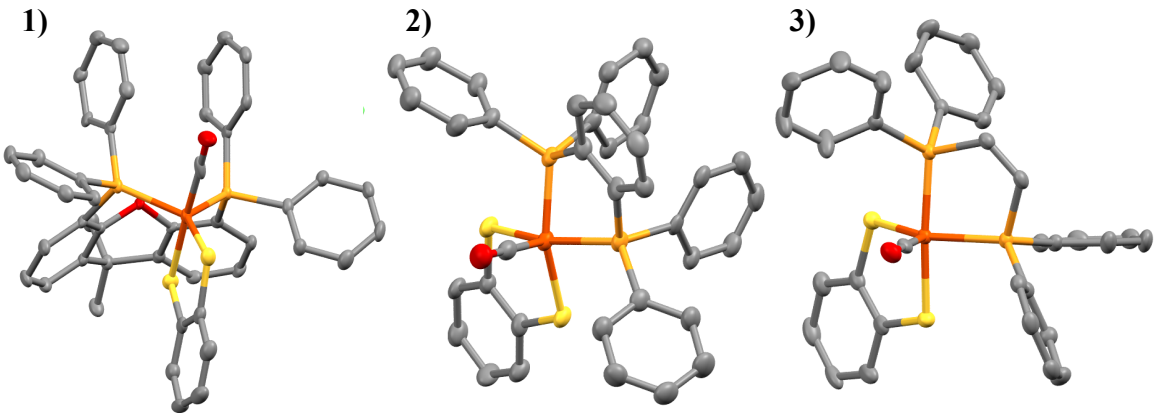

Figure 3-3. Molecular structures of **1**, **2**, and **3**, obtained from single crystal X-ray diffraction with thermal ellipsoids drawn at a probability level of 50%. Hydrogen atoms have been omitted for clarity. Coloring scheme: grey, orange, red, rust, and yellow designate carbon, phosphorus, oxygen, iron, and sulfur atoms, respectively.

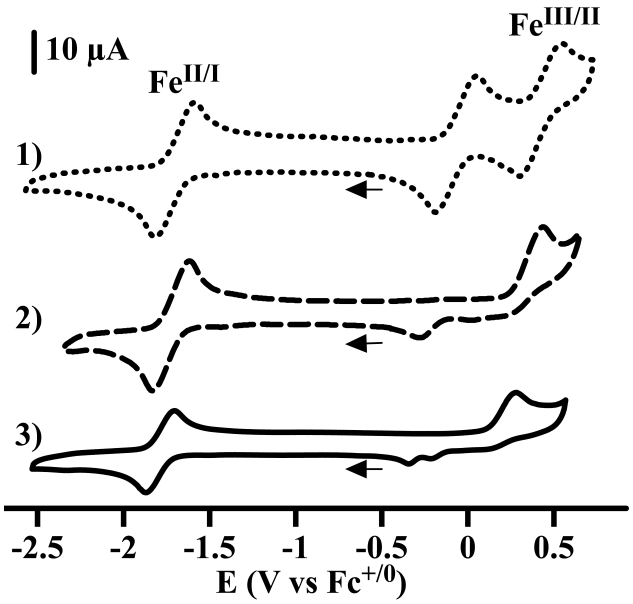

Figure 3-4. Cyclic voltammograms of **1** (dotted trace, 1.04 mM), **2** (dashed trace; 0.79 mM), and **3** (solid trace; 0.45 mM) in 0.1 M $TBAPF_6$/THF at a scan rate of 0.05 V s^{-1}. Arrows indicate the initiation point and potential scan direction of the voltammogram.

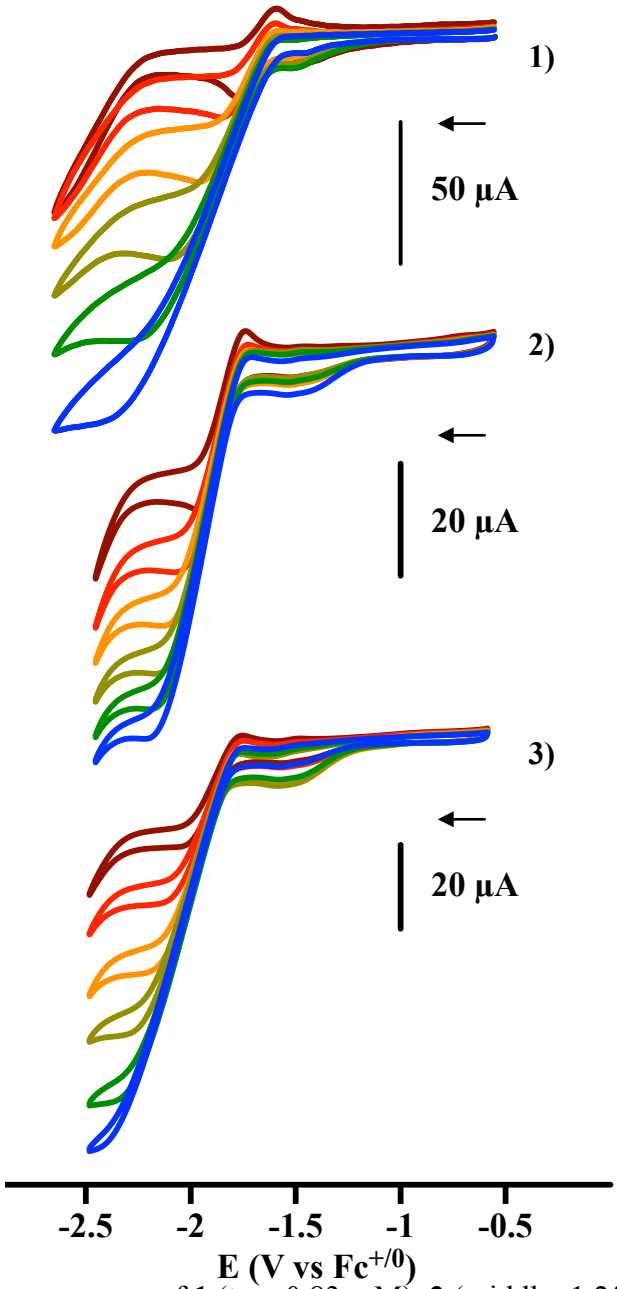

Figure 3-5. Cyclic voltammograms of **1** (top; 0.83 mM), **2** (middle; 1.25 mM), and **3** (bottom; 0.45 mM) in the presence of various concentrations of AcOH in 0.1 M $TBAPF_6$/THF at a scan rate of 0.2 V s^{-1}. The acid concentrations used are 0.2, 0.6, 1.2, 1.8, 2.4, and 3.0 M for **1**, and 0.2, 0.3, 0.4, 0.5, 0.6, 0.7 M for **2** and **3**. Arrows indicate the initiation point and potential scan direction of the voltammograms.

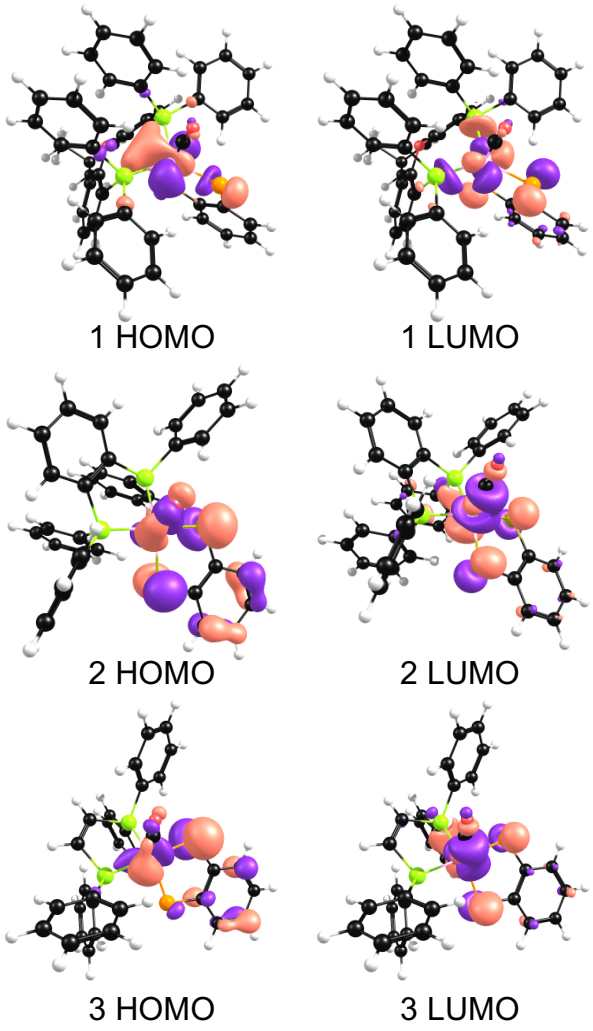

Figure 3-6. Electron density profiles of the HOMOs and LUMOs of **1**, **2**, and **3** determined at density functional level of theory.

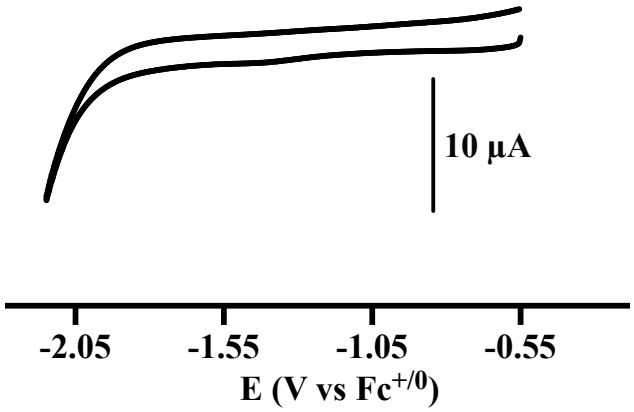

Figure 3-7. Cyclic voltammogram of a bare glassy carbon electrode in the absence of a catalyst in 0.1 M $TBAPF_6$/THF with 1.0 M AcOH. Scan rate is 0.2 V s^{-1}.

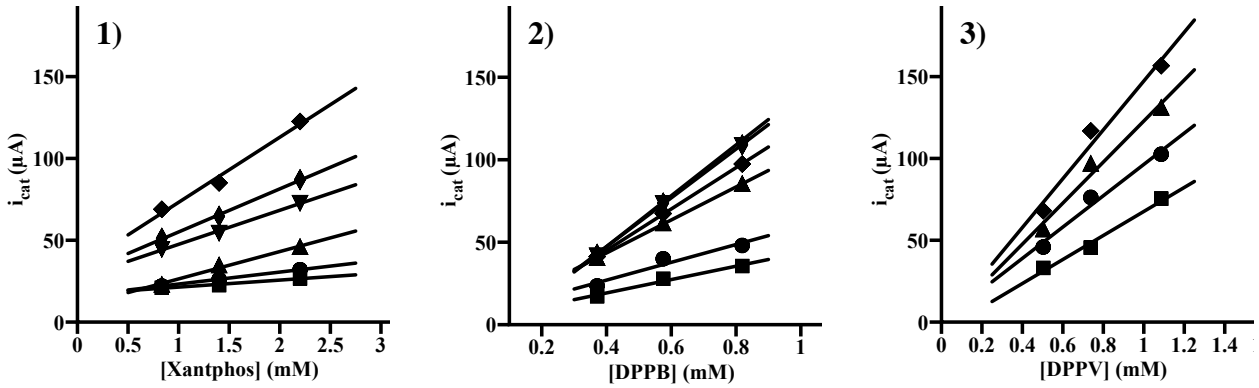

Figure 3-8. Dependence of i_{cat} on catalyst concentration for **1**, **2**, and **3** at constant concentrations of acetic acid. The straight lines are the lines of best fit. The acetic acid concentrations used are: (A) 0.2 mM (■, k = 2.1), 0.4 mM (●, k = 1.3), 0.6 mM (▲, k = 1.2), 1.0 mM (▼, k = 2.2), 1.2 mM (♦, k = 2.5), and 1.6 mM (◆, k = 3.5); (B) 0.1 mM (■, k = 17.1), 0.2 mM (●, k = 16.4), 0.4 mM (▲, k = 20.8), 0.5 mM (◆, k = 20.5), 1.0 mM (▼, k = 12.9), and 1.4 mM (♦, k = 9.4); (C) 0.3 mM (■, k = 13.4), 0.4 mM (●, k = 20.1), 0.5 mM (▲, k = 26.3), and 0.6 mM (◆, k = 31.5), where k is the trimolecular rate constant. Experimental conditions: 0.1 M $TBAPF_6$/THF with various [AcOH], and the scan rate is 0.2 V s^{-1}.

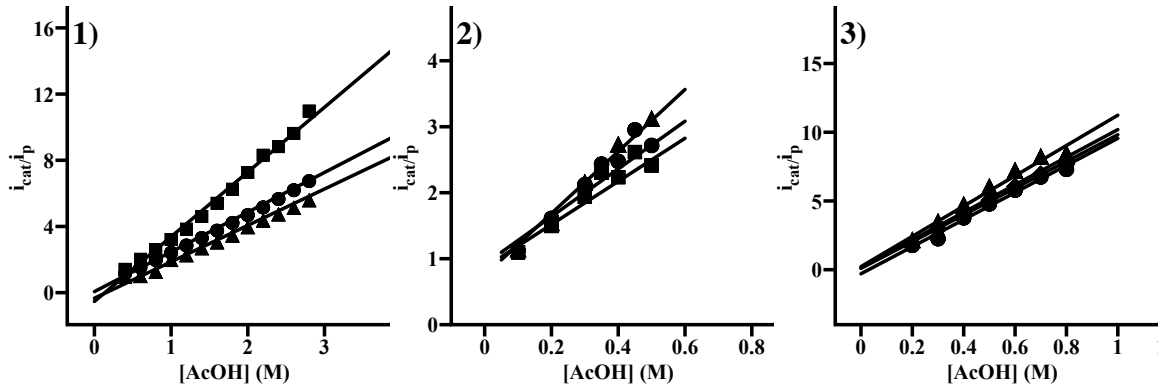

Figure 3-9. Dependence of i_{cat}/i_p on the concentration of acetic acid present during the experiment for **1**, **2**, and **3**. The straight lines are the lines of best fit. The catalyst concentrations used are: (A) 0.83 mM (▲), 1.4 mM (●), and 2.2 mM (■); (B) 0.4 mM (■), 0.60 mM (●), and 0.82 mM (▲); (C) 0.50 mM (◆), 0.75 mM (●), and 1.1 mM (▲).

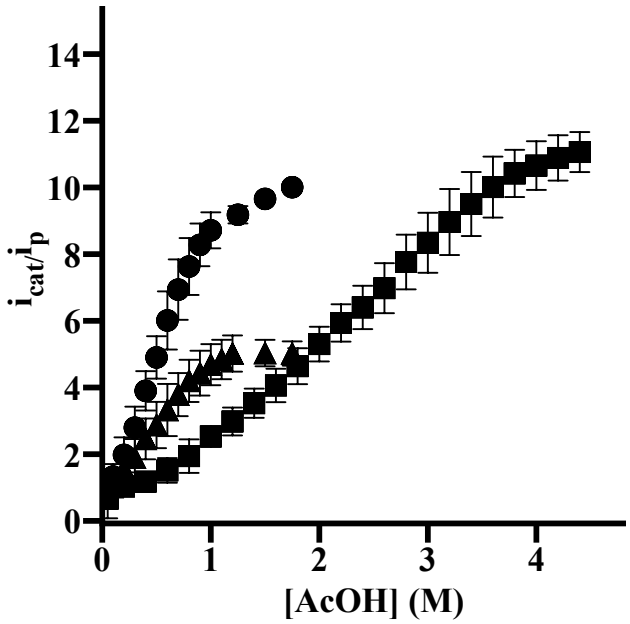

Figure 3-10. Dependence of i_{cat}/i_p on the concentration of acetic acid present in the experiment to the region in which i_{cat} is independent of acid concentration for **1** (■, k = 45 s^{-1}), **2** (▲, k = 10 s^{-1}), and **3** (●, k = 35 s^{-1}), where k is the observed first order rate constant. Error bars represent one standard deviation from three individual experiments. Experiments were completed using catalyst concentrations between 0.5 and 2.0 M, 0.4 to 0.8 M, and 0.5 and 1.2 M for complexes **1-3**, respectively.

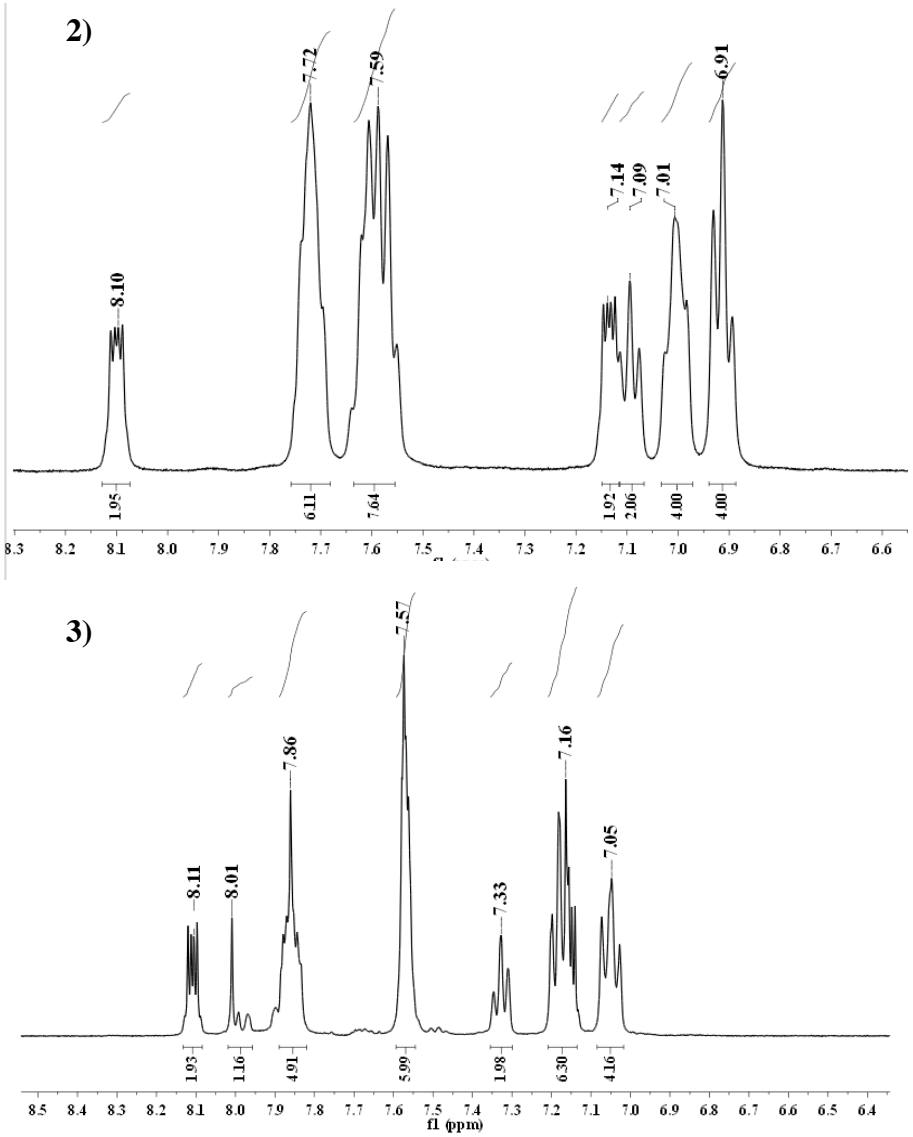

Figure 3-11. ^{1}H NMR spectra in $CDCl_3$ from **2** and **3**.

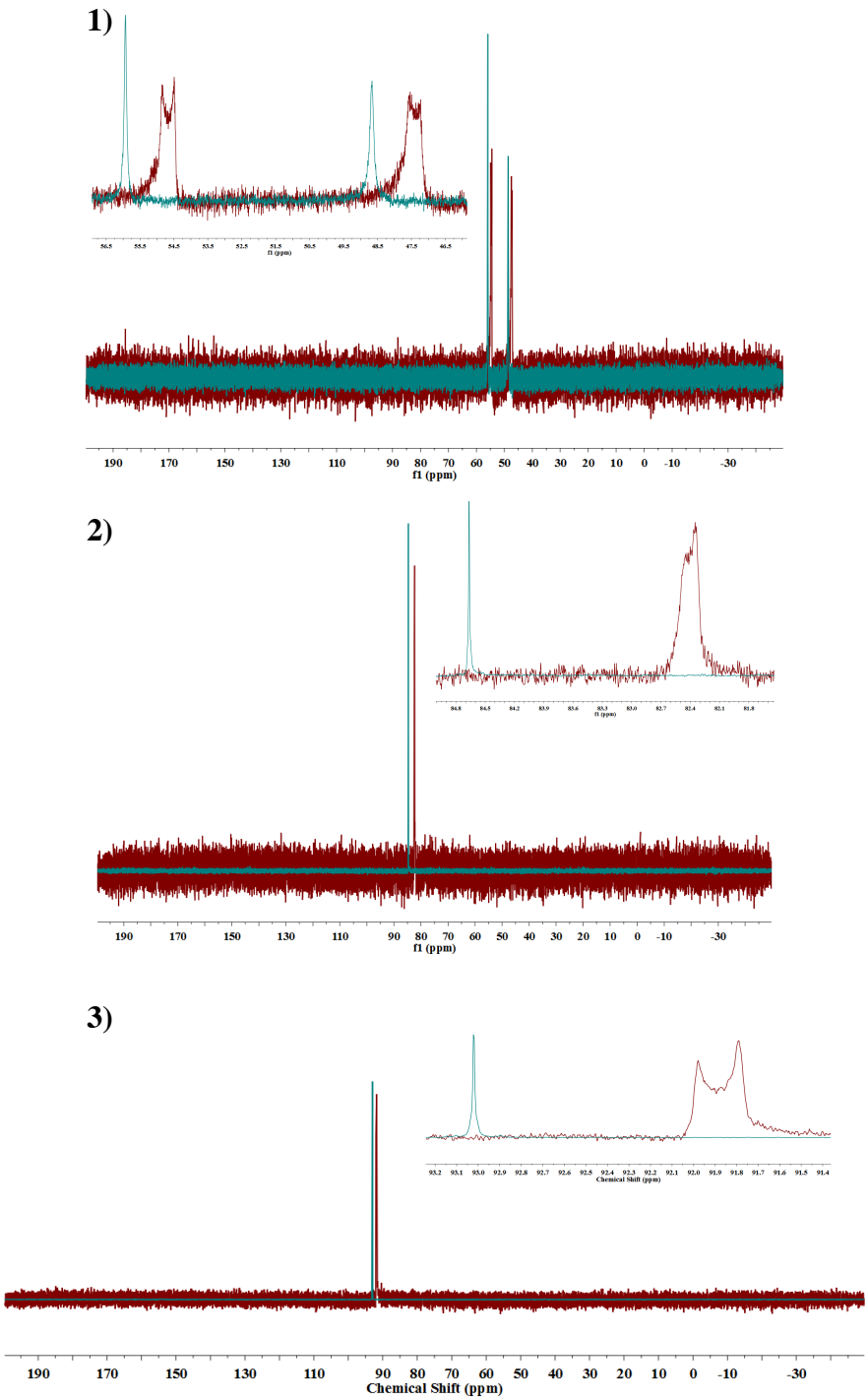

Figure 3-12. ^{31}P NMR of **1-3** before (teal) and after (red) exposure to CO. Inset(s) highlight the upfield shift and peak splitting that occurs upon binding CO.

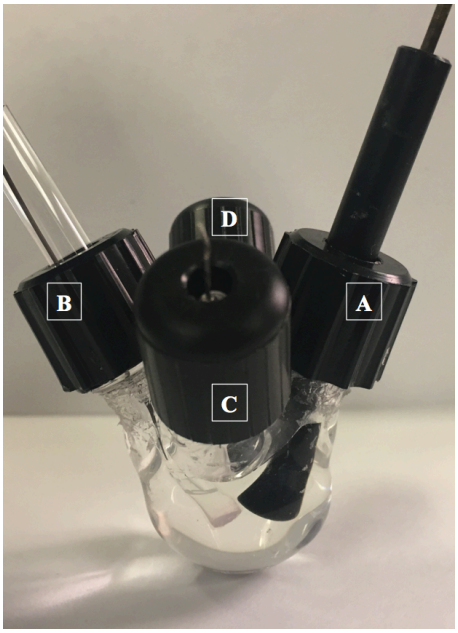

Figure 3-13. Custom sealed electrochemical cell created for Faradaic efficiency experiments. Cell components are as follows: glassy carbon working electrode (A), chloride coated silver wire in 0.1 $TBAPF_6$ (B), platinum wire encased in boro-silicate glass (C), and gas sampling port (D).

Table 3-1. Selected bond lengths (Å) and bond angles (deg) for **1-5**.

Bond Lengths

	1[a]	**2**[a]	**3**[a]	**4**[b]	**5**[b]
Fe1-S1	2.1885	2.1952	2.21	2.1719	2.2007
Fe1-S2	2.2328	2.2045	2.1652	2.2243	2.1767
Fe1-P1	2.2338	2.2268	2.1868	2.2405	2.2222
Fe1-P2	2.245	2.2099	2.2042	2.2241	2.2249
Fe1-C7	1.767	1.755	1.735	1.732	1.715
C41-O41	1.107	1.136	1.156	1.162	1.154

Bond Angles

	1[a]	**2**[a]	**3**[a]	**4**[b]	**5**[b]
P2-Fe1-P1	101.19	83.11	86.6	101.18	87.49
S1-Fe1-S2	87.86	90.09	89.61	89.21	89.31
C7-Fe1-S1	85.78	107.28	96.59	134.57	101.3
C7-Fe1-S2	173.6	104.08	124.44	88.52	106.58
C7-Fe1-P1	95.39	94.44	89.63	90.19	94.11
C7-Fe1-P2	90.36	92.13	89.11	96.69	93.28
S1-Fe1-P2	129.57	160.01	173.79	128.48	165.14
S2-Fe1-P1	89.2	160.39	145.61	171.74	159.2
O1-C7-Fe1	175.6	177.7	178.8	173.4	176.7

[a]values from this work, [b]values from Roy and coworkers[9]

Table 3-2. Bond distances (Å) in the 1,2-Benzenedithiolate ligand in complexes **1-5**

Bond lengths of BDT ligand

	1[a]	**2**[a]	**3**[a]	**4**[b]	**5**[b]
C1-C6	1.407	1.401	1.412	1.398	1.412
C1-C2	1.402	1.402	1.397	1.404	1.386
C2-C3	1.412	1.419	1.409	1.41	1.407
C3-C4	1.345	1.381	1.375	1.365	1.373
C4-C5	1.451	1.389	1.396	1.401	1.394
C5-C6	1.361	1.399	1.368	1.38	1.385
C1-S1	1.759	1.765	1.744	1.745	1.746
C2-S2	1.721	1.752	1.743	1.735	1.757

[a]values from this work, [b]values from Roy and coworkers[9]

Table 3-3. Overpotentials for for electrocatalytic hydrogen production from acetic acid by complexes **1**, **2**, and **3**.

[AcOH] C_0/M	Potential ($E_{1/2}$) / V vs. $Fc^{+/0}$		
	1		
	Calculated ($E^T_{1/2}$)	Experimental ($E^E_{1/2}$)	Overpotential ($E^T_{1/2}$-$E^E_{1/2}$)
0.1	-1.464	-1.784	0.320
1.1	-1.494	-1.877	0.382
1.5	-1.498	-1.883	0.385
1.9	-1.501	-2.043	0.542
2.1	-1.503	-2.142	0.639
2.5	-1.505	-2.223	0.718
3.1	-1.508	-2.370	0.862
3.5	-1.509	-2.497	0.988
4.1	-1.511	-2.525	1.014
4.5	-1.512	-2.544	1.031

[AcOH] C_0/M	Potential ($E_{1/2}$) / V vs $Fc^{+/0}$				
		2		**3**	
	Calculated ($E^T_{1/2}$)	Experimental ($E^E_{1/2}$)	Overpotential ($E^T_{1/2}$-$E^E_{1/2}$)	Experimental ($E^E_{1/2}$)	Overpotential ($E^T_{1/2}$-$E^E_{1/2}$)
0.05	-1.455	-1.836	0.382	-1.815	0.360
0.1	-1.464	-1.843	0.379	-1.830	0.367
0.2	-1.472	-1.866	0.394	-1.862	0.389
0.3	-1.478	-1.890	0.413	-1.886	0.408
0.4	-1.481	-1.906	0.425	-1.912	0.430
0.5	-1.484	-1.921	0.437	-1.928	0.444
0.6	-1.486	-1.932	0.446	-1.942	0.456
0.7	-1.488	-1.948	0.460	-1.963	0.475
0.8	-1.490	-1.951	0.461	-1.972	0.482
0.9	-1.492	-1.957	0.465	-1.971	0.480
1	-1.493	-1.966	0.473	-1.984	0.491

Table 3-4. Additional X-ray data.

Parameter	1	2	3
Empirical formula	$C_{47}H_{38}Cl_2FeO_2P_2S_2$	$C_{37}H_{28}FeOP_2S_2$	$C_{33}H_{26}FeOP_2S_2$
Formula weight	887.58	670.50	620.45
Temperature (K)	123(2)	123(2)	123(2)
Wavelength (Å)	0.71073	0.71073	0.71073
Z	4	8	4
Crystal system	monoclinic	orthorhombic	monoclinic
Space group	P 1 21/n 1	P b c a	P 1 21/n 1
a (Å)	10.7058(5)	17.762(2)	10.5784(5)
b (Å)	22.5704(10)	18.130(2)	17.6524(8)
c (Å)	16.9729(7)	19.758(2)	15.4867(7)
α (°)	90	90	90
β (°)	91.7710(10)	90	99.8020(10)
γ (°)	90	90	90
Volume ($Å^3$)	4099.3(3)	6362.6(12)	2849.7(2)
Density ($g\ cm^{-3}$)	1.438	1.400	1.446
μ (mm^{-1})	0.718	0.736	0.814
Goodness-of-fit	1.190	1.139	1.044
R_1, wR_2 [$I > 2\sigma(I)$]	0.0546, 0.1254	0.0574, 0.1185	0.0348, 0.0815
R_1, wR_2 (all data)	0.0594, 0.1277	0.0940, 0.1490	0.0441, 0.0865

Table 3-5. Geometrical parameters from the DFT calculations. On average, these parameters are within ~2% of the experimental values from the X-ray measurements.

	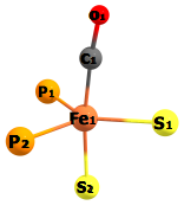	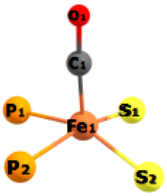	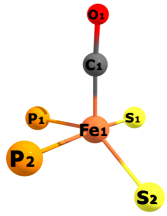	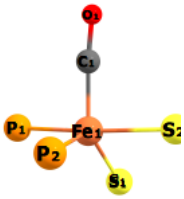	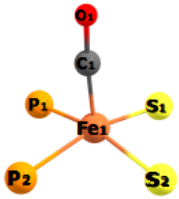
PARAMETER	**1**[a]	**2**[a]	**3**[a]	**4**[b]	**5**[b]
FE-S1	2.177	2.178	2.202	2.209	2.227
FE-S2	2.210	2.174	2.159	2.290	2.222
FE-P1	2.182	2.174	2.143	2.297	2.285
FE-P2	2.188	2.177	2.176	2.266	2.292
FE-C	1.735	1.697	1.714	1.730	1.724
P1-FE-P2	101.4	82.9	85.5	101.9	91.1
S1-FE-S2	88.7	90.5	90.1	88.4	88.9
P1-FE-S1	129.4	90.4	89.3	87.1	86.8
P2-FE-S2	92.7	89.1	89.4	86.9	88.1

*Bond angles and lengths are reported in degree and angstrom respectively.
[a]values from this work, [b]values from Roy and coworkers[9]

References

1. Lubitz, W.; Ogata, H.; Rüdiger, O.; Reijerse, E. *Chem. Rev.* **2014**, *114* (8), 4081.

2. Vignais, P. M.; Billoud, B. *Chem. Rev.* **2007**, *107* (10), 4206.

3. Liaw, W.-F.; Lee, N.-H.; Chen, C.-H.; Lee, C.-M.; Lee, G.-H.; Peng, S.-M. *J. Amer. Chem. Soc.* **2000**, *122* (3), 488.

4. Sellmann, D., Kleine-Kleffmann, U., & Zapf, L. (1984). *J. Organomet. Chem.* (263), 321–331.

5. Rauchfuss, T. B.; Contakes, S. M.; Hsu, S. C. N.; Reynolds, M. A.; Wilson, S. R. *J. Amer. Chem. Soc.* **2001**, *123* (28), 6933.

6. Beyler, M.; Ezzaher, S.; Karnahl, M.; Santoni, M.-P.; Lomoth, R.; Ott, S. *Chem. Commun.* **2011**, *47* (42), 11662.

7. Gardner, J. M.; Beyler, M.; Karnahl, M.; Tschierlei, S.; Ott, S.; Hammarström, L. *J. Amer. Chem. Soc.* **2012**, *134* (47), 19322.

8. Orthaber, A.; Karnahl, M.; Tschierlei, S.; Streich, D.; Stein, M.; Ott, S. *Dalton T.* **2014**, *43* (11), 4537.

9. Roy, S.; Mazinani, S. K. S.; Groy, T. L.; Gan, L.; Tarakeshwar, P.; Mujica, V.; Jones, A. K. *Inorg. Chem.* **2014**, 140811095919002.

10. Ray, K.; Weyhermüller, T.; Goossens, A.; Crajé, M. W. J.; Wieghardt, K. *Inorg. Chem.* **2003**, *42* (13), 4082.

11. Gan, L.; Groy, T. L.; Tarakeshwar, P.; Mazinani, S. K. S.; Shearer, J.; Mujica, V.; Jones, A. K. *J. Amer. Chem. Soc.* **2015**, *137* (3), 1109.

12. Kamer, P. C., van Leeuwen, P. W., & Reek, J. N. (2001). Wide bite angle diphosphines: xantphos ligands in transition metal complexes and catalysis. *Accounts Chem. Res. 34*(11), 895–904. http://doi.org/10.1021/ar000060.

13. Eady, S. C.; Breault, T.; Thompson, L.; Lehnert, N. *Dalton T.* **2016**, *45* (3), 1138.

14. Addison, A. W.; Rao, T. N.; Reedijk, J.; van Rijn, J.; Verschoor, G. C. *Dalton T.* **1984**, No. 7, 1349.

15. Ray, K.; Weyhermüller, T.; Neese, F.; Wieghardt, K. *Inorg. Chem.* **2005**, *44* (15), 5345.

16. Barrón, D.; Butí, S.; Ruiz, M.; Barbosa, J. *Phys. Chem. Chem. Phys.* **1999**, *1* (2),

295.

17. Fourmond, V.; Jacques, P.-A.; Fontecave, M.; Artero, V. *Inorg. Chem.* **2010**, *49* (22), 10338.

18. Helm, M. L.; Stewart, M. P.; Bullock, R. M.; DuBois, M. R.; DuBois, D. L. *Science.* **2011**, *333* (6044), 863.

19. Neese, F. In ORCA - an ab initio, density functional and semiempirical program package, MPI for Chemical Energy Conversion.

20. Becke, A. (1988). Density-functional exchange-energy approximation with correct asymptotic behavior. *Phys. Rev., A-Gen. Phys*. ***38***(6), 3098–3100.

21. Perdew, J.; Yue, W. *Phys. Rev., B Condens. Matter* **1986**, *33* (12), 8800.

22. van Wüllen, C. *J. Chem. Phys.* **1998**, *109* (2), 392.

23. Pantazis, D. A.; Chen, X.-Y.; Landis, C. R.; Neese, F. *J. Chem. Theory. Comput.* **2008**, *4* (6), 908.

24. Grimme, S. *J. Comput. Chem.* **2004**, *25* (12), 1463.

25. Grimme, S. *J. Comput. Chem.* **2006**, *27* (15), 1787.

Chapter 4

Hydrogen Production from Water using a bis(imino)pyridine Molybdenum Electrocatalyst

Raja Pal,‡ Joseph A. Laureanti,‡ Thomas L. Groy, Anne K. Jones* and Ryan J. Trovitch*

School of Molecular Sciences,
Arizona State University, Tempe, AZ 85287

Reproduced with permission from:

Pal, R., Laureanti, J. A., Groy, T. L., Jones, A. K., & Trovitch, R. J. (2016). Hydrogen production from water using a bis(imino)pyridine molybdenum electrocatalyst. *Chemical Communications*, *52*(77), 11555–11558. http://doi.org/10.1039/C6CC04946J

Abstract

In 5.0 M H_2O/acetonitrile, [(^{Ph2PPr}PDI)MoO][PF_6]$_2$ produces H_2 with 96% Faradaic efficiency at 2.5 V vs. $Fc^{+/0}$ and a rate of 55 s^{-1}. Reactivity studies and isolation of a Mo(II) oxo intermediate, (^{Ph2PPr}PDI)MoO, shed light on the H_2 evolution mechanism.

Introduction

The search for renewable, carbon-neutral energy sources remains the central challenge for scientists in the 21st century.[1-3] Conversion of electricity into high-energy chemical bonds has emerged as a promising energy storage method that may be used to meet future demands.[4-6]Due to its high energy density and eco-friendly combustion to water, H_2 is an attractive replacement for fossil fuels.[4,6] Water electrolysis is a mature industrial technology; however, Ni/C cathodes require highly basic conditions while Pt cathodes are costly and operate under highly acidic conditions.[7] Therefore, sustainable electrocatalysts, which mediate H_2 evolution from earth-abundant substrates, such as neutral pH water, may offer a desirable alternative to current energy sources.[2,8] To be deployable on an industrial scale, such catalysts should be comprised of inexpensive and abundant elements.[9] Accordingly, researchers have focused on the development of homogeneous electrocatalysts featuring low-cost and earth-abundant first row-transition metals.[10,11] These catalysts generally require weak organic acid H^+ sources[12] and are known to suffer in the presence of water.[11]

Conversely, molybdenum compounds show unusual tolerance towards water and have exhibited interesting water activation chemistry. Tyler and co-workers demonstrated that low-valent bis(cyclopentadienyl) molybdenum compounds oxidatively add H_2O and

undergo 1,2-elimination to yield H_2 and the corresponding oxo complex, $CP_2Mo{=}O$.[13-15] Recently, high-valent molybdenum precatalysts have shown promising H_2 evolution activity and robustness in neutral pH water[16] or acidified solutions.[17,18] Notably, the molybdenum(IV) oxo precatalyst, $[(PY_5Me_2)MoO][PF_6]_2$, generates H_2 from a pH = 7 aqueous solution with a turnover frequency (TOF) of 2.3 s^{-1} at an overpotential of 1.0 V.[16] The disulfide analogue, $[(PY_5Me_2)Mo(S_2)][OSO_2CF_3]_2$, was found to catalyze H_2 production from pH = 3 solution with TOFs as high as 480 s^{-1} at an overpotential of 0.78 V.[17] Inspired by these reports, this manuscript describes the preparation of a robust Mo(IV) oxo precatalyst, its electrocatalytic activity for H_2 production from water, and its mechanism of operation. Notably, this catalyst operates with H_2 production rates that are an order of magnitude greater than $[(PY_5Me_2)MoO][PF_6]_2$ in water.

Results and Discussion

We recently reported the synthesis of $[(^{Ph2PPr}PDI)MoI][I]$ (**1**, **Scheme 4-1**)[19] from $(^{Ph2PPr}PDI)Mo(CO)$[20] following I_2 oxidative addition and thermal CO ligand removal. For this study, a one- step synthesis of **1** from $^{Ph2PPr}PDI$[21] and $(CH_3CN)_2(CO)_3MoI_2$[22] was utilized.[23] Heating an acetonitrile solution of **1** and styrene oxide at 60° C in the presence of two equivalents of $AgPF_6$ produced a bright orange compound within hours. A singlet at 22.9 ppm and septet at 143.6 ppm in the ^{31}P NMR spectrum indicate symmetric phosphine substituent coordination about Mo with outer-sphere PF_6 counter anions. The formation of styrene and a C_S-symmetric chelate environment with six methylene resonances[21] was observed by ^1H NMR spectroscopy. Moreover, analysis of the product by infrared spectroscopy revealed a stretch at 840 cm^{-1}, suggesting the presence of an oxo

ligand[13] and the formation of [(^{Ph2PPr}PDI)MoO][PF_6]$_2$ (**2**, **Scheme 4-1**). The solid-state structure of **2** (**Figure 4-1A**) was determined by single crystal X-ray diffraction and was found to have a distorted octahedral geometry with N(1)–Mo(1)–N(3) and P(1)–Mo(1)–P(2) angles of 139.92(9) and 176.84(2)°, respectively. The short Mo(1)–O(1) distance of 1.693(2) Å is consistent with the presence of a triple bond,[16] rendering **2** an 18-electron complex.

The redox properties of **2** were then probed by cyclic voltammetry in dry acetonitrile. As shown in **Figure 4-2A**, reversible transitions corresponding to $Mo^{IV/III}$ and $Mo^{III/II}$ are observed at $E_{1/2}$ = 0.70 V (i_p^a/i_p^c = 1.20, ΔE_p = 0.08 V) and $E_{1/2}$ = 1.26 V vs. $Fc^{+/0}$ (i_p^a/i_p^c = 0.85, ΔE_p = 0.08 V, Fc = ferrocene), respectively. Irreversible reductions corresponding to $Mo^{II/I}$ and $Mo^{I/0}$ are centered at 1.53 and 1.95 V vs. $Fc^{+/0}$, respectively. Cycling to potentials more oxidizing than +0.5 V vs. $Fc^{+/0}$ results in the loss of the peaks attributed to the $Mo^{IV/III}$ and $Mo^{III/II}$ transitions. However, when the potential is maintained at potentials less oxidizing than +0.5 V $Fc^{+/0}$, the $Mo^{IV/III}$ and $Mo^{III/II}$ transitions do not diminish in reversibility.

The electrocatalytic activity of **2** for the reduction of water was determined in dry acetonitrile within a potential range of 1.3 to 2.8 V vs. $Fc^{+/0}$. The direct reduction of H_2O by glassy carbon is negligible in this region (**Figure 4- 4**). In the presence of **2**, the addition of 0.5 to 4.0 M water produces a catalytic wave with a linear increase in the current as a function of [H_2O] (**Figure 4-2B**). The peak current in the presence of >4.0 M water is independent of concentration (**Figure 4-5**). The overpotential required for catalysis was determined for each water concentration by measuring the open circuit

potential (OCP) and referencing to $Fc^{+/0}$ as described by Roberts and Bullock. The overpotentials range from 1.65 to 1.70 V for 0.2 to 6.0 M H_2O, respectively (**Table 4-1**). Marginally higher overpotentials (1.70–1.87 V) are observed when catalysis is conducted under an atmosphere of H_2. At water concentrations >2.0 M, a reversible redox transition at $E_{1/2}$ = 1.96 V (i_p^a/i_p^c = 1.07, ΔE_p = 0.09 V for [H2O] = 3.5 M) appears, which is not observed at lower concentrations of water (**Figure 4-2C**). The development of the new transition strictly requires water and is independent of time. The catalyst resting at low [H_2O] does not develop the reversible couple, while a dramatic increase of H_2O from 0 to 2.0 M results in this additional feature.

Analysis of the headspace gas following controlled potential electrolysis at 2.5 V vs. $Fc^{+/0}$ in 5.0 M H_2O /ACN shows that **2** electrocatalytically produces H_2 with 96% Faradaic efficiency under these conditions. The ‘‘rinse test’’ shows that **2** does not decompose to form a heterogeneous nanocatalyst on the electrode surface. Immediately following an electrocatalytic experiment with **2**, the working electrode was rinsed with acetonitrile. As shown in **Figure 4-4**, cyclic voltammetry in a fresh ACN or 5.0 M H_2O/ACN solution showed no detectable faradaic peaks or electrocatalysis. This indicates that **2** remains in solution through- out the electrocatalytic experiments.

The kinetics for the reduction of H_2O to H_2 by **2** were evaluated using eqn (1)–(3), where i_{cat} is the catalytic peak current, $\frac{i_{cat}}{i_p}$ is the ratio of the peak catalytic current (i_{cat}) to peak current (i_p) in the absence of substrate, n is the number of electrons, F is Faraday’s constant, A is the electrode area, D is the diffusional coefficient of the catalyst, k is the rate constant, R is the ideal gas constant, and T is the temperature in Kelvin. **Figure 4-6**

shows that i_{cat} is linear with respect to the quantity of catalyst in solution, indicating a first order dependence on **2**. **Figure 4-7** shows that normalized catalytic current, $\frac{i_{cat}}{i_p}$, is linear with respect to [H_2O]. This reveals a second order dependence with respect to acid at a scan rate of 0.2 V s^{-1}. Using eqn (4) for the acid-independent region (4.5–6.0 M H_2O) of electrocatalytic experiments, k = 55 15 s^{-1} is obtained.

eqn

$$i_{cat} = nFA[\text{cat}]\sqrt{D(k[\text{acid}]^x)} \quad (1)$$

$$\frac{i_{cat}}{i_p} = \left(\frac{n}{0.4463}\right)\sqrt{RT(k[\text{acid}]^x)/Fv} \quad (2)$$

$$\frac{i_{cat}}{i_p} = \left(\frac{n}{0.4463}\right)\sqrt{RTk/Fv} \quad (3)$$

Considering that **2** exhibits two reversible reductions before the onset of catalysis (**Figure 4-2A**), efforts were made to prepare a reduced intermediate relevant to the catalytic cycle. Addition of two equiv of potassium naphthalenide to **2** results in a reddish-brown diamagnetic product identified as the neutral molybdenum(II) oxo compound, (^{Ph2PPr}PDI)MoO (**3**, **Scheme 4-2**). Notably, multinuclear NMR spectroscopic analyses reveal an upfield-shifted ^{31}P NMR singlet at 4.88 ppm.

To confirm the identity of **3**, the solid-state structure of this complex was elucidated by single crystal X-ray diffraction (**Figure 4-1B**). The coordination geometry of **3** is consistent with that of **2**; however, **3** features a significantly elongated Mo–O bond of 1.797(3) Å (compared to 1.693(2) Å for **2**). This observation is consistent with reduction of the metal oxidation state and the presence of a Mo–O double bond. Reduction to Mo(II) is further evidenced by the N(1)–C(2) and N(3)–C(8) distances of

1.355(5) and 1.363(5) Å and contracted C(2)–C(3) and C(7)–C(8) distances of 1.420(7) and 1.401(7) Å, respectively. Although ^{Ph2PPr}PDI can behave in a redox non-innocent fashion when bound to a low-valent first row metal,[24] the expanded d-orbitals of second row metals efficiently p-backbond into the PDI LUMOs to form low energy d/PDI(π*) bonding orbitals. Destabilized d/PDI(π*) antibonding combinations are also formed, but are far too high in energy to be populated.[21] Therefore, the chelate bond lengths determined for **3** indicate considerable Mo-PDI p-backbonding rather than electron transfer to PDI, as reported for other ^{Ph2PPr}PDI Mo(II) complexes.[19,23] Formal Mo(II) oxo complexes are rare and the lone examples reported by Wieghardt and co-workers were found to have Mo–O distances between 1.754(4)–1.781(3) Å.[25]

It is hypothesized that the reduced Mo–O bond order in **3** leads to increased oxo ligand nucleophilicity,[16] allowing for consecutive proton-coupled electron-transfer (PCET) processes to give (^{Ph2PPr}PDI)Mo^{I}(OH) (**4**, **Figure 4-3**) and [(^{Ph2PPr}PDI)Mo^{0}(OH_2)] (**5**, **Figure 4-3**) under electrocatalytic conditions. The possibility that **4** undergoes protonation at Mo to generate **6** cannot be ruled out; however, formation of **5** is supported by accumulation of the reversible transition with $E_{1/2}$ = 1.96 V at higher water concentrations (>2 M) during catalytic experiments (**Figure 4-2C**). A C_2-symmetric complex presumed to be **5** has also been observed by ^{31}P NMR spectroscopy upon adding 4 atm of H_2 to **3**. When H_2 is removed under vacuum, this complex converts back to **3**, indicating the 1,2-elimination and O–H oxidative addition steps in **Figure 4-3** are reversible.

In the absence of H_2O, zerovalent (κ^5-^{PPh2PPr}PDI)Mo is known to undergo chelate

C–H activation to yield (κ^6-*P,N,N,N,C,P*-^{PPh2PPr}PDI)MoH.[19] Therefore, a ligand-assisted pathway where protonation of (κ^6-*P,N,N,N,C,P*-^{PPh2PPr}PDI)MoH liberates H_2 and 1,2-elimination of the chelate affords **3** was also considered. To gain further mechanistic insight, a stoichiometric quantity of H_2O was added to (κ^6-*P,N,N,N,C,P*-^{PPh2PPr}PDI)MoH and slow formation of **3** with concomitant release of H_2 was observed by multinuclear NMR spectroscopy over the course of 12 h at 25° C. Having observed **3**, a controlled potential electrolysis experiment using **2** and excess D_2O was performed to check for chelate deuteration, an expected outcome of chelate 1,2-elimination. After continuous passing of charge for 30 min, the post-electrolysis solution was analyzed using multinuclear NMR spectroscopy. The ^{31}P NMR spectrum showed a singlet at 22.9 ppm corresponding to **2**; however, resonances resulting from chelate deuteration were not observed by ^{2}H NMR spectroscopy. Only acetonitrile H/D exchange in the presence of deuteroxide was detected.[26] Therefore, it is evident that 2-mediated H_2 production from H_2O occurs via the pathway in **Figure 4-3**, as opposed to the ligand-assisted pathway.

The synthesis, characterization, and activity of a well-defined (PDI)Mo catalyst for the reduction of water to H_2 have been established. While **2** operates at higher overpotentials than the Mo catalysts described by Long and Chang,[16] it also catalyzes water reduction at a faster rate (55 s^{-1}). Importantly, the π-acidity of ^{PPh2PPr}PDI has allowed for the isolation of a key Mo(II) oxo complex, **3**, which is proposed to mediate electrocatalytic H_2 production via PCET, O–H oxidative addition, and subsequent 1,2-elimination. In contrast to the mechanism of H_2O reduction using $[(PY_5Me_2)\text{-}MoO][PF_6]_2$,[27] our results suggest that this reaction can proceed through low oxidation state Mo intermediates, a finding that may guide the development of improved

catalysts for this transformation.

Acknowledgements

Support for electrochemical aspects was provided by the U.S. Department of Energy, Office of Science, Office of Basic Energy Sciences under Award Number DE-SC0008074 to AKJ. JL acknowledges the NSF IGERT-SUN program for a graduate fellowship. RJT acknowledges ASU for start-up support. The authors declare no competing financial interests.

Experimental Section

General Considerations. All chemical manipulations were performed in an MBraun glovebox under an atmosphere of purified nitrogen. Diethyl ether, pentane, tetrahydrofuran, and toluene (Sigma-Aldrich) were dried using a Pure Process Technology (PPT) solvent system, and stored in the glove box over activated 4Å molecular sieves and metallic sodium (Alfa Aesar) before use. Acetonitrile was dried by distillation over calcium hydride. Acetonitrile-d_3, benzene-d_6(Cambridge Isotope Laboratories) were dried over 3Å and 4Å molecular sieves, respectively, and metallic potassium (for benzene-d_6, Sigma-Aldrich) prior to use. The compounds 2,6-diacetylpyridine (TCI America), Celite (Acros Organics), silver hexafluorophosphate (Strem), and tetrabutylammonium hexafluorophosphate ($TBAPF_6$) (Sigma-Aldrich) were used without further manipulation and 3-(diphenylphosphino)-1-propanamine,[28] ^{PPh2PPr}PDI[21] and [(^{PPh2PPr}PDI)MoI]I (1)[19] were prepared according to literature procedures. Solution phase ^{1}H, ^{13}C, and ^{31}P nuclear magnetic resonance (NMR) spectra were recorded at room temperature on either a 400 MHz or 500 MHz Varian NMR

Spectrometer. All ^{1}H and ^{13}C NMR chemical shifts are reported relative to $Si(CH_3)_4$ using ^{1}H (residual) and ^{13}C chemical shifts of the solvent as secondary standards. ^{31}P NMR data are reported relative to H_3PO_4. Elemental analyses were performed at Robertson Microlit Laboratories Inc. (Ledgewood, NJ).

Electrochemistry. Electrochemical investigations were carried out under a nitrogen or hydrogen atmosphere using a PG-STAT 128N Autolab electrochemical analyzer. A conventional three- electrode cell was used for recording cyclic voltammograms. Glassy carbon working electrodes (3 mm diameter) were prepared by successive polishing with 1.0 and 0.3 μm alumina slurries (Buehler), followed by sonication (5 min) in ultrapure water after each polishing step. The supporting electrolyte was 0.1 M $TBAPF_6$ in acetonitrile. The Ag/Ag^+ pseudoreference electrode was prepared by immersing a silver wire anodized with AgCl in a glass sheath equipped with a Vycor or CoralPor frit (BASi: West Lafayette, IN) and loaded with 0.1 M $TBAPF_6$ in acetonitrile. A platinum wire was used as the counter electrode. All potentials are reported relative to the ferrocene/ferrocenium ($Fc^{+/0}$) couple as a reference.

Controlled potential experiments were completed in a custom-made, airtight electrochemical cell equipped with a gas-tight sampling port. The electrochemical cell mirrors the conventional three- electrode cell described above. The quantity of H_2 produced was determined by sampling the headspace via gastight syringe at the end of the experiment. Headspace gas was analyzed with an SRI model 310 gas chromatograph (GC) equipped with a thermal conductivity detector (TCD) and a 6' molecular sieve 13X packed column; argon was used as the carrier gas. The GC-TCD was calibrated using

known concentrations of H_2 in N_2.

Open circuit potential determination. Open circuit potentials (OCP) were determined using the method described by Roberts and Bullock in a 10 mL four-neck, airtight electrochemical cell equipped with three electrodes as described above and a gas-tight sampling port.[29] An acetonitrile solution containing 0.1 M $TBAPF_6$ was purged with 1 atm H_2 gas. The working electrode was then connected to the platinum counter electrode (now the working electrode) and water was introduced to the desired molar concentration. The OCP was recorded following stabilization. Potentials were adjusted to the $Fc^{+/0}$ reference scale using a cyclic voltammogram of Fc at each water concentration obtained with glassy carbon as the working electrode. Results are provided in **Table 4-1**.

X-ray crystallography. Single crystals suitable for X-ray diffraction were coated with polyisobutylene oil in the glovebox and transferred to glass fiber with Apiezon N grease before mounting on the goniometer head of a Bruker APEX Diffractometer (Arizona State University) equipped with Mo Kα radiation. A hemisphere routine was used for data collection and determination of the lattice constants. The space group was identified and the data was processed using the Bruker SAINT+ program and corrected for absorption using SADABS. The structures were solved using direct methods (SHELXS) completed by subsequent Fourier synthesis and refined by full-matrix, least-squares procedures on [F^2] (SHELXL). The solid state structure of **2** was found to feature two acetone molecules, one of which was modelled over three partially occupied sites (two were refined anisotropically with H atoms).

Preparation of [(^{Ph2PPr}PDI)MoO][PF_6]$_2$ (2). A 20 mL reaction vial was wrapped

with electrical tape, and charged with 0.090 g (0.093 mmol) of 1, 0.012 g (0.1 mmol) of styrene oxide, and 3 mL of acetonitrile. To this solution, 0.048 g (0.19 mmol) of $AgPF_6$ in 5 mL of acetonitrile was added slowly while stirring. The reaction vial was sealed and allowed to heat at 60° C for 12 h. The orange solution was cooled to room temperature for precipitation of AgI, after which the solution was filtered through Celite and dried under vacuum. A bright orange compound was extracted from acetone and dried under vacuum to afford 0.069 g (73%) of solid identified as **2**. Single crystals suitable for X-ray diffraction were grown from acetone/THF at -15 °C. Elemental analysis for $C_{39}H_{41}N_3MoP_4OF_{12}$: Calcd. C, 46.12%; H, 4.07%; N, 4.14%. Found: C, 46.40%; H, 4.16%; N, 4.05%. ^{1}H NMR (acetonitrile-d_3, 400 MHz): 7.82 (m, 4H, Ph), 7.60 (m, 9H, Ph), 7.44 (t, 7.6 Hz, 2H, Ph), 7.30 (t, 7.6 Hz, 4H, Ph), 7.21 (t, 8.0 Hz, 1H, Py), 6.30 (d, 8.0 Hz, 2H, Py), 4.25 (d, 13.2 Hz, 2H, CH_2), 3.65 (m, 2H, CH_2), 3.44 (m, 2H, CH_2), 2.59 (m, 4H, CH_2), 2.35 (m, 2H, CH_2), 2.10 (s, 6H, CH_3). ^{13}C NMR (acetonitrile-d_3, 100.49 MHz): 172.4 (C=N), 155.2 (Ar), 145.2 (Ar), 134.3 (t, 6.7 Hz, Ph), 133.3 (Ar), 133.2 (t, 2.5 Hz, Ph), 132.8 (Ar), 131.9 (t, 20.9, Ph), 130.8 (t, 5.0 Hz, Ph), 130.7 (t, 5.0 Hz, Ph), 126.7 (t, 23.1 Hz, Ph), 126.2 (Ar), 57.3 (NCH_2), 29.0 (t, 10.6 Hz, PCH_2), 26.8 (PCH_2CH_2), 16.6 (CH_3). ^{31}P NMR (benzene-d_6, 161.78 MHz): 22.9 ppm (s, PPh^2), -143.6 (sept, J_{PF} = 705 Hz, PF_6).

Preparation of (^{Ph2PPr}PDI)MoO (3). Method 1. A 20 mL vial was charged with 0.0038 g (0.098 mmol) of freshly cut potassium, 0.0122 g (0.095 mmol) of naphthalene, and 2 mL of THF. The solution was stirred for 30 min to form green potassium naphthalenide solution. To it, 0.051 g (0.050 mmol) of 2 in 10 mL of THF was slowly

added and the mixture was stirred at 25 °C for 24 h. The resulting brown solution was filtered through Celite and the solvent was removed in vacuo. After washing with cold pentane and drying, 0.025 g (68%) of a brownish-red solid identified as **3** was isolated. Method 2. A 20 mL vial was charged with 0.030 g (0.042 mmol) of (κ^6-*P,N,N,N,C,P*-^{PPh2PPr}PDI)MoH,[3] and dissolved in 2 mL of toluene. Following addition of 0.001 mL H_2O, the mixture was stirred at ambient temperature for 12 h. The reddish-brown solution was filtered through Celite, and dried in vacuo. After washing with cold pentane, 0.025 g (81%) of a brown solid identified as 3 was isolated. Single crystals suitable for X-ray diffraction were grown from a concentrated ether solution at -35° C. Elemental analysis for $C_{39}H_{41}N_3MoP_2O$: Calcd. C, 64.55%; H, 5.69%; N, 5.79%. Found: C, 63.54%; H, 5.60%; N, 5.30%. ^{1}H NMR (benzene-d_6, 500 MHz): 7.88 (m, 4H, Ph), 7.66 (d, 8.0 Hz, 2H, Py), 7.39 (br, 1H, Py), 7.07 (t, 7.5 Hz, 4H, Ph), 7.01 (m, 2H, Ph), 6.67 (t, 7.5 Hz, 2H, Ph), 6.53 (d, 7.5 Hz, 4H, Ph), 5.58 (t, 12.5 Hz, 2H, NCH_2), 5.45 (m, 4H, Ph), 4.85 (d, 12.5 Hz, 2H, NCH_2), 3.35 (t, 12.0 Hz, 2H, CH_2), 2.80 (s, 6H, CH_3), 2.20 (br, 2H, CH_2), 1.79 (br, 2H, CH_2), 1.59 (m, 2H, CH_2). ^{13}C NMR (benzene-d_6, 100.49 MHz): 138.95 (t, 10.0 Hz, Ph), 136.64 (Ar), 133.07 (t, 7.0 Hz, Ar), 132.41 (t, 7.0 Hz, Ph), 130.01 (Ar), 129.26 (Ar), 128.84 (Ar), 128.64 (m, Ph), 128.3 (Ar), 128.18 (Ar), 127.58 (t, 3.0 Hz, Ph), 112.60 (Py), 109.07 (Py), 58.53 (NCH_2), 28.69 (t, 8.0 Hz, PCH_2), 27.41 (PCH_2CH_2), 13.50 (CH_3). ^{31}P NMR (benzene-d_6, 161.78 MHz): 4.88 ppm (s, PPh_2).

Figures

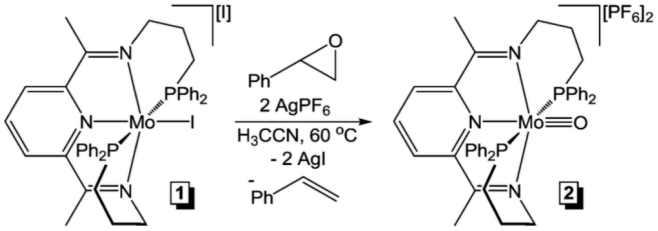

Scheme 4-1. Synthetic route from **1** to **2**.

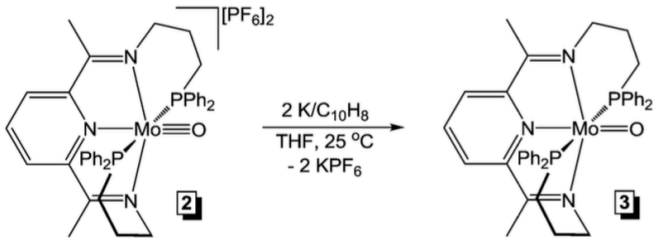

Scheme 4-2. Synthetic route from **2** to **3**.

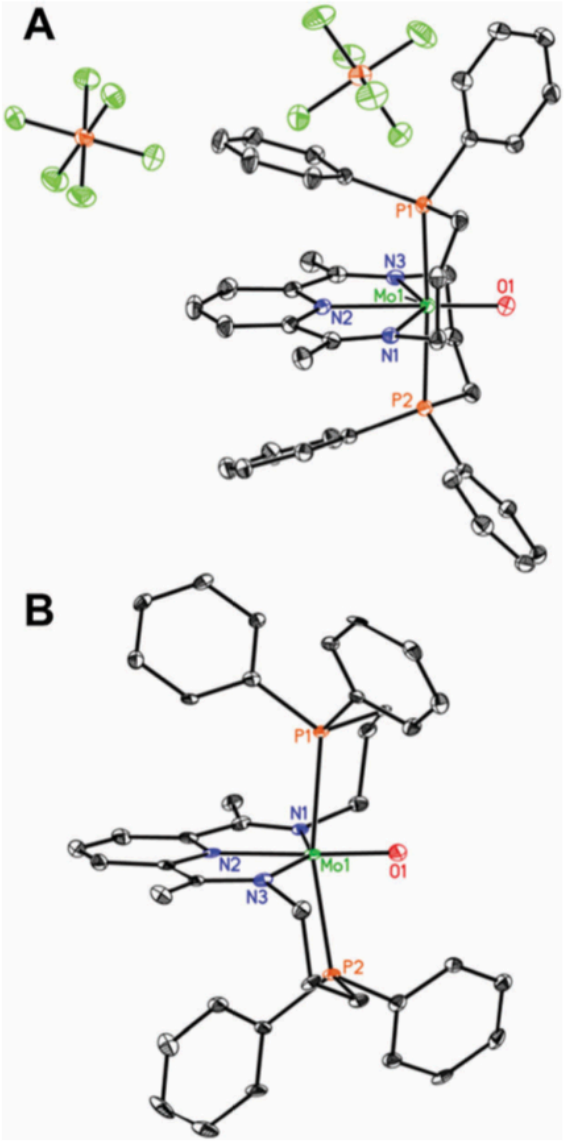

Figure 4-1. Solid state structures of 2 (A) and 3 (B) at 30% probability ellipsoids. Hydrogen atoms and co-crystallized acetone molecules (for 2) omitted for clarity.

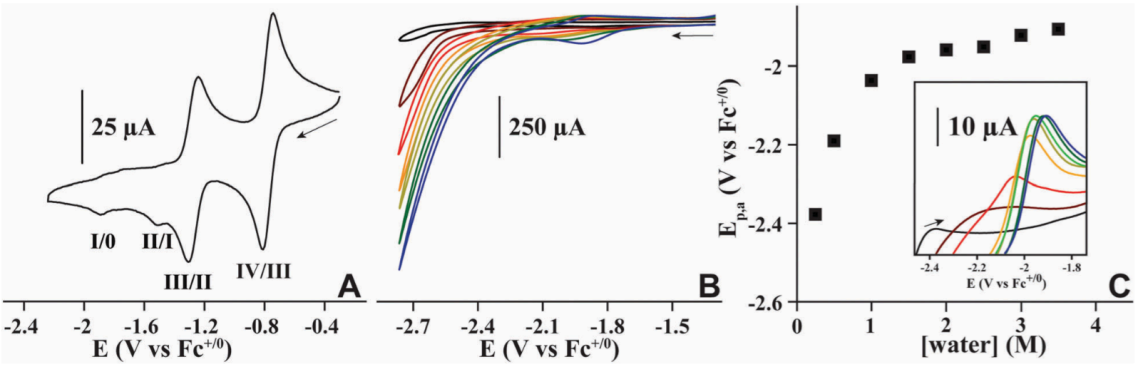

Figure 4-2. (A) Cyclic voltammogram of 2.1 mM **2** in dry acetonitrile containing 0.1 M $TBAPF_6$. (B) Cyclic voltammograms of 1.25 mM **2** in acetonitrile. $[H_2O]$ = 0.0 M (black), 0.5 M (dark red), 1.0 M (red), 1.5 M (orange), 2.0 M (yellow-green), 3.0 M (green), and 6.0 M (blue). (C) Anodic peak that develops with increasing water concentration. Inset (B constrained to the potential window of the developing anodic transition) shows the linear sweep voltammograms from which the potentials are derived. $[H_2O]$ = 0.25 M (black), 0.5 M (dark red), 1.0 M (red), 1.5 M (orange), 2.0 M (yellow-green), 2.5 M (light green), 3.0 M (dark green) and 3.5 M (blue). The scan rate for all panels is 0.2 V s^{-1}.

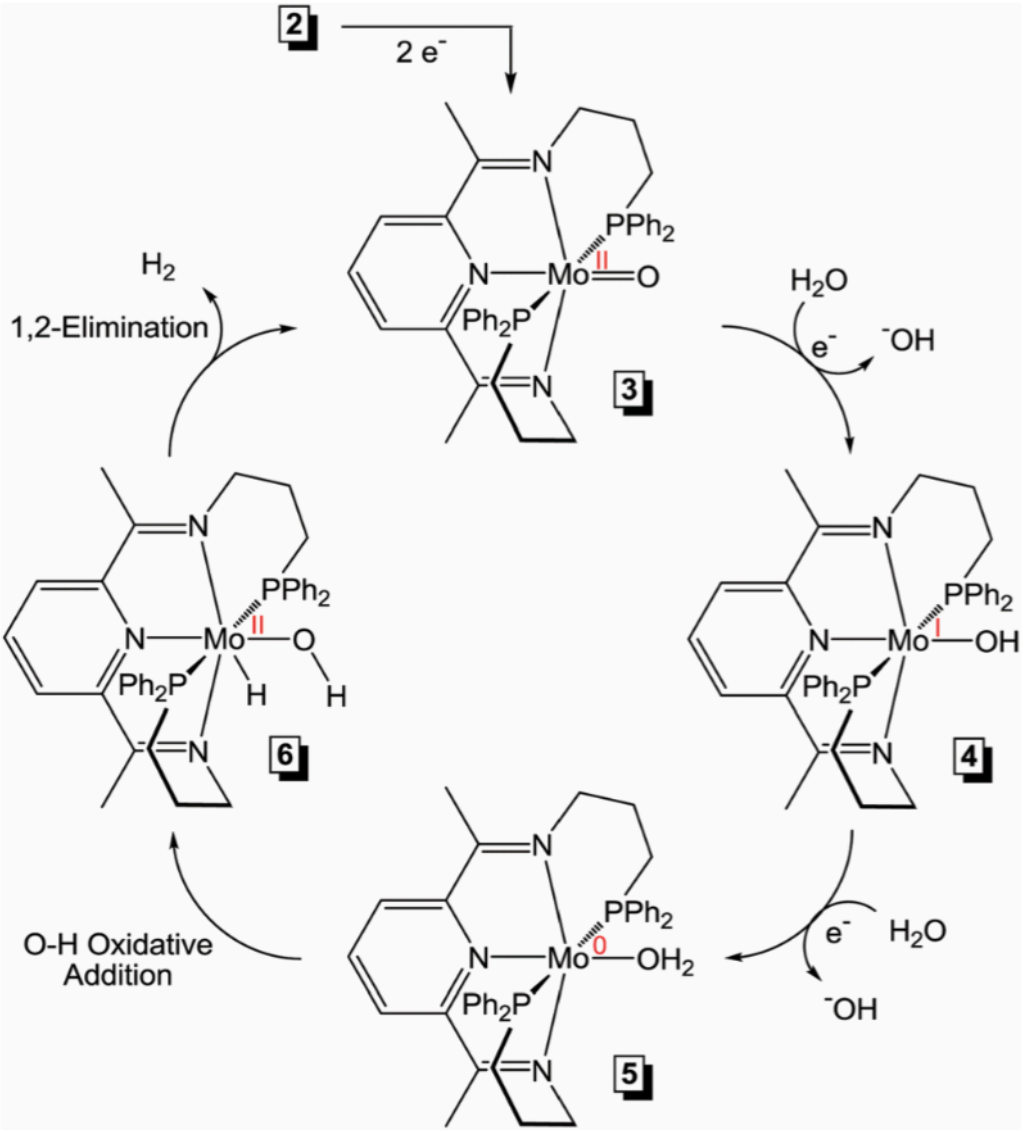

Figure 4-3. Proposed mechanism for 2-mediated hydrogen evolution from water.

.

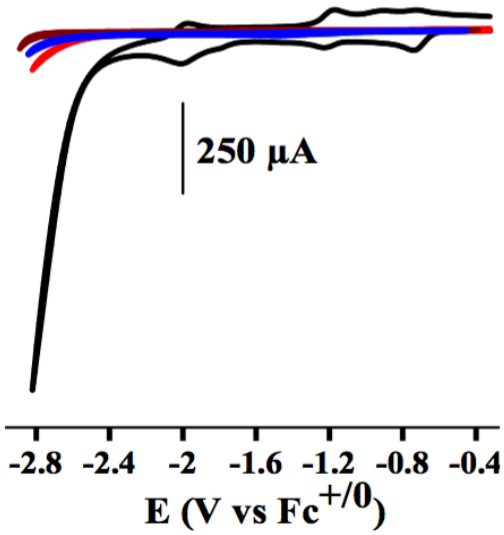

Figure 4-4. Cyclic voltammogram from 2.0 mM 2 in 3.5 M water in acetonitrile containing 0.1 M $TBAPF_6$ (black). Control experiments employing a rinsed working electrode immediately following electrocatalysis and transferred to a neat acetonitrile solution containing 0 M (dark red) and 5.0 M water (red). To illustrate that catalysis at a glassy carbon electrode is negligible, a solution of acetonitrile containing 6.0 M water in the absence of catalyst is shown (blue). Potential scan rate is 0.2 V s^{-1}.

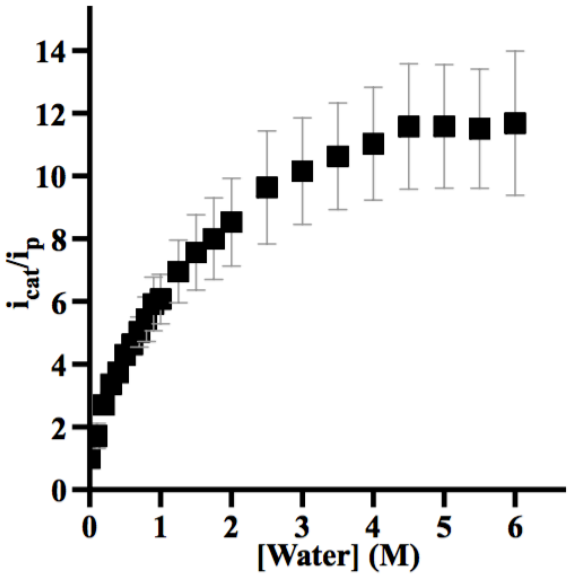

Figure 4-5. Dependence of normalized catalytic current (i_{cat}/i_p) on the concentration of water present. Data (squares, $k = 55 \pm 15$ s^{-1}) are averaged from three individual experiments and error bars represent one standard deviation. Experimental conditions: acetonitrile containing 0.1 M $TBAPF_6$ and a scan rate of 0.2 V s^{-1}.

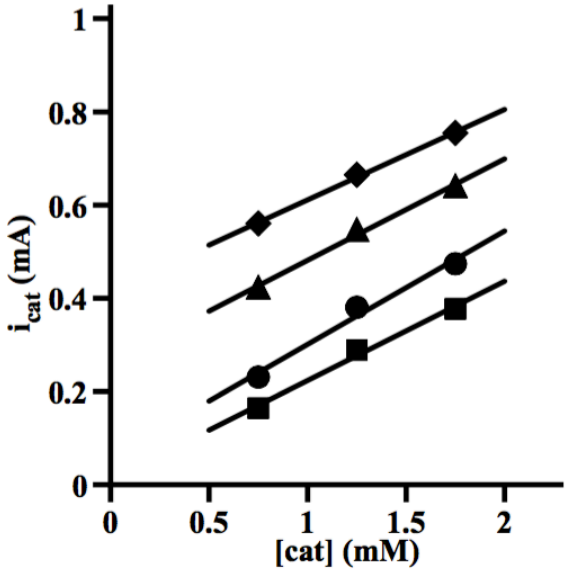

Figure 4-6. Catalytic current depends linearly on the concentration of **2** present in the experiment irrespective of water concentrations. Squares, circles, triangles, and diamonds refer to 0.3, 0.6, 1.75, and 3.0 M water, respectively. Solid lines are the lines of best fit with $R^2 = 0.99$.

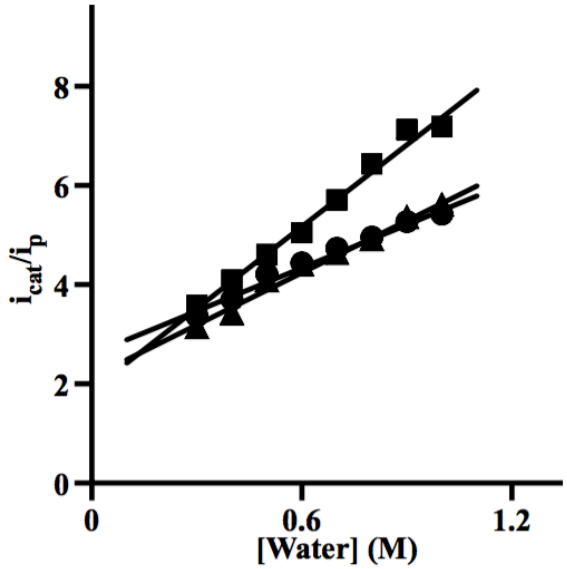

Figure 4-7. Dependence of normalized catalytic current on water concentration. Triangles, squares, and circles refer to currents extracted from cyclic voltammograms at -2.8 V vs $Fc^{+/0}$ for solutions containing **2** at 0.75, 1.25, and 1.75 mM, respectively. Solid lines are the lines of best fit ($R^2 = 0.98$). Experimental conditions: acetonitrile containing 0.1 M $TBAPF_6$ with a scan rate of 0.2 V s^{-1}. Averaging the rate constant obtained from these three individual experiments (in the water concentration range of 0.3 to 1.0 M) yields $k = 25 \pm 5$ s^{-1}.

Table 4-1. Overpotential calculated from the open circuit potential (OCP) vs $Fc^{+/0}$ and $E_{p/2}$ of the catalytic wave associated with **2** at the specified concentration of water in acetonitrile.

[H_2O] (M)	**OCP (V vs $Fc^{+/0}$)**	**$E_{p/2}$ (V vs $Fc^{+/0}$)**	**Overpotential, OCP - $E_{p/2}$ (V)**
0.2	-1.10	-2.75	1.65
0.4	-1.07	-2.74	1.67
0.6	-1.12	-2.70	1.58
1.8	-1.08	-2.68	1.60
2.0	-1.08	-2.69	1.61
3.5	-1.03	-2.65	1.62
4.0	-1.03	-2.65	1.62
5.0	-1.01	-2.64	1.63
6.0	-0.94	-2.64	1.70

Notes and References

1. Bard, A. J. & Fox, M. A. Artificial Photosynthesis: Solar Splitting of Water to Hydrogen and Oxygen. *Acc. Chem. Res.* **28,** 141–145 (1995).

2. Lewis, N. S. & Nocera, D. G. Powering the planet: chemical challenges in solar energy utilization. *P. Natl. Acad. Sci. U.S.A.* **103,** 15729–15735 (2006).

3. Gust, D., Moore, T. A. & Moore, A. L. Solar Fuels via Artificial Photosynthesis. *Acc. Chem. Res.* **42,** 1890–1898 (2009).

4. Esswein, A. J. & Nocera, D. G. Hydrogen Production by Molecular Photocatalysis. *Chem. Rev.* **107,** 4022–4047 (2007).

5. Walter, M. G. *et al.* Solar Water Splitting Cells. *Chem. Rev.* **110,** 6446–6473 (2010).

6. Thoi, V. S., Sun, Y., Long, J. R. & Chang, C. J. Complexes of earth-abundant metals for catalytic electrochemical hydrogen generation under aqueous conditions. *Chem. Soc. Rev.* **42,** 2388–2400 (2013).

7. Carmo, M., Fritz, D. L., Mergel, J. & Stolten, D. A comprehensive review on PEM water electrolysis. *Int. J. Hydrogen Energ.* **38,** 4901–4934 (2013).

8. Zee, D. Z., Chantarojsiri, T., Long, J. R. & Chang, C. J. Metal–Polypyridyl Catalysts for Electro- and Photochemical Reduction of Water to Hydrogen. *Acc. Chem. Res.* **48,** 2027–2036 (2015).

9. Nocera, D. G. The Artificial Leaf. *Acc. Chem. Res.* **45,** 767–776 (2012).

10. Du, P. & Eisenberg, R. Catalysts made of earth-abundant elements (Co, Ni, Fe) for water splitting: Recent progress and future challenges. *Energy Environ. Sci.* **5,** 6012 (2012).

11. DuBois, D. L. Development of Molecular Electrocatalysts for Energy Storage. *Inorg. Chem.* **53,** 3935–3960 (2014).

12. First row metal electrocatalysts for H_2O reduction have been reported, see: (a) J. P. Collin, A. Jouaiti and J. P. Sauvage, Inorg. Chem., 1988, 27, 1986; (b) P. V. Bernhardt and L. A. Jones, *Inorg. Chem*., 1999, 38, 5086.

13. Silavwe, N. D., Bruce, M., Philbin, C. E. & Tyler, D. R. Descriptive photochemistry and electronic structure of the Cp2MoO and (MeCp) 2MoO complexes. *Inorg. Chem*. 1988.

14. Yoon, M. & Tyler, D. R. Activation of water by permethyltungstenocene; evidence

for the oxidative addition of water. *Chem. Commun.* 639–670 (1997). doi:10.1039/a700087a

15. Baxley, G. T., Avey, A. A., Aukett, T. M. & Tyler, D. R. Photoactivation of water by Cp′ 2 Mo and photochemical studies of Cp 2 MoO. Investigation of a proposed water-splitting cycle and preparation of a water-soluble molbdocene dihydride. *Inorg. Chim. ACTA*. (2000).

16. Karunadasa, H. I., Chang, C. J. & Long, J. R. A molecular molybdenum-oxo catalyst for generating hydrogen from water. *Nature.* **464,** 1329–1333 (2010).

17. Karunadasa, H. I. *et al.* A Molecular MoS2 Edge Site Mimic for Catalytic Hydrogen Generation. *Science.* **335,** 698–702 (2012).

18. Thoi, V. S., Karunadasa, H. I., Surendranath, Y., Long, J. R. & Chang, C. J. Electrochemical generation of hydrogen from acetic acid using a molecular molybdenum–oxo catalyst. *Energy Environ. Sci.* **5,** 7762 (2012).

19. Pal, R., Groy, T. L. & Trovitch, R. J. Conversion of Carbon Dioxide to Methanol Using a C–H Activated Bis(imino)pyridine Molybdenum Hydroboration Catalyst. *Inorg. Chem.* **54,** 7506–7515 (2015).

20. Pal, R., Groy, T. L., Bowman, A. C. & Trovitch, R. J. Preparation and Hydrosilylation Activity of a Molybdenum Carbonyl Complex That Features a Pentadentate Bis(imino)pyridine Ligand. *Inorg. Chem.* **53,** 9357–9365 (2014).

21. Ben-Daat, H., Hall, G. B., Groy, T. L. & Trovitch, R. J. Rational Design of Rhodium Complexes Featuring κ 4- N, N, N, N- and κ 5- N, N, N, P, P-Bis(imino)pyridine Ligands. *Eur. J. Inorg. Chem.* **2013,** 4430–4442 (2013).

22. Baker, P. K., Fraser, S. G. & Keys, E. M. The synthesis and spectral properties of some highly reactive new seven-coordinate molybdenum (II) and tungsten (II) bisacetonitrile dihalogenotricarbonyl complexes. *J. Organomet. Chem.* (1986).

23. Pal, R., Cherry, B. R., Flores, M., Groy, T. L. & Trovitch, R. J. Isolation of a bis(imino)pyridine molybdenum(i) iodide complex through controlled reduction and interconversion of its reaction products. *Dalton T.* **45,** 10024–10033 (2016).

24. Mukhopadhyay, T. K., Flores, M., Groy, T. L. & Trovitch, R. J. A Highly Active Manganese Precatalyst for the Hydrosilylation of Ketones and Esters. *J. Am. Chem. Soc. U.S.A.* **136,** 882–885 (2014).

25. Böhmer, J., Haselhorst, G., Wieghardt, K. & Nuber, B. The First Mononuclear Nitrosyl(oxo)molybdenum Complex: Side-On Bonded and μ3-Bridging NO Ligands in [{MoL(NO)(O)(OH)}2]NaPF6·H2O. *Angew. Chem. Int. Ed. Engl.* **33,**

1473–1476 (1994).

26. Balaj, O. P. *et al.* Base-Catalyzed Hydrogen/Deuterium Exchange between Water and Acetonitrile in Anionic Water Clusters. *J. Phys. Chem. A*. **108,** 7506–7512 (2004).

27. Sundstrom, E. J. *et al.* Computational and Experimental Study of the Mechanism of Hydrogen Generation from Water by a Molecular Molybdenum-Oxo Electrocatalyst. *J. Am. Chem. Soc. U.S.A.* **134,** 5233–5242 (2012).

28. Li, Y., Li, Z., Li, F., Wang, Q. & Tao, F. Preparation of a Nafion–Teflon bimembrane-supported palladium catalyst and its use in the Heck reaction. *Tetrahedron Lett.* **46,** 6159–6162 (2005).

29. Roberts, J. A. S. & Bullock, R. M. Direct Determination of Equilibrium Potentials for Hydrogen Oxidation/Production by Open Circuit Potential Measurements in Acetonitrile. *Inorg. Chem.* **52,** 3823–3835 (2013).

Chapter 5

Thiol-Functionalized Self-Assembled Reduced Graphene Oxides for Electrochemical Applications

Ki-Wan Jeon[a], Joseph A. Laureanti[a], Lei Yu[b], Nathan Newman[b], Anne K. Jones[a], Dong-Kyun Seo[a,*]

[a]School of Molecular Sciences, Arizona State University
Tempe, AZ 85287-1604

[b]School for Engineering of Matter, Transport and Energy, Arizona State University,
Tempe, AZ, 85287-6106

*Corresponding author: dseo@asu.edu

Abstract

Langmuir-Blodgett (LB) films of highly thionated reduced graphene oxide (mRGO) were assembled on a Au disk electrode surface (2 mm diameter). Ferrocene carboxylic acid (FcCA) was covalently immobilized on the mRGO films via thioester formation, and the electrochemical properties were interrogated in an aqueous solution buffered at pH 9.0. The experimentally determined surface coverage of FcCA on the mRGO films is 50±20 pmol cm^{-2} and the observed electron transfer rate (k^0_{ET}) = 15±10 s^{-1}.

Introduction

Since graphene was successfully isolated in 2004,[1] its extraordinary optical and electronic properties have made it a promising material for many applications including nanoelectronics, transparent electrodes, photonics, and chemical or biological sensing[2-6] However, bulk production of chemically synthesized graphene or mechanically exfoliated graphene has proven challenging. Thus researchers have actively sought alternative synthetic approaches. Chemical modification or functionalization of carbon surfaces has been successfully employed as a relatively simple means to tune the physical and chemical properties of carbon nanomaterials.[7-10] In an analogous approach, chemical modification of graphene is thought to be a promising strategy for large-scale production. Oxygen-functionalized graphene is an electrically insulating material, which is not desirable for many applications. To date, much research has been paid attention to manipulate both the physical and chemical properties of graphene through chemical modification or reduction of the oxygen functionalized graphene namely graphene oxide (GO).[8,11,12]

The aromatic rings of graphite are relatively inert, such that reactions with pristine graphene often employ radicals or dienophiles.[13] Alternatively, reactions may occur with functional groups present at defect sites, but this dramatically limits the available surface area for reactivity. To obtain a more even distribution of immobilized molecules, GO, with its myriad of reactive oxygen functional groups, is often used as a substrate in which that carboxyl and hydroxyl groups are used as linking units.[9,14] The utilization of chemically modified graphene with alternative, multifunctional groups, however, could open up new directions. In particular, thiols can be employed in a number of reactions including cross-linking through disulfide formation,[15,16] click chemistry,[17] tethering self-assembled monolayers (SAMs) on gold surfaces,[18] and coordinating heavy metals.[19,20] Each of these reactions enables new applications such as biosensors,[21,22] biomedical applications,[23] and passivation and stabilization of noble metal nanoparticles for biological applications.[24]

Herein, we report an effective synthetic route to thionated graphene oxides and a simple fabrication method for their Langmuir-Blodgett (LB) films. We also demonstrate that the thiols in this material provide a reactive handle for covalent immobilization of molecules via thioester formation. In particular, ferrocene carboxylic acid (FcCA) can be stably immobilized without detectable impact on the redox functionality of the molcule. Thus mRGO is a promising platform for immobilization of redox active molecules and development of electrochemical sensors.

Experimental Section

Fabrication of mRGO Thin Films on Glass or Au Substrates: Langmuir-Blodgett (LB) films of mRGO were fabricated without using a Langmuir-Blodgett trough. A

dispersion of mRGO in ethanol (6 μg mL^{-1}) was prepared first by mixing 10 mg of a wet mRGO sample (~0.6% solid weight in ethanol) with 10 mL of absolute ethanol and sonicating the mixture 15 minutes in an ultrasonication bath. The dispersion was then centrifuged at 4000 rpm for 10 minutes, and the gray supernatant collected. Using a pipet (5 mL), the supernatant dispersion was gently introduced dropwise into a 6-cm diameter petri dish half full of deionized water. Following addition of approximately six drops of the dispersion, thin grey patches (~ 1 mm) of mRGOs begin to appear on the water surface. The patches drift around on the surface until they spontaneously coalesce into a continuous film (mRGO Langmuir film).

Glass slides were cleaned by sonication in absolute ethanol, followed by acetone for 15 minutes, rinsing with deionized water, and drying under a stream of nitrogen gas. Langmuir films of mRGO were transferred onto glass surfaces by careful scooping using the glass substrate. The transferred film on glass was dried by N_2-gas stream, and it was visually checked that the area of the glass surface was covered by a translucent grey film. Films of tRGO can be fabricated similarly, but the quality (thickness and roughness) is lower since tRGO is not well dispersed in ethanol.

An analogous procedure was used to generate mRGO Langmuir films on 100 Å Au (111) layers on glass slides (Sigma Aldrich). The slide was placed in a petri dish half full of water and the mRGO dispersion added dropwise to form grey patches on the surface of the water. The water was then allowed to drain from the bottom of the petri dish, thereby assembling an mRGO Langmuir film on the Au coated glass slide.

Application of mRGO Langmuir films to Au electrode surfaces was completed by gently tapping an mRGO Langmuir film with the electroactive electrode surface parallel

to the film. The transferred films were dried under an N_2-gas stream, and the electrode surface visually examined to ensure complete coverage by the translucent grey film.

Immobilization of ferrocene carboxylic acid (FcCA) at Au, Au/RGO, and Au/mRGO. Substrates were incubated in an aqueous solution of 10 mM FcCA buffered with potassium phosphate (20 mM, pH 6.9) for 5.5 hrs and thoroughly rinsed thoroughy with deionized water before analysis.

Electrochemical Measurements. Either a CH Instruments 1200A Electrochemical Analyzer or a PG-STAT 128N Autolab electrochemical analyzer was used for electrochemistry. Experiments were performed in a three-electrode cell with a bare Au or modified Au/mRGO assembly as the working electrode, platinum counter electrode and a Ag/AgCl (3.5 M KCl) reference electrode. Electrochemical experiments involving FcCA were completed in 0.1 M potassium phosphate buffer adjusted to pH 9.0. Potentials were referenced using potassium ferricyanide as an external standard in the same electrochemical cell and adjusted to the standard hydrogen electrode (SHE) using the relation $E_{SHE} = E_{Ag/AgCl} + 0.205$ V.[25,26] Oxygen was purged from solutions by sparging for 15 min with argon gas, and the anaerobic environment was maintained by applying a constant stream of argon to the headspace of the electrochemical cell during experiments. The potential was cycled between +0.3 and +0.9 V vs SHE at the scan rate indicated in the text. The program SOAS[27] was used to remove non-faradaic signals and to tabulate data including peak potentials (E_p^a, E_p^c), peak currents (i_p^a, i_p^c), and total charge (Q), as defined by the integration of the area under the oxidation/reduction curves. The electron transfer rate at zero overpotential (k^0_{ET}) was determined by fitting peak potentials as a function of potential scan rate to the Butler-Volmer model[26] using the program Jellyfit.[28]

Preparation of Au disk electrodes. Au electrodes (2 mm diameter) were polished sequentially with 1.0 and 0.3 μm aqueous alumina slurries, sonicated sequentially in absolute ethanol then deionized water for 2 min each, and the electrode surfaces were chemically etched by incubation in a solution of 50 mM KOH and 25% v/v H_2O_2 for 10 min. Finally, the Au electrodes were cleaned electrochemically by potential cycling once between 0 V and -1.0 V vs SHE in aqueous 50 mM KOH and rinsed with deionized water. RGO or mRGO Langmuir films were deposited on the surface of clean Au gold electrodes, yielding Au/mRGO assemblies.

Results and Discussion

Typical GOs have a C:O ratio of 4:2 with oxygen present primarily in the form of carbonyl, hydroxyls/ether, and carboxyl groups (~6:~2:1).[29] Our goal is to convert a large fraction of these various functional groups of GOs to sulfur-based functionalities generating mRGOs, and it is desirable to achieve these transformations in a single reaction step. P_4S_{10} is a highly efficient thionating agent for various organic compounds including alcohols, ketones, ethers and esters, with reasonably high reaction yields (50 – 98 %). However, the selectivity for many of these reactions is not impressive.[30] For our purposes this promiscuity is advantageous because the various types of oxygen-based functional groups on GOs can be simultaneously converted to their sulfur-based analogues.

Table 5-1 summarizes the chemical compositions and functional group distributions in three classes of materials produced in the course of this work: GOs, mRGOs, and thermally reduced graphene oxides (tRGOs). As described in detail above and in the methods section, the mRGOs were prepared in solvothermal reactions using P_4S_{10} as a

thionating agent. For comparison, the tRGOs were prepared using the same reaction conditions without adding P_4S_{10}. Each sample is named according to the class of material and the temperature of preparation: 120, 150, or 180 °C.

The relative atomic ratios of C, O, S and P were obtained from the survey scans and are summarized in **Table 5-1**. The C:(O+S) ratios for mRGOs indicate the extent of functionalization with oxygen- and sulfur-functional groups relative to the carbon framework. As the reaction temperature increases from 120 to 180 °C, the C:(O+S) ratio in the resulting mRGO increases inconsequentially from 5.8 to 5.9. An effect of temperature is more pronounced in the relative amounts of oxygen- and sulfur-functional groups. In mRGO-120, the amount of oxygen atoms is larger than that of sulfur at the ratio of 1:0.7. However, the sulfur amount is larger than the oxygen amount by the factor of 1.2 in mRGO-180. This decrease in the amount of the oxygen-functional groups for materials synthesized at higher temperature is also observed at a similar rate for the tRGO series. Since thionating reagent is not present in these syntheses, this indicates that the reduction of the oxygen-functional groups is mainly a temperature effect. Judging from the C:O and C:(O+S) ratios, the amounts of the functional groups in both the mRGOs and tRGOs solvothermally produced in this work are slightly larger than those produced hydrothermally or in refluxing organic solvents but less than those of RGOs prepared by chemical reduction. Hydrothermally reduced GOs in water at 180 °C are reported to have a C:O ratio of 5.3. RGOs prepared under refluxing conditions in various organic solvents (boiling points: 153 to 204 °C) are reported to have C:O ratios from 2.8 to 4.4.[31] Chemical reduction of GOs by hydrazine produces RGOs with C:(O+N) ratios from 7 to 8.[32,33]

The distribution of carbon atoms within particular functional groups was determined by deconvolution of high-resolution XPS spectra in the C1s, O1s and S2p energy regions (**Table 5-1**). Deconvolution of the C1s peaks indicates that at least 74 at% of the carbon atoms are graphitic for all the mRGO and tRGO samples. The number increases only slightly with increasing temperature. When all samples are considered collectively, 6-9 at% of the carbon atoms are functionalized. Considering only the mRGOs, 6-8 at% of the carbon atoms are part of thiols. The amount of both the thiol and thiocarbonyl groups increases as the reaction temperature increases. The maximum sulfur content (7.6 at%) found in the mRGOs is more than 10 times higher than the highest amount reported for a nanostructured carbon material synthesized using P_4S_{10}.[34] Assuming there are no carbon defects in the structure and the thiols are equally distributed on both sides of graphene sheets, the thiol content estimated from the XPS data corresponds on average to one SH per 6.5 unit cells, or, equivalently, a surface coverage of 1.3 SH/nm^2 on each side of a graphene sheet. The presence of the thiols can be confirmed by comparing the ATR FT-IR spectrum of mRGO-180 with that of tRGO-180. While the tRGO-180 spectrum is featureless, the mRGO-180 spectrum exhibits an absorption peak at 665 cm^{-1} which has been attributed in the literature to C–S stretching in thiols.[35]

Ferrocene carboxylic acid can be immobilized at mRGO Langmuir films via reaction with the sulfur functionalities creating a redox-active assembly. To demonstrate the ability to covalently functionalize mRGO using the sulfur-based functionalities, we have immobilized ferrocene carboxylic acid (FcCA) on its surface and characterized the resulting assemblies using XPS and electrochemistry. The FcCA was immobilized on langmuir films of mRGO on gold (Au/mRGO) simply by incubating the substrate in a

buffered (pH 6.9) aqueous solution of the ferrocene, and the resulting assemblies were analyzed using X-ray photoelectron spectroscopy (XPS). **Figure 5-1** shows XPS spectra in the region of Fe 2p signals. As expected, before exposure to FcCA, the mRGO alone does not have any detectable signals in this region of the spectrum (**Figure 5-1B**). On the other hand, following incubation in the FcCA solution, two prominent peaks with binding energies of 708.5 and 721 eV are observed in the XPS spectrum. These correspond to the Fe $2p_{3/2}$ and Fe $2p_{1/2}$ transitions, respectively, and indicate that an iron-containing species has been immobilized (**Figure 5-1A**).[36] Analogous experiments using a film of tRGO on gold (Au/tRGO) or a bare gold-coated slide did not yield detectable iron signals, indicating that both the mRGO material and the sulfur-based functionalities within it are essential for the immoblization of FcCA on the surface.

Figure 5-2A shows cyclic voltammograms of a Au/mRGO film before and after exposure to FcCA for 5.5 hours. Immobilization of FcCA results in a reversible pair of oxidation/reduction peaks centered at +526 mV vs. SHE (all potentials are reference to SHE). The electrochemical signals are not observed for Au/mRGO assemblies prior to exposure to FcCA, and there is no FcCA in solution during the cyclic voltammetry, indicating that the signals arise from immobilized FcCA. In contrast, cyclic voltammograms from Au/tRGO/FcCA do not display any faradaic signals (**Figure 5-2B**), i.e. FcCA is stably immobilized at mRGO but not RGO. **Figure 5-4** highlights this result more clearly by displaying the first three cyclic voltammograms following removal of each electrode from their respective coupling reactions, rinsing thoroughly with water, and immediate introduction to the electrochemical cell. These results suggests that the interaction between FcCA and the mRGO is not primarily through π-π interactions.

Instead, the FcCA is likely immobilized via reaction of the carboxylic acid functionality with the sulfurs of mRGO to form a thioester.

The electroactive surface coverage of an immobilized redox center is directly related to the area under a voltammetric peak in cyclic voltammetry according to $\Gamma = \frac{Q}{nFAv}$ in which Γ is the electroactive surface coverage, Q is area of the voltammetric peaks obtained by integration following baseline removal, n is the number of electrons in the reaction, F is the Faraday constant, A is the surface area of the electrode, and v is the potential scan rate. The average electroactive surface coverage (Γ) of FcCA on mRGO is 50±20 pmol cm^{-2}. Direct comparison of the calculated Γ for FcCA at mRGO to that of a densely packed monolayer of FcCA at an electroactive surface area of 0.031 cm^2, results in a Γ = 1320 pmol cm^{-2} (using a radius = 2.0 Å for FcCA), which results in an ~4% efficiency for coupling FcCA to mRGO. However, interpreting this value in terms of the efficiency of the functionalization reaction is not simple or straightforward. Three key factors should be taken into account when determining a coupling efficiency in this context: 1) availability of solvent exposed thiols, 2) the physical assembly of mRGO sheets at the Au surface, and 3) surface defects within the stacked mRGO assemblies. However, we devised one possible method for analyzing the efficiency of the coupling reaction between FcCA and mRGO based on the atomic ratios shown in **Table 5-1**, C:O:S:P = 13:1:1.2:1.8, which result in mRGO containing >7% sulfur. Roughly 50% of these sulfurs will be available for coupling with FcCA, and results in ~4% of the total surface area available for coupling FcCA to thiols of mRGO (assuming complete coverage of mRGO at the Au electrode surface). The results is an adjusted theoretical

maximum of Γ = 53 pmol cm^{-2}. Using our adjusted theoretical maximum for Γ, which accounts for sulfur availability, our coupling efficiency 94%.

Electrochemical properties of FcCA immobilized at mRGO/Au. To determine whether immobilization of FcCA on mRGO impacted its redox properties, they were compared to values measured for FcCA in solution and theoretical expectations for an immobilized species. A cyclic voltammogram obtained from a solution of FcCA is shown in **Figure 5-2C**. The reduction potential of FcCA measured in this solution experiment, +537 mV, is well within the range previously reported for this compound of +520 to +550 mV and very similar to the +526 observed for the immobilized species.[37,38] This suggests that the electronic properties of FcCA are not detectably perturbed by immobilization on Au/mRGO. **Figure 5-3B** shows that the peak current resulting from the oxidation/reduction peaks of Au/mRGO/FcCA assemblies, increases linearly with the scan rate. This trend is expected for immobilized redox species and provides further evidence that the FcCA is immobilized on the electrode surface. The peak width for an immobilized one-electron redox couple should theoretically be 90 mV.[26] Thus it is worth noting that the full width at half maximum (FWHM) of 130±10 mV for FcCA immobilized on mRGO is relatively broad. It is, however, not much broader than reported values for other systems.[39-41] This may be an indication that the FcCA is immobilized in a heterogeneous environment or that the FcCA entities are close enough to interact with one another.

Kinetics of electron transfer. **Figure 5-3A** shows the dependence of FcCA peak potentials on potential scan rate. An electron transfer rate at zero overpotential k^0_{ET} = 15±10 s^{-1} was determined by fitting this data to the Butler-Volmer kinetic model.

This value is within the range predicted by Creager and co-workers for a redox active species immobilized at a conductive mediator coating an electroactive surface and separated from the electrode by a distance in excess of 4 nm.[42]

Conclusions

Highly conducting mercapto-functionalized reduced graphene oxides have been successfully prepared using a new thionation method. The maximum thiol content was higher than 7%, coresponding on average to one SH per 6.5 unit cells, or, equivalently, a surface coverage of 1.3 SH/nm^2 on each side of the graphene sheet. The new method employs P_4S_{10} as a thionating agent in pyridine which acts as both solvent and a co-reagent. Up to 180 °C, thionation was more effective at higher temperatures allowing concomittant thermal reduction of the graphene oxides under solvothermal conditions. Despite similar degrees of reduction, thiol-functionalized reduced graphene oxides have superior electrical conductivity compared to thermally reduced graphene oxides prepared without P_4S_{10}. Furthermore, the mRGOs are remarkably dispersibile in various solvents including DMF, alcohols and even water. The estimated electronic band gap of the mRGOs is only 0.1 eV, indicating an innately high conductivity in comparison to chemically-reduced graphene oxides with a similar degree of reduction. The unique combination of high thiol content, high electrical conductivity and good water dispersibility of the mRGOs may lead to their use in diverse applications including self-assembled monolayers (SAM) on gold substrate,[18] scavenging of heavy metals[19] and biosensors.[21] Furthermore, it is envisaged that this new thionation method may be applicable to other carbon nanomaterials, opening up new possible applications for those materials.

Acknowledgements

Conception and preliminary experiments demonstrating the synthetic method were supported by the Center for Bio-Inspired Solar Fuel Production, an Energy Frontier Research Center funded by the US Department of Energy, Office of Science, Office of Basic Energy Sciences under award number DE-SC0001016. Detailed characterization of the products was supported by a Multidisciplinary University Research Initiative (MURI) project funded by the Department of Defense through the Army Research Office (ARO) under award number W911NF-12-1-0420. We gratefully acknowledge the use of facilities within the LeRoy Eyring Center for Solid State Science at Arizona State University. During the course of this work, JL was supported by an IGERT-SUN fellowship provided by the National Science Foundation.

Figures

Table 5-1 Relative atomic ratios and relative proportions of functional groups in GO, mRGO and tRGO prepared at different reaction temperatures.

Sample	Relative atomic ratios		% C atoms bearing indicated functional group							
	C:O:S:P	C/(O+S)	graphitic[a]	C-OH[b]	C=O[b]	COO[a]	C-O-C[b]	C-SH	C=S	$C\text{-}SO_3^-$
GO	2.1:1:0.07:0	1.96	41.4	24.3	8.5	3.6	18.8	0	0	3.3
mRGO-120	9.7:1:0.68:0.12	5.77	74.1	7.8	2.5	0	0	6	0.6	0.3
mRGO-150	11:1:0.91:0.18	5.76	76.6	6.5	2.5	0	0	6.7	1.0	0.6
mRGO-180	13:1:1.2:0.18	5.91	77.5	5.9	1.8	0	0	7.7	1.1	0.5
tRGO-120	4.9:1:0:0	4.90	73.8	10.2	10.0	0	0	0	0	0
tRGO-150	5.8:1:0.03:0	5.63	76.8	9.6	7.6	0	0	0	0	0.5
tRGO-180	6.6:1:0.06:0	6.23	78.6	10.3	4.8	0	0	0	0	0.9

[a] estimated from high-resolution C1s XPS spectrum
[b] estimated from high-resolution O1s XPS spectrum

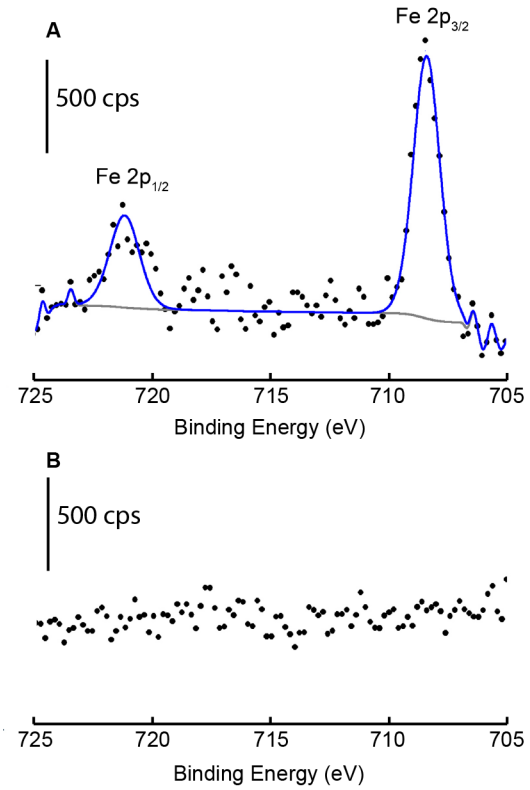

Figure 5-1. High resolution X-ray photoelectron spectra in the energy range of Fe 2p signals from (A) FcCA immobilized at layers of mRGO deposited on a 100 Å Au (111) layer on a glass slide and (B) an mRGO covered gold slide that was not exposed to FcCA. The peaks with binding energies of 708.5 and 721 eV arise from the Fe $2p_{3/2}$ and Fe $2p_{1/2}$ transitions, respectively.

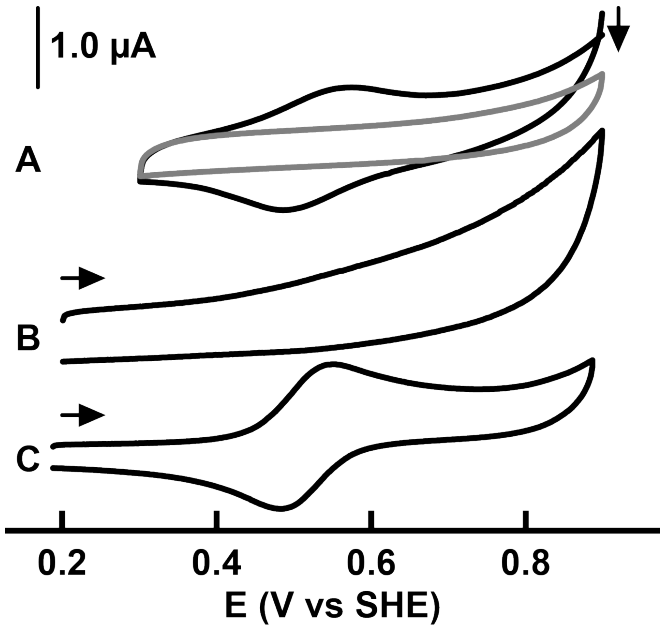

Figure 5-2. (A) Cyclic voltammograms from Au/mRGO/FcCA (black) and the same Au/mRGO electrode before exposure to the FcCA (grey trace). (B) Cyclic voltammogram from Au/tRGO/FcCA. (C) Cyclic voltammogram from a 0.5 mM aqueous FcCA solution using a gold electrode. The black arrows indicate the initiation point of the cycle and the direction of the potential scan. Experimental conditions: aqueous solution buffered with 0.1 M potassium phosphate pH 9.0, scan rate = 100 mV s^{-1}. Arrows indicate the starting point and direction of potential cycling.

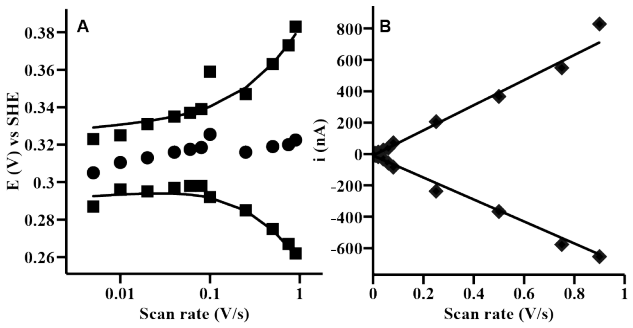

Figure 5-3. Scan rate dependence of (A) peak potential ($E_{p,a}$, $E_{p,c}$) and (B) peak current from Au/mRGO/FcCA assemblies. (A) Data (squares) were fit (black lines) to a Butler-Volmer kinetic model using the program Jellyfit[28], resulting in an average k^0_{ET} value of 15±10 s^{-1} (note the logarithmic scale). Circles show the average of the anodic and cathodic values. (B) Data (diamonds) show peak current scaling linearly with increasing scan rate. The lines represent the fit. Anodic and cathodic peak currents have correlation coefficients (R^2) of 0.98 and 0.99, respectively. Experimental conditions are identical to **Figure 5-2** with the exception that the scan rate is varied from 5 to 900 mV s^{-1}.

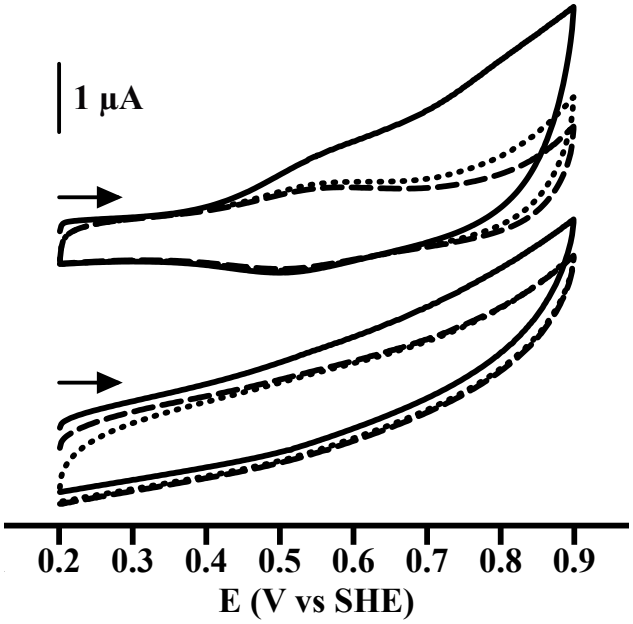

Figure 5-4. Cyclic voltammograms from Au/mRGO/FcCA (top) and Au/tRGO/FcCA (bottom) electrodes. Each panel shows the first three potential cycles following incubation of Au/mRGO or Au/tRGO assemblies in a solution of FcCA. Solid, dotted, and dashed traces show the first, second, and third potential sweeps, respectively. Black arrows indicate the initiation point and direction of the potential sweep. Experimental conditions: aqueous solution buffered with 0.1 M potassium phosphate at pH 9.0, scan rate = 100 mV s^{-1}.

References

1. Novoselov, K. S.; Geim, A. K.; Morozov, S. V.; Jiang, D.; Zhang, Y.; Dubonos, S. V.; Grigorieva, I. V.; Firsov, A. A. *Science.* **2004**, *306* (5696), 666.

2. Eda, G.; Fanchini, G.; Chhowalla, M. *Nat. Nanotech.* **2008**, *3* (5), 270.

3. Neto, A. C.; Guinea, F.; Peres, N.; Novoselov, K. S.; Geim, A. K. *Rev. Mod. Phys.* **2009**, *81* (1), 109.

4. Vashist, S. K.; Luong, J. H. T. *Carbon.* **2015**, *84* (C), 519.

5. Ge, S.; Lan, F.; Yu, F.; Yu, J. *New J. Chem.* **2015**, *39*, 2380.

6. Yin, P. T.; Shah, S.; Chhowalla, M.; Lee, K.-B. Design, Synthesis, and Characterization of Graphene–Nanoparticle Hybrid Materials for Bioapplications *Chem. Rev.* **2015**, *115* (7), 2483.

7. Quintana, M.; Vazquez, E.; Prato, M. Organic Functionalization of Graphene in Dispersions. *Acc. Chem. Res.* **2012**, *46* (1), 138.

8. Xu, Y.; Liu, Z.; Zhang, X.; Wang, Y.; Tian, J.; Huang, Y.; Ma, Y.; Zhang, X.; Chen, Y. *Adv. Mater.* **2009**, *21* (12), 1275.

9. Stankovich, S.; Piner, R. D.; Chen, X.; Wu, N.; Nguyen, S. B. T.; Ruoff, R. S. *J. Mater. Chem.* **2006**, *16* (2), 155.

10. Banerjee, S.; Hemraj Benny, T.; Wong, S. S. Covalent surface chemistry of single-walled carbon nanotubes. *Adv. Mater. Weinheim.* **2005**, *17* (1), 17.

11. Si, G.; Wang, W.-G.; Wang, H.-Y.; Tung, C.-H.; Wu, L.-Z. *Inorg. Chem.* **2008**, *47* (18), 8101.

12. Moon In, K.; Lee, J.; Ruoff, R. S.; Lee, H. Reduced graphene oxide by chemical graphitization. *Nat. Commun.* **2010**, *1*, 73.

13. Chan, C. K.; Beechem, T. E.; Ohta, T.; Brumbach, M. T.; Wheeler, D. R.; Stevenson, K. J. Electrochemically Driven Covalent Functionalization of Graphene from Fluorinated Aryl Iodonium Salts. *J. Phys. Chem. C* **2013**, *117* (23), 12038.

14. Chen, C.; Wang, L.; Liu, Y.; Chen, Z.; Pan, D.; Li, Z.; Jiao, Z.; Hu, P.; Shek, C.-H.; Wu, C.-M. L. Assembling Tin Dioxide Quantum Dots to Graphene Nanosheets by a Facile Ultrasonic Route. *Langmuir.* **2013**, *29*, 4111.

15. Miyata, K.; Kakizawa, Y.; Nishiyama, N.; Harada, A.; Yamasaki, Y.; Koyama,

H.; Kataoka, K. Block catiomer polyplexes with regulated densities of charge and disulfide cross-linking directed to enhance gene expression. *J. Amer. Chem. Soc.* **2004**, *126* (8), 2355.

16. Choh, S.-Y.; Cross, D.; Wang, C. Facile synthesis and characterization of disulfide-cross-linked hyaluronic acid hydrogels for protein delivery and cell encapsulation. *Biomacromolecules.* **2011**, *12* (4), 1126.

17. Lowe, A. B. Thiol-ene 'click' reactions and recent applications in polymer and materials synthesis. *Polym. Chem.* **2010**, *1* (1), 17.

18. Vericat, C.; Vela, M. E.; Benitez, G.; Carro, P.; Salvarezza, R. C. Self-assembled monolayers of thiols and dithiols on gold: new challenges for a well-known system. *Chem. Soc. Rev.* **2010**, *39* (5), 1805.

19. Yantasee, W.; Warner, C. L.; Sangvanich, T.; Addleman, R. S.; Carter, T. G.; Wiacek, R. J.; Fryxell, G. E.; Timchalk, C.; Warner, M. G. Removal of heavy metals from aqueous systems with thiol functionalized superparamagnetic nanoparticles. *Environ. Sci. Technol.* **2007**, *41* (14), 5114.

20. Li, G.; Zhao, Z.; Liu, J.; Jiang, G. Effective heavy metal removal from aqueous systems by thiol functionalized magnetic mesoporous silica. *J. Hazard Mater.* **2011**, *192* (1), 277.

21. Dong, S.; Li, J. Self-assembled monolayers of thiols on gold electrodes for bioelectrochemistry and biosensors. *Bioelectroch. Bioener.* **1997**, *42* (1), 7.

22. Xu, S.; Han, X. A novel method to construct a third-generation biosensor: self-assembling gold nanoparticles on thiol-functionalized poly (styrene- co-acrylic acid) nanospheres. *Biosens. Bioelectron.* **2004**, *19* (9), 1117.

23. Potta, T.; Chun, C.; Song, S.-C. Chemically crosslinkable thermosensitive polyphosphazene gels as injectable materials for biomedical applications. *Biomaterials.* **2009**, *30* (31), 6178.

24. Zhang, Z.; Pendse, N. D.; Phillips, K. N.; Cotner, J. B.; Khodursky, A. *BMC Genomics.* **2008**, *9* (1), 344.

25. Park, R. M. *Materials Performance.* **2009**, 1.

26. Bard, A. J.; Faulkner, L. R. *Electrochemical Methods: Fundamentals and Applications*. Wiley, 2000.

27. Fourmond, V.; Hoke, K.; Heering, H. A.; Baffert, C.; Leroux, F.; Bertrand, P.; Léger, C. SOAS: A free program to analyze electrochemical data and other one-

dimensional signals. *Bioelectrochemistry.* **2009**, *76* (1-2), 141.

28. Jeuken, L. JellyFit. http://www.personal.leeds.ac.uk/~phyljcj/Software.htm.

29. Shin, H.-J.; Kim, K. K.; Benayad, A.; Yoon, S.-M.; Park, H. K.; Jung, I.-S.; Jin, M. H.; Jeong, H.-K.; Kim, J. M.; Choi, J.-Y.; Lee, Y. H. Efficient Reduction of Graphite Oxide by Sodium Borohydride and Its Effect on Electrical Conductance. *Adv. Funct. Mater.* **2009**, *19* (12), 1987.

30. Bergman, J.; Pettersson, B.; Hasimbegovic, V.; Svensson, P. H. Thionations Using a P4S10− Pyridine Complex in Solvents Such as Acetonitrile and Dimethyl Sulfone. *J. Org. Chem.* **2011**, *76* (6), 1546.

31. Compton, O. C.; Jain, B.; Dikin, D. A.; Abouimrane, A.; Amine, K.; Nguyen, S. T. Chemically active reduced graphene oxide with tunable C/O ratios. *ACS Nano.* **2011**, *5* (6), 4380.

32. Tung, V. C.; Allen, M. J.; Yang, Y.; Kaner, R. B. High-throughput solution processing of large-scale graphene. *Nat. Nanotech.* **2009**, *4* (1), 25.

33. Park, S.; An, J.; Jung, I.; Piner, R. D.; An, S. J.; Li, X.; Velamakanni, A.; Ruoff, R. S. Colloidal suspensions of highly reduced graphene oxide in a wide variety of organic solvents. *Nano Lett.* **2009**, *9* (4), 1593.

34. Curran, S. A.; Cech, J.; Zhang, D.; Dewald, J. L.; Avadhanula, A.; Kandadai, M.; Roth, S. Thiolation of carbon nanotubes and sidewall functionalization. *J. Mater. Res.* **2006**, *21* (4), 1012.

35. Socrates, G. Infrared and Raman characteristic group frequencies: tables and charts, 3rd ed.; John Wiley & Sons: Chichester, 2001.

36. Le Goff, A., Artero, V., Metayé, R., & Moggia, F. (2010). Immobilization of FeFe hydrogenase mimics onto carbon and gold electrodes by controlled aryldiazonium salt reduction: an electrochemical, XPS and ATR-IR study. *Inter. J. Hydrogen Energ.* (35), 10790–10796.

37. Fernández, L.; Carrero, H. *Electrochim ACTA.* **2005**, *50* (5), 1233.

38. Raoof, J.-B.; Ojani, R.; Kiani, A. *J. Electroanal.Chem.* **2001**, *515*, 45.

39. Nkosi, D.; Pillay, J.; Ozoemena, K. I.; Nouneh, K.; Oyama, M. *Phys. Chem. Chem. Phys.* **2010**, *12* (3), 604.

40. Sikes, H. D. *Science.* **2001**, *291* (5508), 1519.

41. Ashur, I.; Jones, A. K. Immobilization of azurin with retention of its native electrochemical properties at alkylsilane self-assembled monolayer modified indium tin oxide. *Electrochim ACTA.* **2012**, *85*, 169.

42. Creager, S.; Yu, C. J.; Bamdad, C.; O'Connor, S.; MacLean, T.; Lam, E.; Chong, Y.; Olsen, G. T.; Luo, J.; Gozin, M.; Kayyem, J. F. Electron Transfer at Electrodes through Conjugated 'Molecular Wire' Bridges. *J. Amer. Chem. Soc.* **1999**, *121* (5), 1059.

Chapter 6

Photosynthetic Microbial Fuel Cells

Joseph A. Laureanti, Anne K. Jones

School of Molecular Sciences,

Arizona State University, Tempe, AZ 85287

Reproduced with permission from:

Laureanti, J. A., & Jones, A. K. (2017). Photosynthetic Microbial Fuel Cells. In *Advances in Biochemical Engineering/Biotechnology*. Berlin, Heidelberg: Springer Berlin Heidelberg. http://doi.org/10.1007/10_2016_48

Abstract

This chapter presents the current state of research on bioelectrochemical systems that include phototrophic organisms. First, we describe what is known of how phototrophs transfer electrons from internal metabolism to external substrates. This includes efforts to understand both the source of electrons and transfer pathways within cells. Second, we consider technological progress toward producing bio-photovoltaic devices with phototrophs. Efforts to improve these devices by changing the species included, the electrode surfaces, and chemical mediators are described. Finally, we consider future directions for this research field.

Introduction

Solar energy is a highly available resource that is shared by all terrestrial organisms. However, because sunlight is dilute and intermittent, the search for ways to capture, utilize, and store it efficiently has become the great scientific challenge of the twenty-first century. Blankenship and coauthors have demonstrated that short-term photosynthetic conversion yields of phototrophic microorganisms come within a factor of 2–3 of the best photovoltaic systems and opportunities for increasing photosynthetic conversions yields via synthetic biology provide a compelling case for utilization of photosynthetic organisms in energy production and storage applications.[1] One approach is to use phototrophic organisms in microbial electrochemical technologies (MET) or bioelectrochemical systems (BES). This chapter describes recent progress in constructing and optimizing BES that employ an intact phototrophic organism at the cathode or anode and utilize the mechanisms of electron transfer from phototrophs to electrodes.

Microorganisms can be employed at either the anode or the cathode (or both) in a BES (**Figure 6-1**). The most common type of MET is a system known as a microbial fuel cell (MFC) in which microorganisms are used as anode catalysts to oxidize an externally provided fuel and to transfer the resulting electrons to the voltaic system (**Figure 6-1a**). This is usually coupled to the reduction of oxygen to water at the cathode. In the case where the fuel is a component of wastewater, the MFC can be used simultaneously both to treat the wastewater and to produce electricity.[2] Employing a microorganism instead at the cathode, that is, feeding electricity into the microorganism, results in a process known as electrosynthesis in which electrical energy is used to drive the production of a desired chemical (**Figure 6-1b**).[3,4] Although not strictly speaking a microbial fuel cell, this is also an important application of bioelectrochemistry.

Photosynthetic microbial fuel cells (PMFC) and bio-photovoltaic cells (BPV) are two types of BES that employ at least one photosynthetic organism. In both cases, a phototroph is used at the anode to produce electrons. They differ in the source of those electrons. PMFCs utilize a sacrificial chemical fuel as the ultimate electron source (**Figure 6-1c**). They may employ anaerobic phototrophs that are incapable of water-splitting.[5] On the other hand, a BPV uses an oxygenic photosynthetic organism at the bioanode to catalyze sunlight-driven photolysis of water in a traditional Z-scheme (**Figure 6-1d**) and provides the resulting electrons to the voltaic system.

There is a natural comparison between light-harvesting BES and traditional photovoltaic devices. Because photosynthetic microorganisms are self-sustaining and inexpensive to culture, light-harvesting BES can offer tremendous advantages.

Furthermore, generation of power from stored metabolites means microbial cells can also generate current under dark conditions, abrogating some of the challenge created by the intermittency of solar energy. However, development of BES is in its infancy. In particular, the efficiency of BPVs is relatively low, and understanding of the mechanisms that allow electrical communication between photosynthetic organisms and electrodes is less advanced than understanding of the analogous processes for other types of microorganisms. In this chapter, we first describe what is known of the mechanisms of electron transfer from phototrophs to extracellular substrates. We then consider the current state of the art in PMFC and BPV. We close by identifying promising future research directions.

Mechanisms of Electron Transfer Between Phototrophs and Electrodes

In microbial fuel cells, anode-respiring bacteria transfer electrons extracted from a fuel to the external electrode by moving them through respiratory pathways (**Figure 6-1a**). A diverse array of phototropic species, especially cyanobacteria, also possess electrogenic activity, that is, the ability to transfer electrons from internal metabolism to an extracellular electrode. In many cases this activity is light- dependent.[6] However, it is often unclear whether the electrons are derived directly from photosynthesis or from some other metabolic process. In this section, we consider what is known of the electron transfer pathways that shuttle electrons from phototrophs to external electrodes. In so doing, we also see that BPVs serve as a unique tool to probe the interconnectivity of electron transfer pathways in phototrophs. Mechanistic understanding of extracellular electron transfer (EET) by phototrophs is relatively limited. Herein we describe what is known against a backdrop of the knowledge gleaned

from the better-studied, anode-respiring *Shewanella* and *Geobacter* sp.

Indirect EET in Anode-Respiring Bacteria and Phototrophs

Studies of anode-respiring bacteria have identified two distinct mechanisms for EET: direct and indirect (**Figure 6-2**). Indirect mechanisms are those that rely on a soluble redox mediator to shuttle electrons between the cell interior and the electrode. This shuttle can be either microbially produced or exogenously added. For example, *Shewanella oneidensis* MR-1 has been shown to reduce extracellular minerals using endogenously produced and secreted flavins.[7-11] As much as 80% of EET by *Shewanella* is thought to be indirect.[10] Many phototrophs are also able to reduce exogenous mediators for indirect EET. The earliest BPVs relied almost exclusively on indirect transfer of electrons using such artificial mediators as viologens, napthoquinone derivatives[12,13], and ferricyanide[14]. However, these mediators have largely fallen out of fashion because they offer significant problems for device scale-up and toxicity. As the natural electron acceptor of Photosystem II (PSII) is plastoquinone, Lemaître and colleagues hypothesized that quinones might serve as more effective mediators. They developed a fluorescence-based method to screen interactions with PSII rapidly and found that 2,6-dichlorobenzoquinone, 2,5-dichlorobenzoquinone, and p-phenylbenzoquinone can mediate electron transfer from the model green algae *Chlamydomonas reinhardtii* to electrodes.[15] Although there is no evidence that electrogenic phototrophs secrete flavins, they may naturally employ other endogenously-produced mediators to transfer reducing equivalents to electrodes. For example, hydrogen is a common photosynthetic product,[16] and it can serve as a natural electron mediator between microbes and an anode.[17-20] Similarly, quinones have been hypothesized to serve as natural mediators of indirect EET

in BPV.[21,22] Several mediatorless BPVs have been described that may unwittingly rely on these endogenous mediators.

Direct EET in Anode-Respiring Bacteria

Direct transfer of electrons from microorganisms to an electrode is transfer that does not require an intervening chemical mediator. Instead, it occurs via physical contact between outer membrane proteins and/or conductive appendages and the extracellular substrate (**Figure 6-2**). Direct EET by anode-respiring bacteria is hypothesized to employ conductive appendages that have been variously referred to in the literature as microbial nanowires or conductive pili.[23,24] Recent studies have shown that the nanowires of *Shewanella* are not pili, as initially suggested, but rather outer membrane and periplasmic extensions.[25] Furthermore, *Shewanella* sp. are known to produce a collection of multiheme cytochromes that form multiple, interconnected electron transfer pathways from intracellular respiration and the quinone pool to the outer membrane.[26-28] These pathways are now relatively well-defined. In fact, heterologous expression of one, the MtrCAB pathway, confers on Escherichia coli the ability to reduce solid Fe_2O_3, an activity not present in the wild-type organism.[29] Understanding of direct EET by phototrophs, as we will see below, is not nearly so well-developed. Nonetheless, in the future, genetic manipulation may also be possible.

Direct EET by Phototrophs: Where Do Electrons Originate?

Initial reports of bio-nanowires in *S. oneidensis* MR-1 included preliminary evidence that the cyanobacterium *Synechocystis* sp. PCC 6803 can also produce electrically conductive nanowires under low carbon conditions.[30] However, this initial

report has never been confirmed and additional evidence of conductive appendages has not been reported for this or any other phototroph. Thus it remains unclear whether phototrophs can participate in direct electron exchange with electrodes. Nonetheless, a broad range of phototrophs, including purple bacteria,[20] cyanobacteria,[6,31-33] and eukaryotic algae,[17,34] have been shown to produce photocurrent at electrodes often without addition of an exogenous mediator.[32,35] The question of the source of this current is further complicated by the anatomy of photosynthetic organisms and the location of the photosynthetic machinery. In algae, for example, photosynthesis occurs in the sub-cellular organelle known as a chloroplast, and the components are isolated from the electrode by a thick cell wall, making it likely that direct interaction between these components and an electrode is not a major component of photocurrent production. Similarly, the majority of cyanobacteria have two membrane systems: the cytoplasmic membrane and a collection of internal thylakoid membranes that house the photosynthetic and respiratory electron transport complexes.[36] Thus, transfer of photosynthetically-derived electrons to the cytoplasmic membrane must employ carriers that link the two membrane systems.

Observation of light-dependent current production by phototrophs in BPVs has led to the hypothesis that these electrons are derived not from biochemical oxidation of organic compounds but rather from light-driven water splitting. Herein, we first consider evidence that photocurrents in BPVs depend on oxygenic photosynthesis and water splitting. Then we explore hypotheses for the mechanisms of transport of photosynthetically-derived reducing equivalents to the cell surface.

Figure 6-3 shows the prototypical Z-scheme of oxygenic photosynthesis, highlighting site-specific inhibitors that can be used to probe the pathways of electrons from the photosystems to the cell exterior. PSII is the site of water oxidation, and Photosystem I (PSI) used to generate reductants for other cellular processes. The two photosystems are linked via the diffusing carrier plastoquinone and the cytochrome b_6f complex. Photosynthetic electron flow is also linked to other metabolic processes such as respiration via soluble carriers. This can make it particularly difficult to ascertain the source of electrons.

Baskakov and colleagues suggested that the electrogenic activity of cyanobacteria is a means to protect the plastoquinone pool from overreduction at high light intensity.[37] Similarly, Freguia and coworkers have shown that cyanobacteria-dominated biofilms only produced photocurrent at solid electrodes when stressed with limited CO_2 or high light levels.[38] These "light stress" hypotheses have fueled the idea that EET by phototrophs is largely the result of excess electrons from photosynthesis, and a number of mechanistic studies explore this idea. Photosynthetic chemical inhibitors have been used to disrupt electron flow in BPVs employing cyanobacteria as a means to trace the electron transfer pathway. Pisciotta and coworkers used the PSII inhibitor 3-(3,4-dichloro-phenyl)-1,1- dimethylurea (DCMU) to demonstrate that in *Lyngbya* and *Nostoc* electrons transferred to extracellular electron acceptors originate from the water splitting function of PSII.[37] The authors also concluded that plastoquinone is a key carrier in the pathways because addition of 2,5-dibromo-3-methyl-6-isopropyl benzoquinone (DBMIB), an inhibitor that prevents interactions between plastoquinones and cytochrome b_6f, enhanced electrogenic activity. Because oxidation of plastoquinol by cytochrome b_6f

has been hypothesized to be a rate-limiting step in photosynthetic electron transfer,[39] these results suggest that EET may serve phototrophs as a shunt to dissipate extra photosynthetic reducing equivalents. On the other hand, Bombelli and coworkers used analogous inhibitor studies to suggest that photosynthetically-derived electrons detected in a BPV employing *Synechocystis* are derived from the reducing end of PSI.[14] In a complementary approach, Cereda and coworkers demonstrated that circa 80% of extracellular electrons produced by *Synechocystis* in a BPV are derived from the water splitting activity of PSII by measuring current produced by a mutant strain lacking this activity.[32] This result suggests that, although the majority of photocurrent arises from photosynthetic water splitting, a considerable minority of electrons are unaccounted for photosynthetically and likely derived from respiratory electron transport. Thus it is likely that most photocurrent produced in BPV is derived from water splitting, but there is cross-talk with other metabolic pathways. This situation is not unlike that of *Shewanella* sp. in which many metabolic pathways compete with the electrode for electrons.

Transfer of Electrons from the Site of Photosynthesis to the Cell Surface

As photosynthetic membranes are typically localized in the interior of phototrophic cells, EET requires a pathway for reducing equivalents to be transferred from the site of production to the cell surface. Ferredoxins and NADPH both connect a multitude of pathways in algae and cyanobacteria and have been considered possible candidates for electron shuttles. In this section, we consider studies that address this hypothesis and efforts to enhance EET by introducing non-native electron carriers.

There is evidence suggesting that the thylakoid and cytoplasmic membranes are

connected in *Synechocystis*.[40] However, it is unclear whether their electron transport chains are also connected. Howe and coworkers have hypothesized that proteins or mediators transfer reducing equivalents from the thylakoid membranes to the cytoplasmic membrane. Candidate carriers include the eight putative ferredoxins encoded by *Synechocystis*, soluble cytochromes, plastoquinol, and NADPH generated by ferredoxin-$NADP^+$ reductase. From the cytoplasmic membrane, electrons may then be transferred to ferredoxin or cytochromes in the periplasm to effect EET.[41]

A similar mechanism may operate in algae. Transgenic *Chlamydomonas reinhardtii* strains overexpressing PETF and FDX5, the genes encoding two of the native ferredoxins for this model algae, have lower levels of reactive oxygen species, are more tolerant to heat and salt stress, accumulate more starch, and generate up to five times more power density in a PMFC.[34] Although these initially sound like unrelated phenotypes, ferredoxin is thought to be a central linker between photosynthetic electron production and these downstream reductive processes. Some of these pathways may serve as protection from the reactivity of energetic electrons produced under high level light conditions, and the results suggest that activity in PMFCs may be enhanced by eliminating competing pathways and forcing electrons toward the extracellular acceptor. Alternatively, it is possible that increased starch or simply biomass is necessary for enhanced activity in the PMFC. This biomass may be converted to NADPH which then feeds into the EET pathway.

Power densities in BPVs are approximately two orders of magnitude lower than those in MFCs employing anode-respiring bacteria such as *Geobacter* or *Shewanella*.

This suggests that the natural electrogenic activity of phototrophs may be substantially lower than that of the anode-respiring bacteria. To improve this natural activity, Ramasamy and coworkers have heterologously overexpressed the *Geobacter* outer membrane cytochrome S (OmcS), a key component in EET, in the cyanobacterium *Synechococcus elongatus* PCC 7942. The variant cyanobacterium produced nine times more current than wild-type.[42] This preliminary result suggests that genetic engineering may offer significant opportunities to enhance the efficiency of EET by phototrophs. At the moment, the main challenge is identifying the genetically- tractable phototrophs most likely to be successfully deployed in BES.

Engineering of PMFC and BPV

The first PMFC was reported in 1964 by Berk and Canfield.[18] The anode of this cell consisted of planktonic Rhodospirillum rubrum cells fed by malate. The cells grow photoheterotrophically with concomitant production of hydrogen which is oxidized at the platinum anode. The resulting electrons are used at the cathode to reduce oxygen to water. The oxygen was produced by a photosynthetic biofilm of the marine algae *Oscillatoriaceae*. The algae grow photoautotrophically via fixa- tion of atmospheric CO_2. The device could operate for several days as long as nutrients were regularly replenished, and conversion efficiency of incident solar irradiation to electrical power was 0.1–0.2%. Although this seems low, overall photosynthetic yields for converting solar irradiation to chemical energy range from <1% for agricultural crops to <3% for relatively productive algae. So this initial PMFC effort was within an order of magnitude of theoretical yields. Importantly, current devices have similar yield.

Following the work of Berk and Canfield, there have been numerous attempts to improve the power outputs of PMFCs. McCormick and coworkers reviewed efforts to engineer BPVs, and **Figure 6-4** shows evolution of performance over the last 30 years. Unfortunately, there has been no consistent improvement. To date, the greatest current density reported, 1.5 mA/cm,^{2} is from a BPV employing *Chlamydomonas reinhardtii* at a bioanode. Similar to the original Berk and Canfield cell, this BPV also relies on hydrogen produced by the microbe, in this latter case a green algae, to be oxidized at the platinum anode.[43] In light of scalability concerns, there is a trend away from platinum electrodes. Carbon electrode materials have become the standard in MFCs, and current densities as high as only fourfold lower than those on platinum have been reported by Yagishita and coworkers for a carbon-based BPV. As hydrogen is not efficiently oxidized at carbon substrates, carbon-based devices require alternative electron mediators. Thus Yagishita employed not just a different electrode surface but also a different redox mediator. He chose the soluble redox mediator 2-hydroxy-1,4-naphthoquinone in concert with *Synechococcus* PCC UTEX 2380 at the anode.[13] Addition of an exogenous mediator, however, also introduces concerns about scale-up and toxicity. Ideally, devices would be produced using only cheap, renewable, non-toxic materials. However, such a system with good performance metrics has not yet been created. Selection of organisms and electrode/mediator are two active areas of research being pursued to improve devices. Each is considered in turn below.

Identifying Organisms for Use in BPV

BPV devices have been constructed using both single species and microbial consortia as well as planktonic and benthic, biofilm forming, species.[44-46] Metagenomic

evaluation of biofilm consortia in anerobic experiments demon- strates that these communities contain largely cyanobacteria as their photosynthetically active members.[47] Nonetheless, studies in pure culture have shown that phototrophs including purple bacteria,[20] cyanobacteria,[6,13,31-33] and eukaryotic algae[34,48] can produce photocurrent at an electrode, but there is no consensus as to which are the best phototrophs for use in BES.

There are very few studies that report comparison of different species or consortia in the same electrochemical apparatus. Three key examples stand out. First, McCormick and coworkers compared four green algae and cyanobacteria, Chlorella vulgaris, Dunaliella tertiolecta, *Synechocystis* sp. PCC 6803, and *Synechococcus* sp. WH 5701, in a mediatorless BPV [35]. They concluded that all species demonstrated light-dependent activity. Second, Packer and co-workers designed a cost-effective cell to screen phototrophs (**Figure 6-5**). They used it to evaluate the performance of 25 different benthic cyanobacteria and algal isolates from Antarctica and New Zealand. The same genera of cyanobacteria, *Pseudoanabaena, Leptolyngbya, Chroococales, M. vaginatus, Nostoc*, and *Phormidium* were consistently represented in highly functioning BPV. However, electrogenic performance does not strictly correlate with the genus. For example, highly electrogenic species from Antarctic samples were often from genera with modest or poor activity in samples from New Zealand.[49] Third, Fisher and coworkers used a similar approach to evaluate electrogenic activity from four algal strains. Interestingly, this group started from 16 strains, but 12 were eliminated before electrochemical testing for poor biofilm formation or poor overall photosynthetic performance. The power output by the four strains tested, *Synechococcus elongatus* (UMACC 105), *Chlorella vulgaris* UMACC 051, *Chlorella* sp. (UMACC 313), and

Spirulina platensis (UMACC 159), varied by over an order of magnitude.[50] This highlights the importance of screening more environmental samples for electrogenic activity to allow better matching of microbial properties to desired applications.

Materials for Electrodes

Similar to the impact of the microorganism employed, the role of the anode material in BPV performance has not been systematically evaluated.[51] Carbon anodes are de rigueur in microbial fuel cells, but preliminary evidence suggests that other materials may be highly advantageous for BPVs. For example, because BPVs require the microorganism to absorb light, there are obvious advantages to using transparent electrodes made of materials such as conducting metal oxides. McCormick and coworkers compared the performance of the fresh-water, filamentous cyanobacterium *Pseudanabaene limnetica* in a BPV on four different anode surfaces: indium tin oxide coated polyethylene tetraphthlate (ITO), stainless steel, glass coated with conductive polymer, and carbon paper. Carbon had the lowest power output in this system. The best performing materials were ITO and stainless steel.[52] Cameron and coworkers showed that *Chlorella vulgaris* biofilms grew more successfully on a porous fluorine-doped tin oxide coated titanium dioxide anode. The power density from this system was 16 times higher than a comparable carbon anode. Similar results were obtained with planar FTO coated glass, but the biofilms were less stable.[53]

Conductive polymer electrodes have also been evaluated as a means to transfer electrons more effectively from the microorganisms to the electrode. For example, Baskakov and coworkers employed nanostructured fibrillar polypyrrole as an anode

material to harvest electrons from photosynthetic biofilms. Relative to measurements without the polymer, power density increased 450%.[54] Similarly, Gorton and coworkers have shown that Os-polymers can be used to mediate electron transfer from the green algae *Paulschulzia pseudovolvox* to graphite with current densities an order of magnitude higher than unmediated transfer. Interestingly, the current density can be further improved by an order of magnitude to 6.97 $\mu A\ cm^{-2}$ by inclusion of the diffusing redox mediator benzoquinone.[55] These results suggest that development of systems that combine multiple mediators with transparent electrodes may prove an exciting future research direction.

Conclusions

Creation of bioelectrochemical systems that employ phototrophs is a rapidly growing field which benefits from enhanced mechanistic understanding. Recent work shows that electrons can be derived from photosynthetic water splitting, but the pathway of the electron from PSII to the cell exterior remains unclear. Elucidating these details and mapping the interconnectivity between cellular electron transfer pathways may help improve performance metrics for devices. On the other hand, the native electrogenic activity of phototrophs appears to be much lower than that of model anode-respiring bacteria. As the understanding of the pathways in chemotrophs expands, genetic manipulation and synthetic biology is also becoming a viable approach to enhancing the activity of phototrophs. Finally, perhaps the most exciting application on the horizon is employing phototrophs as bio-factories for solar-driven production of chemicals from electricity. This chapter describes EET from phototrophs, but achievement of this dream requires a concerted effort to understand how electrons can be transferred into microbes

for electrosynthesis.

Figures

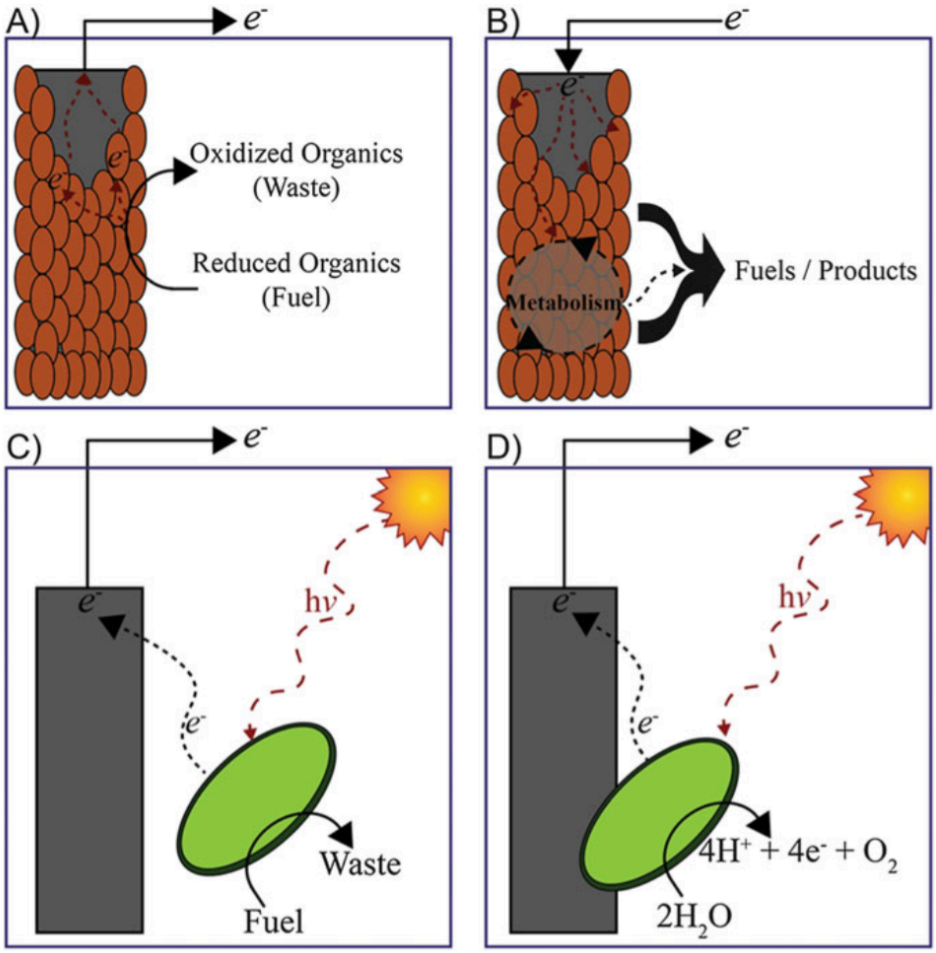

Figure 6-1. Diagrams of bioelectrochemical systems. (a) Microbial fuel cell in which an anode- respiring bacterium produces current using electrons from a sacrificial, organic carbon source. (b) Electrosynthetic cell in which a microbe at the cathode uses electricity to drive chemical synthesis. (c) Photosynthetic microbial fuel cell in which a chemical electron donor is provided to an anoxygenic phototroph. (d) Biophotovoltaic system in which an oxygenic phototroph derived electrons at the anode from water.

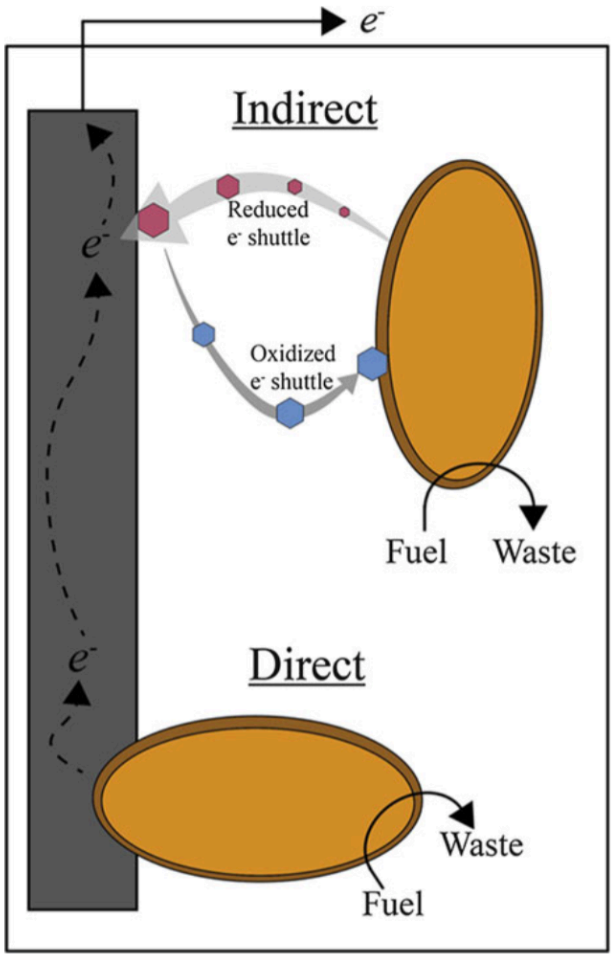

Figure 6-2. Schematic depiction of direct and indirect mechanisms of extracellular electron transfer from a microbe to a solid electrode surface.

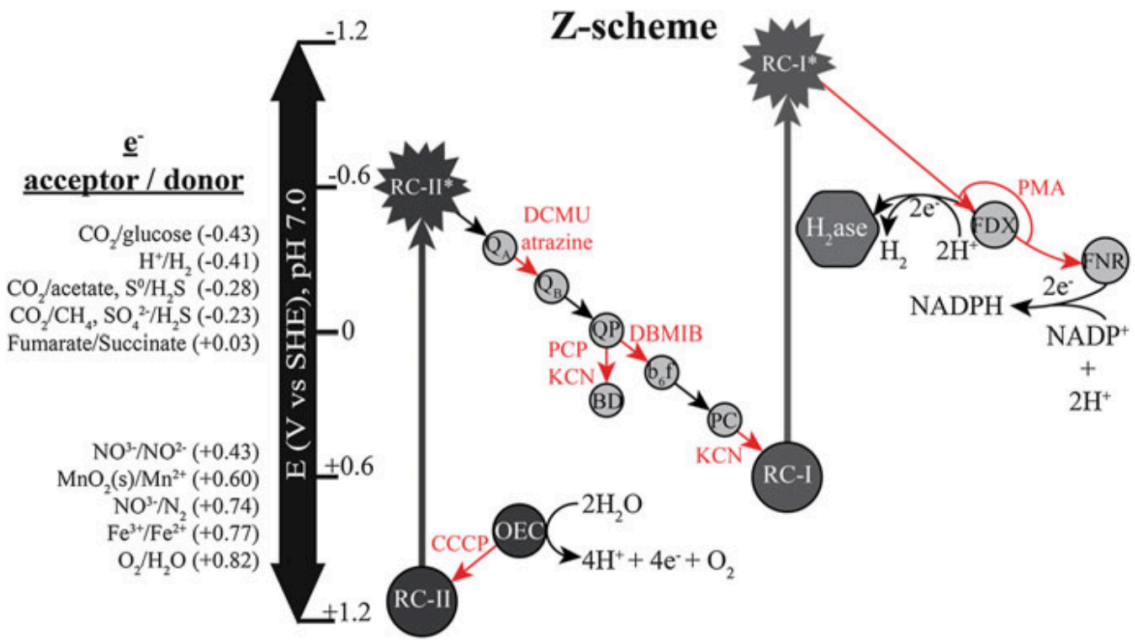

Figure 6-3. Photosynthetic Z-scheme with reduction potentials of intermediates of the photosynthetic electron transport chain. Reduction potentials of common metabolic electron sources/sinks (left) are quoted relative to the standard hydrogen electrode, SHE, at pH 7.0 and are shown next to an energy level diagram oriented with the most reducing species at the top. Red arrows designate the inhibition of electron transfer using an exogenous chemical. Inhibitor abbreviations can be found in the abbreviation table. Z-scheme abbreviations are as follows: RC-II type-II reaction center, OEC oxygen evolving complex, RC-I type-I reaction center, Q_A quinone A, Q_B quinone b, QP quinone pool, BD cytochrome bd quinol oxidase, b6f cytochrome b6f complex, PC plastocyanin, FDX ferredoxin, FNR ferredoxin-$NADP^+$ reductase, H2ase proton reducing hydrogenase.

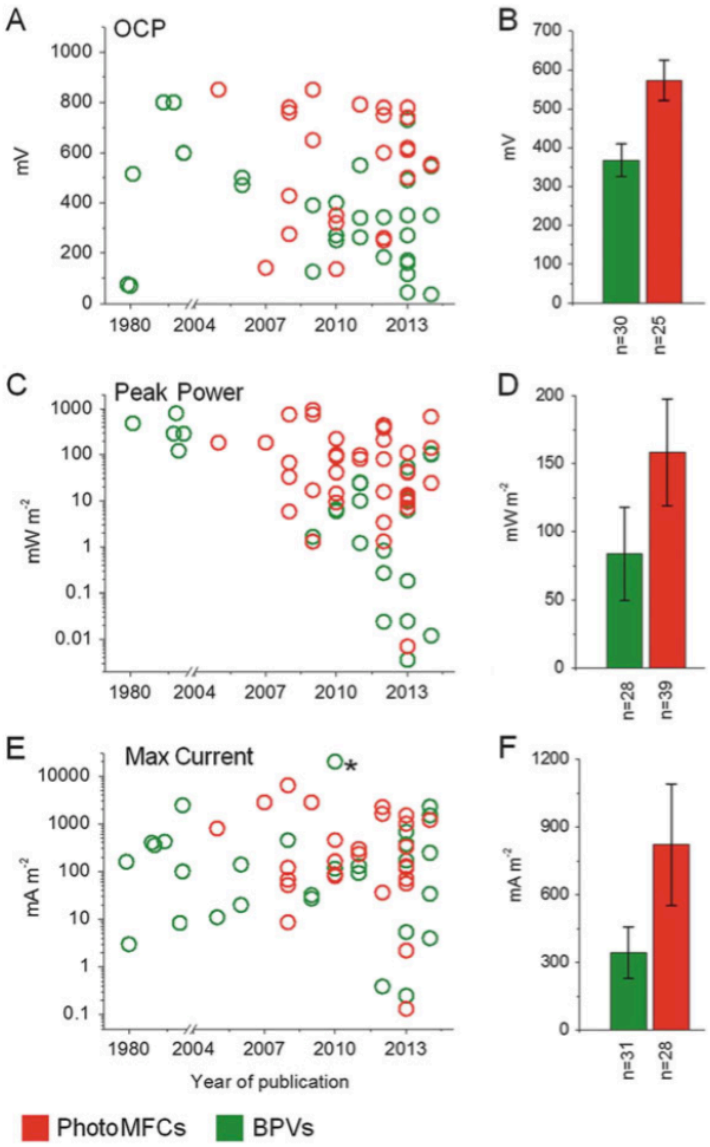

Figure 6-4. Overview of BPV (green) and PMFC (red) performances. OCP stands for open circuit potential. (b, d, f) Averages for (a, c, e), respectively in which n indicates the number of studies considered. Asterisk indicates that point was not included in the averages. Reproduced with permission from A. J. McCormick, P. Bombelli, R. W. Bradly, R. Thorne, T. Wenzel, and C. J. Howe, Energy Environ. Sci., 2015, 8, 1092 – Published by the Royal Society of Chemistry.

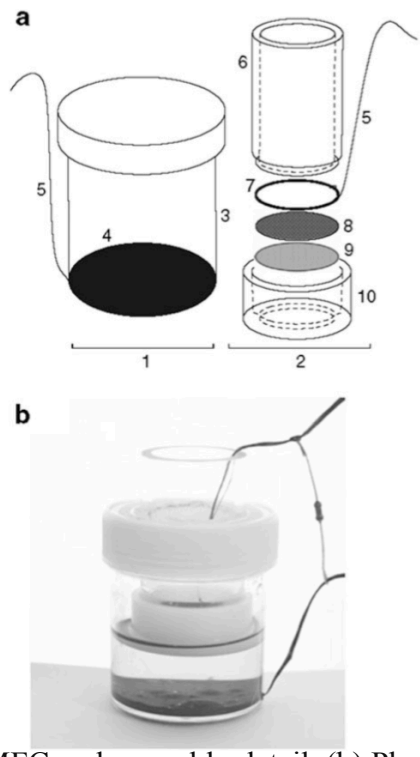

Figure 6-5. (a) Schematic of PMFC and assembly detail. (b) Photograph of a PMFC containing a 1-month culture of Paulschulzia pseudovolvox. The anode chamber (1) is comprised of a polysty- rene sample pottle (3) coated with Wire GlueTM (4). The cathode assembly insert (2) is comprised of a clear polycarbonate barrel (6) and a machines polyethylene cap (10). The cap fits tightly over the barrel, sealing a stack of Ultrex cathode exchange membrane (9), carbon cloth containing 10% platinum (8, Pt face down) and a titanium ring (7) to act as a charge collector which fits into lip machines on the end of 6. Threads from a woven carbon fiber cloth were used as leads for the fuel cell (5); for the cathode, this was simply wrapped around the titanium ring before being pressed into place. The anode chamber was glued around the base of the chamber, acting as the charge collector.[49]

References

1. Blankenship, R. E. *et al.* Comparing Photosynthetic and Photovoltaic Efficiencies and Recognizing the Potential for Improvement. *Science.* **332,** 805–809 (2011).

2. Logan, B. E. & Rabaey, K. Conversion of Wastes into Bioelectricity and Chemicals by Using Microbial Electrochemical Technologies. *Science.* **337,** 686–690 (2012).

3. Nevin, K. P., Woodard, T. L., Franks, A. E., Summers, Z. M. & Lovley, D. R. Microbial Electrosynthesis: Feeding Microbes Electricity To Convert Carbon Dioxide and Water to Multicarbon Extracellular Organic Compounds. *mBio.* **1,** (2010).

4. Rabaey, K. & Rozendal, R. A. Microbial electrosynthesis - revisiting the electrical route for microbial production. *Nat. Rev. Micro.* **8,** 706–716 (2010).

5. Chandra, R., Modestra, J. A. & Mohan, S. V. Biophotovoltaic cell to harness bioelectricity from acidogenic wastewater associated with Microbial Community Profiling. *Fuel.* **160,** 502–512 (2015).

6. Zou, Y., Pisciotta, J., Billmyre, R. B. & Baskakov, I. V. Photosynthetic microbial fuel cells with positive light response. *Biotechnol. Bioeng.* **104,** 939–946 (2009).

7. Brutinel, E. D. & Gralnick, J. A. Shuttling happens: soluble flavin mediators of extracellular electron transfer in *Shewanella*. *Appl. Microbiol. Biotechnol.* **93,** 41–48 (2012).

8. Okamoto, A., Nakamura, R., Nealson, K. H. & Hashimoto, K. Bound Flavin Model Suggests Similar Electron-Transfer Mechanisms in *Shewanella* and *Geobacter*. *ChemElectroChem.* **1,** 1808–1812 (2014).

9. Edwards, M. J. *et al.* Redox Linked Flavin Sites in Extracellular Decaheme Proteins Involved in Microbe-Mineral Electron Transfer. *Sci. Rep.* **5,** 11677 (2015).

10. Kotloski, N. J. & Gralnick, J. A. Flavin Electron Shuttles Dominate Extracellular Electron Transfer by *Shewanella oneidensis*. *mBio.* **4,** (2013).

11. Marsili, E. *et al. Shewanella* Secretes flavins that mediate extracellular electron transfer. *Proc. Natl. Acad. Sci. U.S.A.* **105,** 3968–3973 (2008).

12. Ochiai, H., Shibata, H., Sawa, Y., Shoga, M. & Ohta, S. Properties of Semiconductor Electrodes Coated with Living Films of Cyanobacteria. *Appl Biochem. Biotechnol.* **8,** 289–303 (1983).

13. Yagishita, T., Sawayama, S., Tsukahara, K.-I. & Ogi, T. Effects of intensity of incident light and concentrations of *Synechococcus* sp. and 2-hydroxy-1,4-naphthoquinone on the current output of photosynthetic electrochemical cell. *Sol. Energy.* **61,** 347–353 (1997).

14. Bombelli, P. *et al.* Quantitative analysis of the factors limiting solar power transduction by *Synechocystis* sp. PCC 6803 in biological photovoltaic devices. *Energy Environ. Sci.* **4,** 4690–4698 (2011).

15. Longatte, G. *et al.* Evaluation of photosynthetic electrons derivation by exogenous redox mediators. *Biophys. Chem.* **205,** 1–8 (2015).

16. Beer, L. L., Boyd, E. S., Peters, J. W. & Posewitz, M. C. Engineering algae for biohydrogen and biofuel production. *Curr. Opin. Biotech.* **20,** 264–271 (2009).

17. Rosenbaum, M., Schroder, U. & Scholz, F. Utilizing the green alga *Chlamydomonas reinhardtii* for microbial electricity generation: a living solar cell. *Appl. Microbiol. Biotechnol.* **68,** 753–756 (2005).

18. Berk, R. S. & Canfield, J. H. Bioelectrochemical Energy Conversion. *Appl. Microbiol.* **12,** 10–& (1964).

19. Rosenbaum, M., Schroder, U. & Scholz, F. In situ electrooxidation of photobiological hydrogen in a photobioelectrochemical fuel cell based on *Rhodobacter sphaeroides*. *Environ. Sci. Technol.* **39,** 6328–6333 (2005).

20. Cho, Y. K. *et al.* Development of a solar-powered microbial fuel cell. *J. Appl. Microbiol.* **104,** 640–650 (2008).

21. Newman, D. K. & Kolter, R. A role for excreted quinones in extracellular electron transfer. *Nature.* **405,** 94–97 (2000).

22. Bradley, R. W., Bombelli, P., Rowden, S. J. L. & Howe, C. J. Biological photovoltaics: intra- and extra-cellular electron transport by cyanobacteria. *Biochm. Soc. Trans.* **40,** 1302–1307 (2012).

23. El-Naggar, M. Y. *et al.* Electrical transport along bacterial nanowires from *Shewanella oneidensis* MR-1. *Proc. Natl. Acad. Sci. U.S.A.* **107,** 18127–18131 (2010).

24. Reguera, G. *et al.* Extracellular electron transfer via microbial nanowires. *Nature.* **435,** 1098–1101 (2005).

25. Pirbadian, S. *et al. Shewanella oneidensis* MR-1 nanowires are outer membrane and periplasmic extensions of the extracellular electron transport components.

Proc. Natl. Acad. Sci. U.S.A. **111,** 12883–12888 (2014).

26. Alves, M. N. *et al.* Characterization of the periplasmic redox network that sustains the versatile anaerobic metabolism of *Shewanella oneidensis* MR-1. *Front. Microbiol.* **6,** (2015).

27. Fonseca, B. M. *et al.* Mind the gap: cytochrome interactions reveal electron pathways across the periplasm of *Shewanella oneidensis* MR-1. *J. Biochem.* **449,** 101–108 (2013).

28. Sturm, G. *et al.* A dynamic periplasmic electron transfer network enables respiratory flexibility beyond a thermodynamic regulatory regime. *Isme. Journal.* **9,** 1802–1811 (2015).

29. Jensen, H. M. *et al.* Engineering of a synthetic electron conduit in living cells. *Proc. Natl. Acad. Sci. U.S.A.* **107,** 19213–19218 (2010).

30. Gorby, Y. A. *et al.* Electrically conductive bacterial nanowires produced by *Shewanella oneidensis* strain MR-1 and other microorganisms. *Proc. Natl. Acad. Sci. U.S.A.* **103,** 11358–11363 (2006).

31. Pisciotta, J. M., Zou, Y. & Baskakov, I. V. Light-Dependent Electrogenic Activity of Cyanobacteria. *PLoS ONE.* **5,** (2010).

32. Cereda, A. *et al.* A Bioelectrochemical Approach to Characterize Extracellular Electron Transfer by *Synechocystis* sp PCC6803. *PLoS ONE.* **9,** (2014).

33. Sekar, N., Umasankar, Y. & Ramasamy, R. P. Photocurrent generation by immobilized cyanobacteria via direct electron transport in photo-bioelectrochemical cells. *Phys. Chem. Chem. Phys.* **16,** 7862 (2014).

34. Huang, L. F., Lin, J. Y., Pan, K. Y., Huang, C. K. & Chu, Y. K. Overexpressing Ferredoxins in *Chlamydomonas reinhardtii* Increase Starch and Oil Yields and Enhance Electric Power Production in a Photo Microbial Fuel Cell. *IJMS.* **16,** 19308–19325 (2015).

35. McCormick, A. J. *et al.* Photosynthetic biofilms in pure culture harness solar energy in a mediatorless bio-photovoltaic cell (BPV) system. *Energy Environ. Sci.* **4,** 4699 (2011).

36. Mullineaux, C. W. Co-existence of photosynthetic and respiratory activities in cyanobacterial thylakoid membranes. *BBA - Bioenergetics.* **1837,** 503–511 (2014).

37. Pisciotta, J. M., Zou, Y. & Baskakov, I. V. Role of the photosynthetic electron transfer chain in electrogenic activity of cyanobacteria. *Appl. Microbiol.*

Biotechnol. **91,** 377–385 (2011).

38. Darus, L., Ledezma, P., Keller, J. & Freguia, S. Marine phototrophic consortia transfer electrons to electrodes in response to reductive stress. *Photosynth. Res.* **127,** 347–354 (2016).

39. Trubitsin, B. V. *et al.* EPR study of electron transport in the cyanobacterium *Synechocystis* sp PCC 6803: Oxygen-dependent interrelations between photosynthetic and respiratory electron transport chains. *BBA - Bioenergetics.* **1708,** 238–249 (2005).

40. Pisareva, T. *et al.* Model for Membrane Organization and Protein Sorting in the Cyanobacterium *Synechocystis* sp PCC 6803 Inferred from Proteomics and Multivariate Sequence Analyses. *J. Proteome Res.* **10,** 3617–3631 (2011).

41. Lea-Smith, D. J., Bombelli, P., Vasudevan, R. & Howe, C. J. Photosynthetic, respiratory and extracellular electron transport pathways in cyanobacteria. *BBA - Bioenergetics.* **1857,** 247–255 (2016).

42. Sekar, N., Jain, R., Yan, Y. & Ramasamy, R. P. Enhanced photo-bioelectrochemical energy conversion by genetically engineered cyanobacteria. *Biotechnol. Bioeng.* **113,** 675–679 (2015).

43. Rosenbaum, M., Schröder, U. & Scholz, F. Utilizing the green alga *Chlamydomonas reinhardtii* for microbial electricity generation: a living solar cell. *Appl. Microbiol. Biotechnol*. **68,** 753–756 (2005).

44. Cao, X. X., Huang, X., Boon, N., Liang, P. & Fan, M. Z. Electricity generation by an enriched phototrophic consortium in a microbial fuel cell. *Electrochem. Commun.* **10,** 1392–1395 (2008).

45. Darus, L., Lu, Y., Ledezma, P., Keller, J. & Freguia, S. Fully reversible current driven by a dual marine photosynthetic microbial community. *Bioresour. Technol.* **195,** 248–253 (2015).

46. Badalamenti, J. P., Torres, C. I. & Krajmalnik-Brown, R. Light-responsive current generation by phototrophically enriched anode biofilms dominated by green sulfur bacteria. *Biotechnol. Bioeng.* **110,** 1020–1027 (2013).

47. Nishio, K., Hashimoto, K. & Watanabe, K. Light/electricity conversion by a self-organized photosynthetic biofilm in a single-chamber reactor. *Appl. Microbiol. Biotechnol.* **86,** 957–964 (2010).

48. Fu, C. C., Hung, T. C., Wu, W. T., Wen, T. C. & Su, C. H. Current and voltage responses in instant photosynthetic microbial cells with Spirulina platensis.

Biochem. Eng. J. **52,** 175–180 (2010).

49. Luimstra, V. M. *et al.* A cost-effective microbial fuel cell to detect and select for photosynthetic electrogenic activity in algae and cyanobacteria. *J. Appl. Phycol.* **26,** 15–23 (2013).

50. Ng, F. L., Phang, S. M., Periasamy, V., Yunus, K. & Fisher, A. C. Evaluation of Algal Biofilms on Indium Tin Oxide (ITO) for Use in Biophotovoltaic Platforms Based on Photosynthetic Performance. *PLoS ONE.* **9,** 13 (2014).

51. Schneider, K., Thorne, R. J. & Cameron, P. J. An investigation of anode and cathode materials in photomicrobial fuel cells. *Philos. T. R. Soc. A.* **374,** (2016).

52. Bombelli, P. *et al.* Surface morphology and surface energy of anode materials influence power outputs in a multi-channel mediatorless bio-photovoltaic (BPV) system. *Phys. Chem. Chem. Phys.* **14,** 12221–12229 (2012).

53. Thorne, R. *et al.* Porous ceramic anode materials for photo-microbial fuel cells. *J. Mater. Chem.* **21,** 18055–18060 (2011).

54. Zou, Y. J., Pisciotta, J. & Baskakov, I. V. Nanostructured polypyrrole-coated anode for sun-powered microbial fuel cells. *Bioelectrochemistry.* **79,** 50–56 (2010).

55. Hasan, K. *et al.* Photoelectrochemical Wiring of *Paulschulzia pseudovolvox* (Algae) to Osmium Polymer Modified Electrodes for Harnessing Solar Energy. *Adv. Energy Mater.* **5,** (2015).

Chapter 7

Photosynthetically Driven Bio-Electrosynthesis of Hydrogen using *Heliobacterium modesticaldum*

Joseph A. Laureanti[1], Christopher Gisriel[1], Kevin E. Redding[1], Anne K. Jones[1]

[1]School of Molecular Sciences, Arizona State University, Tempe, AZ 85287, USA

josephl@asu.edu, cgisriel@asu.edu, kevin.redding@asu.edu, jonesak@asu.edu

Abstract

Only a few examples of microbial electrosynthesis, a process in which microorganisms consume electricity to synthesize a chemical, have been reported, and there are no examples employing a phototrophic microorganism. Herein, we demonstrate light-dependent electron uptake by *Heliobacterium modesticaldum,* an anaerobic photoheterotroph, with concomitant production of hydrogen. Observation of photocurrent requires the cells be in an argon or nitrogen atmosphere and removal of alternative electron sources from the solution. Furthermore, growing the cells in ammonium-depleted medium under nitrogen results greater hydrogen production suggesting that the nitrogenase catalyzes this reaction. Photocurent also strictly requires an applied potential sufficient to reduce the mediator, the presence of live microbial cells, and light. In the absence of any one of these things, hydrogen is not produced. These initial results show that a microorganism can directly convert light energy to chemical energy, aided by reducing equivalents provided by an electrode.

Introduction

Renewable energy sources, such as solar energy, have the capacity to supply the current and future global energy demands.[1] Unfortunately, solar energy is inherently intermittent and current technologies for energy capture, conversion for storage as fuel, and further conversion of fuel to energy are inefficient and lack methods for implementation on an industrial scale. A promising although relatively young method for storing renewable energy is the process of microbial electrosynthesis in which electrons, optimistically derived from renewable energy, are delivered to a cathode for incorporation into microbial metabolic pathways and storage as metabolic products.[2]

Microbial electrosynthesis is the reverse of the more widely known anodic respiration, a process in which an inorganic substrate (electrode) acts as the terminal electron acceptor for a growing biofilm of bacteria under anaerobic conditions.[3,4] Whereas anodic respiration is exploited in microbial fuel cells to generate electricity from inexpensive electron sources, electrosynthesis offers the means to use excess electricity to produce a chemical product.

Two types of chemical transformations catalyzed by microorganisms are of particular interest for microbial electrosynthesis: 1) reduction of CO_2 and its incorporation into carbon chains, and 2) reversible reduction of protons to hydrogen. Using intact microorganisms for chemical synthesis instead of isolated enzymes or pathways has the advantage that microorganisms provide a mechanism to continuously replace damaged or inhibited proteins. Thus electrosynthesis may prove interesting in a number of applications.

Biocathodes have been described using both enzymes and intact microbial cells. For example, Guan and co-workers showed that laccase, an enzyme capable of continuous oxygen reduction, containing unnatural amino acids for site-specific use of click chemistry for immobilization at carbon nanotubes, can be immobilized at carbon nanotubes in an orientation favoring rapid electron transfer, stable current generation, and the electrodes showed only 15% decrease in activity after one week of incubation in a buffered solution.[5] Rasmussen and co-workers used a bioanode composed of thylakoid membranes and a laccase biocathode to demonstrate simultaneous water oxidation and oxygen reduction in the same electrochemical cell.[6] The examples above relied on using the biocathode as an electron sink for the reaction $4e^- + 4H^+ + O_2 \rightarrow 2H_2O$. However,

other reactions are possible. Nevin and co-workers showed that >80% of electrons passed from a cathode to a biofilm of the acetogenic bacterium *Clostridium ljungdahlii* could be incorporated into acetate.[7] Additionally, Pham and co-workers have shown that metabolites produced by one part of a microbial community, *Pseudomonas* sp., can be used by another organism, in this case the gram-positive bacterium *Brevibacillus* sp., to dramatically increase the observed electricity generation during anodic respiration.[8]

Anodic respiration provides a mechanism for organisms to employ the electrode as a terminal electron acceptor. In contrast, recent work from Yang shows that bacteria not natively capable of photosynthesis can be successfully photosensitized with CdS nanoparticles, which provide a mechanism for introducing extracellular electrons to metabolic processes.[9] In these experiments, acetogenic bacteria are incubated with CdS nanoparticles and a direct interaction between microorganism and the CdS nanoparticles can be observed using scanning electron microscopy. Additionally, Yang showed that CO_2 could be converted to acetic acid in the presence of light with reducing equivalents provided via CdS nanoparticles.[10] This work demonstrates the first example of self-photosensitization of a bacterium capable of using light energy to drive metabolic reactions.

Heliobacterium modesticaldum is an obligate anaerobic and thermophilic photoheterotroph with several interesting properties for electrosynthetic applications. First, they have genes for both [FeFe]-hydrogenase and [NiFe]-hydrogenase.[11] Second, they are capable of nitrogen fixation using a molybdenum-dependent, group I nitrogenase, an enzyme that also produces hydrogen under reducing conditions.[11] Furthermore, expression of the nitrogenase operon and an increase in nitrogenase activity

can be upregulated by growth without fixed nitrogen.[11,12] Third, the common electron carrier ferredoxin, which is reduced by the Heliobacterial reaction center (HbRC), is responsible for providing reducing equivalents for many different pathways including proton reduction via hydrogenase, ammonia and hydrogen production via nitrogenase, and carbon metabolism. Fifth, The HbRC is a homodimeric type I RC localized in the cellular membrane.[13] Advantageously, P800 of the HbRC is orientated towards the exterior of the cell and *H. modesticaldum* does not contain intracellular membranes such-as thylakoids or chlorosomes.[14] This simplified architecture should facilitate interaction with an extracellular mediator and electron uptake. Herein, we show that planktonic *H. modesticaldum*, is capable of extracellular electron uptake (EEU) from a reduced redox mediator to generate photocurrent. Concomitantly, the system produces hydrogen gas, likely from the nitrogenase. **Figure 7-1** displays the photosynthetic reaction machinery of *H. modesticaldum* and depicts known electron transfer pathways, as well as, possible electron transfer pathways for the artificial dye employed in this study to produce photocurrent.

Methods

General. All reagents were of the highest grade commercially available and were used without further purification. Solutions for electrochemical experiments were prepared using purified water (resistivity = 18.2 M▶ cm^{-1}). The mixed buffer system (referred to as MMT) consists of 15 mM each of the following sodium salts: 2-(N-Morpholino)ethanesulfonic acid (MES), 3-(N-Morpholino)propanesulfonic acid (MOPS), and N-tris(Hydroxymethyl)methyl-3-aminopropanesulfonic acid (TAPS) and 0.1 M KCl as supporting electrolyte. The pH was adjusted to 6.5 using dilute hydrochloric acid. A

conventional three-electrode electrochemical cell was employed with a carbon cloth working electrode (generally 1.5 x 1.5 cm with the edges fixed with silicone glue (L.H. Dottie, Commerce, CA)), Ag/AgCl (3.5 M KCl) reference electrode, and a platinum counter electrode. The counter and reference electrodes were encased within glass sheaths equipped with CoralPor frits (BASi, West Lafayette, IN) and filled with 3.5 M KCl or MMT buffer, respectively. Illumination was provided by a custom 780 nm LED array (λ_{max} = 780 nm; Marubeni, Tokoyo, JP) connected to a programmable and variable power source or by 660 nm LEDs (λ_{max} = 660 nm; Hansatech, Kings Lynn, UK) connected to a variable power source. Mediators evaluated in this study are the sodium salts of toluidine blue O (TB) and methylene blue (MB), and the potassium salt of indigotetrasulfonate (ITS). All potentials are referenced to the standard hydrogen electrode using the equation $E_{SHE} = E_{Ag/AgCl} + 0.205$ V.[15] Controlled potential experiments were conducted with the working electrode poised at -0.35 or -0.02 V vs. SHE as indicated in the text accompanying the experiment. BChl *g* content was determined by UV-vis spectroscopy using the extinction coefficient of 110 mM^{-1} cm^{-1} at 788 nm and a mass of 785 g mol^{-1}.[16]

Heliobacterium modesticaldum *growth conditions*. *H. modesticaldum* were grown anaerobically under a nitrogen atmosphere in modified pyruvate yeast extract (PYE) without NH_4[12,17] under 780 nm light at 51°C to late exponential phase. Cells were harvested by centrifugation (10,000 RCF) and washed with MMT buffer twice before electrochemical experiments.

Saturation of the HbRC. Dependence of current consumption on light intensity was measured over the range 100 to 3400 µmol photons m^{-2} s^{-1}. Each experiment

maintained a constant cell density of *H. modesticaldum* (generally 100 – 200 μg BChl *g*) and 0.1 mM ITS. The electrochemical cell, under stationary conditions, was exposed to dark and light cycles of either 50 s or 45 min each. Stirred electrochemical cells were exposed to dark and light cycles of 20 min. Photocurrents were averaged over three dark to light cycles and are reported with error bars corresponding to one standard deviation.

Electrosynthetic hydrogen production by H. modesticaldum *in the presence of ITS*. In an anaerobic chamber (Vacuum Atmospheres Company; Hawthorne, CA) under nitrogen, a custom electrochemical cell was loaded with MMT buffer, 0.1 mM ITS, and *H. modesticaldum* (generally 100 – 200 μg BChl *g* equivalent) and sealed before removal from the chamber. The solution and headspace of the electrochemical cell was then saturated with argon by sparging for 15-30 min. The electrochemical cell was then illuminated by a 780 nm LED array, and the working electrode was poised at -0.35 V vs. SHE for 1 hr. Hydrogen evolution was monitored by gas chromatography (GC; SRI model 310 equipped with a 6' molecular sieve 13X packed column and Ar as the carrier gas for separation) using a thermal conductivity detector (TCD). The GC-TCD was calibrated using the peak area resulting from an injection of a known concentration of H_2 in N_2 and creating a standard curve for H_2 on a ppm basis. To sample headspace gas, a gas-tight syringe was purged of ambient air using Ar gas. Ar (500 μL) was injected into the sealed electrochemical cell *via* the gas-tight syringe before 500 μL was removed. Henry's law was used to calculate the concentration of dissolved H_2 from GC-TCD data. Analogous negative control experiments did not contain electrodes.

Results

Figure 7-2 shows a representative current trace from a chronoamperometry experiment containing *H. modesticaldum* in the presence of the redox mediator indigotetrasulfonate (ITS) and an electrode poised at -350 mV (all potentials are referenced to the standard hydrogen electrode, SHE). The system is cycled between light (780 nm) and dark conditions and the current difference is referred to as photocurrent. In the presence of light, the current becomes more negative, and a return from light to dark conditions results in less negative current. Three different redox mediators, methylene blue, toluidine blue O, and indigotetrasulfonate (ITS), were evaluated for their ability to promote EEU by *H. modesticaldum*. **Figure 7-3** shows the photocurrent produced in the presence of each of these mediators as a function of the quantity of BChl *g* in solution.

Figure 7-6 shows that photocurrent depends on four components: live *H. modesticaldum*, an appropriate redox mediator, an electrode poised at a potential more reducing than mediator employed, and light. Notably, photocurrent was not observed from *H. modesticaldum* in the presence of ITS at an electrode poised at a potential more positive than the reduction potential of the mediator, i.e. under conditions in which the mediator is oxidized. Additionally, *H. modesticaldum* cells which are harvested and immediately washed with MMT buffer, followed by an autoclave cycle, do not generate photocurrent in the presence of ITS and an appropriately poised electrode.

Figure 7-4 shows the effect of photon flux, in the range 0 to 3500 μE, on photocurrent. The photocurrent is derived from chronoamperometric data as the difference between the average current consumed over the entire light period and the average current consumed during the last 50 seconds of the dark period prior to

illumination. **Figure 7-4** shows that the photocurrent, for an electrochemical solution in the absence of mechanical stirring (black squares), depends linearly on photon flux up to ~650 μE, and it is independent of light intensities > 1100 μE with a half saturation intensity of approximately 260 ! E. Introduction of mechanical stirring via a "flea" stir bar produces greater photocurrent compared to a stationary solution up to light intensities ~1000 μE, **Figure 7-4** grey squares.

Electrosynthesis of hydrogen by H. modesticaldum. To determine whether photocurrent consumed by *H. modesticaldum* can be used in electrosynthetic production of hydrogen, bulk electrolysis experiments were undertaken in a sealed electrochemical cell under both Ar and N_2 atmospheres. **Figure 7-5** shows chronoamperometric data for representative electrosynthetic experiments, and **Table 7-1** summarizes the quantity of hydrogen produced under various experimental conditions. **Figure 7-6** shows that the photocurrent produced as well as electrosynthetic production of H_2 was greatest under an Ar atmosphere, 0.35 nmol H_2 μg^{-1} BChl *g* hr^{-1}, with a Faradaic efficiency of 52±16%, while an N_2 atmosphere yielded 0.2 nmol H_2 μg^{-1} BChl *g* hr^{-1} and a Faradaic efficiency of 20±4%.

Discussion

Photocurrent production with H. modesticaldum. The results show that photocurrent can be generated from *H. modesticaldum* in the presence of a soluble redox mediator. Each mediator has optical absorbances near 625 nm that prevent direct quantification of cell density so the [BChl *g*] present in solution was used as a proxy for cellular density. To optimize the electrochemical system, photocurrents produced in the presence of indigotetrasulfonate, methylene blue, and toluidine blue O were directly

compared and under the conditions tested, experiments employing ITS provided demonstrably higher photocurrents than employing either of the other two mediators and was selected for use in all other experiments. Additionally, compared to the other two mediators, ITS carries a more negative charge and is expected to be localized in the electrochemical medium as the negative charges should prevent diffusion into the cellular interior of *H. modesticaldum*. As these experiments were completed with planktonic *H. modesticaldum* cells, it is of interest to note that although cyanobacteria, such as *Synechocystis* sp. PCC 6803, have the capacity to be immobilized at carbon cloth electrodes by application of a concentrated suspension followed by a brief drying period,[18] attempts to immobilize *H. modesticaldum* via the same procedure did not yield a photoactive system. Instead, *H. modesticaldum* immediately diffuses away from the electrode into the surrounding medium.

Saturation of photocurrent production. Photocurrent was linear up to a photon flux of ~650 μE and is independent of a photon flux above ~ 1100 μE. These light intensities may correspond to a saturation limit of the HbRC. Cereda and co-workers have shown that for the model cynanobacterium *Synechocystis* photocurrent plateaus at a light intensity of approximately 55 μE with half saturation at 30 μE, i.e. much lower than HbRC.[18] In terms of photosynthetic anatomy, whereas *H. modesticaldum* relies exclusivedly on the HbRC for photon harvesting and conversion to reducing equivalents, cyanobacteria, by comparison, employ extended antenna complexes to enable efficient photon harvesting. The electrochemical data may reflect the ability of cyanobacteria to harvest photons more effectively at low light.

Electrosynthetic production of H_2 by H. modesticaldum. Since hydrogen production by *H. modesticaldum* is thought to be catalyzed primarily by the molybdenum dependent group-I nitrogenase, expression was stimulated by anaerobic growth, under chemotrophic conditions, employing pyruvate as the sole electron source, and in the absence of ammonia. Catalysis by nitrogenase requires $8H^+$, $8e^-$, and 16 ATP, to reduce N_2 to $2NH_3$. Consequently, one molecule of H_2 is produced for every $2NH_3$ during the nitrogenase catalytic cycle. Due to this, in the absence of N_2, we hypothesized that hydrogen production would be greater under an atmosphere of argon as compared to nitrogen, since nitrogenase would reduce a greater quantity of protons in the absence of the natural substrate di-nitrogen. Comparing hydrogen produced under nitrogen or argon atmospheres shows that although more hydrogen was produced, on average, under an atmosphere of argon, **Table 7-1**, the data are not statistically significant. This results in comparable hydrogen production under Ar or N_2. Additionally, *H. modesticaldum* is known to express two other hydrogen related catalysts: a hydrogen evolving [FeFe]-hydrogenase and a hydrogen uptake [NiFe]-hydrogenase. Due to this, hydrogen production could also have been facilitated by an [FeFe]-hydrogenase, a process known to occur under pyruvate fermentation.[11] Also, expression of the [NiFe]-hydrogenase is thought to be related to a scavenging mechanism involed with nitrogenase, since H_2 is obligatorily produced during reduction of N_2, the [NiFe]-hydrogenase provides a means to collect electrons that would be otherwise wasted as H_2 is evolved from the system.

Conclusion

We have presented the first evidence that a photosynthetic organism, *H. modesticaldum*, is capable of extracellular electron uptake from an exogenous dye to

generate a chemical product, i.e. hydrogen. Catalysis likely occurs largely via a group I molybdenum-dependent nitrogenase, but the two hydrogenases encoded in the genome may also play a role. To distinguish these two possibilities, it is necessary either to create a targeted deletion mutant or to specifically inhibit one of the enzymes.

Figures

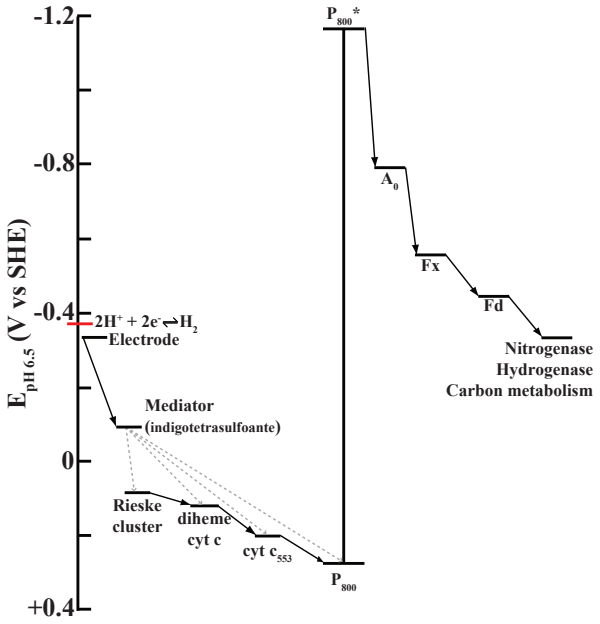

Figure 7-1. Midpoint potentials at pH 6.5 of the indigotetrasulfonate dye, the electron transfer machinery upstream of the HbRC, and the electron acceptors downstream of HbRC. Known and plausible electron transfer pathways are depicted as black solid and grey dashed lines, respectively.

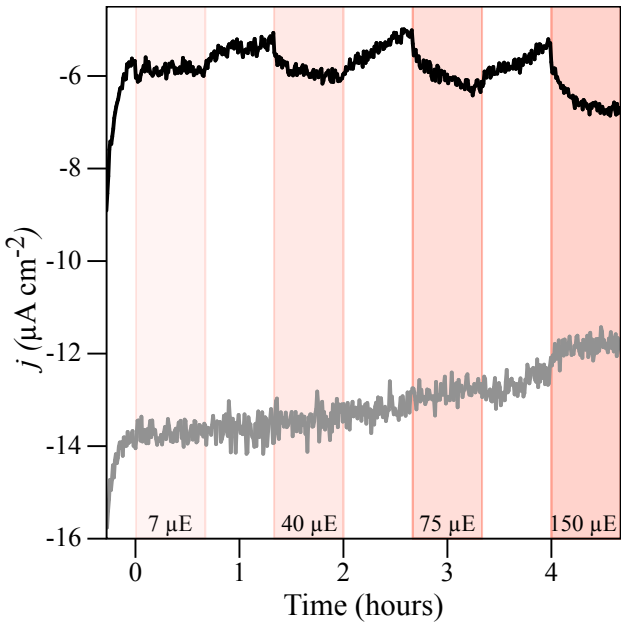

Figure 7-2. Chronoamperometric traces in light (red background) and dark (white background) conditions for only mediator (indigotetrasulfonate (ITS)) (grey trace) or *H. modesticaldum* in the presence of ITS (black trace). Values at the bottom of figure indicate the photon flux (μmol photons m^{-2} s^{-1}) during illumination. Experimental conditions: a stirred solution of MMT buffer (15 mM each of MES, MOPS, and TAPS buffered at pH 6.5, 0.1 M KCl), 0.1 mM ITS, under an Ar atmosphere, at room temperature. Each period of light or dark is 40 minutes, and the electrode is poised at -0.35 V.

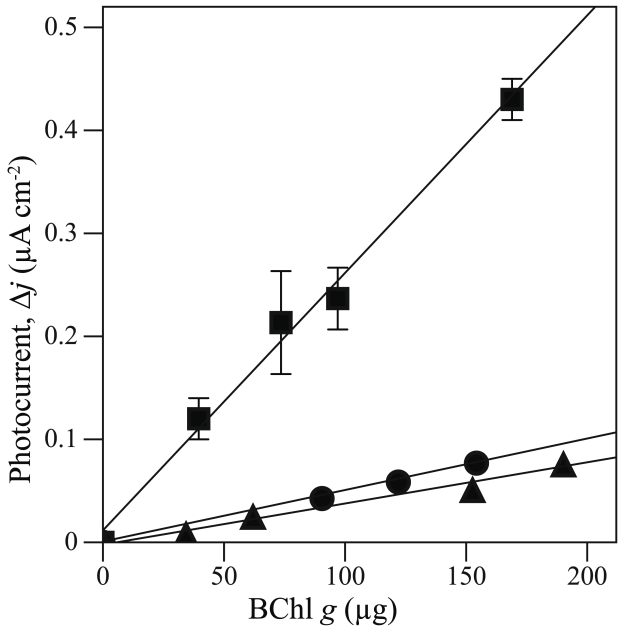

Figure 7-3. Dependence of photocurrent on the quantity of BChl *g* in the electrochemical cell using three different mediators: methylene blue (▲), toluidine blue O (●), and indigotetrasulfonate (■). Each point is the average of the photocurrent observed from three independent dark/light cycles. Solid lines are the lines of best fit. Error bars represent one standard deviation. Experimental conditions are equivalent to **Figure 7-2** with the exception that the quantity of BChl *g* was varied from 35 – 210 μg BChl *g* under a nitrogen atmosphere and the photon flux was 600 μE.

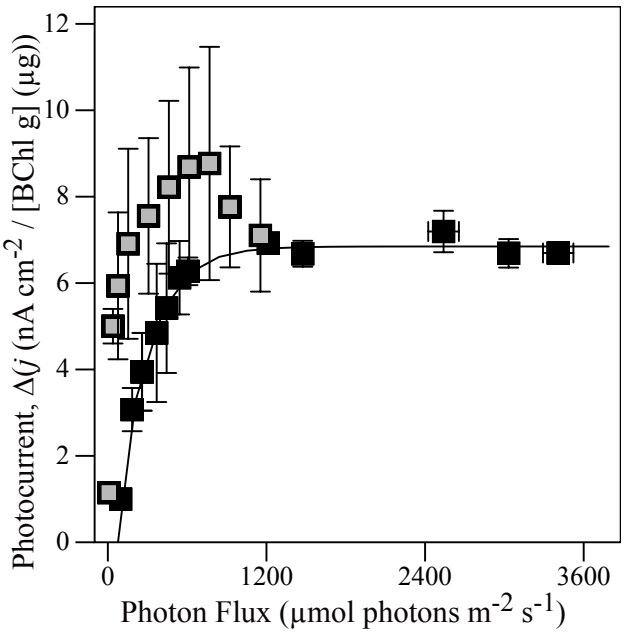

Figure 7-4. Dependence of photocurrent normalized to the quantity of BChl *g* on photon flux. Grey and black squares represent stirred and stationary solutions, respectively. Each point is the average of current derived from three independent dark/light cycles at the specified light intensity and error bars represent one standard deviation. Experimental conditions and buffer compositions are identical to **Figure 7-2**, with the exception that the light intensity is varied and the atmosphere for the black squares is either nitrogen or argon.

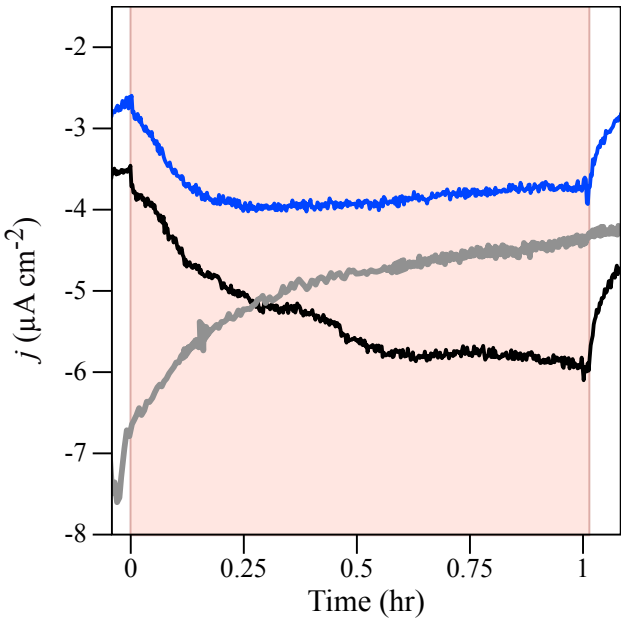

Figure 7-5. Photosynthetic current consumption at -350 mV vs. SHE by *H. modesticaldum*. Control experiment containing ITS in the absence of *H. modesticaldum* (grey trace) and experiments with *H. modesticaldum* in the presence of 0.1 M ITS under an atmosphere of Ar (black) or N_2 (blue). Red background indicates illumination with 600 μE and white background denotes a period of darkness. Other experimental conditions are as noted in **Figure 7-2**.

Table 7-1. Quantity of hydrogen produced photo-electrochemically by *H. modesticaldum* under a variety of conditions

No electrode, no applied potential[c]		
Argon atmosphere[a]	**Light (nmol H_2/µg BChl *g*)**	**Dark (nmol H_2/µg BChl *g*)**
H. modesticaldum (-NH_4)	0	0
H. modesticaldum (-NH_4) + ITS	0	0
With electrode poised at -350 mV		
Argon atmosphere	**Light**	**Dark**
ITS	0	ND
H. modesticaldum (-NH_4)	0	0
H. modesticaldum (-NH_4) + ITS[b]	0.35±0.07	0
H. modesticaldum (+NH_4) + ITS	0	0
Nitrogen atmosphere	**Light**	**Dark**
H. modesticaldum (-NH_4) + ITS[b]	0.2±0.1	0

[a]Experimental conditions are equivalent to **Figure 7-2** with the exception that the illuminated periods (600 µE) were 1 hr.
[b]Faradaic efficiencies for –NH_4 cells under an atmosphere of Ar or N_2 are 52±16% and 20±4%, respectively.
[c]Experiments without applied potential were incubated for 1 hr under the designated experimental conditions without any electrochemical equipment.

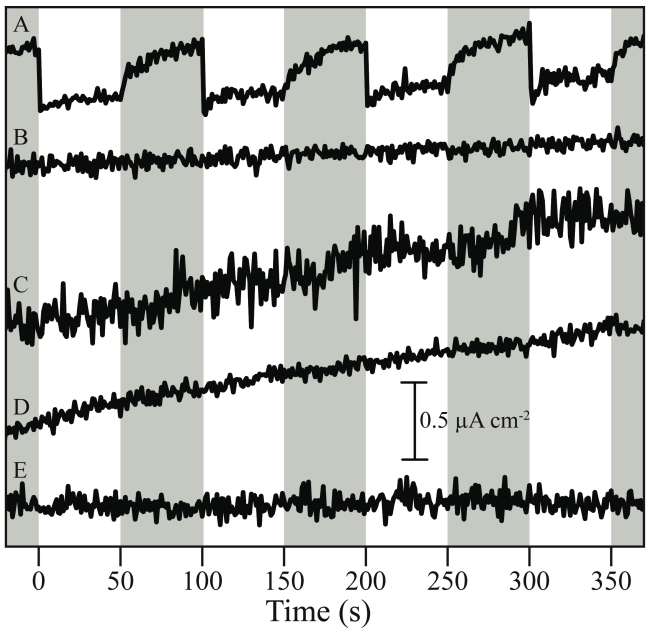

Figure 7-6. Chronoamperometric traces highlighting the requirement of active *H. modesticaldum*, mediator, and an electrode poised at the appropriate potential for observation of catalytic hydrogen production. A) *H. modesticaldum* in the presence of indigotetrasulfonate (ITS). B) *H. modesticaldum* in the absence of a mediator. C) ITS in the absence of *H. modesticaldum*. D) *H. modesticaldum* in the presence of ITS at an applied potential of -20 mV. E) Heat inactivated *H. modesticaldum* and 0.1 mM ITS. Experimental conditions: 15 mM each MES, MOPS, TAPS buffer, pH 6.5, Ar atmosphere, 780 nm LED array at 600 μE m^{-2} s^{-1}, and the electrode is poised at -350 mV (except panel D).

References

1. Blankenship, R. E. *et al.* Comparing Photosynthetic and Photovoltaic Efficiencies and Recognizing the Potential for Improvement. *Science.* **332,** 805–809 (2011).

2. Nevin, K. P. *et al.* Electrosynthesis of Organic Compounds from Carbon Dioxide Is Catalyzed by a Diversity of Acetogenic Microorganisms. *Appl. Environ. Microb.* **77,** 2882–2886 (2011).

3. Torres, C. I. *et al.* A kinetic perspective on extracellular electron transfer by anode-respiring bacteria. *FEMS Microbiol. Rev.* **34,** 3–17 (2010).

4. El-Naggar, M. Y. *et al.* Electrical transport along bacterial nanowires from *Shewanella oneidensis* MR-1. *Proc. Natl. Acad. Sci. U.S.A.* **107,** 18127–18131 (2010).

5. Guan, D., Kurra, Y., Liu, W. & Chen, Z. A click chemistry approach to site-specific immobilization of a small laccase enables efficient direct electron transfer in a biocathode. *Chem. Commun.* **51,** 2522–2525 (2015).

6. Rasmussen, M., Shrier, A. & Minteer, S. D. High performance thylakoid bio-solar cell using laccase enzymatic biocathodes. *Phys. Chem. Chem. Phys.* **15,** 9062 (2013).

7. Nevin, K. P. *et al.* Anode Biofilm Transcriptomics Reveals Outer Surface Components Essential for High Density Current Production in *Geobacter sulfurreducens* Fuel Cells. *PLoS ONE.* **4,** e5628 (2009).

8. Pham, T. H. *et al.* Metabolites produced by *Pseudomonas* sp. enable a Gram-positive bacterium to achieve extracellular electron transfer. *Appl. Microbiol. Biotechnol.* **77,** 1119–1129 (2007).

9. Sakimoto, K. K., Wong, A. B. & Yang, P. Self-photosensitization of nonphotosynthetic bacteria for solar-to-chemical production. *Science.* **351,** 74–77 (2015).

10. Kornienko, N., Sakimoto, K. K., Herlihy, D. M., Nguyen, S. C., Alivisatos, A. P., Harris, C. B., Schwartberg, A. Yang, P. (2016). Spectroscopic elucidation of energy transfer in hybrid inorganic–biological organisms for solar-to-chemical production. *Proc. Natl. Acad. Sci. U.S.A.* ***113***(42), 11750–11755..

11. Sattley, W. M. *et al.* The Genome of Heliobacterium modesticaldum, a Phototrophic Representative of the Firmicutes Containing the Simplest Photosynthetic Apparatus. *J. Bacteriol.* **190,** 4687–4696 (2008).

12. Kimble, L. K. & Madigan, M. T. Nitrogen fixation and nitrogen metabolism in

Heliobacteria. *Arch. Microbiol.* **158,** 155–161 (1992).

13. Heinnickel, M. & Golbeck, J. H. *Heliobacterial* photosynthesis. *Photosynth. Res.* **92,** 35–53 (2007).

14. Kimble, L. K., Mandelco, L., Woese, C. R. & Madigan, M. T. *Heliobacterium modesticaldum*, sp. nov., a thermophilic *Heliobacterium* of hot springs and volcanic soils. *Arch. Microbiol.* **163,** 259–267 (1995).

15. Bard, A. J. & Faulkner, L. R. (Wiley).

16. Kleinherenbrink, F. A. M. & Amesz, J. Stoichiometries and rates of electron transfer and charge recombination in *Heliobacterium chlorum*. *BBA - Bioenergetics.* **1143,** 77–83

17. Sarrou, I. *et al.* Purification of the photosynthetic reaction center from *Heliobacterium modesticaldum*. *Photosynth. Res.* **111,** 291–302 (2012).

18. Cereda, A. *et al.* A Bioelectrochemical Approach to Characterize Extracellular Electron Transfer by *Synechocystis* sp. PCC6803. *PLoS ONE.* **9**(3)

Chapter 8

Conclusion

Joseph A. Laureanti

School of Molecular Sciences
Arizona State University, Tempe, AZ 85287

This dissertation is focused in two areas: synthesis and characterization of inorganic biomimetic proton reduction catalysts using spectroscopic and electrochemical techniques and electrochemical interrogation of photosynthetic microorganisms as a means to understand light driven production of reducing equivalents and chemicals.

Chapter 2 describes preparation of four asymmetric diiron complexes featuring redox active, chelating N-donor ligands, 2,2′-bipy and 2,2′-bpym, and two μ-dithiolate-bridges, 1,3-propanedithiolate (pdt) and 1,2-benzenedithiolate (bdt). Electrochemical studies show that both the pdt and bdt analogs containing 2,2′-bipy are electrocatalysts for hydrogen evolution from weak acid in organic solvent. However, analogs containing 2,2′-bpym are not electrocatalysts. These complexes may have lost activity because the 2,2′-bpym ring protonates at the second nitrogen site. Functionalization of this site may restore activity and could represent a future research direction. Furthermore, spectroscopic and electrochemical data showed that replacing 2,2′-bipy with 2,2′-bpym reduces the electron density at the iron atoms. Future work will aim to produce diiron analogs containing redox active ligands that force greater geometric strain on the diiron site to promote a geometry that is more rotated and less eclipsed to weaken the Fe-Fe bond and enhance catalysis.

Chapter 3 describes three new pentacoordinated Fe^{II} carbonyls, all of which are trigonal bipyramidal (TBP) and capable of electrocatalytic proton reduction. Each complex is of the general form $[(\mu\text{-bdt})Fe(CO)(PPh_2)_2]$, where PPh_2 is one of the chelating bis-phosphines Xantphos, dppb, or dppv. Although each complex is a distorted TBP, the ligand arrangements are not equivalent. In the complexes with dppb or dppv, the CO is in the equatorial plane with the bdt and bis-phosphine ligands each occupying

one equatorial and one axial position. Conversely, in the complex employing Xantphos the CO is in an axial position. That means that although the bdt ligand in still in both an axial and an equatorial position, the Xantphos ligand occupies only equatorial positions. Interestingly, the catalytic activity in these complexes correlates directly with the bis-phosphine bite angle. Additionally, the complex with Xantphos proved to be the most stable catalyst. The stability of this complex may be due to the strained geometry that prevents effective delocalization of electron density into the HOMO of the bdt ligand. Future directions for this project will employ the use of bis-phosphine ligands that promote immobilization of the catalysts at a synthetic peptide chain or within a protein environment to investigate the role of a secondary coordination sphere on the activity and stability of the complexes during catalytic experiments.

Chapter 4 describes the preparation, catalytically relevant crystallographic intermediates, and electrochemical activity of a molybdenum pincer compound capable of electrocatalytic hydrogen evolution from water in a binary mixture of acetonitrile and water. Although the complex requires substantial overpotential for catalysis, the catalytic rate is an order of magnitude higher than previously reported for water reduction by a molybdenum-containing electrocatalyst.

Chapter 5 describes covalent immobilization of a small redox active molecule, ferrocenecarboxylic acid (FcCA), on a mercaptan reduced graphene oxide (mRGO) film. The FcCA is specifically immobilized via thioester formation between its carboxylic acid and the mRGO thiolates. Cyclic voltammetry of mRGO/FcCA electrode assemblies shows highly reversible transitions. Importanly, FcCA does not exhibit affinity for tRGO, the synthetic precursor to mRGO, and faradaic processes were not observed for

tRGO/FcCA electrode assemblies during cyclic voltammetry experiments. This indicates that the covalent interaction is necessary for the immobilization of the redox probe.

In **Chapter 6**, I describe the state of the art for microbial electrochemical systems and bioelectrochemical systems employing phototrophic organisms. Recent work has shown that the photocurrent produced in these systems can be directly derived from PSII and the water splitting reaction occurring there. However, further work is required to elucidate the electron transfer pathway from PSII to an electroactive surface.

In **Chapter 7**, I describe the first example of extracellular electron uptake by an anaerobic photoheterotroph, *Heliobacterium modesticaldum*. Photocurrent depends on an artificial dye, an electrode poised at an appropriately reducing potential, live *H. modesticaldum*, and the photon flux. Saturation of the HbRC is approximately ~1000 μE (μmol photons m^{-2} s^{-1}), with a ½ saturation point of 250 μE. Additionally, we show that *H. modesticaldum* cells grown in the presence of pyruvate and absence of fixed nitrogen evolve hydrogen in an electrochemical cell under controlled potential conditions. The group I, molybdenum-dependent nitrogenase is the likely source of hydrogen production. Thus it is surprising that the quantities of hydrogen produced under an atmosphere of argon or nitrogen are equivalent. Future studies will aim to distinguish the source of hydrogen production.

Bibliography

1. Dewar, M. J., & Storch, D. M. (1985). Alternative view of enzyme reactions. *P. Natl. Acad. Sci. USA*. ***82***(8), 2225–2229.

2. Warshel, A., Sharma, P. K., Kato, M., Xiang, Y., Liu, H., & Olsson, M. H. M. (2006). Electrostatic basis for enzyme catalysis. *Chem. Rev. 106*(8), 3210–3235. http://doi.org/10.1021/cr0503106.

3. Albery, W. J. & Knowles, J. R. (1976) Free-energy profile of the reaction catalyzed by triosephosphate isomerase. *Biochemistry.* **15,** 5627–5631.

4. Kedishvili, N. Y. *et al.* Expression and kinetic characterization of recombinant human stomach alcohol dehydrogenase. Active-site amino acid sequence explains substrate specificity compared with liver isozymes. *J. Biol. Chem.* **270,** 3625–3630 (1995).

5. Chambon, P. (1975). Eukaryotic nuclear RNA polymerases. *Annu. Rev. Biochem.* ***44***, 613–638. http://doi.org/10.1146/annurev.bi.44.070175.003145.

6. Waldron, K. J., Rutherford, J. C., Ford, D. & Robinson, N. J. Metalloproteins and metal sensing. *Nature.* **460,** 823–830 (2009).

7. Shafaat, H. S., Rüdiger, O., Ogata, H. & Lubitz, W. *BBA - Bioenergetics.* **1827,** 986–1002 (2013).

8. Lubitz, W.; Ogata, H.; Rüdiger, O.; Reijerse, E. Hydrogenases. *Chem. Rev*. **114,** 4081–4148 (2014).

9. Frey, M. Hydrogenases: hydrogen-activating enzymes. (2002) *Chem. Eur. J. of Chem. Bio.* **3,** 153–160

10. Wang, X. *et al.* The iron centre of the cluster-free hydrogenase (Hmd): low-spin Fe(ii) or low-spin Fe(0)? *Chem Commun.* **3555** (2008). doi:10.1039/b805262j

11. Salomone-Stagni, M. *et al.* The iron-site structure of [Fe]-hydrogenase and model systems: an X-ray absorption near edge spectroscopy study. *Dalton T.* **39,** 3057 (2010).

12. Guo, Y. *et al.* Characterization of the Fe Site in Iron−Sulfur Cluster-Free Hydrogenase (Hmd) and of a Model Compound via Nuclear Resonance Vibrational Spectroscopy (NRVS). *Inorg. Chem.* **47,** 3969–3977 (2008).

13. Shima, S. & Ataka, K. Isocyanides inhibit [Fe]-hydrogenase with very high affinity. *FEBS Lett.* **585,** 353–356 (2010).

14. Vignais, P. M., Billoud, B., & Meyer, J. (2001). Classification and phylogeny of hydrogenases. *FEMS Microbiol. Rev.* ***25***(4), 455–501.

15. Vignais, P. M. & Billoud, B. Occurrence, Classification, and Biological Function of Hydrogenases: An Overview. *Chem. Rev.* **107,** 4206–4272 (2007).

16. Tamagnini, P. *et al.* Hydrogenases and Hydrogen Metabolism of Cyanobacteria. *Microbiol. Mol. Biol. R.* **66,** 1–20 (2002).

17. Tamagnini, P. *et al.* Cyanobacterial hydrogenases: diversity, regulation and applications. *FEMS Microbiol. Rev.* **31,** 692–720 (2007).

18. Thauer, R. K. *et al.* Hydrogenases from Methanogenic Archaea, Nickel, a Novel Cofactor, and H_2 Storage. *Annu. Rev. Biochem.* **79,** 507–536 (2010).

19. Goris, T. *et al.* A unique iron-sulfur cluster is crucial for oxygen tolerance of a [NiFe]-hydrogenase. *Nat. Chem. Biol.* **7,** 310–318 (2011).

20. Abou Hamdan, A. *et al.* O_2-independent formation of the inactive states of NiFe hydrogenase. *Nat. Chem. Biol.* **9,** 15–17 (2012).

21. Nicolet, Y., Piras, C., Legrand, P., Hatchikian, C. E. & Fontecilla-Camps, J. C. *Desulfovibrio desulfuricans* iron hydrogenase: the structure shows unusual coordination to an active site Fe binuclear center. *Structure* **7,** 13–23 (1999).

22. Tard, C. & Pickett, C. J. Structural and Functional Analogues of the Active Sites of the [Fe]-, [NiFe]-, and [FeFe]-Hydrogenases. *Chem. Rev.* **109,** 2245–2274 (2009).

23. Peters, J. W., Lanzilotta, W. N., Lemon, B. J. & Seefeldt, L. C. (1998) X-ray crystal structure of the Fe-only hydrogenase (CpI) from *Clostridium pasteurianum* to 1.8 angstrom resolution. *Science.* **282,** 1853–1858

24. Berk, R. S. & Canfield, J. H. Bioelectrochemical energy conversion. *Appl. Microbiol.* (1964).

25. Hernandez, M. E. & Newman, D. K. Extracellular electron transfer. *Cell. Mol. Life Sci.* (2001).

26. Lovley, D. R. *et al. Geobacter metallireducens* gen. nov. sp. nov., a microorganism capable of coupling the complete oxidation of organic compounds to the reduction of iron and other metals. *Arch. Microbiol*. **159,** 336–344 (1993).

27. Torres, C. I. *et al.* A kinetic perspective on extracellular electron transfer by anode-respiring bacteria. *FEMS Microbiol. Rev.* **34,** 3–17 (2010).

28. Smith, J. A. *et al.* Going Wireless: Fe(III) Oxide Reduction without Pili by *Geobacter sulfurreducens* Strain JS-1. *Appl. Environ. Microb.* **80,** 4331–4340 (2014).

29. Lovley, D. R. Bug juice: harvesting electricity with microorganisms. *Nat. Rev. Micro.* **4,** 497–508 (2006).

30. Yates, M. D. *et al.* Measuring conductivity of living *Geobacter sulfurreducens* biofilms. *Nat. Nanotechnol.* **11,** 910–913 (2016).

31. Pirbadian, S. *et al. Shewanella oneidensis* MR-1 nanowires are outer membrane and periplasmic extensions of the extracellular electron transport components. *P. Natl. Acad. Sci. USA*. **111,** 12883–12888 (2014).

32. Yang, Y. *et al.* Enhancing Bidirectional Electron Transfer of *Shewanella oneidensis* by a Synthetic Flavin Pathway. *ACS Synth. Biol.* **4,** 815–823 (2015).

33. Marsili, E. *et al. Shewanella* secretes flavins that mediate extracellular electron transfer. *P. Natl. Acad. Sci. USA*. **105,** 3968–3973 (2008).

34. Canstein, von, H., Ogawa, J., Shimizu, S. & Lloyd, J. R. Secretion of Flavins by *Shewanella* Species and Their Role in Extracellular Electron Transfer. *Appl. Environ. Microb.* **74,** 615–623 (2008).

35. Xu, S., Jangir, Y. & El-Naggar, M. Y. Disentangling the roles of free and cytochrome-bound flavins in extracellular electron transport from *Shewanella oneidensis* MR-1. *Electrochim. Acta.* **198,** 49–55 (2016).

36. Gray, H. B. Powering the planet with solar fuel. *Nat. Chem.* **1,** 7–7 (2009).

37. Thapper, A. *et al.* Artificial Photosynthesis for Solar Fuels – an Evolving Research Field within AMPEA, a Joint Programme of the European Energy Research Alliance. *Green.* **3,** 43–57 (2013).

38. Fontecilla-Camps, J. C., Volbeda, A., Cavazza, C. & Nicolet, Y. Structure/function relationships of [NiFe]- and [FeFe]-hydrogenases. *Chem. Rev.* **107,** 4273–4303 (2007).

39. Lubitz, W., Ogata, H., Rüdiger, O. & Reijerse, E. Hydrogenases. *Chem. Rev.* **114,** 4081–4148 (2014).

40. Happe, R. P., Roseboom, W., Pierik, A. J., Albracht, S. P. J. & Bagley, K. A. Biological activition of hydrogen. *Nature.* **385,** 126–126 (1997).

41. Cammack, R., Frey, M. & Robson, R. *Hydrogen as a Fuel: Learning from Nature*. (Talor & Francis, 2001).

42. Frey, M. Hydrogenases: Hydrogen-activating enzymes. *Chem. Eur. J. of Chem. Bio.* **3,** 153–160 (2002).

43. Evans, D. J. & Pickett, C. J. Chemistry and the hydrogenases. *Chem. Soc. Rev.* **32,** 268–275 (2003).

44. Peters, J. W., Lanzilotta, W. N., Lemon, B. J. & Seefeldt, L. C. X-ray crystal structure of the Fe-only hydrogenase (CpI) from *Clostridium pasteurianum* to 1.8 angstrom resolution. *Science.* **282,** 1853–1858

45. Nicolet, Y., Piras, C., Legrand, P., Hatchikian, C. E. & Fontecilla-Camps, J. C. *Desulfovibrio desulfuricans* iron hydrogenase: the structure shows unusual coordination to an active site Fe binuclear center. *Structure.* **7,** 13–23 (1999).

46. Berggren, G. *et al.* Biomimetic assembly and activation of [FeFe]-hydrogenases. *Nature.* **499,** 66–69 (2013).

47. Adamska-Venkatesh, A. *et al.* Artificially maturated [FeFe] hydrogenase from *Chlamydomonas reinhardtii*: a HYSCORE and ENDOR study of a non-natural H-cluster. *Phys. Chem. Chem. Phys.* **17,** 5421–5430 (2015).

48. Gloaguen, F. & Rauchfuss, T. B. Small molecule mimics of hydrogenases: hydrides and redox. *Chem. Soc. Rev.* **38,** 100–108 (2009).

49. Heinekey, D. M. Hydrogenase enzymes: Recent structural studies and active site models. *J. Organomet. Chem.* **694,** 2671–2680 (2009).

50. Tard, C. & Pickett, C. J. Structural and Functional Analogues of the Active Sites of the [Fe]-, [NiFe]-, and [FeFe]-Hydrogenases. *Chem. Rev.* **109,** 2245–2274 (2009).

51. Simmons, T. R., Berggren, G., Bacchi, M., Fontecave, M. & Artero, V. Mimicking Hydrogenases: From Biomimetics to Artificial Enzymes. *Coordin. Chem. Rev.* **270–271,** 127–150 (2014).

52. Rauchfuss, T. B. Diiron Azadithiolates as Models for the [FeFe]-Hydrogenase Active Site and Paradigm for the Role of the Second Coordination Sphere. *Acc. Chem. Res.* **48,** 2107–2116 (2015).

53. Gan, L., Jennings, D., Laureanti, J. & Jones, A. K. in *Top. Organometal. Chem.* **59,** 233–272. Springer International Publishing, 2015.

54. Felton, G. A. N. *et al.* Review of electrochemical studies of complexes containing the Fe2S2 core characteristic of [FeFe]-hydrogenases including catalysis by these complexes of the reduction of acids to form dihydrogen. *J.Organomet. Chem.* **694,** 2681–2699 (2009).

55. Schwab, D. E. *et al.* On the electronic structure of the hydrogenase H-cluster. *Chem. Commun.* 3696–3698 (2006). doi:10.1039/b604994j

56. Tard, C. *et al.* Synthesis of the H-cluster framework of iron-only hydrogenase. *Nature.* **433,** 610–613 (2005).

57. Si, Y. *et al.* Non-innocent bma ligand in a dissymetrically disubstituted diiron dithiolate related to the active site of the [FeFe] hydrogenases. *J. Inorg. Biochem.* **104,** 1038–1042 (2010).

58. Camara, J. M. & Rauchfuss, T. B. Combining acid-base, redox and substrate binding functionalities to give a complete model for the [FeFe]-hydrogenase. *Nat. Chem.* **4,** 26–30 (2012).

59. Roy, S., Groy, T. L. & Jones, A. K. Biomimetic model for [FeFe]-hydrogenase: asymmetrically disubstituted diiron complex with a redox-active 2,2'-bipyridyl ligand. *Dalton T.* **42,** 3843–3853 (2013).

60. Lansing, J. C., Camara, J. M., Gray, D. E. & Rauchfuss, T. B. Hydrogen Production Catalyzed by Bidirectional, Biomimetic Models of the [FeFe]-Hydrogenase Active Site. *Organometallics.* **33,** 5897–5906 (2014).

61. Roy, S. *et al.* Catalytic Hydrogen Evolution by Fe(II) Carbonyls Featuring a Dithiolate and a Chelating Phosphine. *Inorg. Chem.* **53,** 8919–8929 (2014).

62. Karnahl, M. *et al.* Mixed-valence [FeIFeII] hydrogenase active site model complexes stabilized by a bidentate carborane bis-phosphine ligand. *Dalton T.* **41,** 12468–12477 (2012).

63. Ghosh, S. *et al.* Hydrogenase biomimetics: $Fe_2(CO)_4$(dppf)(μ-pdt) (dppf = 1,1'-bis(diphenylphosphino)ferrocene) both a proton-reduction and hydrogen oxidation catalyst. *Chem. Commun.* **50,** 945–947 (2014).

64. Hsieh, C.-H. *et al.* Redox active iron nitrosyl units in proton reduction electrocatalysis. *Nat. Commun.* **5,** (2014).

65. Allgeier, A. M. & Mirkin, C. A. Ligand design for electrochemically controlling stoichiometric and catalytic reactivity of transition metals. *Angew. Chem. Int. Ed.* **37,** 894–908 (1998).

66. Liu, Y.-C., Yen, T.-H., Chu, K.-T. & Chiang, M.-H. Utilization of Non-Innocent Redox Ligands in [FeFe] Hydrogenase Modeling for Hydrogen Production. *Comment. Inorg. Chem.* **36,** 141–181 (2016).

67. Balzani, V., Juris, A., Venturi, M., Campagna, S. & Serroni, S. Luminescent and Redox-Active Polynuclear Transition Metal Complexes. *Chem. Rev.* **96,** 759–834 (1996).

68. Kaes, C., Katz, A. & Hosseini, M. W. Bipyridine: The Most Widely Used Ligand. A Review of Molecules Comprising at Least Two 2,2'-Bipyridine Units. *Chem. Rev.* **100,** 3553–3590 (2000).

69. Armentano, D. *et al.* 2,2'-Bipyrimidine- and 2,3-bis(2-pyridyl)pyrazine-containing manganese(ii) compounds: structural and magnetic properties. *Dalton T.* 4626–4634 (2003). doi:10.1039/b311007a

70. Concepcion, J. J. *et al.* Making Oxygen with Ruthenium Complexes. *Acc. Chem. Res.* **42,** 1954–1965 (2009).

71. Ernst, S. & Kaim, W. Coordination characteristics of four isomeric .alpha.-diimine ligands. .pi. Molecular orbital perturbation calculations for the bidiazines and their correlation with the properties of group 6 metal carbonyl complexes. *J. Am. Chem. Soc.* **108,** 3578–3586 (1986).

72. Tye, J. W., Darensbourg, M. Y. & Hall, M. B. De novo design of synthetic di-iron(I) complexes as structural models of the reduced form of iron-iron hydrogenase. *Inorg. Chem.* **45,** 1552–1559 (2006).

73. Eisenberg, R. & Gray, H. B. Noninnocence in Metal Complexes: A Dithiolene Dawn. *Inorg. Chem.* **50,** 9741–9751 (2011).

74. Capon, J.-F., Gloaguen, F., Schollhammer, P. & Talarmin, J. Electrochemical proton reduction by thiolate-bridged hexacarbonyldiiron clusters. *J. Electroanal. Chem.* **566,** 241–247 (2004).

75. Capon, J.-F., Gloaguen, F., Schollhammer, P. & Talarmin, J. Activation of proton by the two-electron reduction of a di-iron organometallic complex. *J. Electroanal. Chem.* **595,** 47–52 (2006).

76. Schwartz, L. *et al.* Influence of an electron-deficient bridging o-carborane on the electronic properties of an [FeFe] hydrogenase active site model. *Dalton T.* 2379–2381 (2008). doi:10.1039/B802908N

77. Schwartz, L., Singh, P. S., Eriksson, L., Lomoth, R. & Ott, S. Tuning the electronic properties of Fe_2(μ-arenedithiolate)$(CO)_6$−n(PMe_3)n (n=0, 2) complexes

related to the [Fe–Fe]-hydrogenase active site. *C.R. Chim.* **11,** 875–889 (2008).

78. Ezzaher, S., Gogoll, A., Bruhn, C. & Ott, S. Directing protonation in [FeFe] hydrogenase active site models by modifications in their second coordination sphere. *Chem. Commun.* **46,** 5775–5777 (2010).

79. Ezzaher, S. *et al.* Diiron chelate complexes relevant to the active site of the iron-only hydrogenase. *C.R. Chim.* **11,** 906–914 (2008).

80. Kaur-Ghumaan, S., Schwartz, L., Lomoth, R., Stein, M. & Ott, S. Catalytic Hydrogen Evolution from Mononuclear Iron(II) Carbonyl Complexes as Minimal Functional Models of the [FeFe] Hydrogenase Active Site. *Angew. Chem. Int. Ed. Engl.* **49,** 8033–8036 (2010).

81. Beyler, M. *et al.* Pentacoordinate iron complexes as functional models of the distal iron in [FeFe] hydrogenases. *Chem. Commun.* **47,** 11662 (2011).

82. Gao, S. *et al.* Di/mono-nuclear iron(i)/(ii) complexes as functional models for the 2Fe2S subunit and distal Fe moiety of the active site of [FeFe] hydrogenases: protonations, molecular structures and electrochemical properties. *Dalton T.* **41,** 12064–12074 (2012).

83. Cabeza, J. A., Martínez-García, M. A., Riera, V., Ardura, D. & García-Granda, S. Binuclear Iron(I), Ruthenium(I), and Osmium(I) Hexacarbonyl Complexes Containing a Bridging Benzene-1,2-dithiolate Ligand. Synthesis, X-ray Structures, Protonation Reactions, and EHMO Calculations. *Organometallics* **17,** 1471–1477 (1998).

84. Lyon, E. J., Georgakaki, I. P., Reibenspies, J. H. & Darensbourg, M. Y. Carbon Monoxide and Cyanide Ligands in a Classical Organometallic Complex Model for Fe-Only Hydrogenase. *Angew. Chem. Int. Ed. Engl.* **38,** 3178–3180

85. Irwin, M. *et al.* Experimental and Computational Study of the Structural and Electronic Properties of Fe-II(2,2 '-bipyridine)(mes)(2) and [Fe-II(2,2'-bipyridine)(mes)(2)](-), a Complex Containing a 2,2'-Bipyridyl Radical Anion. *Inorg. Chem.* **49,** 6160–6171 (2010).

86. Fernholt, L., Rømming, C. & Samdal, S. On the Structure of 2,2'-Bipyrimidine. Gas and Solid Phase Structure and Barrier to Internal Rotation. *Acta Chem. Scand. A.* **35A,** 707–715 (1981).

87. Gore-Randall, E., Irwin, M., Denning, M. S. & Goicoechea, J. M. Synthesis and Characterization of Alkali-Metal Salts of 2,2′- and 2,4′-Bipyridyl Radicals and Dianions. *Inorg. Chem.* **48,** 8304–8316 (2009).

88. Justice, A. K. *et al.* Chelate control of diiron(I) dithiolates relevant to the [Fe-Fe]-hydrogenase active site. *Inorg. Chem.* **46,** 1655–1664 (2007).

89. Orain, P.-Y. *et al.* Use of 1,10-phenanthroline in diiron dithiolate derivatives related to the [Fe-Fe] hydrogenase active site. *Dalton T.* 3754–3756 (2007). doi:10.1039/b709287c

90. Ezzaher, S. *et al.* Evidence for the formation of terminal hydrides by protonation of an asymmetric iron hydrogenase active site mimic. *Inorg. Chem.* **46,** 3426–3428 (2007).

91. Palmer, R. A. & Piper, T. S. 2,2‘-Bipyridine complexes. I. Polarized crystal spectra of tris(2,2’-bipyridine)copper(II), -nickel(II), -cobalt(II), -iron(II), and -ruthenium(II). *Inorg. Chem.* **5,** 864–& (1966).

92. Zhao, J., Wei, Z., Zeng, X. & Liu, X. Three diiron complexes bearing an aromatic ring as mimics of the diiron subunit of [FeFe]-hydrogenase: synthesis, electron transfer and coupled chemical reactions. *Dalton T.* **41,** 11125–11133 (2012).

93. Felton, G. A. N. *et al.* Hydrogen Generation from Weak Acids: Electrochemical and Computational Studies of a Diiron Hydrogenase Mimic. *J. Am. Chem. Soc.* **129,** 12521–12530 (2007).

94. Fourmond, V., Jacques, P.-A., Fontecave, M. & Artero, V. H_2 Evolution and Molecular Electrocatalysts: Determination of Overpotentials and Effect of Homoconjugation. *Inorg. Chem.* **49,** 10338–10347 (2010).

95. Capon, J.-F. *et al.* Electrochemical and theoretical investigations of the reduction of $[Fe_2(CO)_5L\{\mu\text{-}SCH_2XCH_2S\}]$ complexes related to [FeFe] hydrogenase. *New J. Chem.* **31,** 2052–2064 (2007).

96. Roy, S., Nguyen, T.-A. D., Gan, L. & Jones, A. K. Biomimetic peptide-based models of [FeFe]-hydrogenases: utilization of phosphine-containing peptides. *Dalton T.* **44,** 14865–14876 (2015).

97. Gloaguen, F. Electrochemistry of Simple Organometallic Models of Iron–Iron Hydrogenases in Organic Solvent and Water. *Inorg. Chem.* **55,** 390–398 (2016).

98. Donovan, E. S., McCormick, J. J., Nichol, G. S. & Felton, G. A. N. Cyclic Voltammetric Studies of Chlorine-Substituted Diiron Benzenedithiolato Hexacarbonyl Electrocatalysts Inspired by the [FeFe]-Hydrogenase Active Site. *Organometallics.* **31,** 8067–8070 (2012).

99. Saveant, J.-M. Molecular Catalysis of Electrochemical Reactions. Mechanistic Aspects. *Chem. Rev.* **108,** 2348–2378 (2008).

100. Lyon, E. J., Georgakaki, I. P., Reibenspies, J. H. & Darensbourg, M. Y. Carbon monoxide and cyanide ligands in a classical organometallic complex model for Fe-only hydrogenase. *Angew. Chem. Int. Ed.* **38,** 3178–3180 (1999).

101. Zhao, J., Wei, Z., Zeng, X. & Liu, X. Three diiron complexes bearing an aromatic ring as mimics of the diiron subunit of [FeFe]-hydrogenase: synthesis, electron transfer and coupled chemical reactions. *Dalton T.* **41,** 11125 (2012).

102. Morvan, D. *et al.* N-heterocyclic carbene ligands in nonsymmetric diiron models of hydrogenase active sites. *Organometallics.* **26,** 2042–2052 (2007).

103. Tokel-Takvoryan, N. E., Hemingway, R. E. & Bard, A. J. Electrogenerated chemiluminescence. XIII. Electrochemical and electrogenerated chemiluminescence studies of ruthenium chelates. *J. Am. Chem. Soc.* **95,** 6582–6589 (1973).

104. Ohsawa, Y., Hanck, K. W. & DeArmond, M. K. A systematic electrochemical and spectroscopic study of mixed-ligand ruthenium(II) 2,2'-bipyridine complexes $[Ru(bpy)_3\text{-}nLn]^{2+}$ (n=0,1,2 and 3). *J. Electroanal. Chem. Inter. Electrochem.* **175,** 229–240 (1984).

105. Chong, D. *et al.* Electrocatalysis of hydrogen production by active site analogues of the iron hydrogenase enzyme: structure/function relationships. *Dalton T.* 4158–4163 (2003). doi:10.1039/B304283A

106. Liaw, W.-F.; Lee, N.-H.; Chen, C.-H.; Lee, C.-M.; Lee, G.-H.; Peng, S.-M. *J. Amer. Chem. Soc.* **2000**, *122* (3), 488.

107. Sellmann, D., Kleine-Kleffmann, U., & Zapf, L. (1984). *J. Organomet. Chem.* (263), 321–331.

108. Rauchfuss, T. B.; Contakes, S. M.; Hsu, S. C. N.; Reynolds, M. A.; Wilson, S. R. *J. Amer. Chem. Soc.* **2001**, *123* (28), 6933.

109. Gardner, J. M.; Beyler, M.; Karnahl, M.; Tschierlei, S.; Ott, S.; Hammarström, L. *J. Amer. Chem. Soc.* **2012**, *134* (47), 19322.

110. Orthaber, A.; Karnahl, M.; Tschierlei, S.; Streich, D.; Stein, M.; Ott, S. *Dalton T.* **2014**, *43* (11), 4537.

111. Roy, S.; Mazinani, S. K. S.; Groy, T. L.; Gan, L.; Tarakeshwar, P.; Mujica, V.; Jones, A. K. *Inorg. Chem.* **2014**, 140811095919002.

112. Ray, K.; Weyhermüller, T.; Goossens, A.; Crajé, M. W. J.; Wieghardt, K. *Inorg.*

Chem. **2003**, *42* (13), 4082.

113. Gan, L.; Groy, T. L.; Tarakeshwar, P.; Mazinani, S. K. S.; Shearer, J.; Mujica, V.; Jones, A. K. *J. Amer. Chem. Soc.* **2015**, *137* (3), 1109.

114. Kamer, P. C., van Leeuwen, P. W., & Reek, J. N. (2001). Wide bite angle diphosphines: xantphos ligands in transition metal complexes and catalysis. *Accounts Chem. Res. 34*(11), 895–904. http://doi.org/10.1021/ar000060.

115. Eady, S. C.; Breault, T.; Thompson, L.; Lehnert, N. *Dalton T.* **2016**, *45* (3), 1138.

116. Addison, A. W.; Rao, T. N.; Reedijk, J.; van Rijn, J.; Verschoor, G. C. *Dalton T.* **1984**, No. 7, 1349.

117. Ray, K.; Weyhermüller, T.; Neese, F.; Wieghardt, K. *Inorg. Chem.* **2005**, *44* (15), 5345.

118. Barrón, D.; Butí, S.; Ruiz, M.; Barbosa, J. *Phys. Chem. Chem. Phys.* **1999**, *1* (2), 295.

119. Fourmond, V.; Jacques, P.-A.; Fontecave, M.; Artero, V. *Inorg. Chem.* **2010**, *49* (22), 10338.

120. Helm, M. L.; Stewart, M. P.; Bullock, R. M.; DuBois, M. R.; DuBois, D. L. *Science.* **2011**, *333* (6044), 863.

121. Neese, F. In ORCA - an ab initio, density functional and semiempirical program package, MPI for Chemical Energy Conversion.

122. Becke, A. (1988). Density-functional exchange-energy approximation with correct asymptotic behavior. *Phys. Rev., A-Gen. Phys*. ***38***(6), 3098–3100.

123. Perdew, J.; Yue, W. *Phys. Rev., B Condens. Matter* **1986**, *33* (12), 8800.

124. van Wüllen, C. *J. Chem. Phys.* **1998**, *109* (2), 392.

125. Pantazis, D. A.; Chen, X.-Y.; Landis, C. R.; Neese, F. *J. Chem. Theory. Comput.* **2008**, *4* (6), 908.

126. Grimme, S. Accurate description of van der Waals complexes by density functional theory including empirical corrections. *J. Comput. Chem.* **2004**, *25* (12), 1463.

127. Grimme, S. Semiempirical GGA-type density functional constructed with a long-range dispersion correction. *J. Comput. Chem.* **2006**, *27* (15), 1787.

128. Bard, A. J. & Fox, M. A. Artificial Photosynthesis: Solar Splitting of Water to Hydrogen and Oxygen. *Acc. Chem. Res.* **28,** 141–145 (1995).

129. Lewis, N. S. & Nocera, D. G. Powering the planet: chemical challenges in solar energy utilization. *P. Natl. Acad. Sci. U.S.A.* **103,** 15729–15735 (2006).

130. Gust, D., Moore, T. A. & Moore, A. L. Solar Fuels via Artificial Photosynthesis. *Acc. Chem. Res.* **42,** 1890–1898 (2009).

131. Esswein, A. J. & Nocera, D. G. Hydrogen Production by Molecular Photocatalysis. *Chem. Rev.* **107,** 4022–4047 (2007).

132. Walter, M. G. *et al.* Solar Water Splitting Cells. *Chem. Rev.* **110,** 6446–6473 (2010).

133. Thoi, V. S., Sun, Y., Long, J. R. & Chang, C. J. Complexes of earth-abundant metals for catalytic electrochemical hydrogen generation under aqueous conditions. *Chem. Soc. Rev.* **42,** 2388–2400 (2013).

134. Carmo, M., Fritz, D. L., Mergel, J. & Stolten, D. A comprehensive review on PEM water electrolysis. *Int. J. Hydrogen Energ.* **38,** 4901–4934 (2013).

135. Zee, D. Z., Chantarojsiri, T., Long, J. R. & Chang, C. J. Metal–Polypyridyl Catalysts for Electro- and Photochemical Reduction of Water to Hydrogen. *Acc. Chem. Res.* **48,** 2027–2036 (2015).

136. Nocera, D. G. The Artificial Leaf. *Acc. Chem. Res.* **45,** 767–776 (2012).

137. Du, P. & Eisenberg, R. Catalysts made of earth-abundant elements (Co, Ni, Fe) for water splitting: Recent progress and future challenges. *Energy Environ. Sci.* **5,** 6012 (2012).

138. DuBois, D. L. Development of Molecular Electrocatalysts for Energy Storage. *Inorg. Chem.* **53,** 3935–3960 (2014).

139. Silavwe, N. D., Bruce, M., Philbin, C. E. & Tyler, D. R. Descriptive photochemistry and electronic structure of the Cp2MoO and (MeCp) 2MoO complexes. *Inorg. Chem*. 1988.

140. Yoon, M. & Tyler, D. R. Activation of water by permethyltungstenocene; evidence for the oxidative addition of water. *Chem. Commun.* 639–670 (1997). doi:10.1039/a700087a

141. Baxley, G. T., Avey, A. A., Aukett, T. M. & Tyler, D. R. Photoactivation of water

by Cp′ 2 Mo and photochemical studies of Cp 2 MoO. Investigation of a proposed water-splitting cycle and preparation of a water-soluble molbdocene dihydride. *Inorg. Chim. ACTA.* (2000).

142. Karunadasa, H. I., Chang, C. J. & Long, J. R. A molecular molybdenum-oxo catalyst for generating hydrogen from water. *Nature.* **464,** 1329–1333 (2010).

143. Karunadasa, H. I. *et al.* A Molecular MoS2 Edge Site Mimic for Catalytic Hydrogen Generation. *Science.* **335,** 698–702 (2012).

144. Thoi, V. S., Karunadasa, H. I., Surendranath, Y., Long, J. R. & Chang, C. J. Electrochemical generation of hydrogen from acetic acid using a molecular molybdenum–oxo catalyst. *Energy Environ. Sci.* **5,** 7762 (2012).

145. Pal, R., Groy, T. L. & Trovitch, R. J. Conversion of Carbon Dioxide to Methanol Using a C–H Activated Bis(imino)pyridine Molybdenum Hydroboration Catalyst. *Inorg. Chem.* **54,** 7506–7515 (2015).

146. Pal, R., Groy, T. L., Bowman, A. C. & Trovitch, R. J. Preparation and Hydrosilylation Activity of a Molybdenum Carbonyl Complex That Features a Pentadentate Bis(imino)pyridine Ligand. *Inorg. Chem.* **53,** 9357–9365 (2014).

147. Ben-Daat, H., Hall, G. B., Groy, T. L. & Trovitch, R. J. Rational Design of Rhodium Complexes Featuring κ 4- N, N, N, N- and κ 5- N, N, N, P, P-Bis(imino)pyridine Ligands. *Eur. J. Inorg. Chem.* **2013,** 4430–4442 (2013).

148. Baker, P. K., Fraser, S. G. & Keys, E. M. The synthesis and spectral properties of some highly reactive new seven-coordinate molybdenum (II) and tungsten (II) bisacetonitrile dihalogenotricarbonyl complexes. *J. Organomet. Chem.* (1986).

149. Pal, R., Cherry, B. R., Flores, M., Groy, T. L. & Trovitch, R. J. Isolation of a bis(imino)pyridine molybdenum(i) iodide complex through controlled reduction and interconversion of its reaction products. *Dalton T.* **45,** 10024–10033 (2016).

150. Mukhopadhyay, T. K., Flores, M., Groy, T. L. & Trovitch, R. J. A Highly Active Manganese Precatalyst for the Hydrosilylation of Ketones and Esters. *J. Am. Chem. Soc. U.S.A.* **136,** 882–885 (2014).

151. Böhmer, J., Haselhorst, G., Wieghardt, K. & Nuber, B. The First Mononuclear Nitrosyl(oxo)molybdenum Complex: Side-On Bonded and μ3-Bridging NO Ligands in [{MoL(NO)(O)(OH)}2]NaPF6·H2O. *Angew. Chem. Int. Ed. Engl.* **33,** 1473–1476 (1994).

152. Balaj, O. P. *et al.* Base-Catalyzed Hydrogen/Deuterium Exchange between Water and Acetonitrile in Anionic Water Clusters. *J. Phys. Chem. A.* **108,** 7506–7512

(2004).

153. Sundstrom, E. J. *et al.* Computational and Experimental Study of the Mechanism of Hydrogen Generation from Water by a Molecular Molybdenum-Oxo Electrocatalyst. *J. Am. Chem. Soc. U.S.A.* **134,** 5233–5242 (2012).

154. Li, Y., Li, Z., Li, F., Wang, Q. & Tao, F. Preparation of a Nafion–Teflon bimembrane-supported palladium catalyst and its use in the Heck reaction. *Tetrahedron Lett.* **46,** 6159–6162 (2005).

155. Roberts, J. A. S. & Bullock, R. M. Direct Determination of Equilibrium Potentials for Hydrogen Oxidation/Production by Open Circuit Potential Measurements in Acetonitrile. *Inorg. Chem.* **52,** 3823–3835 (2013).

156. Novoselov, K. S.; Geim, A. K.; Morozov, S. V.; Jiang, D.; Zhang, Y.; Dubonos, S. V.; Grigorieva, I. V.; Firsov, A. A. *Science.* **2004**, *306* (5696), 666.

157. Eda, G.; Fanchini, G.; Chhowalla, M. *Nat. Nanotech.* **2008**, *3* (5), 270.

158. Neto, A. C.; Guinea, F.; Peres, N.; Novoselov, K. S.; Geim, A. K. *Rev. Mod. Phys.* **2009**, *81* (1), 109.

159. Vashist, S. K.; Luong, J. H. T. *Carbon.* **2015**, *84* (C), 519.

160. Ge, S.; Lan, F.; Yu, F.; Yu, J. *New J. Chem.* **2015**, *39*, 2380.

161. Yin, P. T.; Shah, S.; Chhowalla, M.; Lee, K.-B. Design, Synthesis, and Characterization of Graphene–Nanoparticle Hybrid Materials for Bioapplications *Chem. Rev.* **2015**, *115* (7), 2483.

162. Quintana, M.; Vazquez, E.; Prato, M. Organic Functionalization of Graphene in Dispersions. *Acc. Chem. Res.* **2012**, *46* (1), 138.

163. Xu, Y.; Liu, Z.; Zhang, X.; Wang, Y.; Tian, J.; Huang, Y.; Ma, Y.; Zhang, X.; Chen, Y. *Adv. Mater.* **2009**, *21* (12), 1275.

164. Stankovich, S.; Piner, R. D.; Chen, X.; Wu, N.; Nguyen, S. B. T.; Ruoff, R. S. *J. Mater. Chem.* **2006**, *16* (2), 155.

165. Banerjee, S.; Hemraj Benny, T.; Wong, S. S. Covalent surface chemistry of single-walled carbon nanotubes. *Adv. Mater. Weinheim.* **2005**, *17* (1), 17.

166. Si, G.; Wang, W.-G.; Wang, H.-Y.; Tung, C.-H.; Wu, L.-Z. *Inorg. Chem.* **2008**, *47* (18), 8101.

167. Moon In, K.; Lee, J.; Ruoff, R. S.; Lee, H. Reduced graphene oxide by chemical graphitization. *Nat. Commun.* **2010**, *1*, 73.

168. Chan, C. K.; Beechem, T. E.; Ohta, T.; Brumbach, M. T.; Wheeler, D. R.; Stevenson, K. J. Electrochemically Driven Covalent Functionalization of Graphene from Fluorinated Aryl Iodonium Salts. *J. Phys. Chem. C* **2013**, *117* (23), 12038.

169. Chen, C.; Wang, L.; Liu, Y.; Chen, Z.; Pan, D.; Li, Z.; Jiao, Z.; Hu, P.; Shek, C.-H.; Wu, C.-M. L. Assembling Tin Dioxide Quantum Dots to Graphene Nanosheets by a Facile Ultrasonic Route. *Langmuir.* **2013**, *29*, 4111.

170. Miyata, K.; Kakizawa, Y.; Nishiyama, N.; Harada, A.; Yamasaki, Y.; Koyama, H.; Kataoka, K. Block catiomer polyplexes with regulated densities of charge and disulfide cross-linking directed to enhance gene expression. *J. Amer. Chem. Soc.* **2004**, *126* (8), 2355.

171. Choh, S.-Y.; Cross, D.; Wang, C. Facile synthesis and characterization of disulfide-cross-linked hyaluronic acid hydrogels for protein delivery and cell encapsulation. *Biomacromolecules.* **2011**, *12* (4), 1126.

172. Lowe, A. B. Thiol-ene 'click' reactions and recent applications in polymer and materials synthesis. *Polym. Chem.* **2010**, *1* (1), 17.

173. Vericat, C.; Vela, M. E.; Benitez, G.; Carro, P.; Salvarezza, R. C. Self-assembled monolayers of thiols and dithiols on gold: new challenges for a well-known system. *Chem. Soc. Rev.* **2010**, *39* (5), 1805.

174. Yantasee, W.; Warner, C. L.; Sangvanich, T.; Addleman, R. S.; Carter, T. G.; Wiacek, R. J.; Fryxell, G. E.; Timchalk, C.; Warner, M. G. Removal of heavy metals from aqueous systems with thiol functionalized superparamagnetic nanoparticles. *Environ. Sci. Technol.* **2007**, *41* (14), 5114.

175. Li, G.; Zhao, Z.; Liu, J.; Jiang, G. Effective heavy metal removal from aqueous systems by thiol functionalized magnetic mesoporous silica. *J. Hazard Mater.* **2011**, *192* (1), 277.

176. Dong, S.; Li, J. Self-assembled monolayers of thiols on gold electrodes for bioelectrochemistry and biosensors. *Bioelectroch. Bioener.* **1997**, *42* (1), 7.

177. Xu, S.; Han, X. A novel method to construct a third-generation biosensor: self-assembling gold nanoparticles on thiol-functionalized poly (styrene- co-acrylic acid) nanospheres. *Biosens. Bioelectron.* **2004**, *19* (9), 1117.

178. Potta, T.; Chun, C.; Song, S.-C. Chemically crosslinkable thermosensitive

polyphosphazene gels as injectable materials for biomedical applications. *Biomaterials.* **2009**, *30* (31), 6178.

179. Zhang, Z.; Pendse, N. D.; Phillips, K. N.; Cotner, J. B.; Khodursky, A. *BMC Genomics.* **2008**, *9* (1), 344.

180. Park, R. M. *Materials Performance.* **2009**, 1.

181. Bard, A. J.; Faulkner, L. R. *Electrochemical Methods: Fundamentals and Applications*. Wiley, 2000.

182. Fourmond, V.; Hoke, K.; Heering, H. A.; Baffert, C.; Leroux, F.; Bertrand, P.; Léger, C. SOAS: A free program to analyze electrochemical data and other one-dimensional signals. *Bioelectrochemistry.* **2009**, *76* (1-2), 141.

183. Jeuken, L. JellyFit. http://www.personal.leeds.ac.uk/~phyljcj/Software.htm.

184. Shin, H.-J.; Kim, K. K.; Benayad, A.; Yoon, S.-M.; Park, H. K.; Jung, I.-S.; Jin, M. H.; Jeong, H.-K.; Kim, J. M.; Choi, J.-Y.; Lee, Y. H. Efficient Reduction of Graphite Oxide by Sodium Borohydride and Its Effect on Electrical Conductance. *Adv. Funct. Mater.* **2009**, *19* (12), 1987.

185. Bergman, J.; Pettersson, B.; Hasimbegovic, V.; Svensson, P. H. Thionations Using a P4S10− Pyridine Complex in Solvents Such as Acetonitrile and Dimethyl Sulfone. *J. Org. Chem.* **2011**, *76* (6), 1546.

186. Compton, O. C.; Jain, B.; Dikin, D. A.; Abouimrane, A.; Amine, K.; Nguyen, S. T. Chemically active reduced graphene oxide with tunable C/O ratios. *ACS Nano.* **2011**, *5* (6), 4380.

187. Tung, V. C.; Allen, M. J.; Yang, Y.; Kaner, R. B. High-throughput solution processing of large-scale graphene. *Nat. Nanotech.* **2009**, *4* (1), 25.

188. Park, S.; An, J.; Jung, I.; Piner, R. D.; An, S. J.; Li, X.; Velamakanni, A.; Ruoff, R. S. Colloidal suspensions of highly reduced graphene oxide in a wide variety of organic solvents. *Nano Lett.* **2009**, *9* (4), 1593.

189. Curran, S. A.; Cech, J.; Zhang, D.; Dewald, J. L.; Avadhanula, A.; Kandadai, M.; Roth, S. Thiolation of carbon nanotubes and sidewall functionalization. *J. Mater. Res.* **2006**, *21* (4), 1012.

190. Socrates, G. Infrared and Raman characteristic group frequencies: tables and charts, 3rd ed.; John Wiley & Sons: Chichester, 2001.

191. Le Goff, A., Artero, V., Metayé, R., & Moggia, F. (2010). Immobilization of

FeFe hydrogenase mimics onto carbon and gold electrodes by controlled aryldiazonium salt reduction: an electrochemical, XPS and ATR-IR study. *Inter. J. Hydrogen Energ.* (35), 10790–10796.

192. Fernández, L.; Carrero, H. *Electrochim ACTA.* **2005**, *50* (5), 1233.

193. Raoof, J.-B.; Ojani, R.; Kiani, A. *J. Electroanal.Chem.* **2001**, *515*, 45.

194. Nkosi, D.; Pillay, J.; Ozoemena, K. I.; Nouneh, K.; Oyama, M. *Phys. Chem. Chem. Phys.* **2010**, *12* (3), 604.

195. Sikes, H. D. *Science.* **2001**, *291* (5508), 1519.

196. Ashur, I.; Jones, A. K. Immobilization of azurin with retention of its native electrochemical properties at alkylsilane self-assembled monolayer modified indium tin oxide. *Electrochim ACTA.* **2012**, *85*, 169.

197. Creager, S.; Yu, C. J.; Bamdad, C.; O'Connor, S.; MacLean, T.; Lam, E.; Chong, Y.; Olsen, G. T.; Luo, J.; Gozin, M.; Kayyem, J. F. Electron Transfer at Electrodes through Conjugated 'Molecular Wire' Bridges. *J. Amer. Chem. Soc.* **1999**, *121* (5), 1059.

198. Blankenship, R. E. *et al.* Comparing Photosynthetic and Photovoltaic Efficiencies and Recognizing the Potential for Improvement. *Science.* **332,** 805–809 (2011).

199. Logan, B. E. & Rabaey, K. Conversion of Wastes into Bioelectricity and Chemicals by Using Microbial Electrochemical Technologies. *Science.* **337,** 686–690 (2012).

200. Nevin, K. P., Woodard, T. L., Franks, A. E., Summers, Z. M. & Lovley, D. R. Microbial Electrosynthesis: Feeding Microbes Electricity To Convert Carbon Dioxide and Water to Multicarbon Extracellular Organic Compounds. *mBio.* **1,** (2010).

201. Rabaey, K. & Rozendal, R. A. Microbial electrosynthesis - revisiting the electrical route for microbial production. *Nat. Rev. Micro.* **8,** 706–716 (2010).

202. Chandra, R., Modestra, J. A. & Mohan, S. V. Biophotovoltaic cell to harness bioelectricity from acidogenic wastewater associated with Microbial Community Profiling. *Fuel.* **160,** 502–512 (2015).

203. Zou, Y., Pisciotta, J., Billmyre, R. B. & Baskakov, I. V. Photosynthetic microbial fuel cells with positive light response. *Biotechnol. Bioeng.* **104,** 939–946 (2009).

204. Brutinel, E. D. & Gralnick, J. A. Shuttling happens: soluble flavin mediators of

extracellular electron transfer in *Shewanella*. *Appl. Microbiol. Biotechnol.* **93,** 41–48 (2012).

205. Okamoto, A., Nakamura, R., Nealson, K. H. & Hashimoto, K. Bound Flavin Model Suggests Similar Electron-Transfer Mechanisms in *Shewanella* and *Geobacter*. *ChemElectroChem.* **1,** 1808–1812 (2014).

205. Edwards, M. J. *et al.* Redox Linked Flavin Sites in Extracellular Decaheme Proteins Involved in Microbe-Mineral Electron Transfer. *Sci. Rep.* **5,** 11677 (2015).

207. Kotloski, N. J. & Gralnick, J. A. Flavin Electron Shuttles Dominate Extracellular Electron Transfer by *Shewanella oneidensis*. *mBio.* **4,** (2013).

208. Marsili, E. *et al. Shewanella* Secretes flavins that mediate extracellular electron transfer. *Proc. Natl. Acad. Sci. U.S.A.* **105,** 3968–3973 (2008).

209. Ochiai, H., Shibata, H., Sawa, Y., Shoga, M. & Ohta, S. Properties of Semiconductor Electrodes Coated with Living Films of Cyanobacteria. *Appl Biochem. Biotechnol.* **8,** 289–303 (1983).

210. Yagishita, T., Sawayama, S., Tsukahara, K.-I. & Ogi, T. Effects of intensity of incident light and concentrations of *Synechococcus* sp. and 2-hydroxy-1,4-naphthoquinone on the current output of photosynthetic electrochemical cell. *Sol. Energy.* **61,** 347–353 (1997).

211. Bombelli, P. *et al.* Quantitative analysis of the factors limiting solar power transduction by *Synechocystis* sp. PCC 6803 in biological photovoltaic devices. *Energy Environ. Sci.* **4,** 4690–4698 (2011).

212. Longatte, G. *et al.* Evaluation of photosynthetic electrons derivation by exogenous redox mediators. *Biophys. Chem.* **205,** 1–8 (2015).

213. Beer, L. L., Boyd, E. S., Peters, J. W. & Posewitz, M. C. Engineering algae for biohydrogen and biofuel production. *Curr. Opin. Biotech.* **20,** 264–271 (2009).

214. Rosenbaum, M., Schroder, U. & Scholz, F. Utilizing the green alga *Chlamydomonas reinhardtii* for microbial electricity generation: a living solar cell. *Appl. Microbiol. Biotechnol.* **68,** 753–756 (2005).

215. Berk, R. S. & Canfield, J. H. Bioelectrochemical Energy Conversion. *Appl. Microbiol.* **12,** 10–& (1964).

216. Rosenbaum, M., Schroder, U. & Scholz, F. In situ electrooxidation of photobiological hydrogen in a photobioelectrochemical fuel cell based on

Rhodobacter sphaeroides. *Environ. Sci. Technol.* **39,** 6328–6333 (2005).

217. Cho, Y. K. *et al.* Development of a solar-powered microbial fuel cell. *J. Appl. Microbiol.* **104,** 640–650 (2008).

218. Newman, D. K. & Kolter, R. A role for excreted quinones in extracellular electron transfer. *Nature.* **405,** 94–97 (2000).

219. Bradley, R. W., Bombelli, P., Rowden, S. J. L. & Howe, C. J. Biological photovoltaics: intra- and extra-cellular electron transport by cyanobacteria. *Biochm. Soc. Trans.* **40,** 1302–1307 (2012).

220. El-Naggar, M. Y. *et al.* Electrical transport along bacterial nanowires from *Shewanella oneidensis* MR-1. *Proc. Natl. Acad. Sci. U.S.A.* **107,** 18127–18131 (2010).

221. Reguera, G. *et al.* Extracellular electron transfer via microbial nanowires. *Nature.* **435** 1098–1101 (2005).

222. Pirbadian, S. *et al. Shewanella oneidensis* MR-1 nanowires are outer membrane and periplasmic extensions of the extracellular electron transport components. *Proc. Natl. Acad. Sci. U.S.A.* **111,** 12883–12888 (2014).

223. Alves, M. N. *et al.* Characterization of the periplasmic redox network that sustains the versatile anaerobic metabolism of *Shewanella oneidensis* MR-1. *Front. Microbiol.* **6,** (2015).

224. Fonseca, B. M. *et al.* Mind the gap: cytochrome interactions reveal electron pathways across the periplasm of *Shewanella oneidensis* MR-1. *J. Biochem.* **449,** 101–108 (2013).

225. Sturm, G. *et al.* A dynamic periplasmic electron transfer network enables respiratory flexibility beyond a thermodynamic regulatory regime. *Isme. Journal.* **9,** 1802–1811 (2015).

226. Jensen, H. M. *et al.* Engineering of a synthetic electron conduit in living cells. *Proc. Natl. Acad. Sci. U.S.A.* **107,** 19213–19218 (2010).

227. Gorby, Y. A. *et al.* Electrically conductive bacterial nanowires produced by *Shewanella oneidensis* strain MR-1 and other microorganisms. *Proc. Natl. Acad. Sci. U.S.A.* **103,** 11358–11363 (2006).

228. Pisciotta, J. M., Zou, Y. & Baskakov, I. V. Light-Dependent Electrogenic Activity of Cyanobacteria. *PLoS ONE.* **5,** (2010).

229. Cereda, A. *et al.* A Bioelectrochemical Approach to Characterize Extracellular Electron Transfer by *Synechocystis* sp PCC6803. *PLoS ONE.* **9,** (2014).

230. Sekar, N., Umasankar, Y. & Ramasamy, R. P. Photocurrent generation by immobilized cyanobacteria via direct electron transport in photo-bioelectrochemical cells. *Phys. Chem. Chem. Phys.* **16,** 7862 (2014).

231. Huang, L. F., Lin, J. Y., Pan, K. Y., Huang, C. K. & Chu, Y. K. Overexpressing Ferredoxins in *Chlamydomonas reinhardtii* Increase Starch and Oil Yields and Enhance Electric Power Production in a Photo Microbial Fuel Cell. *IJMS.* **16,** 19308–19325 (2015).

232 McCormick, A. J. *et al.* Photosynthetic biofilms in pure culture harness solar energy in a mediatorless bio-photovoltaic cell (BPV) system. *Energy Environ. Sci.* **4,** 4699 (2011).

233. Mullineaux, C. W. Co-existence of photosynthetic and respiratory activities in cyanobacterial thylakoid membranes. *BBA - Bioenergetics.* **1837,** 503–511 (2014).

234. Pisciotta, J. M., Zou, Y. & Baskakov, I. V. Role of the photosynthetic electron transfer chain in electrogenic activity of cyanobacteria. *Appl. Microbiol. Biotechnol.* **91,** 377–385 (2011).

235. Darus, L., Ledezma, P., Keller, J. & Freguia, S. Marine phototrophic consortia transfer electrons to electrodes in response to reductive stress. *Photosynth. Res.* **127,** 347–354 (2016).

236. Trubitsin, B. V. *et al.* EPR study of electron transport in the cyanobacterium *Synechocystis* sp PCC 6803: Oxygen-dependent interrelations between photosynthetic and respiratory electron transport chains. *BBA - Bioenergetics.* **1708,** 238–249 (2005).

237. Pisareva, T. *et al.* Model for Membrane Organization and Protein Sorting in the Cyanobacterium *Synechocystis* sp PCC 6803 Inferred from Proteomics and Multivariate Sequence Analyses. *J. Proteome Res.* **10,** 3617–3631 (2011).

238. Lea-Smith, D. J., Bombelli, P., Vasudevan, R. & Howe, C. J. Photosynthetic, respiratory and extracellular electron transport pathways in cyanobacteria. *BBA - Bioenergetics.* **1857,** 247–255 (2016).

239. Sekar, N., Jain, R., Yan, Y. & Ramasamy, R. P. Enhanced photo-bioelectrochemical energy conversion by genetically engineered cyanobacteria. *Biotechnol. Bioeng.* **113,** 675–679 (2015).

240. Rosenbaum, M., Schröder, U. & Scholz, F. Utilizing the green alga

Chlamydomonas reinhardtii for microbial electricity generation: a living solar cell. *Appl. Microbiol. Biotechnol*. **68,** 753–756 (2005).

241. Cao, X. X., Huang, X., Boon, N., Liang, P. & Fan, M. Z. Electricity generation by an enriched phototrophic consortium in a microbial fuel cell. *Electrochem. Commun.* **10,** 1392–1395 (2008).

242. Darus, L., Lu, Y., Ledezma, P., Keller, J. & Freguia, S. Fully reversible current driven by a dual marine photosynthetic microbial community. *Bioresour. Technol.* **195,** 248–253 (2015).

243. Badalamenti, J. P., Torres, C. I. & Krajmalnik-Brown, R. Light-responsive current generation by phototrophically enriched anode biofilms dominated by green sulfur bacteria. *Biotechnol. Bioeng.* **110,** 1020–1027 (2013).

244. Nishio, K., Hashimoto, K. & Watanabe, K. Light/electricity conversion by a self-organized photosynthetic biofilm in a single-chamber reactor. *Appl. Microbiol. Biotechnol.* **86,** 957–964 (2010).

245. Fu, C. C., Hung, T. C., Wu, W. T., Wen, T. C. & Su, C. H. Current and voltage responses in instant photosynthetic microbial cells with Spirulina platensis. *Biochem. Eng. J.* **52,** 175–180 (2010).

246. Luimstra, V. M. *et al.* A cost-effective microbial fuel cell to detect and select for photosynthetic electrogenic activity in algae and cyanobacteria. *J. Appl. Phycol.* **26,** 15–23 (2013).

247. Ng, F. L., Phang, S. M., Periasamy, V., Yunus, K. & Fisher, A. C. Evaluation of Algal Biofilms on Indium Tin Oxide (ITO) for Use in Biophotovoltaic Platforms Based on Photosynthetic Performance. *PLoS ONE.* **9,** 13 (2014).

248. Schneider, K., Thorne, R. J. & Cameron, P. J. An investigation of anode and cathode materials in photomicrobial fuel cells. *Philos. T. R. Soc. A*. **374,** (2016).

249. Bombelli, P. *et al.* Surface morphology and surface energy of anode materials influence power outputs in a multi-channel mediatorless bio-photovoltaic (BPV) system. *Phys. Chem. Chem. Phys.* **14,** 12221–12229 (2012).

250. Thorne, R. *et al.* Porous ceramic anode materials for photo-microbial fuel cells. *J. Mater. Chem.* **21,** 18055–18060 (2011).

251. Zou, Y. J., Pisciotta, J. & Baskakov, I. V. Nanostructured polypyrrole-coated anode for sun-powered microbial fuel cells. *Bioelectrochemistry.* **79,** 50–56 (2010).

252. Hasan, K. *et al.* Photoelectrochemical Wiring of *Paulschulzia pseudovolvox* (Algae) to Osmium Polymer Modified Electrodes for Harnessing Solar Energy. *Adv. Energy Mater.* **5,** (2015).

252. Blankenship, R. E. *et al.* Comparing Photosynthetic and Photovoltaic Efficiencies and Recognizing the Potential for Improvement. *Science.* **332,** 805–809 (2011).

254. Nevin, K. P. *et al.* Electrosynthesis of Organic Compounds from Carbon Dioxide Is Catalyzed by a Diversity of Acetogenic Microorganisms. *Appl. Environ. Microb.* **77,** 2882–2886 (2011).

255. Torres, C. I. *et al.* A kinetic perspective on extracellular electron transfer by anode-respiring bacteria. *FEMS Microbiol. Rev.* **34,** 3–17 (2010).

256. El-Naggar, M. Y. *et al.* Electrical transport along bacterial nanowires from *Shewanella oneidensis* MR-1. *Proc. Natl. Acad. Sci. U.S.A.* **107,** 18127–18131 (2010).

257. Guan, D., Kurra, Y., Liu, W. & Chen, Z. A click chemistry approach to site-specific immobilization of a small laccase enables efficient direct electron transfer in a biocathode. *Chem. Commun.* **51,** 2522–2525 (2015).

258. Rasmussen, M., Shrier, A. & Minteer, S. D. High performance thylakoid bio-solar cell using laccase enzymatic biocathodes. *Phys. Chem. Chem. Phys.* **15,** 9062 (2013).

259. Nevin, K. P. *et al.* Anode Biofilm Transcriptomics Reveals Outer Surface Components Essential for High Density Current Production in *Geobacter sulfurreducens* Fuel Cells. *PLoS ONE.* **4,** e5628 (2009).

260. Pham, T. H. *et al.* Metabolites produced by *Pseudomonas* sp. enable a Gram-positive bacterium to achieve extracellular electron transfer. *Appl. Microbiol. Biotechnol.* **77,** 1119–1129 (2007).

261. Sakimoto, K. K., Wong, A. B. & Yang, P. Self-photosensitization of nonphotosynthetic bacteria for solar-to-chemical production. *Science.* **351,** 74–77 (2015).

262. Kornienko, N., Sakimoto, K. K., Herlihy, D. M., Nguyen, S. C., Alivisatos, A. P., Harris, C. B., Schwartberg, A. Yang, P. (2016). Spectroscopic elucidation of energy transfer in hybrid inorganic–biological organisms for solar-to-chemical production. *Proc. Natl. Acad. Sci. U.S.A.* ***113***(42), 11750–11755..

263. Sattley, W. M. *et al.* The Genome of Heliobacterium modesticaldum, a Phototrophic Representative of the Firmicutes Containing the Simplest

Photosynthetic Apparatus. *J. Bacteriol.* **190,** 4687–4696 (2008).

264. Kimble, L. K. & Madigan, M. T. Nitrogen fixation and nitrogen metabolism in *Heliobacteria*. *Arch. Microbiol.* **158,** 155–161 (1992).

265. Heinnickel, M. & Golbeck, J. H. Heliobacterial photosynthesis. *Photosynth. Res.* **92,** 35–53 (2007).

266. Kimble, L. K., Mandelco, L., Woese, C. R. & Madigan, M. T. *Heliobacterium modesticaldum*, sp. nov., a thermophilic *Heliobacterium* of hot springs and volcanic soils. *Arch. Microbiol.* **163,** 259–267 (1995).

267. Kleinherenbrink, F. A. M. & Amesz, J. Stoichiometries and rates of electron transfer and charge recombination in *Heliobacterium chlorum*. *BBA - Bioenergetics.* **1143,** 77–83

268. Sarrou, I. *et al.* Purification of the photosynthetic reaction center from *Heliobacterium modesticaldum*. *Photosynth. Res.* **111,** 291–302 (2012).

269. Cereda, A. *et al.* A Bioelectrochemical Approach to Characterize Extracellular Electron Transfer by *Synechocystis* sp. PCC6803. *PLoS ONE.* **9**(3).

270. Hagen, W. R. Direct electron transfer of redox proteins at the bare glassy carbon electrode. *Eur. J. Biochem.* **182,** 523–530

271. Nikkila, H., Gennis, R. B. & Sligar, S. G. Cloning and expression of the gene encoding the soluble cytochrome b_{562} of *Escherichia coli*. *Eur. J. Biochem.* **202,** 309–313

272. Barker, P. D., Nerou, E. P., Freund, S. M. V. & Fearnley, I. M. Conversion of Cytochrome b_{562} to c-Type Cytochromes. *Biochemistry.* **34,** 15191–15203 (1995).

273. Weiss, R. L. Protoplast Formation in *Escherichia coli*. *J. Bacteriol.* **128,** 668

274. Itagaki, E., Palmer, G. & Hager, L. P. Studies on Cytochrome b_{562} of *Escherichia coli*. *J. Biol. Chem.*

APPENDIX A

CUSTOM ELECTROCHEMICAL EQUIPMENT

Introduction

The method to approach a novel redox protein or enzyme for electrochemical interrogation is unknown *ab initio*. Crystal structures, homology models, and amino acid composition can help determine initial strategies for electrochemical interrogation. However, these may not always provide the correct strategy. Additionally, adsorption/immobilization of a redox protein or enzyme is not always facile and can require methods varying from drop casting and drying to rotating an electrode in a solution of the desired redox protein/enzyme while continuously cycling the potential at the electrode surface. To add to the many techniques available in our laboratory, we designed custom electrochemical cells: two for conducting electrochemical experiments in small volumes, two for quantifying hydrogen evolution, and one for conducting protein film voltammetry in a total volume of 5-20 μL.

Custom electrochemical cells

Evaluation of proteins under diffusional conditions in >1.0 mL while in the presence of a rotating an electrode.

Protein film voltammetry is a powerful tool for interrogating redox active proteins and enzymes when the surface of a protein favors an orientation that promotes electrical communication with an electroactive surface such as carbon (graphite, glassy carbon) or metal oxides (ATO, ITO). Unfortunately, not all redox proteins and enzymes associate with an electroactive surface in a favorable orientation. To overcome this, solution based assays can be conducted that employ a rotating electrode, thus allowing an increase of orientations and interactions to be probed at the electrode surface. Generally these experiments require small volumes in order to obtain high concentrations of diffusional proteins. To facilitate an experiment as described above, the electrochemical cell in **Figure A-1** was designed. This cell allows electrochemical analysis do be conducted in a total volume of 0.5 to 5.0 mL. The counter and reference electrodes are held in place by the Teflon cap and the rotating electrode has freedom to rotate within the large orifice. Additional small openings in the Teflon cap allow for introduction of liquid substrate via micropipette or gaseous substrate via small tubing.

The electrochemical cell was designed by our group and fabricated by the glass blowing facility at Arizona State University.

Figure A-1. Electrochemical cells for interrogation of proteins under diffusional conditions in small volumes of 0.5 to 5.0 mL.

Interrogation of proteins under conditions employing micro-volumes, 5-10 µL.

The design for this electrochemical cell is based on initial experiments conducted by Hagen(Hagen, n.d.) and modified for use in an anaerobic glovebox. The custom cell, shown in **Figure A-2**, employs a T-shape design that allows for the reference electrode to be positioned directly above the working electrode, which are both held tightly in place by compression fittings. The sample is then applied, through the side port, to the tip of the reference electrode and allowed to fall into place before the counter electrode is inserted and fastened *via* a compression fitting. For this setup the counter electrode is fed through a septum fastened at one end of a glass sheath and allowed to protrude through an opening in the other end of the glass sheath. This positioning allows precise control over the location of the counter electrode within the ~10 µL droplet.

The electrochemical cell was designed by our group and fabricated by the glass blowing facility at Arizona State University.

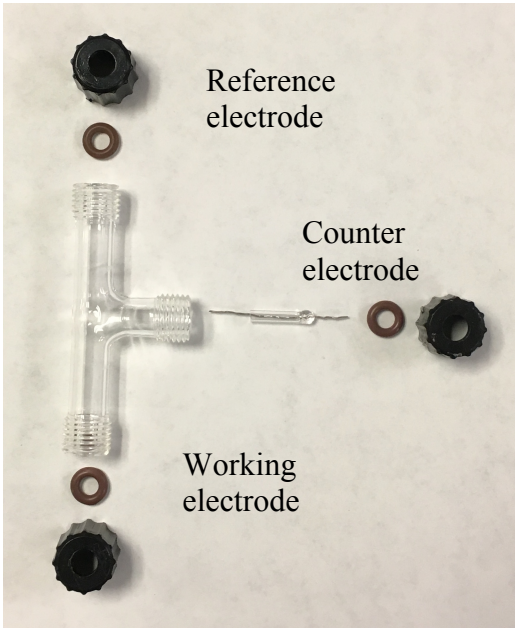

Figure A-2. Electrochemical cells for interrogation of proteins diffusing in small volumes of 5.0 – 15.0 μL.

1.2) Quantification of H_2 produced by a species adsorbed or immobilized on an electroactive surface.

The electrochemical cell shown in **Figure A-3** contains four ports that are sealed via compression fittings. The silver wire of the reference electrode and the platinum wire of the counter electrode are encased within a glass sheath that is sealed at air-exposed end and equipped with a Vycor frit on the solution side. The working, reference, and counter electrode ports are sealed via an o-ring within the compression fitting. The fourth port is sealed via a septum that encases an o-ring. A gas-tight syringe is employed to access the headspace gas for sampling and analysis via gas chromatography.

In most cases the electrochemical cell was employed to detect H_2 or CO gases. Since both gases have a low solubility in water and organic solvent, the majority of the gas will be localized in the headspace. To maximize the probability of detecting a gas in the headspace of the electrochemical cell, the cell was designed to minimize the volume of the headspace portion. The total volume of this electrochemical cell is 6.0 mL. A 2.0 mL headspace was generally employed for experiments aimed at detecting either CO or H_2.

The electrochemical cell was designed by our group and fabricated by the glass blowing facility at Arizona State University.

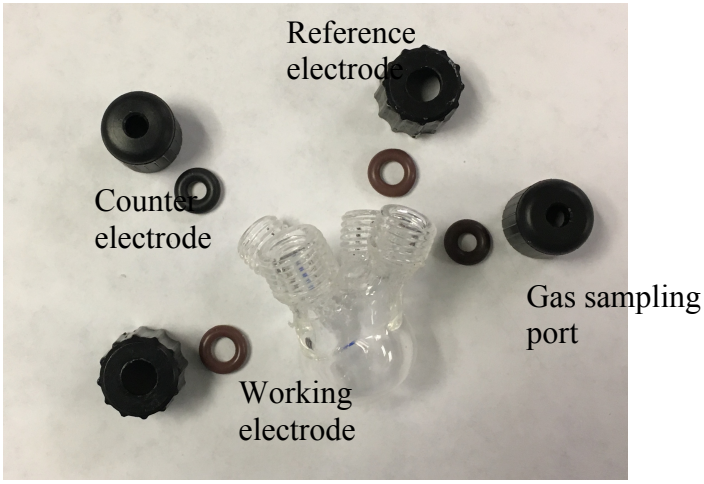

Figure A-3. Custom electrochemical cell that can be completely sealed to enable evaluation of headspace gas following controlled potential experiments. The gas sampling port is sealed by addition of a small septum around the o-ring.

1.3) Quantification of H_2 produced by live microorganisms.

The ability of *Heliobacterium modesticaldum* to produce H_2 under electrosynthetic conditions was evaluated using the custom electrochemical cell in **Figure A-4**. The two lower ports are equipped with the reference and counter electrodes and are sealed using compression fittings. The top port is sealed using an o-ring and a septum. The septum contains a titanium lead fed through that connects to the working electrode. The entire top is sealed with a compression fitting. The fourth port is sealed with a solid silicone o-ring and a compression fitting to facilitate sampling of headspace gases.

The electrochemical cell was designed by our group and fabricated by the glass blowing facility at Arizona State University.

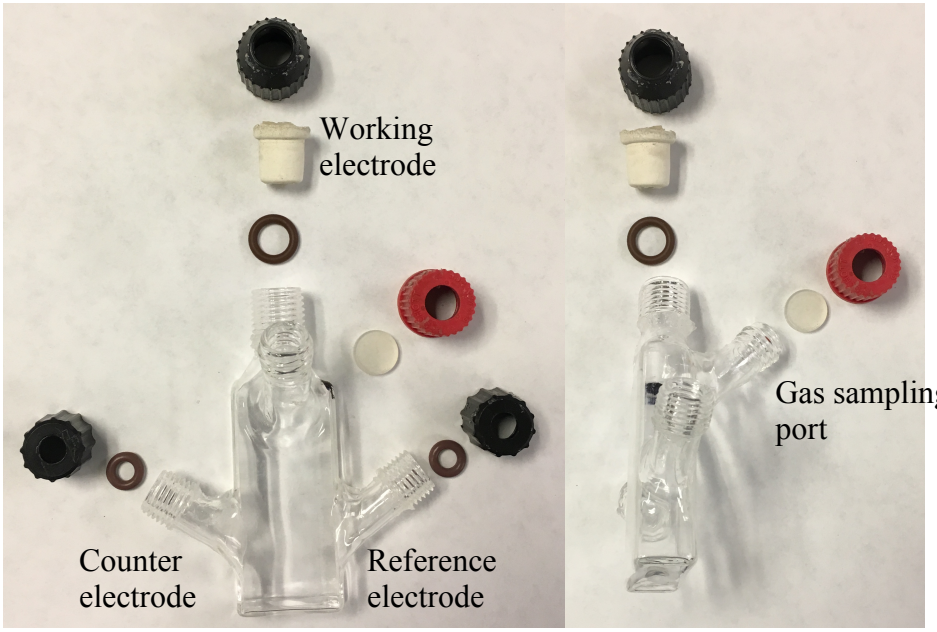

Figure A-4. Photoelectrochemical cell for quantifying metabolic products via sampling of headspace gas. Reference and counter electrodes must be encased in a glass sheath equipped with a Vicor or CoralPor frit and are sealed in the two side ports. The carbon cloth working electrode is fed through the top septum via a tungsten wire. Gas sampling is completed via the port equipped with a red cap.

Custom electrochemical hardware

Adapter for custom built edge-plane pyrolytic graphite electrodes to interface with Pine Instruments MSR rotator.

Cyclic voltammetry or chronoamperometry experiments can be conducted employing a rotating electrode to overcome diffusional limitations. Rotating a disk electrode (1 mm) in a small volume, i.e. < 1.0 mL, required the adaptation of a standard working electrode to allow for use with a Pine Instruments MSR rotator. The designed hardware allows the electrode lead to be fed through a stainless steel cylinder, **Figure A-5**. Two setscrews, on either side of the stainless steel cylinder, are used to secure the electrode lead in place. The stainless steel cylinder in then threaded onto the standard MSR rotating disk electrode shaft.

The electrochemical hardware was designed by our group and fabricated by the OKED Instrument Design and Fabrication Core Facility at Arizona State University.

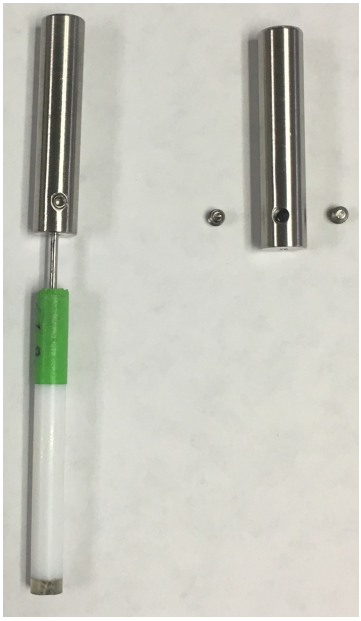

Figure A-5. Hardware to enable rotation with a standard disk electrode. The stainless steel adapter tightly holds the electrode via the two setscrews and allows rotation up to 4k rpm.

Custom illumination source

Illumination source for monitoring photosynthetic hydrogen production. "*The Fluxanator*"

Chronoamperometric experiments employing photosynthetic organisms requires evaluating an increase of the rate of oxidations or reductions occurring at the electrode surface during illuminated periods. This increase in the rate of oxidations or reductions is known as photocurrent and can be attributed to either acceptance or donation of electrons to an electrode. In cyanobacteria the photocurrent is largely attributed to water oxidation by PSII during illuminated periods.

To accurately gauge the photocurrent produced or consumed during photoelectrochemical experiments a custom LED-based light source was assembled that promoted the following three key factors:

1) Multiple wavelengths can be evaluated for their ability to promote photocurrent
2) Power output from the LED's must be variable (from low to high power) and maintain a constant intensity
3) Automatic, programmable, and reliable light changing events must be employed for high level analysis of the effect of light intensity on photocurrent production or consumption.

The custom light source, The Fluxanator, is shown in **Figure A-6**. An Arduino is used as the brain of the light source and allows the user to choose from two operation modes: constant light intensity and variable light intensity. Constant light intensity mode will provide a constant flux until the user defines a new power output. Variable light

intensity mode allows the user to define the number of light cycles, the length of each light cycle, and the repetitions at each light intensity. An example of a calibration curve and custom LED arrays are shown in **Figure A-7**. LED arrays consisted of either 780 or 660 nm LEDs, to be used for *H. modesticaldum* and *Synechocystis* sp. PCC 6803, respectively.

A description of the variable used and an example of the input required for the user-defined mode is below:

> Light on time, Light 0ff time, # of Repeats, WriteValue_1, WriteValue_2, WriteValue_3, WriteValue_4, WriteValue_5, WriteValue_6, WriteValue_7, WriteValue_8, WriteValue_9, WriteValue_10*
>
> 30,15,5,2,4,6,8,10,20,40,80,120, 240*

In the example above, the first and second variables set the length (in seconds) of the light and dark periods, respectively. Here it is 30 seconds on and 15 seconds off. The third variable sets the repetition number, or how many times each light intensity will be repeated. In this example each of the ten light intensities investigated will be repeated five times before moving to the next value. The next ten variables set the analog write value that will be used by the Arduino to send current to the LEDs. A calibration curve, as shown in Figure 7, is necessary to predict the flux provided by a specific LED array at a specific write value. Note that since the MOSFET is used, the correct use of the 5V or 3V output is important. As a greater voltage difference across the MOSFET will provide an increased current to be sent to the LEDs and hence an increased light intensity.

The Arduino is controlled by the freely available software created by Arduino and can be downloaded from the developers website.

https://www.arduino.cc/en/Main/Software

The code to run the fluxanator program is located following **Figure A-7** and at github at:

https://github.com/jlaureanti/fluxanator

A interactive diagram of a minimalistic fluxanator is available online at:

https://circuits.io/circuits/3462693-the-unnamed-circuit

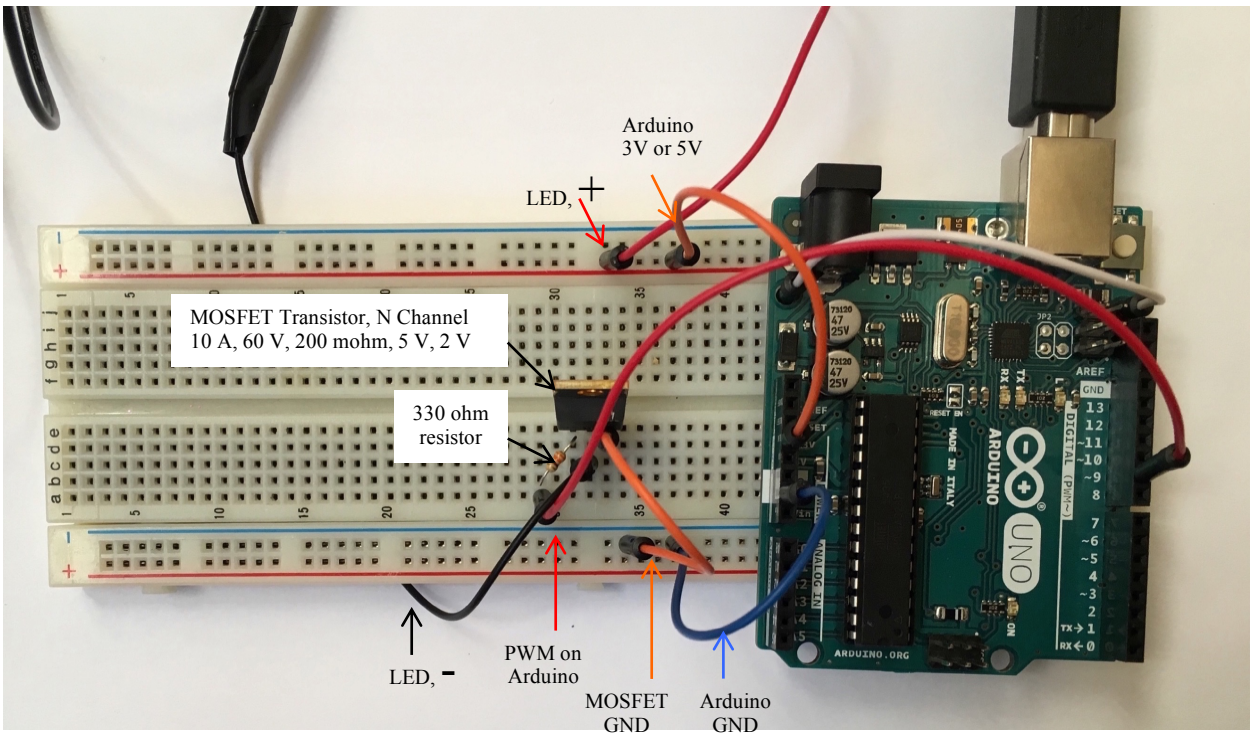

Figure A-6. Wiring diagram for the Fluxanator. The MOSFET is used to amplify the maximum current output from the Arduino. In this setup the ground of the LED is connected to the middle pin (drain) of the MOSFET, the right pin (source) of the MOSFET is connected to the ground of the Arduino, and the left pin (gate) is connected to a PWM channel from the Arduino. The degree of current amplification is dependent on the voltage difference at the gate. Due to this, the maximum power output can be manipulated by using the 3V or 5V power source to the LED, with 5V providing more current to the LEDs than the 3V supply.

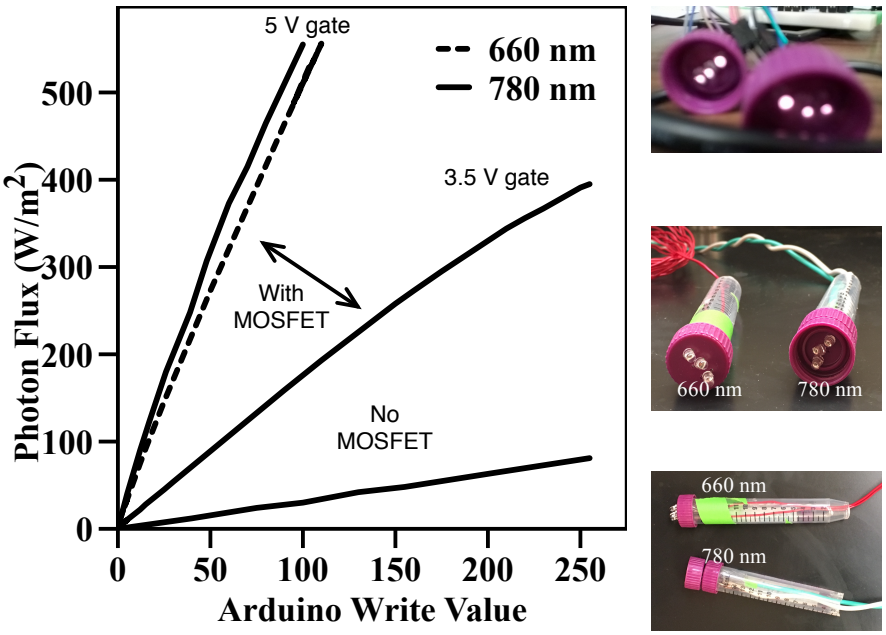

Figure A-7. Dependence of the photon flux on the analog write value sent from the Arduino (left panel) and images of the constructed LED arrays (right panels).

Code for Fluxanator program

```
int ledPins[] = {5, 6, 9, 10, 11};

int ind1;
int ind2;
int ind3;
int ind4;
int ind5;
int ind6;
int ind7;
int ind8;
int ind9;
int ind10;
int ind11;
int ind12;
int ind13;
int lightOnTime;
int lightOffTime;
int cycleNum;
int step1;
int step2;
int step3;
int step4;
int step5;
int step6;
int step7;
int step8;
int step9;
int step10;
int nextStep;
int lightSteps;
int cycleActual;
int bright;
int lLight;
int wm2;
int microE;
int index;
String timeNow;

long highOn;
long lowOn;

String readString;
String onDuration;
String offDuration;
String repeats;
String high1;
String high2;
String high3;
String high4;
String high5;
String high6;
String high7;
```

```
String high8;
String high9;
String high10;

char b;

void setup() {
  int index;
  for (index = 0; index <= 3; index++)
  {
    pinMode(ledPins[index], OUTPUT);
  }
  Serial.begin(9600);

  Serial.println("Welcome to The Fluxanator");
  Serial.println("Lets get fluxing!");
  Serial.println("@ = Set high and low flux");
  Serial.println("# = Constant light flux");
  Serial.println("& = Clears all inputs");
}

void loop() {
  startScreen();
}

void startScreen() {
  while (Serial.available() > 0) {
    b = Serial.read();
    if (b == '@') {
      userDefined();
    }
    if (b == '#') {
      constantFlux();
    }
    if (b == '&') {
      clearAll();
    }
    else {
      readString += b; //makes the string readString
    }
  }
}

void userDefined() {
  Serial.println(); Serial.println("User enters light on duration (s), light off duration (s), repeats (#),");
  Serial.println(" up to 10 high light values separated by commas and terminated with *");
  Serial.println("3660 (time in seconds), 3660 (time in seconds), 3 (each high light exposure completed in
triplicate),1,2,3,4,5,6,7,8,9,10*");
  //expect a string like "high power, high duration,low power, low duration, cycles, power decrease*"
  while (true) {
    while (Serial.available() > 0)  {
      char b = Serial.read();  //gets one byte from serial buffer
      if (b == '*') {
        Serial.println(); Serial.print("captured String is : ");
        Serial.println(readString); //prints string to serial port out
```

```
      ind1 = readString.indexOf(',');  //finds location of first ,
      onDuration = readString.substring(0, ind1);   //captures first data String
      ind2 = readString.indexOf(',', ind1 + 1 ); //finds location of second ,
      offDuration = readString.substring(ind1 + 1, ind2 + 1); //captures second data String
      ind3 = readString.indexOf(',', ind2 + 1 );
      repeats = readString.substring(ind2 + 1, ind3 + 1);
      ind4 = readString.indexOf(',', ind3 + 1 );
      high1 = readString.substring(ind3 + 1, ind4 + 1);
      ind5 = readString.indexOf(',', ind4 + 1 );
      high2 = readString.substring(ind4 + 1, ind5 + 1);
      ind6 = readString.indexOf(',', ind5 + 1 );
      high3 = readString.substring(ind5 + 1, ind6 + 1);
      ind7 = readString.indexOf(',', ind6 + 1 );
      high4 = readString.substring(ind6 + 1, ind7 + 1);
      ind8 = readString.indexOf(',', ind7 + 1 );
      high5 = readString.substring(ind7 + 1, ind8 + 1);
      ind9 = readString.indexOf(',', ind8 + 1 );
      high6 = readString.substring(ind8 + 1, ind9 + 1);
      ind10 = readString.indexOf(',', ind9 + 1 );
      high7 = readString.substring(ind9 + 1, ind10 + 1);
      ind11 = readString.indexOf(',', ind10 + 1 );
      high8 = readString.substring(ind10 + 1, ind11 + 1);
      ind12 = readString.indexOf(',', ind11 + 1 );
      high9 = readString.substring(ind11 + 1, ind12 + 1);
      ind13 = readString.indexOf(',', ind12 + 1 );
      high10 = readString.substring(ind12 + 1); //captures remain part of data after last ,

      lightOnTime = onDuration.toInt(); lightOffTime = offDuration.toInt(); cycleNum = repeats.toInt();
      step1 = high1.toInt(); step2 = high2.toInt(); step3 = high3.toInt(); step4 = high4.toInt(); step5 =
high5.toInt();
      step6 = high6.toInt(); step7 = high7.toInt(); step8 = high8.toInt(); step9 = high9.toInt(); step10 =
high10.toInt();

      chooseHigh();
     }
     else {
      readString += b; //makes the string readString
     }
    }
   }
}

void chooseHigh() {
  int nextStep = 0;
  int lightSteps[] = {step1, step2, step3, step4, step5, step6, step7, step8, step9, step10};

  while (nextStep <= 10) {

    int cycleActual = 0;
    highOn = lightOnTime * 1000L;
    lowOn = lightOffTime * 1000L;

    while (cycleActual < cycleNum) {
      int index; //array index for lights
```

```
    int hPosition; //array for high light value
    int runningLight = (lightSteps[nextStep]);
    // Convert writeValue to lightIntensity
    int wm2 = (((340. / 100.) * runningLight) + (627. / 100.));
    // Convert writeValue to lightIntensity
    int microE = ((2219. / 100.) * runningLight) + (4090. / 100.);
    int wm2_low = (1017. / 2500.) * lLight; // Convert writeValue to lightIntensity
    int microE_low = (780.) * wm2_low * (209. / 25000.); // Convert writeValue to lightIntensity

    Serial.print("WV= "); Serial.print(runningLight); Serial.print(" W/m2= "); Serial.print(wm2);
Serial.print(" uE= "); Serial.print(microE);
    Serial.print(" Time(s)= "); Serial.print(millis() / 1000); Serial.println();

    for (index = 0; index <= 5; index++) // setup lights
    {
     analogWrite(ledPins[index], runningLight);
    };

    delay(highOn); // Pause for cycle

    Serial.print("W/m2= "); Serial.print(wm2_low); Serial.print(" uE= "); Serial.print(microE_low);
    Serial.print(" Time(s)= "); Serial.print(millis() / 1000); Serial.println();

    for (index = 0; index <= 5; index++) // setup lights
    {
     analogWrite(ledPins[index], 0);
    };

    delay(lowOn);  // Pause for cycle
    cycleActual++; // add another cycle
   }
  nextStep++;
  }
  clearAll(); // clear all variables, should reset, but doesn't
  startScreen(); // clear all variables, should reset, but doesn't
}

void constantFlux()
{
  Serial.println(""); Serial.println("Control brightness (0-255),"); Serial.println("then click [send] or press
[return]"); Serial.println();  // Print a blank line

  // In order to type out the above message only once,
  // we'll run the rest of this function in an infinite loop:
  while (true) // "true" is always true, so this will loop forever.
  {
   // First we check to see if incoming data is available:
   while (Serial.available() > 0)
   {
    // If it is, we'll use parseInt() to pull out any numbers:
    bright = Serial.parseInt();
    // Because analogWrite() only works with numbers from
    // 0 to 255, we'll be sure the input is in that range:
    bright = constrain(bright, 0, 256);
    // print message to let you know that the
```

```
    // number was received:
    Serial.println("");
    Serial.print("Setting write value to "); Serial.println(bright);
    for (index = 0; index <= 5; index++)
    {
      // Set the brightness from serial to LEDs
      analogWrite(ledPins[index], bright);
    }

    int wm2 = (((340. / 100.) * bright) + (627. / 100.)); // Convert writeValue to lightIntensity
    int microE = ((2219. / 100.) * bright) + (4090. / 100.) ; // Convert writeValue to lightIntensity

    Serial.print("WV= "); Serial.print(bright); Serial.print(" microE= "); Serial.print(microE);
    Serial.print(" Time(s)= "); Serial.print(millis() / 1000);
    Serial.println();

   }
  }
  clearAll();
  startScreen();
}

void clearAll() {
  Serial.println("Here's the clear that shit app");
  readString = "*"; //clears variable for new input
  onDuration = "";
  offDuration = "";
  repeats = "";
  high1 = "";
  high2 = "";
  high3 = "";
  high4 = "";
  high5 = "";
  high6 = "";
  high7 = "";
  high8 = "";
  high9 = "";
  high10 = "";
  b == '0';

  if (b == '0') {
    startScreen();
  }
}
```

References

1) Hagen, W. R. (n.d.). Direct electron transfer of redox proteins at the bare glassy carbon electrode. *European Journal of Biochemistry / FEBS*, *182*(3), 523–530.

APPENDIX B

PROTEIN EXPRESSION AND PURIFICATION

Abstract

The procedure for the expression and purification of 5 enzymes is contained herein: WT cytochrome b_{562} WT, cytochrome b_{562} H63C, FdI-KSCK, StrepII-FdI-KSCK, FdI-KSCK-StrepII. Expected UV-visible spectra is shown for all protein except FdI-KSCK (no StrepII). Circular dichroism spectra is shown for H63C from 4° C to 90° C and shows T_m = 75° C. Cyclic voltammetry of H63C and FdI-KSCK-StrepII is also shown using EPPG electrodes.

Introduction

Two proteins underwent point mutations to provide a scaffold that was amenable to site specific immobilization of the target protein or also immobilization of synthetic catalyst. H63C provides a solvent exposed cysteine and can undergo site-specific labeling using maleimide chemistry. FdI-KSCK variants containing a StrepII tag one two lysine residues to under amide bond formation at an electroactive surface or with a synthetic catalyst. FdI-KSCK (no strep) has on lysine residue <10Å from the [2Fe2S] active site. Each FdI-KSCK construct has a single cysteine on the interior of the protein that is amenable for reactions using maleimide chemistry.

Materials and Methods

General: All chemicals were of the highest grade commercially available and were used without further purification. Solutions for electrochemical experiments were prepared using double-distilled water (resistivity 18.2 MΩ cm^{-1}). The mixed buffer (MMT) consisted of 5 mM each of 2-[N'-morpholino]ethanesulfonic acid (MES), 3-[N'-morpholino]propanesulfonic acid (MOPS), N'-tris[hydroxymethyl]methyl-3-amino-pr-panesulfonic acid (TAPS) and contained 0.1 M KCl. Solutions were titrated to the desired

experimental pH with either NaOH or HCl. Standard transformation, PCR, and electrophoresis protocols were followed, and strains, plasmids, and primers used are shown in **Table B-1**. Desalting and/or buffer exchange was completed using dialysis tubing (6,000 to 8,000 NMWCO) or centrifugal filter units: 15.0 mL Amicon Ultra-15 (AU15) or 0.5 mL Ultra-0.5 (AU05).

Mutagensis of pNS207 affording H63C mutant. Mutagenesis of plasmid pNS207 (Addgene plasmid 35041) was completed *via* the polymerase chain reaction (PCR) using primers, P1 and P2, located in **Table B-1**. PCR products were separated by agarose gel electrophoresis, excised, and purified by Wizard® SV Gel and PCR Clean-Up System (Promega; Madison, WI). Purified PCR products were circularized using T4 DNA ligase and introduced to *E. coli* (DH5α). Positive transformants were confirmed by DNA sequencing (ASU DNA laboratory).

Mutagenesis and removal of StrepII-tag pJ411 affording FdI-KSCK. Mutagensis of StrepII-FdI plasmid (DNA 2.0, pJ411) was completed by PCR amplification of the native Fd sequence downstream of the DNA sequence encoding for the StrepII-tag. P3 inserted an NdeI site over the ATG of the methionine where native expression of the Fd-KSCK gene product occurs, while P4 ensured the amplification of the XhoI site from the 3' end of the FdI-KSCK gene. PCR reactions were separated by agarose gel electrophoresis, excised, and purified using a PCR clean-up kit. Purified PCR products underwent digestion by restriction endonucleases NdeI and XhoI, and were re-purified using a PCR clean-up kit. In a separate preparation, the DNA sequence encoding the N-terminal StrepII-tag as well as the sequence encoding FdI-KSCK was excised from the StrepII-FdI plasmid by digestion of the N-terminal FdI construct using NdeI and XhoI,

The reaction products were then separated *via* agarose gel electrophoresis and the pJ411 backbone was excised, and purified. The digested and purified pJ411 backbone PCR insert from above were mixed at a 3:1 (insert:vector) molar ratio and exposed to Quick Ligase (NEB) for 30 minutes before introduction to *E. coli* (DH5α) to undergo a transformation procedure. Aliquots of 50 μL were inoculated to LB-plates containing 70 μg mL^{-1} kanamycin. Positive transformants were screened by inoculation of single colonies to 10.0 mL LB, followed by purification of plasmid DNA for sequencing using primer P5, which targeted the T7 promoter sequence.

Expression and preparation of crude cytochrome. Wild type and mutant cytochrome b_{562} were expressed in *E. coli*, BL21(DE3), using the proper glycerol stock for inoculation of a 1.5 L culture in a 2.0 L flask.[14,22] Cultures were shaken (250 rpm, 24 hrs, 37° C) in a microaerobic environment. Periplasmic extracts were obtained by addition of lysozyme to a final concentration of 100 μg/mL in tris(hydroxymethyl)aminomethane (Tris) buffer (0.1 M, 20% sucrose, pH 7.5).[14,31] Resulting protoplasts and cell debris were removed by centrifugation (18,000 g, 1 hr, 4° C) to obtain a clear pink supernatant. The supernatant was dialyzed (6,000 – 8,000 NMWCO) against cation-exchange buffer (potassium phosphate 50.0 mM, pH 4.5) overnight.

Purification of cytochromes. Protein purification of wild type cytochrome b_{562} was completed using fast protein liquid chromatography (FPLC) on an ÄKTAprime plus. Purification required four sequential columns: 1) carboxymethyl cellulose (CM52, 7.0 mL min^{-1}, 7.0 mL fractions, 5.08 cm x 7.62 cm; potassium phosphate buffer, 50.0 mM, pH 4.5), 2) diethylaminoethylene Sephadex A-25 (DEAE, 7.0 mL min^{-1}, 7.0 mL

fractions, 5.08 cm x 7.62 cm; Tris buffer, 50.0 mM, pH 8.0), 3) diethyl-(2-hydroxypropyl)aminoethyl Sephadex A-25 (QAE, 9.0 mL/min, 5.0 mL fractions, 1.5 cm x 8.0 cm; Tris buffer, 50.0 mM, pH 8.0), and 4) Sephadex P-10 gel filtration (0.1 mL min^{-1}, 5.0 mL fractions, 2.5 cm x 23.5 cm; Tris buffer, 50.0 mM, pH 8.0). Cation and anion exchange columns were developed with a KCl gradient using 0.25 M and 0.5 M KCl (in the same buffer) for wild type and H63C, respectively. Following SDS-PAGE analysis of the final chromatography procedure, red fractions were collected and desalted with centrifugal filter units (AU15), concentrated (AU05) to a minimal volume, and frozen in liquid nitrogen. Protein purity was determined from the absorbance ratio, A_{562nm}/A_{280nm}, for 280 nm absorbance from the oxidized species and 562 nm absorbance from the reduced species (pure protein affords a ratio of 1.5).[11]

The variant H63C was expressed and purified as described for wild type cytochrome b_{562} with the exception that buffers for all chromatography steps contained dithiothreitol (DTT, 1 mM) and DEAE, QAE and P-10 gel filtration columns were titrated to pH 7.5 at 4° C.

Expression and preparation of crude FdI: Glycerol stocks of *E. coli* BL21(DE3), harboring the correct plasmid for expression of FdI-KSCK containing no, N-, or C-terminal StrepII-tag, were removed from the -80°C and a small portion was removed, while the glycerol stock was still frozen, and used to inoculate 10 mL of LB medium containing kanamycin (70 μg mL^{-1}). Cultures were propagated overnight (250 rpm, 18 hrs, 37° C) to saturation and 1.0 mL was used to inoculate 1.0 L of 2xYT media containing kanamycin (70 μg mL^{-1}). The 1.0 L culture was shaken in an incubating shaker (250 rpm, 37°C) until the OD_{600} = 0.6 – 1.0 and induction of gene

expression, FdI, was initiated by addition of IPTG (0.1 mM). Following 24 hrs under inducing conditions, the culture was harvested by centrifugation (3700 rcf, 4°C). The supernatant was discarded and the cell paste was resuspended in Tris buffer (0.1 M Tris, pH 8.0). The outer and the inner membranes of *E. coli* were then disrupted by a CelLytic solution (Sigma) under mechanical rocking (30 min). To provide better mixing and cellular breakage, gentle vortexing was introduced for 30 s every 10 min. The crude cell extract was centrifuged (30 min, 13,000 rcf, 4°C), and the cleared supernatant was kept for further analysis while the pellet, containing cellular debris, was discarded.

Ammonium sulfate precipitation for FdI-KSCK variants: The cleared supernatant underwent a two-step ammonium sulfate precipitation: one cut at 50% and the other at 70% ammonium sulfate saturation. Following each ammonium sulfate cut, the solution was centrifuged (30 min, 15,000 rcf, 4°C) forming a pellet of insoluble material, while soluble proteins remained in the supernatant. The pellet was discarded after each centrifugation step. The cleared ammonium sulfate precipitation reaction was applied to a Sepharose 6B column.

Absorption Chromatography on Sepharose 6B for FdI-KSCK variants: Sepharose 6B resin (10 mL) was loaded into a disposable PD-10 column and was equilibrated by washing with three column volumes of Tris buffer (50 mM, pH 7.7) containing ammonium sulfate (70%). The cleared supernatant resulting from the second ammonium sulfate cut was applied to the column, which resulted in a sharp brown band at the top. The column was then washed with 5-10 column volumes of equilibration buffer before elution in Tris buffer (50 mM, pH 7.7). Brown fractions were collected,

pooled, and concentrated using 10 kDa centrifugal filters before application to a StrepTactin column.

StrepTactin column: The pooled and concentrated brown fractions from the Sepharose 6B column were applied to a StrepTactin column previously equilibrated with Tris (50 mM, pH 7.7, 150 mM NaCl), resulting in a brown band at the top of the column following application of all of the sample. The column was then washed with five column volumes of the equilibration buffer before elution with Tris (50 mM, pH 7.7, 150 mM NaCl) containing desthiobiotin (2.0 mM). Brown fractions were collected and pooled. Regeneration of the StrepTactin column was completed by using HABA (2-[4-hydroxy-benzeneazo]benzoic acid) saturated in Tris (50 mM, pH 7.7, 125mM NaCl).

Anion exchange with Diethylaminoethylene (DEAE): Pooled fractions from the StrepTactin column were applied to a DEAE column previously equilibrated with Tris (50 mM, pH 8.2), which resulted in a sharp red/brown band at the top of the column. The column was then washed sequentially with five column volumes of Tris (50 mM, pH 8.2) followed by Tris (50 mM, pH 8.2, 150 mM NaCl). Elution was carried out using Tris (50 mM, pH 8.2, 300 mM NaCl). Brown fractions were pooled, buffer exchanged to the proper electrochemical buffer, and concentrated before being stored in the -80C until further use.

FdI was

Cyclic voltammetry of cytochrome b_{562} while diffusing in solution: Solution phase electrochemistry was completed in a custom glass cell with a machined Teflon cap to stabilize the placement of the three-electrode setup. A platinum wire was used as the

counter electrode and a Ag/AgCl for the reference electrode. All electrochemical measurements were taken under an argon atmosphere by introduction of argon *via* syringe in the headspace of the glass cell. The potentiostat was a CH Instruments 200A electrochemical analyzer. All potentials were corrected to the standard hydrogen electrode (SHE) according to the equation $E_{SHE} = E_{Ag/AgCl} + 197$ mV at 25°C[6]. Edge Plane Pyrolytic Graphite (EPPG) working electrodes were constructed by attaching a cylindrical piece of graphite (r = 1.0 mm, Minteq) to a steel rod via a silver-loaded epoxy (AI Technologies, Princeton Junction, NJ) that was then inserted into a Teflon sheath. The exposed graphite was then encased within an adhesive epoxy (Epoxies Etc., Cranston, RI) and sanded down such that a flat surface of graphite was exposed.

Only pure cytochrome b_{562} with a milimolar extinction coefficient ratio of $562_{Reduced}$:$280_{Oxidized} = 1.5$ were used for the electrochemical experiments. Electrochemical assays were conducted in buffers as described by Barker et al. 1996 or Della Pia et al. 2011. EPPG electrodes were first polished with 1.0 μm aqueous alumina (Buehler) slurry followed by thorough rinsing and sonication. The electrode was then inserted into the glass cell containing a mixed buffer solution as described above and cycled between 0 mV and +500 mV at a scan rate of 50 mV s^{-1}. The electrochemical data were analyzed with SOAS, an electrochemical program freely available for download on the Internet at http://bip.cnrs-mrs.fr/bip06/software.html[8].

Immobilization of FdI-KSCK with neomycin as co-adsorbate. Pure FdI-KSCK with a UV-Vis ratio of 280:420 nm = 0.5 was used for electrochemical interrogation. All electrochemical experiments were conducted in an anaerobic glovebox under an atmosphere of nitrogen. Fresh edge-plane pyrolytic graphite (EPPG) electrode surfaces

were obtained by gentle sanding followed by sonication and drying. FdI-KSCK (2 μL, > 1.0 mg mL^{-1}) and neomycin (2 μL, 5 mM) were applied together to the electrode surface and allowed to dry. (~20 min). The electrode was then placed into a solution of MES, MOPS, TAPS buffer at pH 6.5 and the potential cycled between -0.5 and 0 V vs SHE.

Covalent immobilization using diazonium salts. EPPG electrodes were cleaned as above and immersed in an acetonitrile solution containing 0.2 mM *p*-nitrobenzene diazonium salt for five min to promote spontaneous association with the EPPG surface. Electrodes were rinsed with acetonitrile and water. Cyclic voltammetry over the range 0 to -1.0 V vs SHE at 50 mV s^{-1} was then undertaken for five cycles in 90:10 H_2O:EtOH with 0.1 M KCl to reduce the nitro group to an amine. The amino-terminated electrodes were rinsed thoroughly with ddH_2O before drying. FdI-KSCK (2 μL), N-(3-Dimethylaminopropyl)-N'-ethylcarbodiimide (2 μL, 36 mM), and N-hydroxysuccinimide (2 μL, 18 mM) were applied to the electrode surface, and the droplet evaporated to dryness. The electrode was then rinsed with ddH_2O and electrochemical measurements were conducted using the methods of cyclic voltammetry or square wave.

Results

Expression and purification of WT cytochrome b_{562} of H63C mutant. Inoculation of glycerol stocks containing *E. coli* (BL21(DE3)) containing, the proper plasmid, were suitable for expression. Cultures grown using 2xYT (no sodium chloride) produced the most cytochrome. Cultures were grown microaerobically, 1.5 L in 2.0 L flask. Baffled flasks were not suitable for expression. The pNS207 plasmid contains a constitutive promoter and induction with IPTG in unnecessary. Cultures should be harvested after 24-

36 hours and the resulting cell pellet, post centrifugation, should be pink to dark red. Cell lysis was completed in multiple ways: freeze thaw, lysozyme treatment, CelLytic. Centrifugation of lysed cells should produce a pink to red solution and the cleared solution should undergo an acid precipitation. Note: cytochromes are expelled to the growth medium during expression and can be harvested by use of a tangential flow filter equipped with a 10 kDa membrane, and following buffer exchange the sample can be combined with the cell lysate sample to undergo the acid precipitation. Centrifugation of the acid precipitation reaction and application of the cleared supernatant onto a CM52 column produces an intense red band at the top of the column. An elution gradient can be setup using the FPLC to increase the salt (KCl) from 0 to 0.5 M. Cytochrome eluted ~200 mM. Buffer exchange of the red eluent and application to DEAE and subsequent QAE columns produced sharp red bands at the top of each column. Elution was carried out as described for CM52 for both DEAE and QAE columns. Concentration of the red eluent from size exclusion chromatography afforded pure cytochrome sample as shown in **Figure B-1**. Pure protein suitable for electrochemical interrogation affords a UV-visible spectrum with a 2:1 ratio of the absorbance at 562 nm of the reduced sample to 280 nm of the oxidized sample.

Expression of FdI-KSCK (native to Spirulina platensis). FdI was successfully expressed in one of two constructs designed. Four point mutations were introduced to the coding sequence by DNA 2.0 and inserted intro expression vectors: K4R, S64K, C87S, K980R. Two constructs were ordered from DNA 2.0: one contained an N-terminal StrepII-tag and the other contained a C-terminal StrepII-tag. Expression requires induction with IPTG at OD_{600} = 0.5 -1.0. Expression was best in 2xYT (no sodium

chloride). Cell should be shaken in a heated incubator at 37° C for 24-36 hrs. Successful cell lysis was observed for procedures identical to cytochrome purification. The supernatant resulting from the cleared cell lysate can be directly applied to a StrepTactin column and protein is highly pure after. Increased purity can be obtained by conducting an ammonium sulfate precipitation on the cleared cell lysate. Following centrifugation of the ammonium sulfate precipitation the cleared supernatant is applied to a sepharose 6B column equilibrated with 2.8 M ammonium sulfate. Elution is then carried out in the equilibration buffer for the StrepTactin column and the eluent can be directly added to the StrepTactin column or concentrated first. UV-vis spectra of N-terminal and C-terminal products are shown in **Figure B-2**. Only the C-terminal variant shows a characteristic [2Fe2S] UV-vis spectrum. It is likely that the StrepII tag and/or the four point mutations are interfering with the native fold. A [4Fe4S] is likely the metalloprotein expressed, but this is only speculative. Pure protein suitable for electrochemical interrogation affords a UV-visible spectrum with a 2:1 ratio of the absorbance at 280 nm to 420 nm of the oxidized sample.

CD spectra of cytochrome b_{562} H63C mutant. **Figure B-3A** shows the resulting circular dichroism spectra while maintain the sample at 4° C, 20° C, and 90° C. The spectra at 4° C and 20° C show the desired minima at 222 and 208 nm for alpha-helical peptides. Upon heating to 90° C the adsorption at 222 and 208 nm dissipates and the protein is expected to maintain a random coil secondary structure. Figure 3B monitors the adsorption at 222 nm as a function of temperature and shows that the protein is expected to be relatively stable in solution up to ~75° C.

Electrochemistry of H63C. **Figure B-4** shows a cyclic voltammogram obtained from an EPPG electrode submersed in a purified and dilute solution of H63C. A control voltammogram was taken in phosphate buffer before addition of H63C and is also shown in **Figure B-4** (black trace). An $E_{1/2}$ of +125 mV vs SHE was obtained.

Figures

Table B-1. Strains, plasmids, and oligonucleotides employed in this study.

Strain	Characteristics	Source
E. coli		
DH5	fhuA2 Δ(argF-lacZ)U169 phoA glnV44 Φ80 Δ(lacZ)M15 gyrA96 recA1 relA1 endA1 thi-1 hsdR17 Chemically cloning competent	New England Biolabs (NEB)
BL21(DE3)	ΔhsdS λ DE3 = λ sBamHIo ΔEcoRI-B int::(lacI::PlacUV5::T7 gene1) i21 Δnin5 Chemically expression competent	New England Biolabs (NEB)

Plasmid		Source
pNS207	Wild type cytochrome b_{562}, Amp^r	
pNS207-H63C	Point mutation at position 63 His → Cys	This work
pJ411-SII-FdI-KSCK	N-terminal StrepII-tag, Kan^r, Single Cys residue	DNA 2.0
pJ411-FdI-SII-KSCK	C-terminal StrepII-tag, Kan^r, Single Cys residue	DNA 2.0
pJ411-FdI-KSCK	No StrepII-tag, Kanr, Single Lys residue, single Cys residue	This work

Oligonucleotides		Sequence
P1	H63C_F	5’-tgcGGTTTCGATATTCTGG-3’
P2	H63C_R	5’-GCGGAAATCTTTCATGTC-3’
P3	NoSII_F	5‘-ggccatATGGCAACTTATCGTGTTACGTTAATTAAT-3’
P4	NoSII_R	5’-GGGGCTCGAGTTATCAGTACAGG-3’
P5	T7	5’-TAATACGACTCACTATAGGG-3’
P6	T7_Term	5’-GCTAGTTATTGCTCAGCGG-3’

Δ denotes deletion or disruption of a gene,
^{r} denotes resistance to the specified antibiotic
lower case letters in the oligonucleotide sequence denote mutation sites.

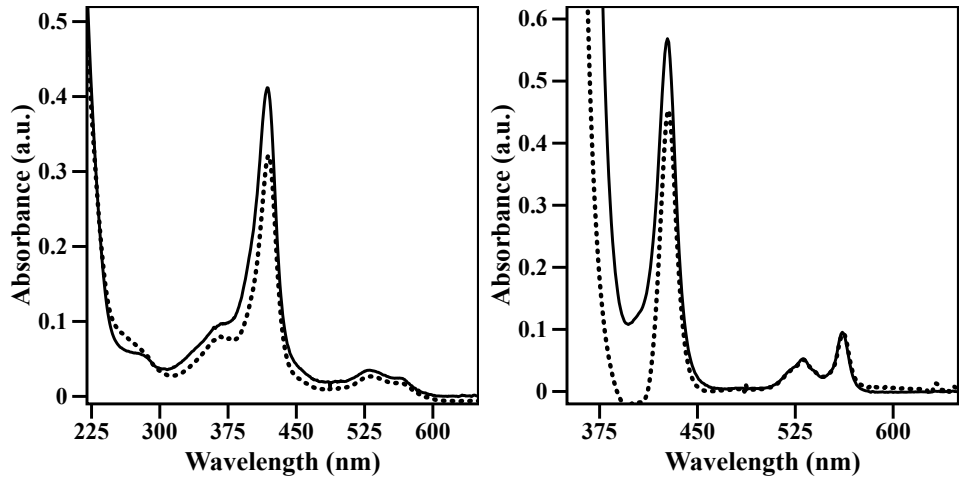

Figure B-1. UV-visible spectra of WT (dotted trace) cytochrome b_{562} and H63C mutant (solid trace). Oxidized (left) and reduced (right).

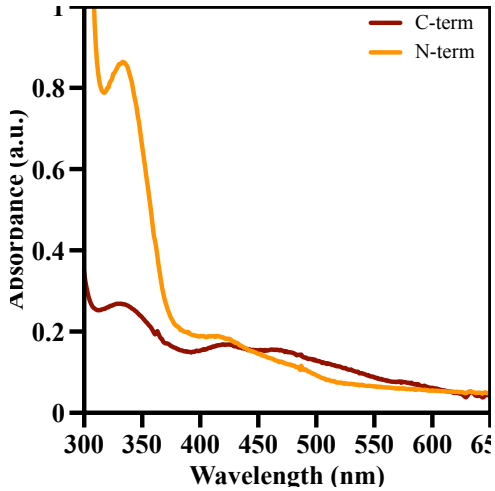

Figure B-2. UV-visible spectra of purified N-terminal FdI-KSCK and C-terminal FdI-KSCK.

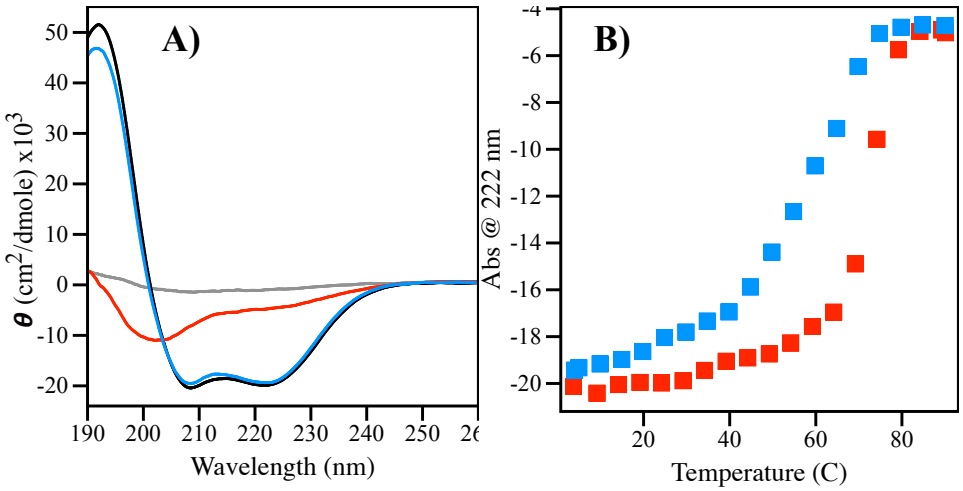

Figure B-3. CD spectra of cytochrome b_{562} mutant H63C in phosphate buffer. A) Blank solution of phosphate buffer (grey trace), spectra collected at 4°C (blue trace), 20°C (black trace), and 90°C (red trace). B) A decrease in intensity for the peak at 222 nm is observed as the solution is warmed from 4° C to 90° C (red squares). The solution was then cooled back to 4° C and a return of peak intensity at 222 nm was monitored (blue squares). 222 nm is used as a proxy for degree of helicity.

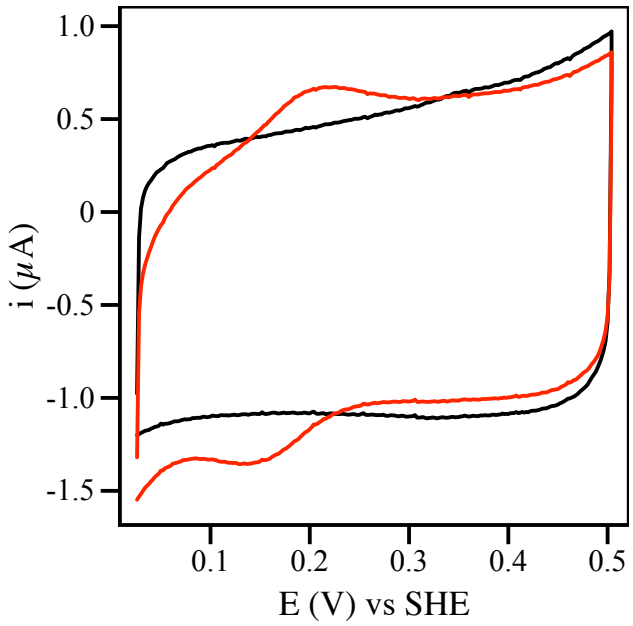

Figure B-4. EPPG electrode in the presence of a dilute solution of H63C in phosphate buffer. Scan rate is 20 mV s^{-1}, room temperature, 2 mM Neomycin.

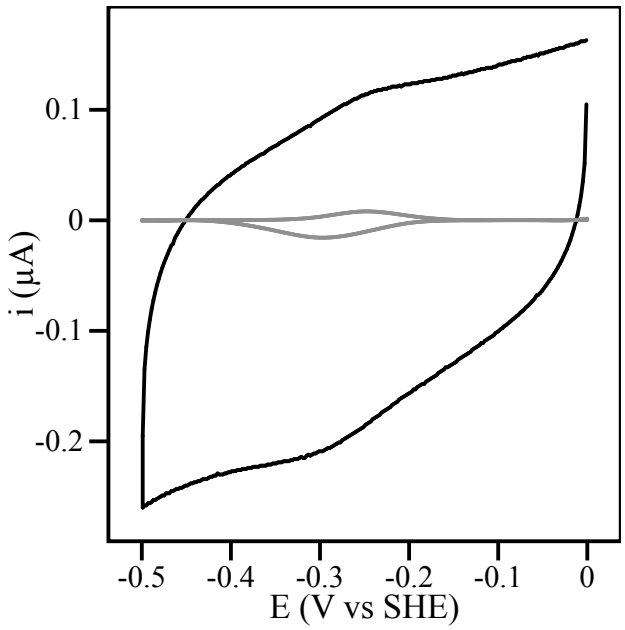

Figure B-5. Cyclic voltammogram of C-terminal FdI-KSCK adsorbed on an EPPG electrode using neomycin (5 mM) as a co-adsorbate. Scan rate is 20 mV s^{-1}, room temperature, MMT buffer pH 6.5.

References

(1) Nikkila, H.; Gennis, R. B.; Sligar, S. G. *Eur. J. Biochem.* **1991**, *202*, 309–313.

(2) Itagaki, E.; Palmer, G.; Hager, L. P. *J. Bio. Chem.* **1967**.

(3) Barker, P. D.; Nerou, E. P.; Freund, S. M. V.; Fearnley, I. M. *Biochemistry.* **1995**, *34*, 15191–15203.

(4) Johnson, B. H.; Hecht, M. H. *Bio. Tech. 12*, 1–4.

(5) Itagaki, E.; Hager, L. P. *J. Bio. Chem.* **1966**.

(6) Bard, A. J.; Faulkner, L. R. **2001**, 1–850.

(7) Pia, E. A. D.; Chi, Q.; Jones, D. D.; Macdonald, J. E.; Ulstrup, J.; Elliott, M. *Nano Lett.* **2011**, *11*, 176–182.

(8) Fourmond, V.; Hoke, K.R.; Heering, H.A.; Baffer, C.; Leroux, F.; Bertrand, P.; Léger, C. Bioelectrochemistry. 2009, 76, 141–147.

APPENDIX C

PERMISSION TO REPRODUCE CHAPTERS 2, 4, AND 6 FROM THE EUROPEAN JOURNAL OF INORGANIC CHEMISTRY, CHEMICAL COMMUNICATIONS, AND SPRINGER, RESPECTIVELY

Hydrogen production from water using a bis(imino)pyridine molybdenum electrocatalyst

R. Pal, J. A. Laureanti, T. L. Groy, A. K. Jones and R. J. Trovitch, *Chem. Commun.*, 2016, **52**, 11555
DOI: 10.1039/C6CC04946J

2/24/2017 Request Permission

SPRINGER LICENSE
TERMS AND CONDITIONS

Feb 24, 2017

This Agreement between Joseph A Laureanti ("You") and Springer ("Springer") consists of your license details and the terms and conditions provided by Springer and Copyright Clearance Center.

License Number	4055551377541
License date	
Licensed Content Publisher	Springer
Licensed Content Publication	Springer eBook
Licensed Content Title	Photosynthetic Microbial Fuel Cells
Licensed Content Author	Joseph A. Laureanti
Licensed Content Date	Jan 1, 2016
Type of Use	Thesis/Dissertation
Portion	Full text
Number of copies	1
Author of this Springer article	Yes and you are the sole author of the new work
Order reference number	
Title of your thesis / dissertation	Bioinspired electrocatalytic hydrogen evolution: Synthetic and biological approaches
Expected completion date	Mar 2017
Estimated size(pages)	250
Requestor Location	Joseph A Laureanti 151 E. Broadway Rd. 209 TEMPE, AZ 85282 United States Attn: Joseph A Laureanti
Billing Type	Invoice
Billing Address	Joseph A Laureanti 151 E. Broadway Rd. 209 TEMPE, AZ 85282 United States Attn: Joseph A Laureanti
Total	0.00 USD
Terms and Conditions	

Introduction
The publisher for this copyrighted material is Springer. By clicking "accept" in connection with completing this licensing transaction, you agree that the following terms and conditions apply to this transaction (along with the Billing and Payment terms and conditions

established by Copyright Clearance Center, Inc. ("CCC"), at the time that you opened your Rightslink account and that are available at any time at http://myaccount.copyright.com).

Limited License

With reference to your request to reuse material on which Springer controls the copyright, permission is granted for the use indicated in your enquiry under the following conditions:

- Licenses are for one-time use only with a maximum distribution equal to the number stated in your request.
- Springer material represents original material which does not carry references to other sources. If the material in question appears with a credit to another source, this permission is not valid and authorization has to be obtained from the original copyright holder.
- This permission
• is non-exclusive
• is only valid if no personal rights, trademarks, or competitive products are infringed.
• explicitly excludes the right for derivatives.
- Springer does not supply original artwork or content.
- According to the format which you have selected, the following conditions apply accordingly:
• **Print and Electronic:** This License include use in electronic form provided it is password protected, on intranet, or CD-Rom/DVD or E-book/E-journal. It may not be republished in electronic open access.
• **Print:** This License excludes use in electronic form.
• **Electronic:** This License only pertains to use in electronic form provided it is password protected, on intranet, or CD-Rom/DVD or E-book/E-journal. It may not be republished in electronic open access.

For any electronic use not mentioned, please contact Springer at permissions.springer@spi-global.com.

- Although Springer controls the copyright to the material and is entitled to negotiate on rights, this license is only valid subject to courtesy information to the author (address is given in the article/chapter).
- If you are an STM Signatory or your work will be published by an STM Signatory and you are requesting to reuse figures/tables/illustrations or single text extracts, permission is granted according to STM Permissions Guidelines: http://www.stm-assoc.org/permissions-guidelines/

For any electronic use not mentioned in the Guidelines, please contact Springer at permissions.springer@spi-global.com. If you request to reuse more content than stipulated in the STM Permissions Guidelines, you will be charged a permission fee for the excess content.

Permission is valid upon payment of the fee as indicated in the licensing process. If permission is granted free of charge on this occasion, that does not prejudice any rights we might have to charge for reproduction of our copyrighted material in the future.

-If your request is for reuse in a Thesis, permission is granted free of charge under the following conditions:

This license is valid for one-time use only for the purpose of defending your thesis and with a maximum of 100 extra copies in paper. If the thesis is going to be published, permission needs to be reobtained.

- includes use in an electronic form, provided it is an author-created version of the thesis on his/her own website and his/her university's repository, including UMI (according to the definition on the Sherpa website: http://www.sherpa.ac.uk/romeo/);
- is subject to courtesy information to the co-author or corresponding author.

Geographic Rights: Scope

Licenses may be exercised anywhere in the world.

Altering/Modifying Material: Not Permitted

Figures, tables, and illustrations may be altered minimally to serve your work. You may not

alter or modify text in any manner. Abbreviations, additions, deletions and/or any other alterations shall be made only with prior written authorization of the author(s).

Reservation of Rights

Springer reserves all rights not specifically granted in the combination of (i) the license details provided by you and accepted in the course of this licensing transaction and (ii) these terms and conditions and (iii) CCC's Billing and Payment terms and conditions.

License Contingent on Payment

While you may exercise the rights licensed immediately upon issuance of the license at the end of the licensing process for the transaction, provided that you have disclosed complete and accurate details of your proposed use, no license is finally effective unless and until full payment is received from you (either by Springer or by CCC) as provided in CCC's Billing and Payment terms and conditions. If full payment is not received by the date due, then any license preliminarily granted shall be deemed automatically revoked and shall be void as if never granted. Further, in the event that you breach any of these terms and conditions or any of CCC's Billing and Payment terms and conditions, the license is automatically revoked and shall be void as if never granted. Use of materials as described in a revoked license, as well as any use of the materials beyond the scope of an unrevoked license, may constitute copyright infringement and Springer reserves the right to take any and all action to protect its copyright in the materials.

Copyright Notice: Disclaimer

You must include the following copyright and permission notice in connection with any reproduction of the licensed material:

"Springer book/journal title, chapter/article title, volume, year of publication, page, name(s) of author(s), (original copyright notice as given in the publication in which the material was originally published) "With permission of Springer"

In case of use of a graph or illustration, the caption of the graph or illustration must be included, as it is indicated in the original publication.

Warranties: None

Springer makes no representations or warranties with respect to the licensed material and adopts on its own behalf the limitations and disclaimers established by CCC on its behalf in its Billing and Payment terms and conditions for this licensing transaction.

Indemnity

You hereby indemnify and agree to hold harmless Springer and CCC, and their respective officers, directors, employees and agents, from and against any and all claims arising out of your use of the licensed material other than as specifically authorized pursuant to this license.

No Transfer of License

This license is personal to you and may not be sublicensed, assigned, or transferred by you without Springer's written permission.

No Amendment Except in Writing

This license may not be amended except in a writing signed by both parties (or, in the case of Springer, by CCC on Springer's behalf).

Objection to Contrary Terms

Springer hereby objects to any terms contained in any purchase order, acknowledgment, check endorsement or other writing prepared by you, which terms are inconsistent with these terms and conditions or CCC's Billing and Payment terms and conditions. These terms and conditions, together with CCC's Billing and Payment terms and conditions (which are incorporated herein), comprise the entire agreement between you and Springer (and CCC) concerning this licensing transaction. In the event of any conflict between your obligations established by these terms and conditions and those established by CCC's Billing and Payment terms and conditions, these terms and conditions shall control.

Jurisdiction

All disputes that may arise in connection with this present License, or the breach thereof,

shall be settled exclusively by arbitration, to be held in the Federal Republic of Germany, in accordance with German law.

Other conditions:

V 12AUG2015

JOHN WILEY AND SONS LICENSE
TERMS AND CONDITIONS

Apr 07, 2017

This Agreement between Joseph A Laureanti ("You") and John Wiley and Sons ("John Wiley and Sons") consists of your license details and the terms and conditions provided by John Wiley and Sons and Copyright Clearance Center.

License Number	4083901089192
License date	Apr 07, 2017
Licensed Content Publisher	John Wiley and Sons
Licensed Content Publication	European Journal of Inorganic Chemistry
Licensed Content Title	Synthesis and Electrocatalytic Activity of [FeFe]-Hydrogenase Model Complexes with Non-Innocent Chelating Nitrogen-Donor Ligands
Licensed Content Author	Souvik Roy,Joseph A. Laureanti,Thomas L. Groy,Anne K. Jones
Licensed Content Date	Apr 7, 2017
Licensed Content Pages	1
Type of use	Dissertation/Thesis
Requestor type	Author of this Wiley article
Format	Print and electronic
Portion	Full article
Will you be translating?	No
Title of your thesis / dissertation	Bioinspired electrocatalytic hydrogen evolution: Synthetic and biological approaches
Expected completion date	Mar 2017
Expected size (number of pages)	250
Requestor Location	Joseph A Laureanti 151 E. Broadway Rd. 209 TEMPE, AZ 85282 United States Attn: Joseph A Laureanti
Publisher Tax ID	EU826007151
Billing Type	Invoice
Billing Address	Joseph A Laureanti 151 E. Broadway Rd. 209 TEMPE, AZ 85282 United States Attn: Joseph A Laureanti
Total	0.00 USD
Terms and Conditions	

TERMS AND CONDITIONS

This copyrighted material is owned by or exclusively licensed to John Wiley & Sons, Inc. or one of its group companies (each a"Wiley Company") or handled on behalf of a society with which a Wiley Company has exclusive publishing rights in relation to a particular work (collectively "WILEY"). By clicking "accept" in connection with completing this licensing transaction, you agree that the following terms and conditions apply to this transaction (along with the billing and payment terms and conditions established by the Copyright Clearance Center Inc., ("CCC's Billing and Payment terms and conditions"), at the time that you opened your RightsLink account (these are available at any time at http://myaccount.copyright.com).

Terms and Conditions

- The materials you have requested permission to reproduce or reuse (the "Wiley Materials") are protected by copyright.

- You are hereby granted a personal, non-exclusive, non-sub licensable (on a stand-alone basis), non-transferable, worldwide, limited license to reproduce the Wiley Materials for the purpose specified in the licensing process. This license, **and any CONTENT (PDF or image file) purchased as part of your order,** is for a one-time use only and limited to any maximum distribution number specified in the license. The first instance of republication or reuse granted by this license must be completed within two years of the date of the grant of this license (although copies prepared before the end date may be distributed thereafter). The Wiley Materials shall not be used in any other manner or for any other purpose, beyond what is granted in the license. Permission is granted subject to an appropriate acknowledgement given to the author, title of the material/book/journal and the publisher. You shall also duplicate the copyright notice that appears in the Wiley publication in your use of the Wiley Material. Permission is also granted on the understanding that nowhere in the text is a previously published source acknowledged for all or part of this Wiley Material. Any third party content is expressly excluded from this permission.

- With respect to the Wiley Materials, all rights are reserved. Except as expressly granted by the terms of the license, no part of the Wiley Materials may be copied, modified, adapted (except for minor reformatting required by the new Publication), translated, reproduced, transferred or distributed, in any form or by any means, and no derivative works may be made based on the Wiley Materials without the prior permission of the respective copyright owner.**For STM Signatory Publishers clearing permission under the terms of the STM Permissions Guidelines only, the terms of the license are extended to include subsequent editions and for editions in other languages, provided such editions are for the work as a whole in situ and does not involve the separate exploitation of the permitted figures or extracts,** You may not alter, remove or suppress in any manner any copyright, trademark or other notices displayed by the Wiley Materials. You may not license, rent, sell, loan, lease, pledge, offer as security, transfer or assign the Wiley Materials on a stand-alone basis, or any of the rights granted to you hereunder to any other person.

- The Wiley Materials and all of the intellectual property rights therein shall at all times remain the exclusive property of John Wiley & Sons Inc, the Wiley Companies, or their respective licensors, and your interest therein is only that of having possession of and the right to reproduce the Wiley Materials pursuant to Section 2 herein during the continuance of this Agreement. You agree that you own no right, title or interest in or to the Wiley Materials or any of the intellectual property rights therein. You shall have no rights hereunder other than the license as provided for above in Section 2. No right, license or interest to any trademark, trade name, service mark or other branding

("Marks") of WILEY or its licensors is granted hereunder, and you agree that you shall not assert any such right, license or interest with respect thereto

- NEITHER WILEY NOR ITS LICENSORS MAKES ANY WARRANTY OR REPRESENTATION OF ANY KIND TO YOU OR ANY THIRD PARTY, EXPRESS, IMPLIED OR STATUTORY, WITH RESPECT TO THE MATERIALS OR THE ACCURACY OF ANY INFORMATION CONTAINED IN THE MATERIALS, INCLUDING, WITHOUT LIMITATION, ANY IMPLIED WARRANTY OF MERCHANTABILITY, ACCURACY, SATISFACTORY QUALITY, FITNESS FOR A PARTICULAR PURPOSE, USABILITY, INTEGRATION OR NON-INFRINGEMENT AND ALL SUCH WARRANTIES ARE HEREBY EXCLUDED BY WILEY AND ITS LICENSORS AND WAIVED BY YOU.

- WILEY shall have the right to terminate this Agreement immediately upon breach of this Agreement by you.

- You shall indemnify, defend and hold harmless WILEY, its Licensors and their respective directors, officers, agents and employees, from and against any actual or threatened claims, demands, causes of action or proceedings arising from any breach of this Agreement by you.

- IN NO EVENT SHALL WILEY OR ITS LICENSORS BE LIABLE TO YOU OR ANY OTHER PARTY OR ANY OTHER PERSON OR ENTITY FOR ANY SPECIAL, CONSEQUENTIAL, INCIDENTAL, INDIRECT, EXEMPLARY OR PUNITIVE DAMAGES, HOWEVER CAUSED, ARISING OUT OF OR IN CONNECTION WITH THE DOWNLOADING, PROVISIONING, VIEWING OR USE OF THE MATERIALS REGARDLESS OF THE FORM OF ACTION, WHETHER FOR BREACH OF CONTRACT, BREACH OF WARRANTY, TORT, NEGLIGENCE, INFRINGEMENT OR OTHERWISE (INCLUDING, WITHOUT LIMITATION, DAMAGES BASED ON LOSS OF PROFITS, DATA, FILES, USE, BUSINESS OPPORTUNITY OR CLAIMS OF THIRD PARTIES), AND WHETHER OR NOT THE PARTY HAS BEEN ADVISED OF THE POSSIBILITY OF SUCH DAMAGES. THIS LIMITATION SHALL APPLY NOTWITHSTANDING ANY FAILURE OF ESSENTIAL PURPOSE OF ANY LIMITED REMEDY PROVIDED HEREIN.

- Should any provision of this Agreement be held by a court of competent jurisdiction to be illegal, invalid, or unenforceable, that provision shall be deemed amended to achieve as nearly as possible the same economic effect as the original provision, and the legality, validity and enforceability of the remaining provisions of this Agreement shall not be affected or impaired thereby.

- The failure of either party to enforce any term or condition of this Agreement shall not constitute a waiver of either party's right to enforce each and every term and condition of this Agreement. No breach under this agreement shall be deemed waived or excused by either party unless such waiver or consent is in writing signed by the party granting such waiver or consent. The waiver by or consent of a party to a breach of any provision of this Agreement shall not operate or be construed as a waiver of or consent to any other or subsequent breach by such other party.

- This Agreement may not be assigned (including by operation of law or otherwise) by you without WILEY's prior written consent.

- Any fee required for this permission shall be non-refundable after thirty (30) days from receipt by the CCC.

- These terms and conditions together with CCC's Billing and Payment terms and conditions (which are incorporated herein) form the entire agreement between you and WILEY concerning this licensing transaction and (in the absence of fraud) supersedes all prior agreements and representations of the parties, oral or written. This Agreement may not be amended except in writing signed by both parties. This Agreement shall be binding upon and inure to the benefit of the parties' successors, legal representatives, and authorized assigns.

- In the event of any conflict between your obligations established by these terms and conditions and those established by CCC's Billing and Payment terms and conditions, these terms and conditions shall prevail.

- WILEY expressly reserves all rights not specifically granted in the combination of (i) the license details provided by you and accepted in the course of this licensing transaction, (ii) these terms and conditions and (iii) CCC's Billing and Payment terms and conditions.

- This Agreement will be void if the Type of Use, Format, Circulation, or Requestor Type was misrepresented during the licensing process.

- This Agreement shall be governed by and construed in accordance with the laws of the State of New York, USA, without regards to such state's conflict of law rules. Any legal action, suit or proceeding arising out of or relating to these Terms and Conditions or the breach thereof shall be instituted in a court of competent jurisdiction in New York County in the State of New York in the United States of America and each party hereby consents and submits to the personal jurisdiction of such court, waives any objection to venue in such court and consents to service of process by registered or certified mail, return receipt requested, at the last known address of such party.

WILEY OPEN ACCESS TERMS AND CONDITIONS

Wiley Publishes Open Access Articles in fully Open Access Journals and in Subscription journals offering Online Open. Although most of the fully Open Access journals publish open access articles under the terms of the Creative Commons Attribution (CC BY) License only, the subscription journals and a few of the Open Access Journals offer a choice of Creative Commons Licenses. The license type is clearly identified on the article.

The Creative Commons Attribution License

The Creative Commons Attribution License (CC-BY) allows users to copy, distribute and transmit an article, adapt the article and make commercial use of the article. The CC-BY license permits commercial and non-

Creative Commons Attribution Non-Commercial License

The Creative Commons Attribution Non-Commercial (CC-BY-NC)License permits use, distribution and reproduction in any medium, provided the original work is properly cited and is not used for commercial purposes.(see below)

Creative Commons Attribution-Non-Commercial-NoDerivs License

The Creative Commons Attribution Non-Commercial-NoDerivs License (CC-BY-NC-ND) permits use, distribution and reproduction in any medium, provided the original work is properly cited, is not used for commercial purposes and no modifications or adaptations are made. (see below)

Use by commercial "for-profit" organizations

APPENDIX D

COAUTHOR APPROVALS AND CONTRIBUTIONS

COAUTHOR APPROVALS

All co-authors have granted permission for use of previously published material presented in Chapters 2, 4, and 6 for the purpose of this dissertation. All co-authors have granted permission for use of previously unpublished material presented in Chapters 3, 5, and 7 for the purpose of this dissertation.

AUTHOR CONTRIBUTIONS

Chapter 2

Souvik Roy. Designed research. Performed research. Contributed new reagents or analytic tools. Analyzed data. Wrote the paper.

Joseph A. Laureanti. Performed research. Contributed new reagents or analytic tools. Analyzed data.

Thomas L. Groy. Performed research. Contributed new reagents or analytic tools. Analyzed data.

Anne K. Jones. Designed research. Analyzed data. Wrote the paper.

Chapter 3

Joseph A. Laureanti. Designed research. Performed research. Contributed new reagents or analytic tools. Analyzed data. Wrote the paper.

Abhishek Debnath. Performed research. Contributed new reagents or analytic tools.

Shobeir K. S. Mazinani. Performed research. Contributed new reagents or analytic tools. Analyzed data.

Thomas L. Groy. Performed research. Contributed new reagents or analytic tools. Analyzed data.

Vladimiro Mujica. Analyzed data.

Anne K. Jones. Designed research. Analyzed data. Wrote the paper.

Chapter 4

Raja Pal. Designed research. Performed research. Contributed new reagents or analytic tools. Analyzed data. Wrote the paper.

Joseph A. Laureanti. Designed research. Performed research. Contributed new reagents or analytic tools. Analyzed data. Wrote the paper.

Thomas L. Groy. Performed research. Contributed new reagents or analytic tools. Analyzed data.

Anne K. Jones. Designed research. Analyzed data. Wrote the paper.

Ryan J. Trovitch. Designed research. Analyzed data. Wrote the paper.

Chapter 5

Ki-Wan Jeon. Designed research. Performed research. Contributed new reagents or analytic tools. Analyzed data. Wrote the paper.

Joseph A. Laureanti. Designed research. Performed research. Contributed new reagents or analytic tools. Analyzed data. Wrote the paper.

Lei Yu. Performed research. Analyzed data.

Nathan Newman. Performed research. Analyzed data.

Anne K. Jones. Designed research. Analyzed data. Wrote the paper.

Dong-Kyun Seo. Designed research. Analyzed data. Wrote the paper.

Chapter 6

Joseph A. Laureanti. Analyzed data. Wrote the paper.

Anne K. Jones. Analyzed data. Wrote the paper.

Chapter 7

Joseph A. Laureanti. Designed research. Performed research. Contributed new reagents or analytic tools. Analyzed data. Wrote the paper.

Christopher Gisriel. Designed research. Performed research. Contributed new reagents or analytic tools. Analyzed data.

Kevin E. Redding. Designed research. Analyzed data. Wrote the paper.

Anne K. Jones. Designed research. Analyzed data. Wrote the paper.